

THESIS / THÈSE

DOCTOR OF SCIENCES

Contribution to the improvement of radiotherapy treatments driven by nanotechnology

Penninckx, Sébastien

Award date:
2019

Awarding institution:
University of Namur

[Link to publication](#)

General rights

Copyright and moral rights for the publications made accessible in the public portal are retained by the authors and/or other copyright owners and it is a condition of accessing publications that users recognise and abide by the legal requirements associated with these rights.

- Users may download and print one copy of any publication from the public portal for the purpose of private study or research.
- You may not further distribute the material or use it for any profit-making activity or commercial gain
- You may freely distribute the URL identifying the publication in the public portal ?

Take down policy

If you believe that this document breaches copyright please contact us providing details, and we will remove access to the work immediately and investigate your claim.

University of Namur – Faculty of Sciences
Namur Research Institute for Life Sciences (NARILIS)

Contribution to the improvement of radiotherapy treatments driven by nanotechnology

Original dissertation presented by
Sébastien Penninckx for the degree
of doctor of sciences

Jury members:

Prof. Stéphane LUCAS (Supervisor)

Laboratoire d'Analyse par Réactions
Nucléaires (LARN - NARILIS)
UNamur, Namur, Belgium

Prof. Carine MICHIELS (Co-supervisor)

Unité de Recherche en Biochimie et
Biologie Cellulaire (URBC - NARILIS)
UNamur, Namur, Belgium

Dr. Philippe MARTINIVE

Service de radiothérapie - oncologie
Institut Bordet, Bruxelles, Belgium

Prof. Nadine MILLOT

Bio-hybrid nanoparticles & nanostructures
Nanosciences department
ICB, Bourgogne, France

Dr. Sylvain COSTES

NASA GeneLab
NASA Ames Research Center, CA, USA

Prof. Thierry ARNOULD (Chairman)

Unité de Recherche en Biochimie et
Biologie Cellulaire (URBC - NARILIS)
UNamur, Namur, Belgium

Remerciement

Ça y est, on y est ... déjà ! La rédaction de ces dernières lignes signe l'aboutissement de 3 ans et 5 mois d'une formidable aventure. Cette thèse représente 1247 jours de travail et tout autant de belles rencontres. Elle est le fruit de beaucoup d'investissement de ma part mais aussi de la part de dizaines de collaborateurs qui y ont contribué de près ou de loin. Il est donc temps de modestement les remercier pour tout ce qu'ils ont fait. Malheureusement, mon Alzheimer précoce implique que je vais oublier une série de personnes. Que celles-ci acceptent déjà mes excuses et soient assurés de toute ma reconnaissance.

Je voudrais tout d'abord remercier mes promoteurs, Stéphane Lucas et Carine Michiels de m'avoir accueilli dans leur équipe. Merci d'avoir donné sa chance à un chimiste sorti de nulle part qui ne demandait qu'à élargir ses horizons scientifiques. Merci Stéphane pour la confiance que vous m'avez témoignée et de m'avoir poussé à systématiquement voir plus loin. Merci Carine pour votre disponibilité et nos échanges toujours constructifs et enrichissants. Ensemble, votre parfaite complémentarité m'aura fait grandir tant d'un point de vue professionnel que personnel. Pour tout ça et bien plus encore, merci !

Je remercie également les professeurs Thierry Arnould et Nadine Millot ainsi que les docteurs Philippe Martinive et Sylvain Costes d'avoir accepté de faire partie de mon jury de thèse et pour leurs commentaires constructifs qui ont permis d'améliorer ce manuscrit.

Pour réaliser ce travail, j'ai été intégré à l'équipe « radiobio », une équipe pluridisciplinaire qui a compris que sa grande force résidait dans nos backgrounds différents. Merci Anne-catherine Heuskin, Anne-catherine Wera, Géraldine Genard, Sha Li et Cécile Bopp. J'ai toujours pu trouver des réponses à mes questions auprès de vous.

Merci aussi à tous les membres du LARN, anciens et nouveaux. Je ne me risquerai pas à les lister tous individuellement parce que ce serait trop long et par peur d'en oublier. Je dirais donc simplement un grand MERCI à tous pour les moments passés ensemble au laboratoire (tartes de 10h30, ...) et en dehors (week-end LARN, ...). Si je ne devenais citer qu'une personne, ce serait un remerciement tout particulier à Tijani pour son aide technique sans laquelle cette thèse ne serait sans doute pas ce qu'elle est aujourd'hui. Je n'oublie pas les membres de l'URBC qui ont animé mes vendredi soir par leur traditionnel « Beer Hour » ainsi que Benjamin Le Calvé qui m'a permis d'élargir mes horizons scientifiques. Merci enfin aux deux autres chimistes de l'URBC, Sébastien Marx et Thomas Dal Maso pour les moments partagés autour des manip. Néanmoins, après l'effort vient le réconfort. Merci donc à mes compagnons de guindaille (Adrien, Polo, Romain, Bruno, Marie, Mathilde et Héloïse) qui ont rendu ces afterworks bien plus intéressants.

Toute ma reconnaissance va également à Sylvain Costes pour m'avoir permis d'intégrer son équipe au NASA Ames Research Center et au Lawrence Berkeley National Laboratory ainsi que pour les bons moments passés en Californie. Thanks to all the Costes' lab members but especially Shayoni Ray, Egle Cekanaviciute, Kaushik Chakravarty, Louise Viger and Elodie Guet. It was very enriching and a real pleasure to work with you guys! Special thanks for Janice Pluth from Nevada-Las Vegas University for their supervision during this research trip.

J'exprime également ma gratitude à Pierre Cambier, Eric Perpète, Catherine Demazy et Anna Usoltseva pour leur disponibilité et leur aide technique avec respectivement l'AAS, les mesures de potentiel zêta, le microscope confocal et le TEM. Sans oublier, Isabelle Derycke pour le support informatique ... dieu sait que j'ai encore du travail à faire dans ce domaine pour me mettre à jour.

Merci aussi à Stéphanie Deroo et Rabia Sarroukh pour m'avoir transmis cette passion pour la recherche. « Tu es fait pour ça mais barre toi d'ici ! » restera le meilleur conseil que l'on m'a donné jusqu'à présent.

Je n'oublie pas de remercier ma famille pour leur soutien moral indéfectible. Enfin, merci à Sophie de m'avoir épaulé et encouragé pendant ces années de thèse mais surtout pour m'avoir évité le mal de mer en passant des heures devant le microscope. Merci de ne pas me prendre pour un fou chaque fois que me vient une nouvelle idée foireuse au milieu de la nuit.

A vous tous, encore merci.

Cette thèse, c'est aussi la vôtre car comme disait Nelson Mandela :

“Aucun de nous, en agissant seul, ne peut atteindre le succès.”

Table of content

Table of content.....	4
Abbreviation list.....	6
List of figures.....	7
List of tables	9
List of publications	10
Résumé	12
Abstract.....	14
PART I: Introduction	
1. Cancer	17
1.1. Generalities.....	17
1.2. Epidemiology.....	18
1.3. Treatment modalities.....	20
2. Radiotherapy: from physical interaction to biological damages.....	22
2.1. Interaction of photons with matter	22
2.2. Charged particle interaction with matter	25
2.3. Interaction of electrons with matter	28
2.4. Water radiolysis	29
2.5. ROS and cell death	31
2.6. Factors influencing the success of radiotherapy	36
2.7. Comparison between conventional radiotherapy and charged particle therapy	38
3. Nanoparticles as radiosensitizers: emergence of a new field in nanomedicine	42
3.1. Modifying the cellular response to radiation. Motivation and available solutions.....	42
3.2. Nanotechnology from chemical applications to nanomedicine	44
3.3. High Z nanoparticle as radiosensitizer: basic principles	47
3.4. High Z nanoparticle as radiosensitizer: state-of-art.....	51
3.5. Confrontation between theoretical physical predictions and experimental evidences.....	57
PART II: Objectives	
4. Objectives	61
PART III: Results	
5. Gold nanoparticle synthesis and characterization	63
5.1. Synthesis	63
5.2. Characterization.....	64
5.3. Scale-up.....	67

6. Gold nanoparticles as radiosensitizer for protontherapy: <i>in vitro</i> proof-of concept and key parameters	68
6.1. Context and goal of this study	68
6.2. First manuscript: “LET-dependent radiosensitization effects of gold nanoparticles for proton irradiation” – Nanotechnology (2016)	68
7. Mechanistic investigations	83
7.1. Physico-chemical insights	83
7.2. Biological insights	89
7.2.1. Context and goal of this study	89
7.2.2. Second manuscript: “The role of thioredoxin reductase in radiosensitization effect of gold nanoparticles” – Nanomedicine (2018)	89
7.2.3. Third manuscript: “Thioredoxin reductase activity predicts gold nanoparticle radiosensitization effect” – Nanomaterials (submitted January 2019)	115
8. Towards a clinical use of GNPs as radiosensitizers	130
8.1. Context and goal of the study	130
8.2. Fourth manuscript: “Antibody-functionalized gold nanoparticles as tumor targeting radiosensitizers for proton therapy”	130
9. Towards a better understanding of DNA damage induced by high-Z particles	155
9.1. Context and goal of the study	155
9.2. Fifth manuscript: The 15-strain irradiation study Part I - Dose, LET and strain dependence of radiation-induced 53BP1+ foci in 15 mouse strains	155
9.3. The 15-strain irradiation study Part II	172
PART IV: Discussion & further directions	
10. The mechanisms responsible for the radiosensitization effect of GNPs	176
10.1. Physical enhancement	176
10.2. Chemical enhancement	178
10.3. Biological enhancement	179
11. Design of the ideal NPs for an optimized enhancement effect	181
12. Towards personalized medicine in radiotherapy	187
PART V: References	
13. References	190

Abbreviation list

3-CCA: Coumarin-3-carboxylic acid

53BP1: 53-binding protein 1

ASC: Ascorbic acid

ATM: Ataxia telangiectasia mutated protein kinase

BSA: Bovine serum albumin

CD: Companion diagnostic

CFRT: Conformal radiotherapy

CTIP: CtBP-interacting protein

DDR: DNA damage response

DEU: Dose enhancement unit

DMSO: Dimethyl sulfoxide

DNA: Deoxyribonucleic acid

DNA-PkC: DNA-dependent protein kinase

DSB: Double-stand break

EGFR: Epithelial growth factor receptor

EMA: European Medicines Agency

EPR: Enhanced permeation and retention

FBS: Fetal bovine serum

FDA: Food & Drug Administration

GNP: Gold nanoparticle

GSH: Glutathione

GWAS: Genome-wide-association study

HBSS: Hank's Balanced Salt Solution

HNSCC: Head & Neck small cell carcinoma

HR: Homologous recombination

IMRT: Intensity Modulated Radiation Therapy

IORT: Intra-operative radiotherapy

IR: Irradiation

LET: Linear energy transfer

MFI: Mean Fluorescence Intensity

NHEJ: Non-homologous end joining

NP: Nanoparticle

NTCP: Normal tissue complication probability

OER: Oxygen enhancement ratio

PCWC: Probability of cure without complication

PD-1: Programmed cell death 1

PD-L1: Programmed cell death ligand 1

PEG: Polyethylene glycol

PTCOG: Proton Therapy Co-Operative Group

RIF: Radiation induced foci

RBE: Relative biological effectiveness

RES: Reticuloendothelial system

RNA: Ribonucleic acid

ROS: Reactive Oxygen Species

SEER: Surveillance, epidemiology and end results

SER: Sensitization enhancement ratio

siRNA: small-interfering ribonucleotide

SNP: Single nucleotide polymorphism

SOBP: Spread-out Bragg peak

SSB: Single-strand break

TA: Thiolic acid

TCD₅₀: Tumor control dose 50 %

TCP: Tumor control probability

Trx: Thioredoxin

TrxR: Thioredoxin reductase

WP: Weight percent

Z: Atomic number

List of figures

Figure 1. Acquired capabilities of a cancer cell, known as “Hallmarks of cancer”	18
Figure 2. Average annual change in cancer death rate for different cancer types	20
Figure 3. Three main processes leading to photon energy loss..	23
Figure 4. Domains over which the different processes triggered when a photon interacts with mater are dominant as a function of the atomic number of the traversed element(s) and the photon energy.	25
Figure 5. Three different types of collision of a charged particle with an atom, depending on the relative value of the impact parameter b and atomic radius a	26
Figure 6. Main reactions occurring during the three stages of water radiolysis	30
Figure 7. Experimental G-values for H_2 (in red) and HO^\bullet (in black) measured by different groups as a function of LET	31
Figure 8. DNA damages/cell/Gy of radiation induced by X-rays, protons, alpha particles and carbon ions.....	33
Figure 9. HR an NHEJ repair pathway mechanism.....	34
Figure 10. Dependence of radiotherapy efficiency to kill cell according to the time between fractions. The influence of 4 Rs parameters is illustrated.	37
Figure 11. Depth-dose profile for a typical 15 MV photon beam and mono-energetic proton beam. The maximum dose point of the red curve is termed the Bragg peak. Scanning thin mono-energetic proton beams are used for intensity-modulated protontherapy leading to the blue curve and a plateau in the depth-dose profile, called the spread-out Bragg peak (SOBP).	39
Figure 12. Example of treatment planning for the irradiation of non-small cell lung carcinoma.	39
Figure 13. Decrease in OER with increasing LET.....	41
Figure 14. Schematic representation showing the TCP (solid line) and NTCP (dashed line) as a function of the radiation dose. The TCP is illustrated for two scenarios, one with a $TCD_{50\%} = 55$ Gy and a second with a $TCD_{50\%} = 45$ Gy, to illustrate the action of a radiosensitizer specifically targeted to the tumor. In each case, the PCWC is shown by the dotted line.....	42
Figure 15. Variation of the theoretical maximal absorption wavelength with the GNP size.	45
Figure 16. Absorption cross section of photons in water (A) or in gold (B) as a function of photon energy. (C) Comparison of photon total absorption cross section for gold (blue curve) and water (red curve) as well as ratio of gold absorption cross section on water absorption cross section (dashed line) depending on photon energy.	48

Figure 17. Total stopping power of proton in water (A) or in gold (B) as a function of proton energy. (C) Comparison of total stopping power for gold (blue line) and water (red line) as well as gold to water ratio of total stopping power (dashed lines) depending on photon energy.	49
Figure 18. Average tumor volume assessed during 1 month after treatment. Balb/C mice bearing subcutaneous EMT-6 mammary carcinomas was used in this study.	55
Figure 19. Comparison of observed in vitro experimental dose enhancement with predicted dose enhancement values for GNPs studies	58
Figure 20. Schematic representation of the GNP synthesis method.....	63
Figure 21. (A) Normalized UV-vis absorption spectra for several Au/PEG molar ratios. (B) Image collected from a series of GNP dispersions in deionized water. Changes in solution color from yellow (Au/PEG: 1/1) to red (Au/PEG: 1,000/1) reflect an increase in the nano-object size.....	64
Figure 22. TEM images for several Au/PEG molar ratios ranging from 1/1 (A) to 10,000/1 (F).....	65
Figure 23. Relationship between Au/TA-PEG ₅₅₀ -OCH ₃ ratio and GNP size measured by TEM. The surface to volume ratio for each NP size was plotted based on theoretical calculations.....	65
Figure 24. GNP stability in HBSS medium supplemented with 10% FBS and incubated during 72h at 37°C. (A) UV-visible spectra at 1h (red curve), 3h (blue curve), 5 h (green curve), 7h (purple curve), 24h (yellow curve), 48h (cyan curve) and 72h (brown curve). Dashed line indicated the position of the maximal absorption wavelength ($\lambda_{\text{max}} = 525 \text{ nm}$). (B) Heterodispersity index calculated from the spectrum for each time point $\pm 1 \text{ SD}$ of three independent experiments.	66
Figure 25. Scale-up of 10 nm GNPs synthesis (Au/PEG: 2000/1)..	67
Figure 26. Survival fractions of A549 and A431 cells irradiated with $25 \text{ keV} \cdot \mu\text{m}^{-1}$ proton beam at 3 Gy in presence or not of DMSO.	84
Figure 27. Validation of ThermoFisher's kit "Amplex Red Hydrogen Peroxide/Peroxidase Assay" according to manufacturer instructions.	84
Figure 28. H ₂ O ₂ production after $25 \text{ keV}/\mu\text{m}$ proton irradiation (3Gy/min).	86
Figure 29. Validation of hydroxyl radical detection test.	87
Figure 30. °OH production after $25 \text{ keV}/\mu\text{m}$ proton irradiation.....	88
Figure 31. DNA damage repair kinetics and Persistent RIF/ μm at 48h compared across different mouse strains	172
Figure 32. Manhattan plot for GWAS analysis of persistent DNA damage observed across the mouse strains after 650 MeV exposition	173
Figure 33. Comparison between photon cross section in water and in different materials. The ratio of absorption cross section in a NP on absorption cross section in water was plotted according to the incident photon energy and atomic number of the material of interest.	184
Figure 34. mRNA expression of TXNRD1 gene in 15 different cancer types.	187

List of tables

Table 1. Epidemiology of cancer. Incidence, death rate and 5 years survival rate were reported by the SEER program in their last report on cancer epidemiology. Optimal recommended radiotherapy and chemo-radiotherapy data are based on updated CCORE report published in 2013. Data about the proportion of cancer patients for whom (chemo-) radiotherapy is recommended were calculated by combining data from the aforementioned reports.	19
Table 2. G-value [$\mu\text{mol/J}$] for the most common reactive oxygen species obtained upon water radiolysis.	30
Table 3. Non-exhaustive list of drug delivery nanocarriers approved in clinic	46
Table 4. Non-exhaustive list of theoretical works predicting physical enhancement of GNPs under photon irradiation.....	50
Table 5. Non-exhaustive list of in vitro studies of cell death enhancement by GNPs. The results are alphabetically listed for the cancer type.....	53
Table 6. In vivo studies of radiosensitization effect of GNPs.....	56
Table 7. List of genes identified by the GWAS analysis to be associated to DNA damage phenotype observed after 650 MeV/n Fe exposition.	174

List of publications

1. Li, S; **Penninckx, S**; Karmani, L; Heuskin, AC; Watillon, K; Marega, R; Zola, J; Corvaglia, V; Genard, G; Gallez, B; Feron, O; Martinive, P; Bonifazi, D; Michiels, C & Lucas S.
“LET-dependent radiosensitization effects of gold nanoparticles for proton irradiation”.
Nanotechnology, 2016, vol 27, no. 45, 455101.
DOI: 10.1088/0957-4484/27/45/455101
Status: Published 3rd October 2016; 16 citations.
2. Genard, G.; Wera, AC; Huart, C.; Le Calve, B.; **Penninckx, S.**; Fattaccioli, A.; Tabarrant, T.; Heuskin, AC.; Lucas, S.; Michiels, C.
“Proton irradiation orchestrates macrophage reprogramming through NFκB signalling.” Cell Death and Disease, 2018, 9(7), [728].
DOI: 10.1038/s41419-018-0757-9
Status: Published 27th June 2018; 8 citations.
3. **Penninckx, S.**; Heuskin, A-C. ; Michiels, C. ; & Lucas, S.
“The role of thioredoxin reductase in gold nanoparticle radiosensitization effects”.
Nanomedicine (2018).
DOI: 10.2217/nnm-2018-0171
Status: Published 14th November 2018
4. Li, S*; Bouchy S.*; **Penninckx, S.***; Marega R.; Fichera, O. ; Gallez B. ; Feron, O. ; Martinive, P.; Heuskin, A-C., Michiels, C., & Lucas, S.
“Antibody-functionalized gold nanoparticles as tumor targeting radiosensitizers for proton therapy”. Nanomedicine (2018).
DOI: 10.2217/nnm-2018-0161
Status: Accepted 14th November 2018
5. **Penninckx, S.**; Heuskin, A-C. ; Michiels, C. ; & Lucas, S.
“Thioredoxin reductase activity predicts gold nanoparticle radiosensitization effect”.
Status: Under review in Nanomaterials
6. **Penninckx, S.***; Cekanaviciute, E*; Degorre, C.; Guiet, E.; Lucas, S. & Costes, S.
“The 15-strain irradiation study Part I: The dose and LET dependence of 53BP1 radiation induced foci in 15 mouse lines”.
Status: Under review in Radiation Research Journal.

7. Daems, N.; **Penninckx, S.**; Van Hoecke, K.; Cardinaels, T.; Baatout, S.; Michiels, C.; Lucas, S. & Aerts, A.
“A comparative study on the cytotoxicity of gold nanoparticles conjugated to Cetuximab in human kidney, liver and endothelial cells”
Status: Submitted in Small
8. Bopp, C.; Hespeels, B.; Baumlé, V.; **Penninckx, S.**; Van Doninck, K.; Heuskin, AC. & Lucas, S.
“Radiation damage to cellular targets: an overview”
Status: To be submit (2019)

* = Authors contributed equally

Résumé

Dans son dernier rapport sur le cancer, l'institut américain de la santé (NIH) indique que 38,5 % de la population développera un cancer durant sa vie et que près de 64 % des patients y survivront. Cependant, ce dernier chiffre cache de grosses disparités en fonction du type de cancer considéré. En effet, bien que le taux de survie général augmente d'environ 1 % chaque année, la mortalité associée à certains cancers, notamment ceux du système nerveux et du pancréas, augmente. Cette augmentation est due entre autres à l'inefficacité des traitements. Ainsi, la recherche portant sur l'amélioration des traitements actuels s'amplifie à travers le monde poussé par le besoin criant de nouvelles stratégies thérapeutiques pour ces cancers. Parmi l'arsenal thérapeutique disponible, cette thèse se focalise sur la radiothérapie. Cette technique consiste à délivrer une dose létale de radiations ionisantes, classiquement des rayons X, au sein de la tumeur. Malheureusement, la radiothérapie moderne est encore limitée par les dommages collatéraux occasionnés aux tissus sains entourant la tumeur. Ainsi, l'un des défis actuels consiste à optimiser la fenêtre thérapeutique, c'est-à-dire maximiser la différence entre la dose de radiation délivrée au sein de la tumeur et celle touchant les tissus sains environnants. L'utilisation de protons à la place des rayons X cadre avec cette démarche car les particules chargées permettent d'assurer un meilleur ciblage tumoral. En parallèle, le développement grandissant de la nano-médecine offre la possibilité de tirer profit de matériaux nanométriques pour diverses applications allant du diagnostic à la thérapie.

Dans le cadre de cette thèse, nous avons étudié l'impact de traitements radiothérapeutiques combinant l'utilisation de particules chargées, des protons en l'occurrence, et de nanoparticules d'or (GNPs) sur diverses lignées cellulaires. Des expériences réalisées à l'UNamur ont permis de démontrer que la présence de GNPs au sein de cellules de carcinome pulmonaire lors de l'irradiation augmente la mortalité cellulaire. Cet effet est rapporté dans la littérature comme l'effet « enhancer ». Ainsi, pour une dose de 2 Gy, une augmentation de 25 % de la mortalité cellulaire a été observée lorsque les GNPs sont présentes au sein des cellules, à la fois pour des irradiations rayons X et protons. Néanmoins, nous avons montré que l'amplitude de cet effet varie avec divers paramètres physico-chimiques dont la taille des GNPs et le transfert linéique d'énergie des particules incidentes ainsi qu'en fonction du type cellulaire considéré.

Dans une volonté de maximiser la mortalité des cellules cancéreuses, nous avons cherché à mieux comprendre le mécanisme à l'origine de l'effet enhancer. Ce problème fut abordé selon deux approches différentes. D'une part, une hypothèse physico-chimique a été émise : l'interaction entre le faisceau de particules chargées et une nanoparticule métallique mène à l'émission d'électrons capables de produire des espèces réactives de l'oxygène (ROS). Celles-ci peuvent alors endommager diverses cibles biologiques importantes. Ces résultats montrent une augmentation significative de la production de peroxyde d'hydrogène et de radicaux hydroxyles dans des solutions colloïdales irradiées par rapport à des solutions ne contenant pas de GNPs. De plus, l'ajout de molécules « scavenger » de radicaux lors de l'irradiation permet de diminuer drastiquement l'effet enhancer, démontrant le rôle important joué par les ROS dans celui-ci. Malgré ces résultats, des simulations attestent que, dans une configuration réaliste, la probabilité de rencontre entre le faisceau de particules chargées et les GNPs est de l'ordre de 1 %. Cette faible valeur indique que l'hypothèse formulée ne permet pas d'expliquer, à elle seule, l'effet enhancer observé. Ainsi, une seconde

hypothèse a été formulée : les GNPs perturberaient l'homéostasie cellulaire, prédisposant ainsi la cellule à mourir lorsque celle-ci est irradiée. Pour valider cette hypothèse, l'effet des GNPs sur diverses voies de signalisation au sein de cellules de carcinome pulmonaire a été étudié. Nous avons montré que l'incubation des GNPs induit une dépolarisation rapide des mitochondries, ce qui fut confirmé par l'observation d'une diminution du contenu d'ATP, un stress oxydatif et une diminution de la vitesse de prolifération. Ces dysfonctionnements biologiques peuvent être expliqués par une inhibition de la thioredoxine réductase (TrxR), une enzyme cytoplasmique impliquée dans la détoxification dans la réponse au stress oxydatif. Des mesures d'activité de la TrxR dans des cellules pré-incubées avec ou sans GNPs, ont montré une diminution de l'activité enzymatique lorsque les GNPs sont présentes au sein des cellules. De plus, nous avons observé que l'amplitude de cette inhibition varie en fonction du type cellulaire considéré et est corrélée à la quantité de NPs internalisées par les cellules. L'identification de cette cible a permis de proposer un nouveau mécanisme global responsable de l'effet radiosensibilisant des GNPs.

Dans une volonté de compléter ces recherches *in vitro* avec des études *in vivo*, nous avons modifié la surface des nanoparticules en y greffant des anticorps dirigés contre l'EGFR, un récepteur surexprimé par certaines cellules cancéreuses. Les études réalisées avec ce nano-objet ont permis de montrer une accumulation plus importante des GNPs au sein de cellules exprimant l'antigène d'intérêt par rapport à des cellules ne l'exprimant pas. Ceci s'est traduit par un effet radiosensibilisant dans les cellules positives pour l'EGFR mais pas dans les cellules négatives pour l'EGFR.

Enfin, la dernière partie de cette thèse est consacrée à l'étude de dommages à l'ADN et de leur réparation dans des fibroblastes murins exposés à des rayons X ou à des particules chargées de LET élevé. Nos résultats montrent que le nombre foyers de réparations par Gy de radiation dépend de la souche murine étudiée et du LET de la particule incidente, laissant présager une influence de la génétique dans le phénotype de réparation des dommages à l'ADN. Ainsi, l'association de ces données phénotypiques avec les informations génétiques en notre possession nous a permis d'identifier des loci génétiques associés à des différences significatives en terme de sensibilité aux radiations. Ces recherches permettent de progresser dans la compréhension fondamentale des conséquences biologiques associées à des expositions aux particules chargées et d'en mieux comprendre les fondements génétiques.

Ensemble, ces recherches permettent d'améliorer les connaissances des interactions complexes entre les nanomatériaux, les cellules et les radiations ionisantes. Le nouveau mécanisme responsable de l'effet enhancer que nous avons proposé ouvre de nouvelles pistes de recherche pour maximiser cet effet d'amplification, augmentant ainsi les chances de curabilité et la qualité de vie des patients. De plus, ces résultats ouvrent la voie à une utilisation seule ou combinée de particules chargées et d'agents radiosensibilisants dans un contexte de médecine personnalisée qui devrait prendre son essor dans la future décennie.

Abstract

In its last cancer report, the National Institute for Health (NIH) indicated that 38.5 % of the population will develop a cancer during their lifetime. For 2017, it was estimated that about 1.7 million new cases would be diagnosed and more than 600,000 people will die in USA, corresponding to 64 % of survival. While this overall survival rate slowly increases over time, it masks significant disparities between the different cancer types. In fact, the death rates of several cancer types, including cancers from nervous system and pancreas, increase each year due to the inefficiency of treatment modalities for these cancers. Therefore, there is a real need for the discovery of new treatment modalities and/or for current treatment improvement. Amongst all the treatment modalities available, this thesis focuses on radiotherapy, which aims at delivering a lethal dose of ionizing radiation into the tumor. However, modern radiotherapy is still limited by the side effects caused to healthy tissues surrounding the tumor. One of the current challenges is to maximize the differential radiation dose deposited in the tumor and in normal healthy tissues (the so-called “therapeutic ratio”). For this purpose, the use of charged particles instead of classical X-ray photons is growing worldwide, ensuring a more effective tumor targeting. In the meantime, the development of nanomedicine offers the possibilities to take advantage of nanoscale materials in a range of diagnosis and therapeutic applications.

In the framework of this thesis, we have investigated the effects induced by a combination of proton irradiation and gold nanoparticles (GNPs) on various carcinoma cells. Our results demonstrate the ability of GNPs to enhance cell death upon irradiation. Thereby, a 25 % increase in cell death was observed when lung carcinoma A549 cells pre-incubated with GNPs were exposed to 225 kV X-rays and 25 keV/ μm protons. Moreover, we evidenced that this radiosensitization effect vary with different physico-chemical parameters including GNP size or particle LET as well as according to the cell line of interest.

In order to maximize the cancer cell death, we investigated the mechanism(s) responsible for this enhancement effect. In this context, two different approaches were investigated. On one hand, a physico-chemical hypothesis was suggested: the interaction between ionizing radiations and GNPs leads to the emission of low-energy electrons from the GNP. These electrons interact with the surrounding medium, producing reactive oxygen species (ROS), which can damage critical biological targets. Our results showed a significant increase in the hydrogen peroxide and hydroxyl radical production in colloidal solutions upon irradiation compared to solutions that did not contain GNPs. Moreover, the use of a radical scavenger during the irradiation enabled to decrease the radiosensitization effect evidencing the key role played by ROS in the mechanism(s) responsible for it. However, simulation works highlighted that the encounter probability between charged particles and GNPs is too low to explain, on its own, the origin of this enhancement effect. Thereby, a second hypothesis was suggested: GNPs disrupt cell homeostasis predisposing it to death after irradiation. To validate this hypothesis, we investigated the effect of GNP incubation on different biological pathways. We reported that GNP incubation with lung carcinoma cells led to a time-dependent mitochondria membrane depolarization, to a decrease in ATP content and to oxidative stress. Moreover, a marked inhibition of thioredoxin reductase (TrxR) activity was observed in cells incubated with GNPs, suggesting that this enzyme is a potential GNP target. Furthermore, we reported that this TrxR activity reduction is cell type-dependent and leads to differences in cell response to X-ray

irradiation. Correlation analyses demonstrated that GNP uptake and TrxR activity inhibition are associated to GNP radiosensitization effect. With all these results, we suggested a new mechanism explaining the radiosensitization effect of GNPs.

Although we demonstrated the potential of GNPs as *in vitro* radiosensitizers, their use for *in vivo* biomedical applications remains challenging due to biodistribution issues. Thereby, we developed targeted NPs, which can recognize the cancer cells. To achieving it, we grafted an antibody against EGFR, an overexpressed receptor in many types of cancers, at the GNP surface. Results obtained with this targeted GNP highlight a higher gold content in EGFR positive cells compared to EGFR negative ones. Consequently, we observed a significant enhanced effect of proton irradiation in EGFR positive cells but not in EGFR negative cells.

Finally, the last part of this thesis focused on the DNA damage and their repair in mice fibroblasts exposed to X-rays or to high-LET particles. We evidenced that the number of radiation-induced foci per Gy of radiation is LET- and mice strain-dependent, suggesting that this phenotype is driven by genetics. By associating phenotype and genetic data, we identified genetic loci associated to significant difference in radiosensitivity phenotype. These researches enable a better understanding of biological consequences associated to charged particle exposition and their genetic basis.

Altogether, these researches enable the improvement of our knowledge of the interaction between nanomaterials, cells and ionizing radiations. The new mechanism responsible for the enhancer effect that we proposed opens new research ways to maximize this amplification effect, thus increasing the chances of curability and the quality of life of patients. In addition, these results pave the way for the use of charged particles and radiosensitizing agents in a personalized medicine framework, which is expected to take off in the next decade.

PART I: Introduction

1. Cancer

1.1. Generalities

Cancer are diseases in which normal cells are transformed into tumor cells from an accumulation of genetic and epigenetic alterations leading to an uncontrollable growth and spread of these abnormal cells. In 2000, Hanahan & Weinberg [1] suggested that these changes observed in neoplastic cells allow them to acquire new features, known as the “hallmarks of cancer” (Figure 1):

- Sustaining proliferative signaling:

While normal cells can only proliferate after mitogenic growth signal reception, cancer cells are much less dependent on external signals. It was reported in several cancer types that neoplastic cells are able to synthesize stimulatory growth factors on their own [1, 2].

- Evading growth suppressors:

In a normal tissue, cell growth is regulated by different signals enabling to keep them in a quiescent state (through anti-proliferative signals) or to initiate cell proliferation when required. Most anti-proliferative signals are transmitted through the retinoblastoma protein (pRb) pathway, which is frequently mutated in cancer cells. Disruption of this pathway triggers cell proliferation even in the presence of anti-proliferative signals.

- Activating invasion and metastasis:

Some cancer cells have the ability to undergo the epithelial to mesenchymal (EMT) transition, a migration and invasive program that enables cancer cells to invade the adjacent tissue as well as the blood and lymphatic vessels. These vessels serve thereafter as pipelines for dissemination to other anatomical sites where the metastases can grow.

- Enabling replicative immortality:

In normal tissues, cells have the ability to divide for a given number of times. When this number is reached, they enter into senescence where they stop dividing. In contrast, cancer cells can circumvent the entry into senescence leading to an unlimited replicative potential [3].

- Inducing angiogenesis:

In order to ensure a sufficient oxygen and nutrients supply, new blood vessels formation is a mandatory step for solid tumors. Although cells initially have no ability to trigger angiogenesis, extensive evidences show that tumors acquire this capacity to ensure the growth of new blood vessels [4, 5].

- Resisting cell death:

Following alterations of cell death mechanisms, cancer cells can become unresponsive to cell death signals. For example, several groups have reported that p53, an key mediator in the regulation of apoptosis, is frequently mutated in cancer cells [6].

In 2011, Hanahan & Weinberg [7] suggested that the acquisition of the aforementioned hallmarks is facilitated by two characteristics: the genome instability and the inflammation. Moreover, they proposed to add two emerging hallmarks that promote the tumorigenesis: the deregulation of cellular energy metabolism and the ability to evade immune system destruction.

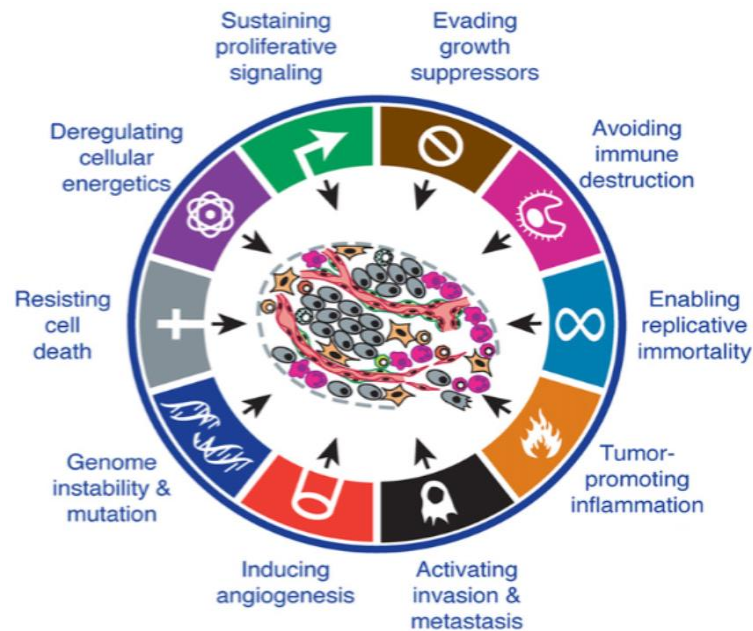


Figure 1. Acquired capabilities of a cancer cell, known as “Hallmarks of cancer”. Adapted from [7]

1.2. Epidemiology

According to the World Health Organization, cancer is responsible for the death of 8.2 million people each year worldwide, constituting the second leading cause of death in developed countries. The most recent report available for cancer statistics was published in 2017 and discussed the incidence and mortality data from 1930 to 2014 ¹ in USA [8]. It highlights that the lifetime probability of being diagnosed with invasive cancer is slightly higher for men (40.8 %) than for women (37.5 %). For 2017, it was estimated that about 1.7 million new cases would be diagnosed and more than 600,000 people will die in USA, corresponding to 64 % of survival. While this overall survival rate slowly increases over the time, it masks significant disparities between the different cancer types. As shown in Table 1, breast, lung, prostate and colon cancers still remain the most common cancer types but are mainly associated to relatively high survival rates (around 90 % for breast cancer for example). However, the diagnosis of pancreatic, hepatic, lung and esophageal tumors are associated to the worst patient overall survival with 5-year survival rates below 20 % (Table 1).

¹ The lags of 3 years is due to the time required for data collection, compilation, quality control and dissemination.

Tumor type	Proportion of all new cancer cases [%]	Proportion of all cancer deaths [%]	5-year relative survival rates [%]	Patients for whom external radiotherapy is recommended [%]	Patients for whom chemo-radiotherapy is recommended [%]	Proportion of cancers for which radiotherapy is recommended [%]	Proportion of cancers for which chemo-radiotherapy is recommended [%]
Breast	15.0	6.8	89.7	87	N.I.	13.1	0
Lung	13.2	25.9	18.1	77	26	10.2	3.4
Prostate	9.6	4.4	98.6	58	N.I.	5.6	0
Colon	5.7	8.4	64.9	4	N.I.	0.2	0
Melanoma	5.2	1.6	91.7	21	N.I.	1.1	0
Bladder	4.7	2.8	77.3	47	9	2.2	0.4
NH Lymphoma	4.3	3.4	71.0	71	N.I.	3.1	0
Kidney	3.8	2.4	74.1	15	N.I.	0.6	0
Oral cavity & Larynx	3.7	2.2	64.5	74	26	2.7	1.0
Uterine	3.6	1.8	81.3	39	N.I.	1.4	0
Thyroid	3.4	0.3	98.2	4	N.R.	0.1	0
Pancreas	3.2	7.2	8.2	49	35	1.6	1.1
Rectum & anus	2.9	0.2	66.9	60	55	1.7	1.6
Liver	2.4	4.8	17.6	N.I.	N.I.	0.0	0
Myeloma	1.8	2.1	49.6	45	N.I.	0.8	0
Stomach	1.7	1.8	30.6	27	20	0.5	0.3
Brain	1.4	2.8	33.6	80	53	1.1	0.7
AM Leukemia	1.3	1.8	26.9	4	N.I.	0.05	0
Ovarian	1.3	2.3	46.5	3.6	N.R.	0.05	0
Esophageal	1.0	2.6	18.8	71	33	0.7	0.3
Cervix	0.8	0.7	67.1	71	51	0.6	0.4
Gall bladder	0.7	0.6	-	17	17	0.1	0.1
Hodgkin Lymphoma	0.5	0.2	86.4	90	N.I.	0.5	0
Testis	0.5	0.1	95.1	7	N.I.	0.04	0
AL Leukemia	0.4	0.2	68.2	25	N.I.	0.1	0
Vulvar	0.4	0.2	72.1	39	15	0.2	0.1
Vagina	0.3	0.2	-	94	78	0.3	0.2
Other	7.2	12.2	-	19.0	5	1.4	0.4
Total	100.0	100.0	-	-	-	49.8	10.1

Table 1. Epidemiology of cancer. Incidence, death rate and 5 years survival rate were reported by the SEER program in their last report on cancer epidemiology [8]. Optimal recommended radiotherapy and chemo-radiotherapy data are based on updated CCORE report published in 2013 [9]. Data about the proportion of cancer patients for whom (chemo-) radiotherapy is recommended were calculated by combining data from the aforementioned reports. N.I. = No indication identified; N.R. = Not recommended; NH = Non-Hodgkin; AM = Acute Myeloid; AL = Acute Lymphoblastic.

Nevertheless, the Surveillance, Epidemiology and End Results (SEER) program has reported a decrease in overall cancer death rates by an average of 1.8 % per year for men and 1.4 % per year for women between 2011 and 2015 (Figure 2). Researchers attributed this decrease to various factors including an early diagnosis (breast cancer), the improvement of treatment quality and the reduced tobacco use (lung cancer). In contrast, the death rates of several cancer types (cancer from nervous system, liver, uterus, oral cavity, pancreas, soft tissue including heart and non-melanoma skin cancer) increase each year. Scientists believe that rising obesity has contributed to the increasing death rates for endometrial, pancreatic and liver cancers, while the increased rate for oral cavity cancer is attributed to human papillomavirus infection. Moreover, for some of them, there is no efficient treatment modalities up to now. Therefore, there is a real need for the discovery of new treatment modalities and/or for current treatment improvement.

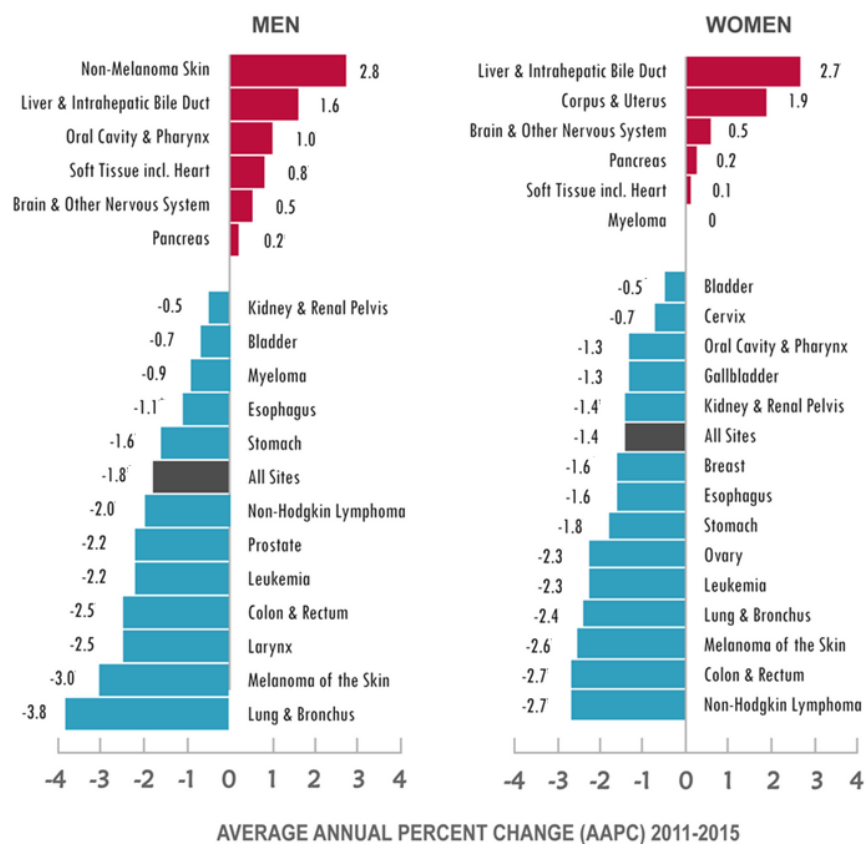


Figure 2. Average annual change in cancer death rate, expressed in percentages for different cancer types [8].

1.3. Treatment modalities

Nowadays, the therapeutic arsenal can be divided in two groups of treatments: systemic and local treatments. The treatment choice depends on a set of factors including cancer type and stage as well as the age of the patient.

Systemic treatments use molecules that travel through the bloodstream, affecting tumor cells wherever they are in the body. In this class of treatments, we find, amongst others, chemotherapy and immunotherapy. Chemotherapy uses drugs that have the ability to disrupt the cancer cell growth. In fact, cancer cells tend to grow and divide faster than normal cells enabling a relative affinity of drugs

for cancer cells, limiting normal tissue side-effects. However, some normal cells (such as digestive system or hair follicles) grow and divide quicker than other cells in the body, making them vulnerable to drug action. This explains the usual hair loss and diarrhea reported in patients undergoing chemotherapy. Although this systemic effect is associated to huge side-effects, it is the most efficient treatment modalities that are available to treat patients with metastases throughout the body. Modern chemotherapy uses a set of drugs with different mechanisms of action: cisplatin, an alkylating agent used in testis cancer, crosslinks purine bases of DNA interfering with DNA replication and repair [10] while paclitaxel, a drug used in ovarian cancer, disturbs cancer cell proliferation by targeting tubulin and influencing the micro-environment [11]. In the 2000's, a new type of systemic treatment has appeared with the aim of helping the patient immune system to fight cancer: the immunotherapy. The development of PD-1/PD-L1 system inhibitor is a well-known example of immunotherapy. In fact, cancer cells can evade the immune system regulation via the association of PD-L1 protein (at cancer cell surface) with its receptor, PD-1 (located at T-cell surface), reducing the T-cell ability to signal the presence of the cancer cell. Thereby, PD-L1 and PD-1 inhibitors were developed to block this PD-1/PD-L1 interaction preventing the cancer cells to escape from the immune system. Although this new therapeutic strategy is accepted for the treatment of some cancers, including melanoma and Hodgkin's lymphoma, more clinical data are needed to fully understand the potential of this promising approach [12, 13].

Compared to systemic treatments, local treatments affect targeted cells and the cells in the area near it. Surgery is one of these therapeutic approaches, when tumors are small, localized and non-metastatic. Radiotherapy, which consists of delivering lethal doses² of radiation into the tumor, is a widely used technique to treat a large majority of cancer types as shown in Table 1. It is a reference treatment in breast, brain and lung tumors for which 87 %, 80 % and 77 % of patients receive radiation therapy respectively. Based on updated guidelines for an optimized use of radiotherapy [9] and the last SEER report on cancer epidemiology [8], it was estimated that 49.8 % of all cancer patients receive radiotherapy, alone or in combination with other techniques, during their treatment (cf. Table 1). Although, all these therapeutic strategies were presented as separate entities, modern oncology generally uses combination of treatments to fight cancers. In fact, surgery is the first-line of treatment for glioblastoma when tumor is accessible and is followed by daily radiotherapy sessions coupled to temozolomide, a chemotherapy drug. The use of radiotherapy-chemotherapy combination is growing worldwide with an estimated recommendation for 10 % of all cancer patients (Table 1).

These statistics highlight the major role played by radiotherapy in the fight against cancers and justify the need of improved radiotherapeutic treatment which would benefit to a large number of patients. In this context, this thesis will focus on radiotherapy. Its physical, chemical and biological concepts will be discussed in the introduction.

² Dose is the energy deposited per mass unit by an ionizing radiation, expressed in Gy.

2. Radiotherapy: from physical interaction to biological damages

As mentioned before, external beam radiotherapy is aimed at delivering a lethal dose of ionizing radiation into the tumor. Since the first use of X-rays for therapeutic applications in the early 20th century, radiotherapy has evolved, driven by a better understanding of radiation characteristics and their interaction with matter. However, it quickly became clear that the dose received by healthy tissues surrounding the tumor is the main limitation of this technique. Indeed, some cases of radiation-induced leukemia, lost fingers or malignant skin changes were already evidenced in 1900 [14]. Thereby, one of the first advances was the fractionation of radiotherapy, which divides the total dose delivered to the patient in fractions of smaller doses, enabling healthy tissues to recover between each irradiation session (1927, cf. section 2.6). Nowadays, this principle is still used and its efficiency was coupled to the improvement of imaging techniques which enable a better tumor size and location determination. Over the years, conventional radiotherapy was gradually replaced by conformal radiotherapy (CFRT) in which the radiation beam is geometrically adjusted to fit the tumor shape while sparing the surrounding organ(s) at risk. Further, the Intensity Modulated Radiation Therapy (IMRT) has firmly established itself as one of the gold standards in radiotherapy treatment. It enables an adjusted irradiation field shape, such as CFRT but its intensity is also modulated within the irradiated area [15]. Nowadays, this technique is coupled to image guided radiotherapy enabling to take into account tumor and organ motions as well as variations of the tumor volume sessions after sessions.

It must be noted that a new irradiation modality which uses charged particles instead of photons, is growing worldwide. This technique, called hadrontherapy, has a major advantage which is its depth-dose profile characterized by a significant increase in the dose deposited at the end of the particle track. This typical profile, explained later (see. Section 2.7), demonstrates that the dose can be deposited in a chosen volume with a high accuracy. Nowadays, research in radiotherapy continues to focus on improved techniques that would allow a maximization of the differential response between cancer cells and healthy tissues as well as a minimization of the total dose delivered to the patient. These researches require the understanding of how ionizing radiations interact with matter.

2.1. Interaction of photons with matter

X-rays used in conventional radiotherapy are photons. These photons are considered as indirect ionizing radiation because they deposit energy in matter through a 2-step process. Energy is first transferred to a “secondary particle” before to be deposited in matter by this particle. There are three main processes leading to the photon loss of energy. A photon can transfer its energy to one electron of the target leading to an electron ejection from the atom, it is the photoelectric effect. Photons can also interact with electrons through an inelastic collision resulting in an incoherent scattering of the photon and the emission of the electron, it is the Compton effect. Finally, highly energetic photons produce an electron-positron pair, it is the pair production. Thereby, a photon creates a shower of lower energy photons, electrons (and positrons in some cases) as it goes through matter. These low energy “secondary” particles will also lose their energy as they travel impacting the global absorption process. To better understand when these different processes occur, their absorption cross-sections³ have to be defined.

³ The likelihood of a given process can be expressed with a physical quantity called cross-section.

2.1.1. Photoelectric effect

When the energy of incident photon ($h\nu$) is higher than the binding energy of orbital electron (E_I), the electron is ejected from the atom (Figure 3A) with a kinetic energy in order to satisfy the energy conservation law:

$$E = h\nu = E_I + \frac{1}{2}mv^2 \quad (1)$$

If we consider an electron in a hydrogen-like atom⁴ of atomic number Z , the photoabsorption cross-section (σ) can be expressed as:

$$\sigma = \frac{16\pi\sqrt{2}}{3} \left(\frac{1}{4\pi\epsilon_0} \right)^2 \frac{e^4}{m_e^2 c^4} \frac{Z^5}{137^4} \left(\frac{m_e c^2}{h\nu} \right)^{7/2} \quad (2)$$

Where e , c and m_e represent the elementary charge, the speed of light and the electron mass respectively. Equation 2 highlights the fast increase in cross-section with the atomic number of the target (Z^5) and the decrease with photon energy. Thereby, photoelectric effect dominates when low energy photons traverse high Z materials.

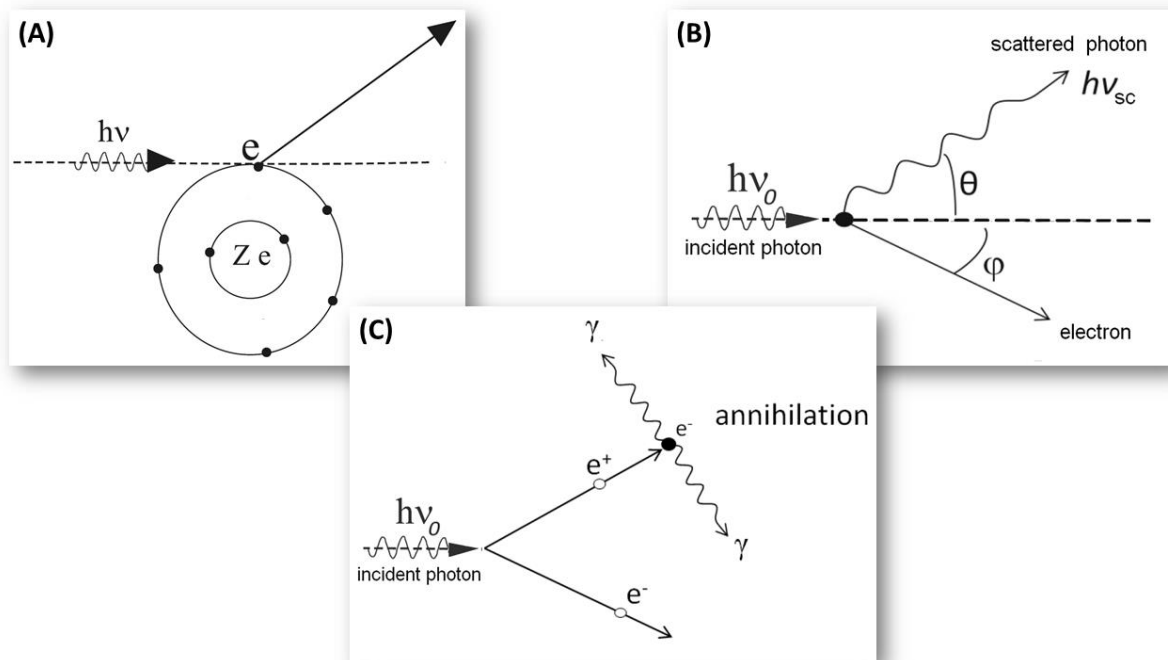


Figure 3. Three main processes leading to photon energy loss. (A) Photoelectric effect. (B) Compton scattering. (C) Pair production and annihilation reaction. Adapted from [16].

⁴ Atom which possesses a single electron

2.1.2. Compton effect

The interaction between an incident photon and an electron can result in a partial energy transfer. This leads to the electron emission, if enough energy is transferred, and the photon scattering in a different direction from the original (angle θ) in order to conserve the overall momentum of the system (Figure 3B). The scattered photon has a higher wavelength and the difference in energy between the two photons is transferred to the electron. If we consider an incident photon which interacts with an electron of mass m_e , the energy relationship between the incident photon ($h\nu_0$) and the scattered one ($h\nu_{sc}$) can be expressed as:

$$h\nu_{sc} = \frac{h\nu_0}{1 + \frac{h\nu_0}{m_e \cdot c^2} [1 - \cos \theta]} \quad (3)$$

The Compton scattering efficiency only depends on the incident photon energy and not on the atomic number of the material they travel through. However, for high energy photons, the cross section is inversely proportional to the incident photon energy.

2.1.3. Pair production

The high density electric field close to an atomic nucleus enables the transformation of a photon in an electron – positron pair (Figure 3C). Each particle created has an associated energy which corresponds to its mass ($= m_e c^2$). Thereby, the pair production process has an energy threshold of $2 m_e c^2 (= 1.02 \text{ MeV})$, e.g. if a photon has an energy above $2 m_e c^2$, the production of an electron and its antiparticle can be observed. This positron slows down in matter and collides with an electron (annihilation reaction) leading to the creation of 2 gamma rays of 0.511 MeV. Photons are emitted in opposite directions in order to conserve the momentum of the electron-positron system (equal to zero). The cross-section of this phenomenon is proportional to the atomic number of the material (Z^2).

2.1.4. Relative importance of these three effects

As shown in the previous section, the photon attenuation in matter is due to three different processes. Thereby, the total absorption cross-section is the sum of photoelectric, Compton scattering and pair production cross-sections. In view of their individual changes with photon energy and atomic number of the material, each phenomenon differently contributes to the total photon attenuation. At low energy (below 100 keV), the photoelectric effect dominates. As shown in Figure 4, the area in which photoelectric effect dominates extends towards higher energy when the atomic number of the traversed element increases. For energies between 0.1 and 10 MeV, the Compton effect becomes dominant whatever the material traversed. Finally, for high energies (above 10 MeV), the pair production process appears. Thereby, the Compton effect is the dominant effect when the photon passes through cells (assimilated to water) at energies used in clinic (usually between 0.3 and 20 MeV).

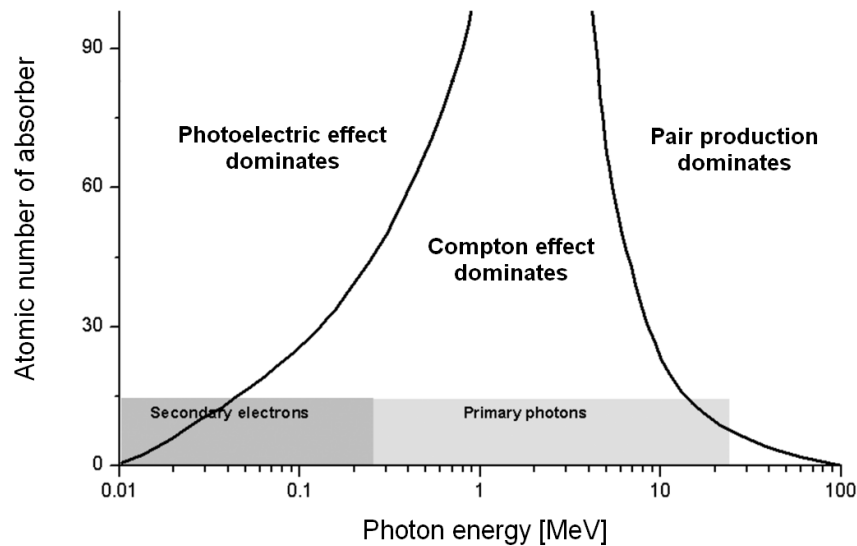


Figure 4. Domains over which the different processes triggered when a photon interacts with mater are dominant as a function of the atomic number of the traversed element(s) and the photon energy. Adapted from [17].

To quantify the decrease of a set of photons passing through matter (a beam of a given intensity), the concept of attenuation was introduced. Due to the three aforementioned processes, the intensity of a photon gamma which passes through matter, is attenuated according to the familiar exponential law of Beer-Lambert. This means that a radiation beam of given energy having intensity I_0 , passing through an absorber of thickness x will have a final intensity (I) given by:

$$I = I_0 \cdot e^{-\mu x} \quad (4)$$

μ is the attenuation coefficient, a value characterizing the loss of beam intensity per unit path length when the beam passes through the medium. Due to its dependence in the different loss of energy processes, the attenuation coefficient varies with the photon energy and the atomic number of the traversed element(s).

2.2. Charged particle interaction with matter

When a charged particle travels through matter, it experiences Coulomb interactions with the nucleus and orbital electrons of all atoms encountered along its path. As a result, each interaction gives rise to a minor loss of incoming particle energy until the particle is at rest. These interactions between a charged particle and matter can be divided into three categories depending on the distance between the charged particle trajectory and the nucleus of the atom atomic with which it interacts (Figure 5). This distance is usually called “impact factor” (referred as b) while the nucleus radius is referred as a .

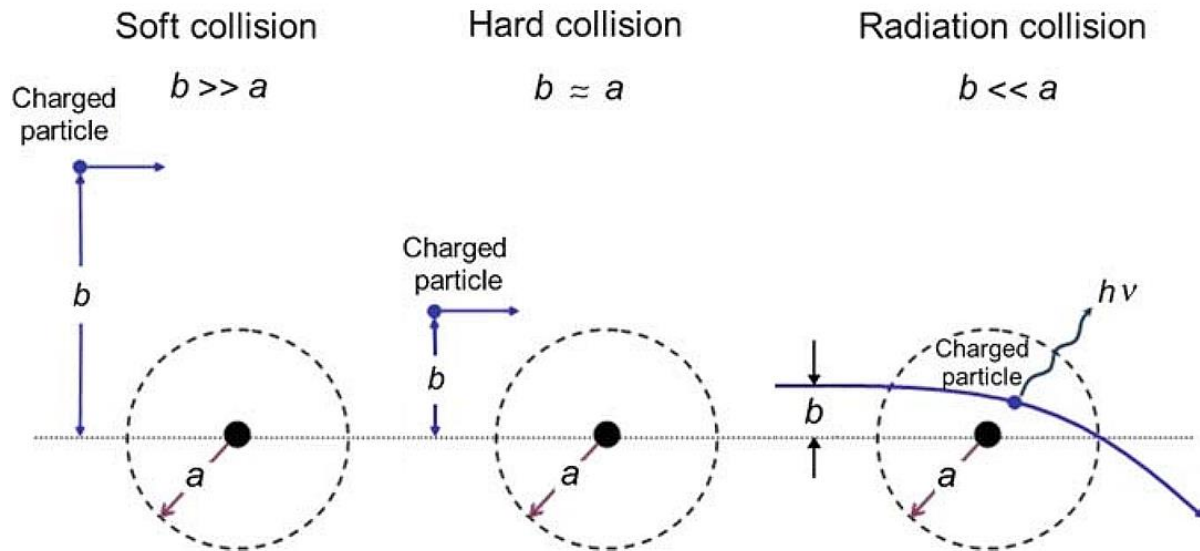


Figure 5. Three different types of collision of a charged particle with an atom, depending on the relative value of the impact parameter b and atomic radius a . Soft collision for $b \gg a$; Hard collision for $b \approx a$; radiation collision for $b \ll a$. Adapted from [18].

2.2.1. Soft collisions

When the impact parameter is larger than the radius of the atom, the Coulomb field of the incident particle interacts with the atom as a whole due to the large distance between the 2 elements. Following these interactions, different effects can take place (distortion of the atom, excitation to a higher energy level or ejection of a valence electron). Despite the low energy transferred during each individual interaction (only few eV), the total number of these soft collisions represents approximately 50 % of the energy lost by a charged particle due to higher likelihood to satisfy the $b \gg a$ condition.

2.2.2. Hard collisions

When the impact parameter is of the order of the atomic radius ($b \approx a$), a charged particle may interact with an electron leading to its ejection from the atom with a high kinetic energy. These electrons, called δ -rays, dissipate their energy along a separate track (cf. section 2.3). The maximal energy (E_{max}) transferred by a charged particle of kinetic energy E_c and mass m_z after collision with an electron of mass m_e is given by:

$$E_{max} = \frac{4 E_c m_z m_e}{(m_z + m_e)^2} \quad (5)$$

Although the likelihood of hard collisions is lower than the soft collisions probability, the energy transferred to the ejected electron is considerable and represents about half the incident particle energy loss.

2.2.3. Radiation collisions

Finally, when the impact parameter of a charged particle is smaller than the atomic radius, Coulomb interaction will take place between the incident particle and the nucleus undergoing either elastic or inelastic scattering. The large majority of these interactions (~ 98 %) are elastic scattering so that the particle is scattered by the nucleus but loses only insignificant amount of its kinetic energy to satisfy the momentum conservation. This will not be taken into account for total energy transfer calculation. In around 2 % of radiation collisions, an inelastic scattering occurs leading to significant energy loss accompanied by an X-ray photon emission (a process referred as bremsstrahlung phenomenon). At a given particle energy, the cross section of this effect is dependent on the square of atomic number of the material and on the inverse square of the mass of the projectile. Consequently, the generation of bremsstrahlung is insignificant for heavier particles than electrons in biological medium (low Z material).

2.2.4. Stopping power

The energy loss of a charged particle which passes through a medium depends on the density of interaction along the particle track. To quantify this, the stopping power has been introduced. It corresponds to the energy loss by an incident particle per unit of path length. It is generally expressed in MeV/cm. Due to the link between the density of interaction caused by the incident particle and the material it travels through, the stopping power is usually normalized by the material density resulting in the introduction of a mass stopping power, expressed in MeV.cm²/g. With respect to interactions discussed before, the mass stopping power can be expressed as a sum of three contributions: a radiation stopping power, a soft collision stopping power and a hard collision stopping power:

$$\left(\frac{dE}{\rho dx}\right)_{tot} = \left(\frac{dE}{\rho dx}\right)_{rad} + \left(\frac{dE}{\rho dx}\right)_{soft} + \left(\frac{dE}{\rho dx}\right)_{hard} \quad (6)$$

As mentioned before the radiation yield of heavy charged particles used in clinic is insignificant and can be ignored. The contribution of soft collision term can be written as:

$$\left(\frac{dE}{\rho dx}\right)_{soft} = \frac{2 C m_e c^2 z^2}{\beta^2} \left[\ln \left(\frac{2 m_e c^2 \beta^2 T}{I^2 (1 - \beta^2)} \right) - \beta^2 \right] \quad (7)$$

$$C = \pi r_0^2 \left(\frac{N_A Z}{A} \right)$$

Where $m_e c^2$ is the rest mass energy of electron; z and Z are atomic number of incident particle and absorbing element respectively; I is the mean excitation potential of atom (proportional to Z); β is velocity normalized by speed of light; T is the energy boundary between soft and hard collision; N_A is the Avogadro number; A is the mass number of absorbing element and r_0 is the electron radius.

The hard collision term can be defined as:

$$\left(\frac{dE}{\rho dx}\right)_{hard} = \frac{2 C m_e c^2 Z^2}{\beta^2} \left[\ln \left(\frac{2 m_e c^2 \beta^2}{(1 - \beta^2)} \right) - \beta^2 \right] \quad (8)$$

Finally, by combining equations (7) & (8), the total mass stopping power can be expressed as:

$$\left(\frac{dE}{\rho dx}\right)_{tot} = \frac{2 \pi r_0^2 N_A Z m_e c^2 Z^2}{A \beta^2} \left[\ln \left(\frac{4 m_e^2 c^4 \beta^4}{I^2 (1 - \beta^2)^2} \right) - 2\beta^2 \right] \quad (9)$$

Equation (9) highlights the dependence of the mass stopping power on three main parameters. The first one is the atomic number of the absorbing element. The mass stopping power decreases for increasing Z , due mainly to the excitation potential term I in the equation. The second one is the β parameter, i.e., the mass stopping power increases when the incident particle velocity decreases. This characteristic explains the known “Bragg peak” observed near the end of a particle track. Lastly, the equation reveals a dependence in square atomic number of the charged particle, meaning that the mass stopping power is 36 times higher for carbon ions (C^{6+}) than protons (H^+) traveled through the same absorbing medium at the same velocity.

As mentioned before the mass stopping power expresses the average quantity of energy lost per unit path length from the projectile point of view. However, this amount of energy loss could be different from the local energy deposited per unit length in the medium surrounding the particle track due to the emission of δ rays. Indeed, high energy δ rays can lose their energy far away from their initial ionization event. To cope with this issue, the Linear Energy Transfer (LET) was defined in order to take into account only the energy deposited locally.

2.3. Interaction of electrons with matter

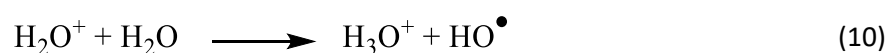
The energy deposited through the interaction of photons or charged particles with matter leads to ionization, thus, emission of electrons. These “secondary” electrons will in turn interact with the matter via different processes:

- Elastic scattering. An electron which penetrates into the electron cloud of an atom is attracted by the nucleus leading to a trajectory deflection without energy loss. The closer the electron comes to the nucleus, the higher the scattering angle. Backscattered electrons can even be observed. The likelihood increases with Z and decreases with the electron energy. These elastic collisions can also happen with orbital electrons.
- Orbital electron inelastic collision. Part of the incident electron energy is transferred to the electron cloud of the atom leading to the scattering of the incident electron scattering. Depending on the energy transferred to the orbital electrons, emission of a secondary electron can be observed. The hole created in the inner-shell can be filled up by an electron from outer shell giving away part of its energy which causes emission of X-ray photons or Auger electrons. The likelihood of these processes is proportional to the atomic number of the material and inversely proportional to the square of the incident electron energy.

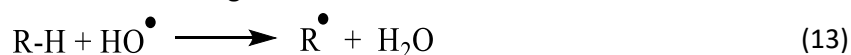
- Nuclear inelastic collision or Bremsstrahlung emission. As mentioned before, when an electron passes near the nucleus of an atom, coulombic attraction can slow down the electron and scatter it. The energy is lost through an X-ray photon emission (a process referred as bremsstrahlung phenomenon). The cross section of this effect is dependent on the square of the atomic number of material and proportional to the incident electron energy.
- Dissociative electron attachment. Low energy (up to 25 eV) electrons have an energy of same magnitude as an electron in the cloud around the nucleus, making them indistinguishable. Due to this indistinguishability, electrons can react with one molecule (M) to give an excited anion ($M^{\bullet-}$) which dissociates to give different molecular fragments such as ions or radicals.

2.4. Water radiolysis

In a radiobiological context, the absorbing medium is a cell which can be considered, in a first approximation, as water. As explained in the previous sections, photon and charged particle interactions with matter produce a set of secondary species (electrons, photons) depending on the interaction mechanism considered. These generated species can also interact with the matter leading to a cascade of events triggered from a single photon. At the end of this stage, usually referred as “physical stage”, energy is deposited in the matter and fast relaxation processes lead to the formation of various ionized water molecules (through ionization processes) or excited water molecules (through the dissociative electron attachment process). Thereafter, numerous processes occur including ion-molecule reaction (10), dissociative relaxation (11) and ion dissociation (12).



This step, called “physico-chemical stage”, leads to the production of radicals, which are highly instable chemical species due to the presence of an unpaired electron in their outermost valence shell. Water radicals are usually called Reactive Oxygen Species (ROS) and can be stabilized via oxidation-reduction reactions with other molecules in the medium. During this “chemical stage”, the ROS are generated along the particle tracks and some of them can diffuse in the surrounding solution and subsequently initiate other chemical reactions. Although the details of all reactions occurring during water radiolysis are not well understood, Figure 6 shows that various species are identified including hydrogen peroxide (H_2O_2), hydroxyl radical (OH^\bullet) or dihydrogen (H_2). In a more realistic view, cells have to be considered as water which contains molecules (RH). These molecules can be a target for ROS leading to the transformation of starting molecules:



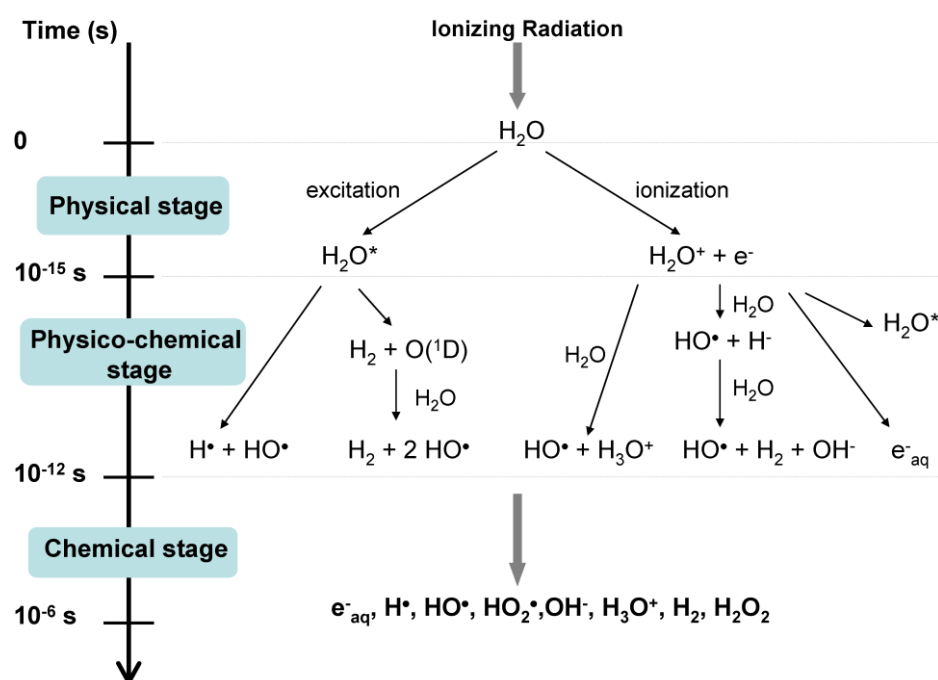


Figure 6. Main reactions occurring during the three stages of water radiolysis [19].

If we consider two distinct molecular radicals, R_1^\bullet and R_2^\bullet , recombination between them can lead to the creation of a new stable compound by crosslinking:



The impact of these reactions on biomolecules will be discussed in the next section. However, to compare the effects of these reactions, we have to introduce a parameter which describes the number of ROS produced per 100 eV of energy delivered to a medium: the G-value. This G-value depends on various factors such as ROS of interest and LET of incident particle (Table 2). Indeed, higher-LET particles will generate more radicals per particle track than lower-LET ones [20]. While this means that per particle track their impact is more important, the radicals are in closer proximity to one another at higher LET. This increases the probability that they interact together and disappear [21]. Consequently, the yield of different radicals per unit dose exhibits different behaviors as a function of LET. As shown in Figure 7, hydroxyl radicals yield decreases with increasing LET, while for molecular radicals (such as hydrogen peroxide or dihydrogen), it increases.

Radiation	OH [•]	H [•]	H ₂ O ₂	H ₂
γ-rays (0.2-0.3 keV/μm)	0.301	0.378	0.081	0.041
5.3 MeV He ²⁺ (140 keV/μm)	0.052	0.062	0.15	0.163

Table 2. G-value [μmol/J] for the most common reactive oxygen species obtained upon water radiolysis. Adapted from [19].

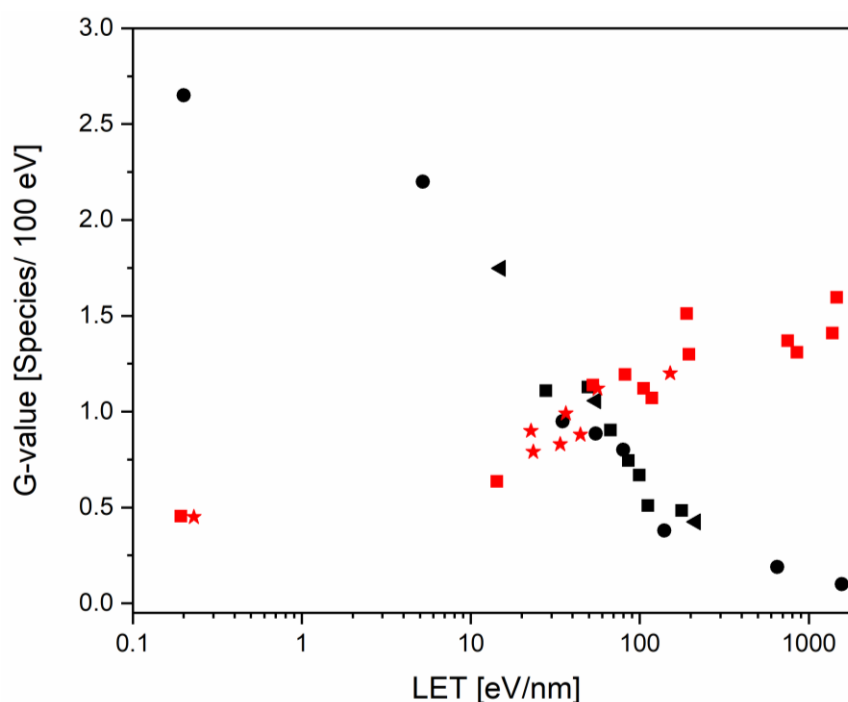


Figure 7. Experimental G-values for H₂ (in red) and HO• (in black) measured by different groups (■ Anderson et al. [22]; ● Burns et al. [23]; ▲ Schuler et al. [24]; ★ Crumière et al. [25]) as a function of LET .

2.5. ROS and cell death

For the successful functioning of cellular processes (respiration chain, enzymatic activities ...), aerobic organisms require oxygen. As a consequence, cells generate partially reduced forms of O₂, leading to an endogenous production of ROS. In physiological conditions, ROS play an effector role in signaling pathways that regulate several cellular processes including gene expression and cell growth [26]. To keep these ROS at a low cellular concentration, cells maintain an endogenous antioxidant capacity, which acts as a detoxification system, that transform ROS into unreactive molecules by metabolic conversion [27]. This system contains lipid-soluble antioxidant compounds (such as alpha-tocopherol), water soluble molecules (such as reduced thiol glutathione (GSH)), and enzymes (such as catalase that catalyzes the transformation of H₂O₂ in O₂) [26]. Moreover, other enzymes reduce cellular oxidized GSH and thioredoxin enabling the regeneration of the antioxidant pool [27]:

- **Thioredoxin Reductase (TrxR):** The thioredoxin system comprises thioredoxin (Trx), NADPH and TrxR. This latter is a NADPH-dependent homodimer oxidoreductase with that reduces oxidized Trx but also a wide spectrum of other compounds including the protein disulfide isomerase (PDI), α-lipoic acid and 5,5'-dithio-bis-2-nitrobenzoic acid (DTNB) [28]. By providing the electrons to small molecules which can react with H₂O₂ directly, mammalian TrxR can function as an antioxidant [29]. In addition, Trx system can also be of major importance for the supply of DNA precursors through its support of ribonucleotide reductase activity [28]. From a structural point of view, TrxR exists in 3 isoforms in mammalian cells: TrxR1 in cytoplasm (gene: TXNRD1), TrxR2 in mitochondria (gene TXNRD2) and TGR, a testis-specific

thioredoxin-glutathione reductase. All isoforms contains selenium in the form of selenocysteine, the naturally occurring selenium analogue of cysteine. This residue is located at the protein C-terminus, within a tetrapeptide motif (-Gly-Cys-Sec-Gly-) conserved between species [30].

- Glutathione Reductase (GR): GR is a NADPH-dependent oxidoreductase that recycles oxidized glutathione back to the reduced form. This enzyme is highly conserved across nature with high degree of similarity between its three-dimensional structures from *E. coli* and human [31]. The sequence analysis indicates the presence of FAD and NADPH binding domains such as in TrxR sequence. Furthermore, a great similarity was observed in the N-terminal FAD domain sequences of GR and TrxR [32].

ROS overproduction can lead to a cellular state, called oxidative stress, where detoxification systems cannot counteract this huge production. In these non-physiological circumstances, ROS can modify and/or degrade cellular metabolites, including DNA, lipids and proteins. Therefore, ROS overproduction can lead to loss of cell function or cell death and is implicated in carcinogenesis [33], aging [34] and in pathology progression, such as cardiovascular diseases [26, 35]. When cells are exposed to ionizing radiations, the aforementioned physical and chemical processes occur leading to critical damages created by either a direct effect (ionization of biomolecules) or indirect effect (biomolecule damages caused by interaction with the ROS produced along the track).

In radiobiology, DNA is considered as the critical target. Contrary to proteins and lipids, which can also be damaged by ionizing radiation, genomic DNA molecules are present in the cell nucleus in only two copies. Because DNA contains all the genetic information, any damage to this molecule could be harmful and potentially lethal for the cell. Consequently, we will only consider damages to DNA in the next section. However, reader can refer to “Radiation damage to cellular targets: an overview”, a review on biomolecule damages caused by ROS to which the author of this thesis contributed.

2.5.1. DNA damage and cellular response

DNA is a macromolecule composed of two helix strands linked one to each other by hydrogen bonds. Its strand backbone is made from alternating phosphate and sugar (2-deoxyribose) residues linked to a nitrogen base (adenine, thymine, cytosine or guanine). These bases are complementary one to another: adenine with thymine and cytosine with guanine. Once ionizing radiations pass through the cell nucleus, DNA can be damaged by direct or indirect way leading to a set of different damage types including:

- Base damages: radiation can generate lesions to the bases mostly through the indirect way. Addition of hydroxyl radicals produced by water radiolysis on unsaturated chemical bonds present in bases first leads to the generation of a radical intermediate which then forms modified base compound after subsequent reactions. Due to the need of ROS to generate base damages, the number of these lesions decreases with LET reflecting the importance of the indirect effect in low-LET irradiation (Figure 8).

- **Single Strand Breaks (SSB):** these lesions occur when the phosphate or deoxyribose backbone is broken on one side of the DNA double helix. They can be produced through direct interaction with ionizing radiations or via oxidation by ROS. Using ROS scavengers, the direct SSB yield was calculated for a mammalian cell exposed to X-rays to be 337/cell/Gy [36]. Considering that the total SSB yield was found to be 1000/cell/Gy, approximately 65 % of the SSB might be caused by ROS [37]. This unequal distribution between direct and indirect effects in SSB formation explains the decrease in SSB number reported with increasing LET (Figure 8).
- **Double Strand Breaks (DSB):** these lesions involve the breakage of the two opposite sides of DNA double helix within a distance of 10 base pairs. While SSB are easy to handle due to the availability of the second strand as template for repair, DSB are more harmful giving them a major role in cell death post-irradiation. Indeed, Banath et al. [38] showed an inverse correlation between non-repaired DSB amount and cell survival. Compared to SSB, DSB are mainly produced through a direct ionization of DNA by the incident particle [39]. Thereby the higher is the LET parameter, the higher is the amount of created DSB, and consequently the lower is the survival fraction [40], as illustrated in Figure 8.

When DNA damages are detected, a variety of DNA repair mechanisms are activated, leading to the removal of the vast majority of damages from the genome. The DNA repair mechanism at play depends on the lesions of interest [41]. In this section, we will only focus on DSB repair mechanisms since their high complexity make them the deadliest ones upon irradiation. This characteristic comes from the cell inability to simply copy the information from the undamaged strand.

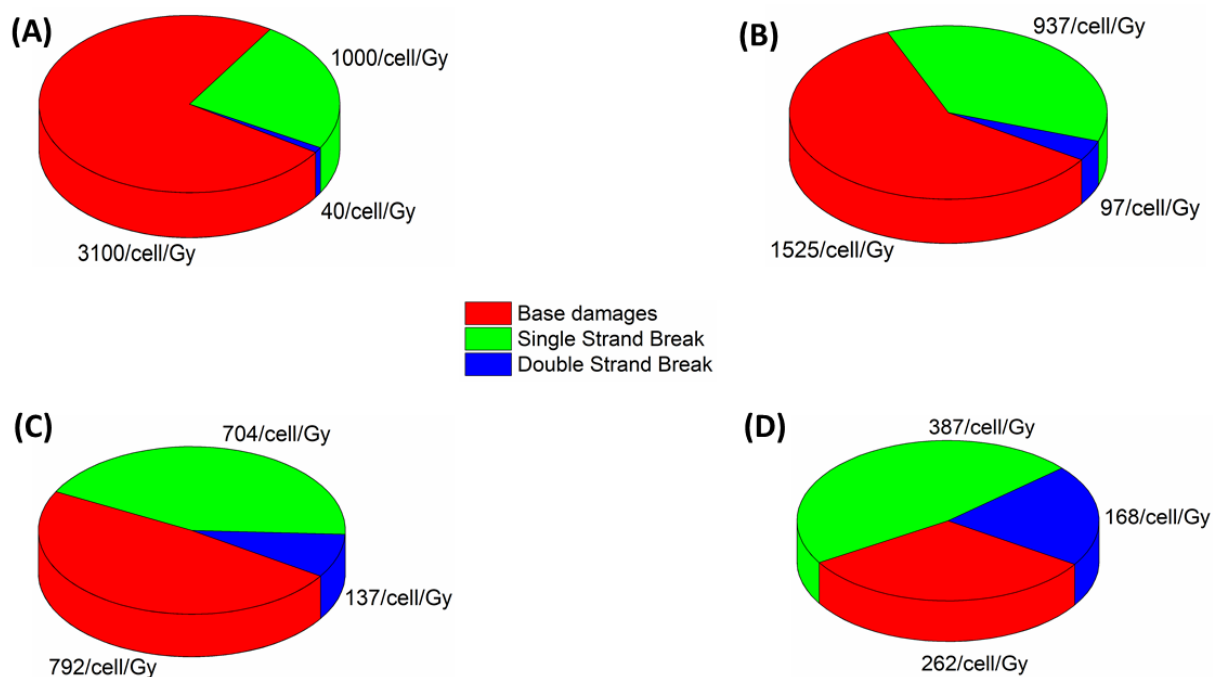


Figure 8. DNA damages/cell/Gy of radiation induced by (A) X-rays ($\approx 1 \text{ KeV}/\mu\text{m}$ [36]), (B) protons ($25 \text{ KeV}/\mu\text{m}$ [42]), alpha particles ($100 \text{ KeV}/\mu\text{m}$ [42]) and carbon ions ($282 \text{ KeV}/\mu\text{m}$ [42]).

To cope with this issue, cells have two main repair mechanisms: the homologous recombination (HR) and the non-homologous end-joining (NHEJ) processes. These mechanisms differ one from each other in terms of involved proteins, speed and repair accuracy. HR repairs DSB by using the undamaged sister chromatid as template enabling an error-free restoration. In contrast, NHEJ directly ligates the DNA break ends, without the need for any template. This process is an error-prone repair process because loss or changes of few nucleotides may occur. However, the main part of DNA is non-coding, thereby limiting the risk of mistakes on critical DNA sequences. It must be noted that, despite its low accuracy in repair, NHEJ enables a faster DSB repair compared to HR. The division of tasks between these two mechanisms is mainly determined by the phase of the cell cycle. As HR requires a homologous sister chromatid as template, it exclusively acts in S- and G₂-phases. In contrast, post-mitotic cells and cycling cells in G₁ phase seal DSB by NHEJ.

Without detailing all the processes of DNA Damage Response (DDR), DNA repair starts by the lesion recognition by protein sensors. These proteins then transmit a signal to downstream effectors through a transduction cascade undertaken by ataxia telangiectasia mutated (ATM) protein kinase. Phosphorylation of effectors enable the loading of other subsequent repair factors. Amongst all these effectors, it has been demonstrated that 53BP1 plays a key role in the mechanism choice by promoting NHEJ process [43, 44].

In HR process, the recognition of DNA ends is followed by their resection by MRN complex and CtBP-interacting protein (CtIP). Subsequently, BRCA2 mediates the coating of DNA extremity by RAD51, forming a nucleoprotein filament which is able to search the homologous sequence on the sister chromatid. Then, a DNA polymerase fills the breaks in the strand using the sister chromatid as template leading to an accurate repair of the DNA lesion [45]. The general mechanism of HR pathway is illustrated in Figure 9 (right panel)

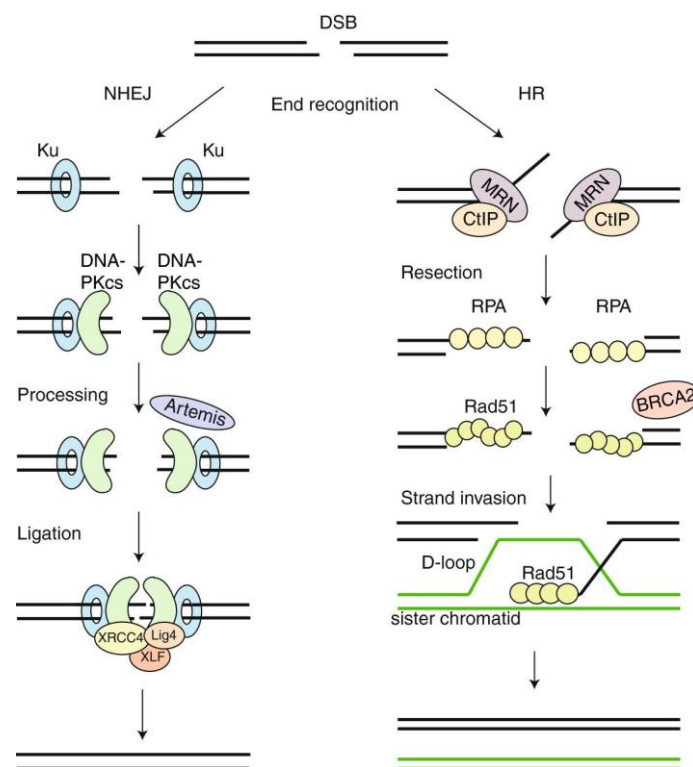


Figure 9. Homologous recombination (HR) and Non-Homologous End Joining (NHEJ) repair pathway mechanism. DSB = Double Strand Break; MRN = protein complex consisting of Mre11, Rad50 and Nbs1. Adapted from [45].

In NHEJ, Ku70/Ku80 heterodimer binds the DNA ends and recruits the catalytic subunit of the DNA-dependent protein kinase (DNA-PKcs). In some cases, DSB cannot directly be connected and must be processed before the ligation process. This optional step involves a set of proteins including Artemis in 10-15 % of the X-ray-induced DSB [36]. Finally, a ligation complex, consisting of DNA ligase IV, XRCC4 and XLF ligates the DNA ends leading to the DNA repair [45]. The general mechanism of NHEJ pathway is illustrated in Figure 9 (left panel).

2.5.2. Cell death

Consequences of DNA damage depend on cell type and lesion severity. While mild DNA damage can be repaired as discussed above, more severe DNA injury can lead to a shift towards cell death induction programs. In radiobiology, cells are considered as dead when they lose their proliferative capacity meaning they can no longer divide and/or spread through the organism. Thereby, cells can be considered as “clonogenically” dead but still possess a metabolic activity. In this respect, five main cell death mechanisms are possible:

- Apoptosis. Apoptosis is a programmed cell death mechanism, often called “cell-suicide” program. In mammalian cells, it is mediated by a group of proteases known as the caspases that keep the apoptotic program under control. Initially expressed as inactive procaspase precursors, these mediators can be activated by oligomerization and cleavage of the precursor form to produce the active effector. These active caspases in turn cleave specific cellular substrates leading to biochemical changes in the cell [36]. Cytochrome c^5 is released from the mitochondria, triggering the apoptosome formation. Subsequently, all cellular components are packaged into membrane-enclosed apoptotic bodies. The apoptotic bodies are eventually phagocytosed by neighboring cells, hence without releasing harmful substances into extracellular environment. This characteristic justifies its title of “clean death” process. It must be noted that apoptosis can be triggered by extrinsic signals (binding of extracellular ligands to a death receptor located on the cell membrane) as well as by intrinsic signals (caspase activation in response to severe cellular damages) [36, 46].
- Necrosis. Necrosis is a form of cell death usually initiated following ion imbalance, energy loss or extreme pH change. These stresses cause cell swelling and membrane distortion leading to the spread of cellular content into the extracellular environment. Thereby, necrosis is associated to strong side-effects for the surrounding cells and so, to infection, inflammation, or ischemia induction [36].
- Autophagy. Autophagy is a cellular process where proteins and organelles are enclosed into a double-membrane vesicle which then fuses with a lysosome, thus provoking the digestion of its content. This digestion enables the cell survival by generating small biomolecule fragments and energy that can be used to maintain the cell metabolic activity [47]. Although this kind of protective mechanism was reported in response to different stresses such as nutrient deprivation or growth factor removal, comprehensive cell component digestion leading to cell death was observed when cells are exposed to chemotherapy agents [36].

⁵ An essential component of the mitochondrial electron transfer chain.

- Senescence. After each cell replication, telomeres of chromosomes become shorter. Following multiple cell divisions, these telomeres become too short and cells become unable to replicate without an important genetic material loss. They enter into a form of permanent cell-cycle arrest stage, known as replicative senescence. Although cell proliferation stops, senescent cells still remain metabolically active, showing a greatly altered pattern of gene expression. It was reported that cellular senescence can be triggered by severe or irreparable DNA damages, in that case, the term used is stress-induced senescence [48].
- Mitotic catastrophe. In normal cells, G₂ checkpoint of the cell cycle enables to block mitosis when a cell has undergone DNA damage. Nevertheless, when the G₂ checkpoint is defective, the cell can enter mitosis prior a complete DNA replication and/or DNA damage repair. This results in giant multinucleated cells that may be able to divide for a few cell cycles until the genetic material in daughter cells is so chaotic that replication is no longer possible [36, 46].

2.6. Factors influencing the success of radiotherapy

As previously discussed, successive physical, chemical and biological processes occur when ionizing radiations interact with matter leading to the tumor cell death. Over the years, it has become clear that a number of factors influences this tumor death and so the success of radiotherapy. Withers [49] summarized these factors as the “four Rs”. By evidencing the time-dependence of them, radiotherapy has move towards the modern fractionation radiotherapy:

- Repair: As discussed previously, cells have complex mechanisms enabling the repair of DNA damage induced by radiation. Although DNA damage produced in tumor cells are easily repaired at low radiation dose, their accumulation at high radiation dose contributes to cell death. However, this goes hand in hand with an increased toxicity to normal tissues as well. According to Corner et al. [50], normal tissues repair DNA damage at a faster rate than cancer cells. Thereby, fractionated treatment can take advantage of this difference. All cells can be damaged, but normal cells will repair faster the radiation-induced DNA damage leading to a better survival compared to cancer cells. Due to differences in organ sensitivity to radiation, the same fraction schedule cannot be used in all cancers. Thus, some dose-fractionation guidelines provide fractionation schemes for different organs based on tissue repair rates [46, 50].
- Reoxygenation: Oxygen plays a key role in radiation therapy through the ROS production during the chemical step as well as for the DNA free radicals fixation. During the uncontrolled proliferation of cancer cells, the tumor quickly exhausts the oxygen supply from the normal vasculature resulting in the generation of hypoxic areas. Cox et al. [51] estimated that the proportion of hypoxic cells in a tumor usually ranges from 10 to 15 %. When a tumor is irradiated, the oxygenated cells are killed more easily than hypoxic ones due to the higher oxygen pressure within them. After irradiation, the proportion of hypoxic cells in the tumor is thus higher than prior the irradiation. Nevertheless, the situation is not static. In fact, irradiation also triggers the nitric oxide synthase activation enabling an arterial vasodilatation which increases the tumor tissue perfusion [52]. This phenomenon allows a tissue reoxygenation during a given time period (12 h – 120 h) after the irradiation. If the interval between radiation doses is long enough to allow reoxygenation to take place, then originally

hypoxic cells can become oxygenated and be more easily killed by the next dose. Thereby, the presence of hypoxic cells has a lower effect on the treatment success if the total dose is divided into fractions enabling a sufficient duration for cell reoxygenation in between these fractions [46] (Figure 10).

- **Redistribution:** It has been demonstrated that cell radiosensitivity considerably varies with the phases of the cell cycle. Cells in the S phase are the most resistant while cells in late G₂ and M phases are the most sensitive [53]. The reason for the resistance in S phase is thought to be an increased homologous recombination capacity due to a greater availability of the undamaged sister template through the S phase. Moreover, it was postulated that conformational changes in DNA during replication facilitate an easier access for the repair complexes [46]. In contrast, the greater sensitivity in late G₂ and M phases is due to the fact that those cells enter in mitosis with DNA damages, leading to quicker cell death. Thereby, the fractionation therapy which takes place over multiple sessions is more effective because it enables the cells in the G₁ and S phases of the cell cycle to move towards more radiosensitive phases (Figure 10).
- **Repopulation:** Repopulation of cancer cells has been considered to be the main cause of radiotherapy failure. It refers to the observed increase in cell division in both normal and cancer cells after irradiation. Thus, if the overall treatment time is too long, the effectiveness of last dose fractions will be ineffective due to the triggering of rapid tumor repopulation [54] (Figure 10).

In 1989, Steel et al. [55] suggested to add “intrinsic radiosensitivity” as a fifth critical parameter influencing the radiotherapy success. In fact, it has been evidenced that patient-related factors account for as much as 80 to 90 % of the variation observed in patient response to radiation [56]. Nowadays, the origin of this variability remains poorly understood but it is generally accepted that it is due to genomic variations.

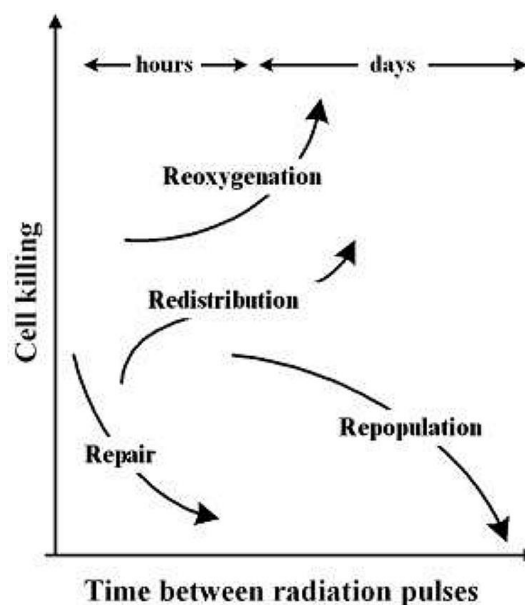


Figure 10. Dependence of radiotherapy efficiency to kill cell according to the time between fractions. The influence of 4 Rs parameters is illustrated. Adapted from [46].

2.7. Comparison between conventional radiotherapy and charged particle therapy

The goal of this section is to compare conventional radiotherapy which uses X-rays and charged particle therapy, based on the physical, chemical and biological insights introduced here above.

2.7.1. Spatial dose distribution

The most famous advantage of particle therapy over conventional one is the spatial dose distribution. Like all photons, X-ray transfers its energy to the body along its path. The energy deposition profile shows an initial increase within a few centimeters. Subsequently, beam intensity is decreased according to Beer-Lambert exponential law (equation 4), irradiating tumor as well as normal tissues upstream and downstream the tumor (Figure 11). This energy deposition in healthy tissues can be dramatic in case of organs at risk. To cope with this limitation, the use of charged particles is growing, driven by their ballistic properties. As discussed before, a charged particle slows down when it travels through the matter due to multiple interactions. Equation 9 shows that when the charged particle velocity decreases, stopping power increases resulting in a particular depth-dose profile with a low entrance dose and a maximal dose deposition at a selective depth, called the Bragg peak, where the particle stops. Since the Bragg peak localization depends on the incident particle energy, a combination of particle beams of different energies enables to obtain a plateau in the dose profile (known as Spread-out Bragg Peak; SOBP) that covers the entire tumor volume (Figure 11). Although normal tissues upstream the tumor still receive part of the radiation dose, healthy tissues downstream the tumor will be completely saved. As shown in Figure 12, proton irradiation of a non-small cell lung carcinoma markedly limits the radiation dose received by the healthy lung and the spinal cord.

2.7.2. Relative biological effectiveness

To compare different radiation types in terms of biological effects, the relative biological effectiveness (RBE) has been proposed. RBE is a ratio of doses required to obtain a same biological endpoint (generally a cell survival) between a reference radiation (usually a 250 kVp X-rays) and the radiation type of interest. RBE of protons in clinic was evaluated to 1.1, meaning protons enable to reach the same cancer cell killing than photons with a 10 % reduced dose of radiation delivered to the patient [57]. For carbon ions, a RBE between 2 and 3 was reported [46]. The RBE indicator depends on several factors including the LET ⁶, meaning that RBE of charged particles varies along the track; e.g. significantly higher near the Bragg peak. This reflects the need of enough energy deposition in the DNA to produce a sufficient amount of DSB and so, to promote cell killing. Sparsely ionizing radiations, such as X-rays, have a relatively low efficiency because more than one particle may have to pass through the cell to produce enough DSB. On the contrary, densely ionizing radiations (high-LET charged particles) produce more DSB due to the spatial proximity from one DNA damage to one other, resulting in complex and clustered DNA lesions that are difficult to repair.

⁶ RBE increases with LET until a maximum around 100 keV/μm regardless the nature of the particle of interest.

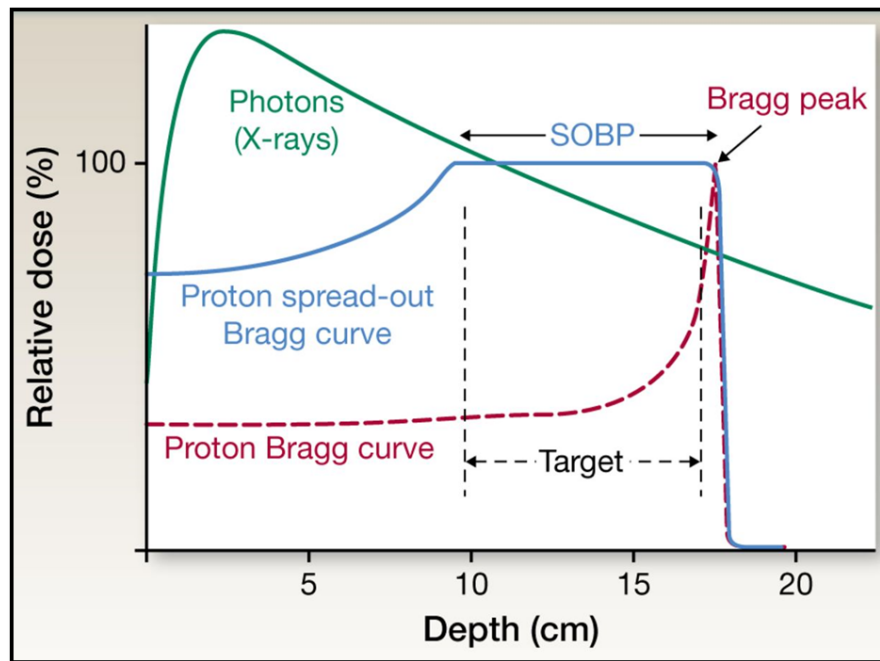


Figure 11. Depth-dose profile for a typical 15 MV photon beam (green curve) and mono-energetic proton beam (red curve). The maximum dose point of the red curve is termed the Bragg peak. Scanning thin mono-energetic proton beams are used for intensity-modulated protontherapy leading to the blue curve and a plateau in the depth-dose profile, called the spread-out Bragg peak (SOBP). Adapted from [58].

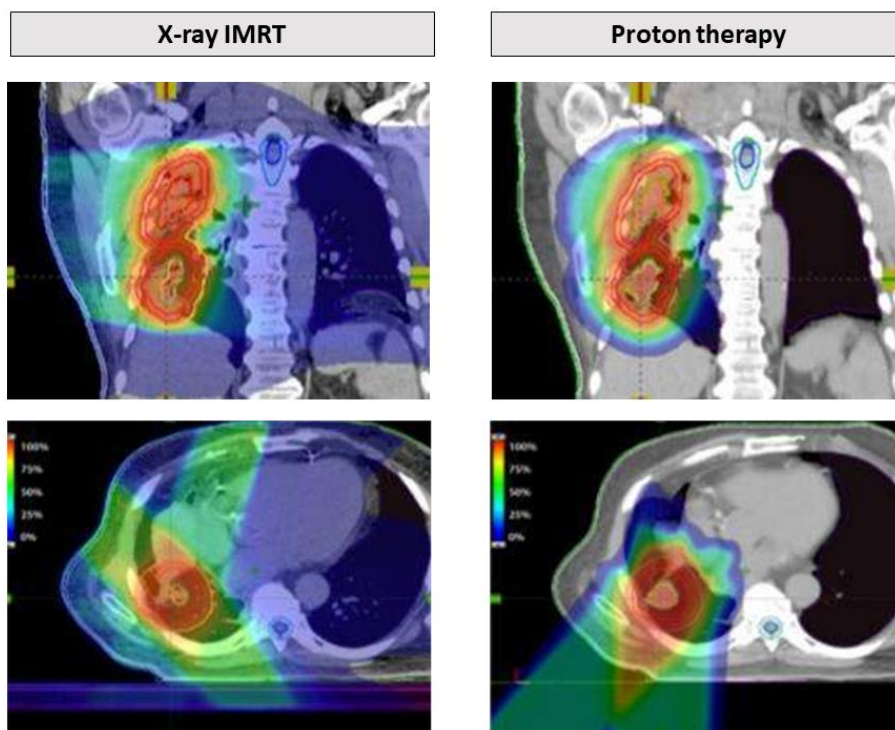


Figure 12. Example of treatment planning for the irradiation of non-small cell lung carcinoma. Compared to X-rays, protons enable a more precise tumor targeting while limiting irradiation of healthy tissues (the opposite lung and spinal cord). Adapted from [59].

2.7.3. Oxygen enhancement ratio

The presence of oxygen in cells is important for ROS production through the indirect effect. Therefore, a more efficient cell killing was reported in oxygenated area compared to hypoxic areas upon X-ray irradiation [36, 46]. However, by increasing LET of radiation, the proportion of direct to indirect effect increases leading to a lower dependence of high-LET particle irradiation on oxygen concentration. Consequently, the oxygen enhancement ratio ⁷ (OER) decreases with increasing LET. The ratio decreases from 2.7 for 250 kVp X-rays to around 1 for 100 keV/μm α-particles (Figure 13), meaning that this last radiation beam kills hypoxic cells with the same efficiency as normoxic cells.

2.7.4. Clinical indications

As mentioned before, hadrontherapy has become one of the most attractive approaches in the cancer management driven by its ability to deal with two key aspects of modern radiation oncology: First, ballistic features that enable a dose optimization into tumor volume, sparing surrounding healthy tissues. Secondly, biological features that allow a greater RBE related with a high LET along their path. The most recent report of PTCOG (Proton Therapy Co-Operative Group) indicates that 174,512 patients have undergone hadrontherapy worldwide [60]. The large majority of these patients (around 86 %) were treated using protons which have shown clear advantages compared to X-rays, in two main settings [61]:

- ✓ Treatment of radioresistant tumor, located close to a radiosensitive organ. Protontherapy is the reference treatment for ocular malignancies, especially uveal melanomas because it allows to preserve radiosensitive optical nerve downstream the tumor. Remarkable results, 95 % local control and 80 % overall survival have been reported by most groups [61]. A second indication is the irradiation of chordomas and chondrosarcomas at the skull base for which protontherapy still remains essential to achieve a permanent local control.
- ✓ Treatment for which the normal tissue sparing is a priority. For pediatric cancer, the extreme sensitivity of organs under development confers a great advantage on protons by reducing long term sequelae [62]. Moreover, pieces of evidence of a decreased risk in radiation-induced secondary malignancies are growing [63]. Protons have also shown beneficial in adults with reduced rates of gastrointestinal, urinary incontinence or other complications following prostate irradiation [64].

Despite their clear theoretical advantages compared to conventional radiotherapy, the use of charged particle therapies has been slowed by technical factors, such as treatment cost. Indeed, the cost of a protontherapy treatment still remains 2 to 4 times higher than the cost of the conventional photontherapy [65]. Moreover, no randomized phase III clinical trial results are available to objectively compare X-ray and proton radiotherapies. This indicates that there is no evidence that protontherapy is more effective than IMRT up to date [46]. All reported proton results come from prospective studies and non-randomized clinical trials. While randomized studies are a mandatory step towards protontherapy development, some commercial insurance medical policies (especially in USA) do not

⁷ OER: Ratio of doses necessary to achieve a same biological endpoint (usually a cell survival) with or without oxygen.

cover this treatment, making it difficult for patients to participate in these investigations. In the 2019 report of KCE, only three ongoing randomized clinical trials were identified comparing proton treatment with photon radiotherapy and results are not expected before 2027. As a result, the lack of evidence for a better outcome with protontherapy is not likely to change within the next 10 years.

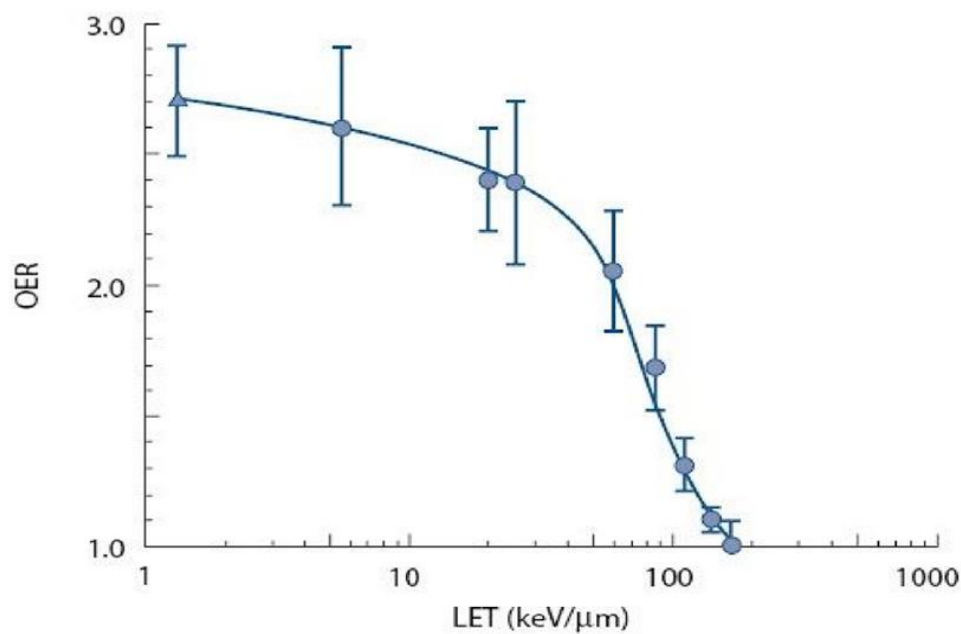


Figure 13. Decrease in OER with increasing LET. Closed circles refer to monoenergetic α -particles and the triangle to 250 kVp X-rays. Adapted from [46].

3. Nanoparticles as radiosensitizers: emergence of a new field in nanomedicine

3.1. Modifying the cellular response to radiation. Motivation and available solutions

As discussed in the previous section, the most important challenge of radiotherapy is to favor the energy deposition into the tumor while sparing surrounding healthy tissues. The likelihood for a tumor being controlled is called the tumor control probability (TCP), while the one for the healthy tissue side-effect is called normal tissue complication probability (NTCP). These probabilities are represented by a sigmoid function according to the dose. From these definitions, it follows that the probability of cure without complication (PCWC) is given by equation 16 and is illustrated in Figure 14:

$$PCWC = TCP \cdot (1 - NTCP) \quad (16)$$

In Figure 14, it appears that dose associated with tumor eradication is not very different from the dose associated with normal tissue complication development. By using a molecule, localized into the tumor and which has the ability to increase cell killing, one can move the TCP curve towards the left. Consequently, a significant increase in PCWC maximum and in its distribution width occurs providing a larger margin for the therapeutic window. These kinds of molecules are called “radiosensitizers” and enable to reach a given tumor cell killing using a reduced total dose delivered to the patient. Besides this radiosensitizing agent, PCWC improvement can also be obtained by using radiation protector molecules that have to be specific for normal cells.

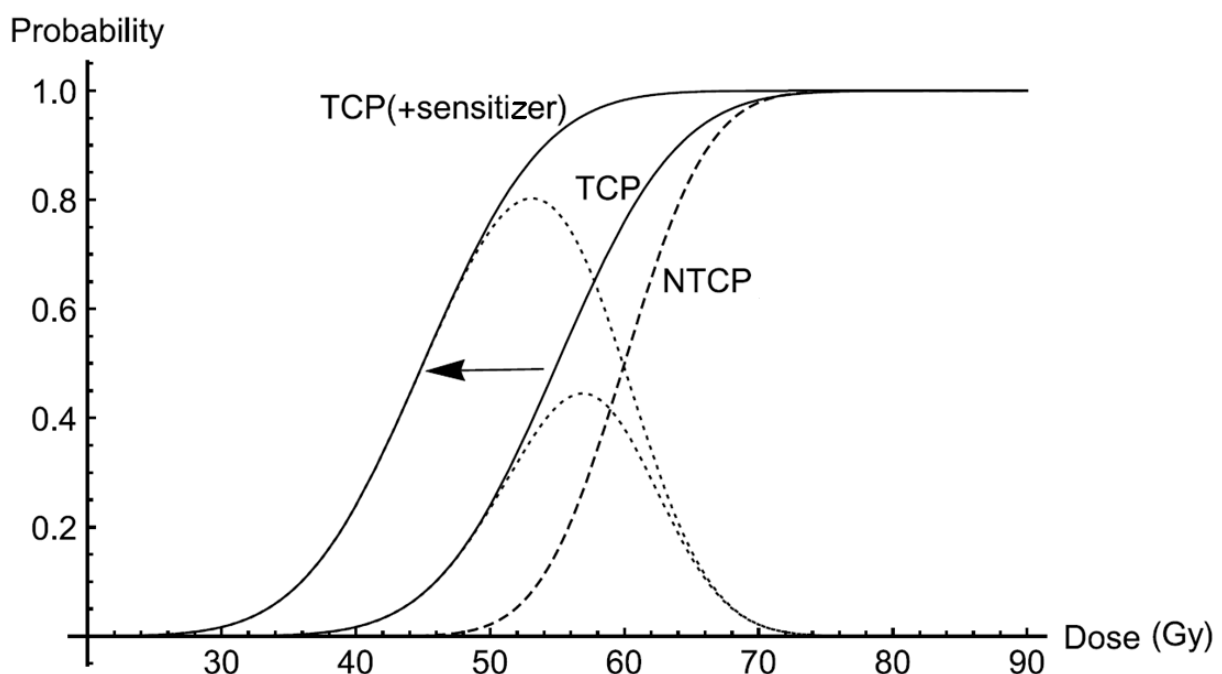


Figure 14. Schematic representation showing the TCP (solid line) and NTCP (dashed line) as a function of the radiation dose. The TCP is illustrated for two scenarios, one with a $TCD_{50\%} = 55$ Gy and a second with a $TCD_{50\%} = 45$ Gy, to illustrate the action of a radiosensitizer specifically targeted to the tumor. In each case, the PCWC is shown by the dotted line. Adapted from [17].

Since the pioneering works of G.E. Adams [67], various radiosensitizer classes have been characterized. The main categories are:

- Molecules that exacerbate DNA damage. In this category, are molecules such as cisplatin or 5-fluorouracyl (5-FU) which are able to increase the DNA damage amount after irradiation. Indeed, when incorporated into DNA, 5-FU causes no additional damage in the absence of radiation but enhances radiation-induced DNA damage through the production of reactive uracyl radicals and halide ions [68]. Cisplatin binds DNA and can act synergistically with ionizing radiation to convert radiation-induced SSBs to DSBs during the DNA repair process.
- Inhibitors of post-irradiation cellular repair processes. Some chemotherapy agents have been shown to inhibit DNA damage repair via a set of mechanism. For example, gemcitabine, a nucleoside analogue, interferes with nucleotide metabolism leading to DNA repair inhibition. Other molecules directly inhibit DDR proteins, such as Olaparib, an inhibitor of poly(ADP-ribose) polymerase (PARP), a protein mainly involved in SSB repair [68].
- Cell cycle disturber. This category gathers molecules such as taxol, an anti-microtubule agent. The binding of taxol to β -subunit of microtubulin leads to a G₂/M cell cycle arrest. As a consequence of this, cells are synchronized in this radiosensitive phase of the cell cycle enabling a radiosensitization effect [68].
- Inhibitors of endogenous radioprotective substances. Ionizing radiation exerts biological effects partly through the production of ROS. To counteract ROS overproduction, cells possess a set of antioxidants and detoxification enzymes. Molecules such as l-buthionine-SR-sulfoximine, a cysteine analogue, have the ability to interfere with the antioxidant biosynthesis, reducing the cell capacity to counteract the oxidative stress [68].
- Oxygen-mimetic sensitizer. Many reports have reported an enhanced radiosensitivity of cells in the presence of oxygen (cf. section 2.6). Molecules, as nitroimidazole, also have this electron affinity property and can mimic the important role played by oxygen in cell killing. This class of sensitizer is interesting for distant hypoxic cells because it was postulated that such agents are not rapidly metabolized by tumor cells enabling a diffusion up to hypoxic cells, which are often far away from blood vessels [69].
- Small interfering RNA (siRNA). siRNA are RNA molecules which have the ability to interfere with the expression of a set of specific genes by complementary binding and degrading their mRNA after transcription. By silencing gene expression related to radioresistance, siRNA can be used as radiosensitizers. This relatively new class of radiosensitizers is currently under clinical investigation. A recent work evidenced an increase in head and neck squamous-cell carcinoma radiosensitivity using a siRNA technology against survivin, a protein which inhibits caspase activation, hence leading to an increased apoptosis [70].

Since the last decade, development of nanotechnology has expanded the horizon of the radiosensitizer field by creating a new class: the nanostructured radiosensitizer on which we will focus in this thesis.

3.2. Nanotechnology from chemical applications to nanomedicine

Nanotechnology is the science that deals with materials or structures in nanometer scale (1 billionth of a meter, e.g. 10^{-9} m), typically ranging from sub nanometers to several hundred nanometers. These materials have attracted enormous attention because the properties of nanostructures are different from the same bulk materials due to the high surface/volume ratio and possible appearance of quantum effects at the nanoscale. All these new properties have allowed the emergence of numerous applications in various fields including catalysis and sensors.

The high surface/volume ratio of nanoparticles (NPs) enables catalytic promotion of reactions via their ability to adsorb and transform chemical compounds. Indeed, large NP surface increases the ability to adsorb or bind chemical compounds, while quantum phenomena at NP interface allow an increased chemical reactivity [71]. The panel of new potential reactions goes from compound decomposition to selective alkene hydrogenation [72].

Metallic nanoparticles also have new optical properties which have permitted the development of sensor technologies in various chemical and biomedical fields [72]. These new properties are due to a collective oscillation of free electrons in the metal, when a photon goes through a NP solution. Indeed, when the electric field from free electron vibration resonates with the electric field of the electromagnetic wave, a light absorption phenomenon called surface plasmon resonance happens. Gustav Mie was the first to model this phenomenon and to give an exact analytic solutions of Maxwell's equations for a sphere immersed in a homogenous medium and irradiated by an electromagnetic wave [73]. He defined the absorption cross-section σ of an electromagnetic wave of wavelength λ as:

$$\sigma_{ext} = \frac{2}{x^2} \sum_{n=1}^{\infty} (2n+1) \cdot (a_n + b_n) \quad (17)$$

$$x = \frac{2\pi r}{\lambda} \quad (18)$$

Where r is the NP radius, a_n et b_n coefficients can be defined using the Riccati-Bessel functions of order n , referred as ψ_n and ζ_n , as well as their derivatives, ψ'_n and ζ'_n :

$$\begin{aligned} a_n &= \frac{\psi'_n(y) \cdot \psi_n(x) - m\psi_n(y) \cdot \psi'_n(x)}{\psi'_n(y) \cdot \zeta_n(x) - m\psi_n(y) \cdot \zeta'_n(x)} \\ b_n &= \frac{m\psi'_n(y) \cdot \psi_n(x) - \psi_n(y) \cdot \psi'_n(x)}{m\psi'_n(y) \cdot \zeta_n(x) - \psi_n(y) \cdot \zeta'_n(x)} \end{aligned} \quad (19)$$

Where y is a variable proportional to x and m is the ratio between the NP complex refractive index and the medium complex refractive index. This analytical development evidences that light absorption depends on NP size (x) as well as on NP and solvent nature (m). Thereby, surface plasmon band spectroscopy can be used to determine the particle size due to the dependence of maximal absorption wavelength in this parameter, as illustrated in Figure 15.

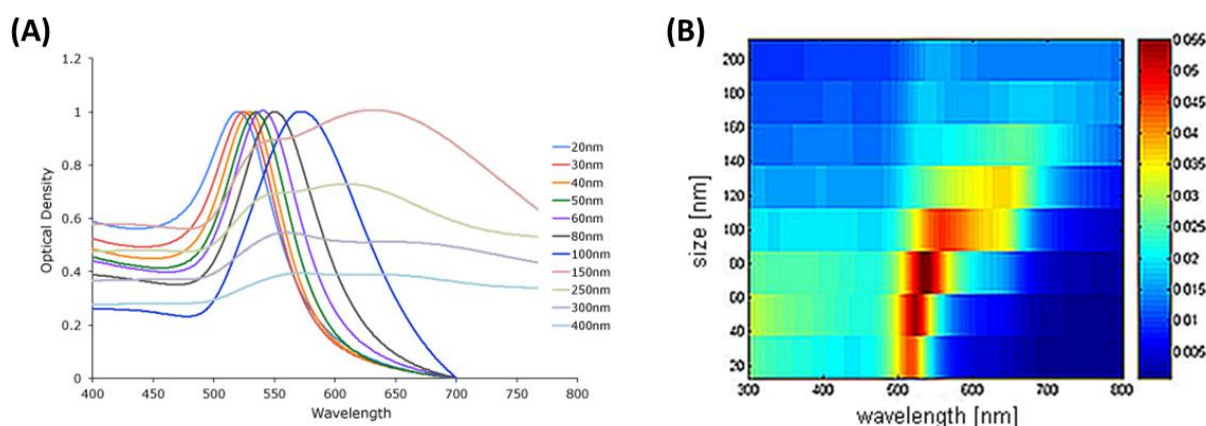


Figure 15. Variation of the theoretical maximal absorption wavelength with the gold nanoparticle size.

Moreover, UV-visible spectra of NP solutions enable to extract the heterodispersity index, a frequently used indicator of colloidal stability, defined as a ratio of absorbance:

$$\text{heterodispersity index} = \frac{A_{\lambda \max}}{A_{650 \text{ nm}}} \quad (20)$$

When NPs aggregate, their size increases leading to a shift towards higher wavelength, as illustrated in Figure 15A. This bathochromic shift is translated to a decrease in the heterodispersity index. By following the evolution of this indicator according to the time, we can assess the colloidal stability through the time.

In addition to these chemical applications, a set of potential nanotechnology-based applications emerges for disease diagnosis and treatment, including cancer. This emerging biomedical field, called nanomedicine, finds its origin in a fact: NPs below 100 nm match the length scales of the pores in the tumor vessel endothelium. In solid tumors, angiogenesis leads to high vascular density of newly formed tumor vessels that are usually abnormal in form and architecture. It consists of poorly aligned defective endothelial cells with large gaps between them. Moreover, tumor tissue lack effective lymphatic drainage [74]. The combination of these two aspects can lead to a selective extravasation of nanoscopic drugs as well as their poor clearance leading to a potential accumulation in tumor tissue. This phenomenon is called enhanced permeation and retention (EPR) effect. It was reported that many nanomaterials (including liposomes, polymer carriers, metallic and inorganic NPs) successfully enter into tumor tissue through this EPR effect [75-77]. The first suggested nanotechnology-based applications for cancer was to use NPs as vehicles for drug delivery. Although a set of chemotherapeutic drugs have proven their ability to kill cells, their use *in vivo* is limited by their low water solubility, their relative stability, their biodistribution and their ability to selectively target tumor cells. To cope with this wild range of limitations, polymeric NPs were suggested as nanocarriers by enveloping the drugs. While a low water solubility will limit the compound bioavailability, the use of nanocarrier increases the delivery of these poorly soluble drugs. For example, wortmannin was suggested as potential radiosensitizer drug due to its ability to inhibit the DNA damage response (inhibitor of ATM protein) [68]. However, its development was stopped due to a poor water solubility (4 mg/L) and chemical instability. Using polymeric nanocarriers, the wortmannin solubility was increased up to 20 g/L [75, 78] and a powerful increase in chemical stability was reported *in vivo* [78]. The increase in stability was explained by the nanocarrier protective action

which prevents drug biodegradation until its entry into tumor. Indeed, protein-based drugs can be cleaved by pepsin or trypsin present in the stomach (in case of *per os* administration). Finally, nanocarrier can improve the biodistribution by accumulating drug in tumor via the EPR effect.

Since the first nanocarrier generation, significant advances were made enabling the development of more sophisticated stimuli-responsive nanocarrier systems. These vehicles act in response to physical, chemical, or biological signals triggering drug release. The advantage of this kind of system is a more accurate drug release in tumor cells, minimizing the usual systemic exposure to the chemotherapeutic agent [75]. Triggers are usually divided into internal and external stimuli. Internal stimuli are based on biochemical characteristics of neoplastic tissue such as pH or redox. In solid tumors, the extracellular pH is more acidic than physiological pH allowing the use of pH-responsive nanocarriers [79]. Another example is the disulphide-containing liposomes. Hypoxic tumors are an environment rich in reductive compounds as glutathione due to the low oxygen pressure. These agents cleave disulphide bonds generating a change in conformation which triggers the drug release in the tumor [80]. On the other hand, external stimuli are based on the use of physical stimuli such as hyperthermia [81], ultrasound [82] or light [83].

Currently, around thirty nanocarrier systems are under investigation in different clinical phases for cancer treatment [77] and several have already been approved for clinical uses (Table 3). The first NP-based drug approved for therapeutic application was Doxil, a liposome containing doxorubicin. Despite good results in terms of biodistribution, no real benefit on overall survival was reported in comparison to doxorubicin treatment alone. However, a better treatment tolerance was evidenced [84].

Product name	Vehicle type	Encapsulated drug	Clinical indication	Approved by (in year)	Ref.
Abraxane	Albumin NPs	Paclitaxel	Advanced NSCLC, metastatic breast and pancreatic cancer	EMA (2008)	[85]
DepoCyt	Liposome	Cytarabine	Neoplastic meningitis	FDA (1999)	[86]
Doxil	PEG-liposome	Doxorubicin	Ovarian and metastatic breast cancer, multiple myeloma	FDA (1995)	[87]
MEPACT	Liposome	Mifamurtide	Osteosarcoma	EMA (2009)	[88]
Oncaspar	PEG conjugated to protein	L-Asparaginase	Leukemia	FDA (2006)	[89]
Onivyde	PEG-liposome	Irinotecan	Metastatic pancreatic cancer (2 nd line)	FDA (2015)	[90]
Zinostatin stimalamer	Protein-conjugated polymer	SMANCS	Renal cancer	Japan (1994)	[91]

Table 3. Non-exhaustive list of drug delivery nanocarriers approved in clinic. NSCLC: non-small cell lung carcinoma

As for Doxil, most of first-generation nanocarriers (PEG-liposome) were reported to change the drug toxicological profile and to bypass drug solubility issues but no significant improvement in therapeutic efficacy compared to the parent drug was demonstrated [92]. More recently, the second nanocarrier generation has demonstrated interesting results. For example, Abraxane, an albumin NP containing paclitaxel, evidenced significantly higher response rates compared to paclitaxel alone in metastatic breast cancer patients [93]. In the same way, a third nanocarrier generation seems to emerge based on the use of metallic NPs as drug delivery platforms. For example, silver NPs have demonstrated their ability to effectively deliver doxorubicin and alendronate to cervical HeLa cancer cells resulting in a greater therapeutic effect than doxorubicin or alendronate alone [94]. Recently, *in vivo* results were obtained by evidencing the ability of hollow mesoporous silica NPs containing doxorubicin to enhance the tumor growth inhibition compared to doxorubicin alone [95].

Despite tremendous successful preclinical results, most nanomaterials have failed to reproduce an improved efficacy in clinic study [96]. One possible explanation could be the EPR model relevance in humans. Although this EPR effect was extensively demonstrated in rodents, there is a lack of evidences in humans. Murine tumor models usually used in preclinical studies, drastically differ from human cancers in terms of development rate and size relative to host. Due to a fast tumor growth in rodents, blood vessels in mouse tumor do not develop properly leading to leakier endothelial cells. In humans, the tumor growth is slower than in rodents and not all tumor vessels are leaky, causing a heterogeneity in pore size distribution and thus in nanomaterial delivery [97, 98]. Moreover, the large tumor-to-weight ratio in mice compared to humans significantly alter the pharmacokinetics of the nanomaterials. In murine models, tumor can be as much as 10 % of the mouse's body weight representing the size of basketball for an equivalent tumor in a 70 kg human patient [98].

3.3. High Z nanoparticle as radiosensitizer: basic principles

Originally, the rationale for using high Z NPs as radiosensitizers was based on their ability to increase the dose deposited in the target volume due to differences in their mass energy absorption coefficient by comparison with water. As mentioned before, in water, the most probable mechanism by which clinical X-rays lose their energy is the Compton effect that leads to the photon scattering and an electron ejection from the atom. The consecutively generated photons, which have a reduced energy, can interact through other processes, such as the photoelectric effect where the X-ray is wholly absorbed by a bound electron leading to its ejection from the atom. Figure 16A shows the contribution of these processes to the total absorption cross-section across the range of energies relevant for radiotherapy (taking account primary beam (typically ranging from 0.3 to 20 MeV) and secondary produced particles (up to 10 MeV)). When the photon interacts with a high Z materials, such as gold ($Z = 79$), the total absorption cross-section is larger due to the higher number of electrons per atom (Figure 16B). Indeed, the two main photon absorption processes result from interactions with electrons, so, higher Z materials correspond to higher numbers of electrons per atom. Moreover, this higher number of electrons implies atomic orbitals with higher binding energies. For each of these binding energies, there is an energy threshold below which no electron can be ejected from the atom. When the photon energy is equal to or higher than this energy threshold, there is a discontinuity in the photoelectric cross-section. These discontinuities are called absorption edges and are characteristic of the atomic species.

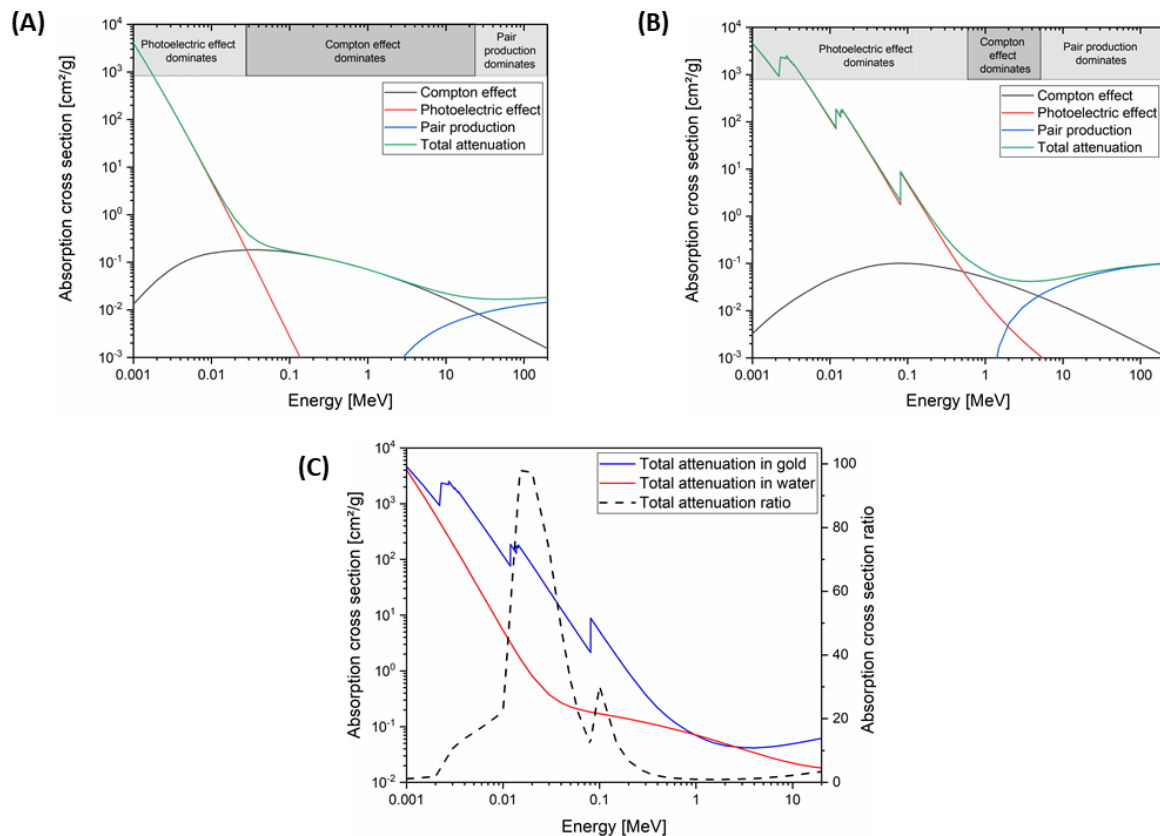


Figure 16. Absorption cross section of photons in water (A) or in gold (B) as a function of photon energy. (C) Comparison of photon total absorption cross section for gold (blue curve) and water (red curve) as well as ratio of gold absorption cross section on water absorption cross section (dashed line) depending on photon energy. Data were derived from the NIST X-ray attenuation database.

As showed on Figure 16B, gold has three absorption edges: M-edge around 3 keV, L-edge around 14 keV and K-edge around 80 keV. The photoelectric effect plays a bigger role in the total absorption cross-section over a wider energy range when material atomic number increases, as already suggested by Figure 4. Taking into account all of these effects, the increased photoelectric cross-section means that high-Z materials absorb substantially more energy per unit mass than water does when X-rays pass through them. By dividing the gold total cross section by the one of water, we observe that gold can be 100 times more effective at absorbing photons energy than water. This effect is translated into a significant increase in local dose when even a small amount of this metal is present in the medium (Figure 16C).

Similarly, when a charged particle passes through water, it interacts by collisions with electron and nuclei of oxygen and hydrogen atoms constituting water. Figure 17 shows the contribution of these two processes to the proton total stopping power across incident proton beam energy in water (A) and in gold (B). As shown on Figure 17C, interaction between protons and a high Z material leads to higher stopping power than with water, translating into a higher energy deposition per unit length than in water. By comparing the stopping power for the two media, we observed that this differential stopping power is proportional with the proton energy and can reach a 10-fold increase in the energy transfer to gold compared to water for a 100 MeV proton beam. This highlights also a potential significant increase in dose when high Z materials are present (Figure 17C).

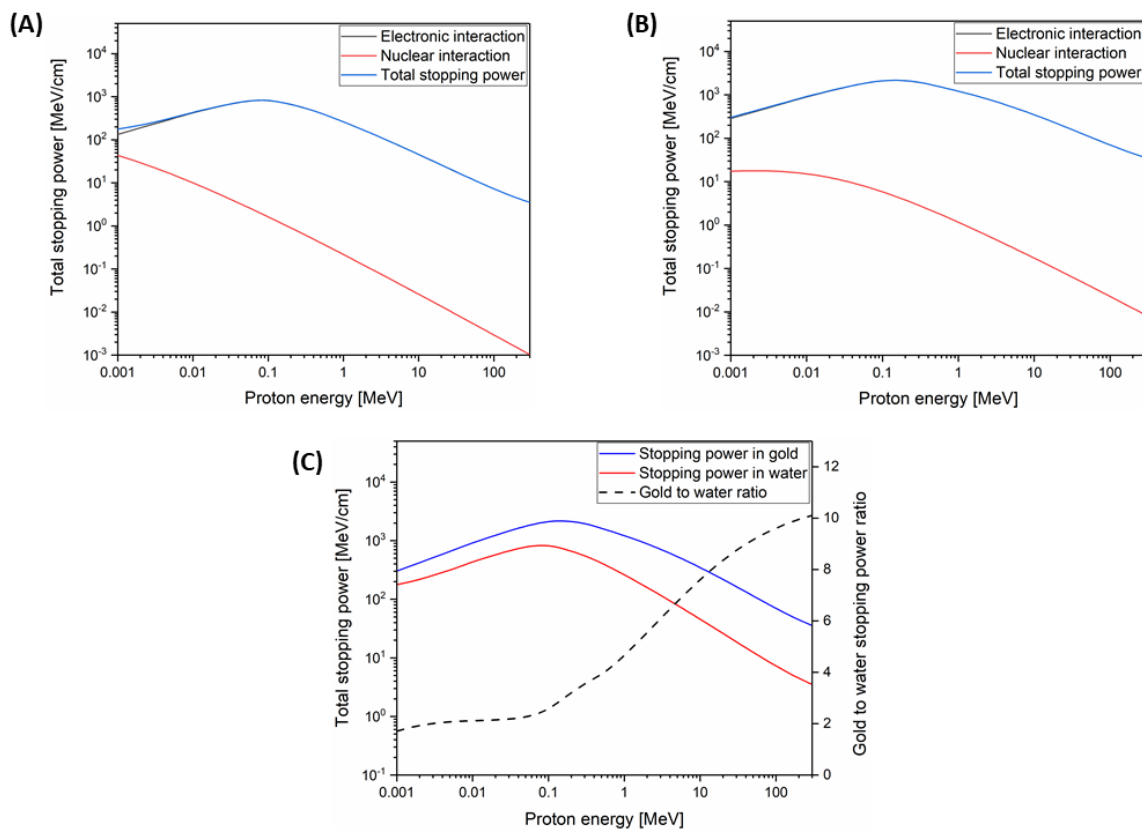


Figure 17. Total stopping power of proton in water (A) or in gold (B) as a function of proton energy. (C) Comparison of total stopping power for gold (blue line) and water (red line) as well as gold to water ratio of total stopping power (dashed lines) depending on photon energy. Data were derived from the pstar database of NIST.

As a consequence of the aforementioned processes, energy deposition is higher in gold than in water. This increase in local dose deposition enables electron emission from NPs which subsequently deposit their energy in the surrounding medium leading to extra H_2O ionization and ROS overproduction. As described before, an increase in ROS can lead to an increase in DNA damage and subsequently to cell death. This suggested cascade of events highlights that high-Z nanoparticle can play the role of radiosensitizer through a physical enhancement mechanism. However, physical enhancement is difficult to verify due to technical issues. Indeed, the most straightforward way to measure this potential physical enhancement should be a measurement of electron emission from NPs in the medium of interest.

Although possible, these experiments involve the use of complex indirect measurement using chemical or biological reactions. Nevertheless, theoretical calculation programs can calculate electron emission and the subsequent physical enhancement. Due to the complexity of the global process, calculation programs divide it into different parts [99]. First, interaction of the beam with water and the NPs occurs. After the photon absorption, electrons are emitted from the NPs and water. The energy deposition events caused by these electrons are tracked and determined. Secondary X-ray fluorescence and scattered Compton photons generated from nanomaterials are generally not included in the calculations due to their negligible contributions. Finally, energy deposition of electrons emitted from NPs is compared to energy of electrons generated in water alone in order to create a dose enhancement value (DE):

$$D_{\text{GNP}} = D_{\text{water}} + D_{\text{water}} * DE$$

$$DE = \frac{D_{\text{GNP}}}{D_{\text{water}}} - 1 \quad (21)$$

This dose enhancement value is expressed in arbitrary units called dose enhancement units (DEU). An enhancement of 1 DEU means that dose delivered double when GNPs are present in the medium. Due to a great dependence of this enhancement ratio with NPs amount in the simulation, theoretical enhancement values are generally reported as DEU per gold weight percent (DEU.WP⁻¹). Cho et al. [100] were the first to report theoretical simulation study of the physical enhancement. Their findings were that enhancement from GNPs was significant around hundred keV X-rays but was minimal under MeV X-rays beam. These results were confirmed by Mesbahi et al. [101] who also observed a strong energy dependency. They showed a decrease in enhancement from 1.4 DEU.WP⁻¹ at 90 keV to 0.03 DEU.WP⁻¹ at 660 keV. The highest enhancement value was observed by Lechtman et al. [102] who found that dose double (1.0 DEU) when 5 mg of gold/g of medium was irradiated with 20 keV X-rays, corresponding to a 2 DEU.WP⁻¹. Results obtained from different groups are summarized in Table 4. In the light of this results, it appears that the addition of 1 % of gold by mass (1 WP) to the tumor would result in approximately a doubling of the amount of energy deposited by a kV X-ray source (= 1 DEU). This ability to increase the energy absorption of an ionizing radiation offers the possibility to use high Z NPs as X-ray radiosensitizers. However, similar studies performed using protons showed a negligible macroscopic physical enhancement around [103-106]. Martinez-Rovira et al. [106] performed simulations to evaluate the dose enhancement when protons pass through a GNP solution. For a realistic configuration of the model, they reported a non-significant energy deposition increase. In another study, Heuskin et al. [104] reported an energy-dependent emission of electron from GNP surface. For a 5 nm GNP, they reported an 8 and 20 % increase in amount of electrons ejected per incident proton after interaction with a 1.3 and 4 MeV protons respectively. However, they highlight their relatively low energy (below 1.5 keV) and the high trapped proportion (around 50 %), meaning that half of these electrons cannot reach the NP surface. Moreover, authors did not report a signature of GNPs in the macroscopic dose delivered. Similar results obtained by Cho et al. [105], showed electron emission from the NP surface. Nevertheless, the average dose enhancement over the entire solution volume was negligible also in this case.

Beam energy [keV]	Theoretical package used in the study	Enhancement values [DEU.WP ⁻¹]	References
20	MCNP5 + PENELOPE	2.0	Lechtman et al. [102]
35	MCNP-4C	1.38	Zabihzadeh et al. [107]
50	MCNPX	1.14	Mesbahi et al. [101]
60	MCNPX	1.00	Mesbahi et al. [101]
73	Geant4	0.9	Byrne et al. [108]
75	MCNP-4C	0.87	Zabihzadeh et al. [107]
95	MCNP-4C	0.96	Zabihzadeh et al. [107]
100	Geant4	1.0	Sharmah et al. [109]
100	EGSnrc	1.06	Kakade et al. [110]
150	EGSnrc	0.89	Kakade et al. [110]
380	Geant4	0.06	Zhang et al. [111]
660	MCNPX	0.03	Mesbahi et al. [101]
6,000	EGS4	0.01	Cho et al. [100]
15,000	EGSnrc	0.005	Kakade et al. [110]

Table 4. Non-exhaustive list of theoretical works predicting physical enhancement of GNPs under photon irradiation.

Finally, Sotiropoulos et al. used a cell model where realistic GNP distribution was implemented to study the DNA damage under proton irradiation. They showed that independently of the proton energy, the GNP size, the GNP concentration and GNP distribution the physical enhancement is negligible. Thereby, the low reported ability of GNPs to increase the macroscopic dose deposition of a charged particle prevents their potential use as radiosensitizer for charged particles.

3.4. High Z nanoparticle as radiosensitizer: state-of-art

In this section, we will focus on *in vitro* studies which have investigated the NP radiosensitization effect (section 3.4.1) prior to discuss *in vivo* and preclinical works (section 3.4.2).

3.4.1. *In vitro* evidences

The high-Z nanoparticle mediated enhanced radiation sensitivity has been achieved by several groups and each of them reported the observed effect with a different indicator. In order to provide a comprehensive understanding of the response to radiation resulting from the presence of radiosensitizing NPs, it is necessary to speak the same language. As recommended by several experts in the field [46], we determined the GNP effect on radiation response in terms of a “sensitization enhancement ratio” (SER) defined as :

$$SER_x = \frac{\text{Radiation dose without GNPs to achieve } x}{\text{Radiation dose with GNPs to achieve } x} \quad (22)$$

The SER is calculated for a given biological effect, usually a 10 % survival fraction and has the advantage to take into account the entire dose-response curve. Values above 1 mean that the drug/NPs of interest enhance the cell death in comparison to the treatment without the drug/NPs.

The ability of high-Z NPs to enhance cell death was mainly studied using gold NPs (GNPs). GNPs have been the most extensively studied NPs as radiosensitizer due to their high absorption coefficient, good biocompatibility and their ability to improve the performance of magnetic resonance imaging diagnosis [112]. We summarized the main *in vitro* works regarding GNP radiosensitization effects in literature into the Table 5. The experimental conditions used in these studies were different in terms of GNP size, GNP surface functionalization, cell model and radiation quality. Chithrani et al. [113] reported a radiosensitization effect of HeLa cells using a combination of GNPs and 220 kVp X-rays. They investigated the impact of GNP size on enhancement effect and demonstrated that a greater SER was obtained using 50 nm than with 14 and 74 nm. The authors explained this observation by a higher cell uptake of 50 nm compared to smaller and bigger GNPs. The same group evidenced that the SER decreases from 1.66 to 1.17 by increasing the energy beam from 105 kVp to 6 MV X-rays respectively [113]. The importance of surface functionalization was shown by Kong et al. [114] which exposed 10 nm GNPs coated with glucose or with cysteamine to 200 kVp X-rays. Although a significant radiosensitization effect was reported for the two NPs, glucose-coated GNPs exhibited the highest SER (1.6 compared to 1.3 for cysteamine one). Further experiments demonstrated that the same 1.9 nm GNP following 225 kVp radiation exposure radiosensitized a large variety of cells from T98G glioblastoma cells (SER = 1.85) to MDA-MB-231 breast cancer cells (SER = 1.22) [115].

Cancer cell type	Cell line	GNP size [nm]	Coating agent	Radiation type	NP uptake [# /cell]	SER 10%	Reference
Bladder	RT 112	50	TAT peptide	250 kVp X-rays	-	1.23*	Jeynes et al. [103]
Brain	T98G	1.9	Thiol	160 kVp X-rays	-	1.04 *	Butterworth et al. [116]
		1.9	Thiol	225 kVp X-rays	-	1.85 *	Taggart et al. [115]
	F98	1.9	Thiol	50 keV X-rays	-	1.92	Bobyk et al. [117]
		15				1.40	
	U87	28	BSA	160 kVp X-rays	-	1.37	Chen et al. [118]
U251	12	PEG	150 kVp X-rays	-	1.30	Joh et al. [119]	
Breast	MCF-7	1.9	thiol	160 kVp X-rays	-	1.04 *	Butterworth et al. [116]
		10.8	Cysteamine Glucose	200 kVp X-rays	- -	1.3 1.6	Kong et al. [114]
	MDA-MB-231	1.9	Thiol	160 kVp X-rays	-	1.12 *	Butterworth et al. [116]
		1.9	Thiol	6 MV photons 15 MV photons	-	1.29 1.16	Jain et al. [120]
		1.9	Thiol	225 kVp X-rays	-	1.22 *	Taggart et al. [115]
		2.7	Tiopronin	225 kVp X-rays	4.0 10 ⁸	1.31	Cui et al. [121]
		16 49	Glucose	6 MV photons	5.3 10 ⁴ 9.4 10 ⁴	1.49 1.86	Wang et al. [122]
Cervix	Hela	50	Citrate	105 kVp X-rays	6.2 10 ³	1.66	Chithrani et al. [113]
				220 kVp X-rays		1.43	
				660 keV γ-rays		1.18	
				6 MV photons		1.17	
		4.8	PEG	662 keV γ-rays	-	1.41	Zhang et al. [123]
12.1	-	1.65					
27.3	-	1.58					
46.6	-	1.42					
7	Glucose	γ-rays 290 keV/μm Carbon	-	1.52 1.39	Kaur et al. [124]		
45	folate	180 kVp X-rays	-	1.25	Khoshgard et al. [125]		

Cancer cell type	Cell line	GNP size [nm]	Coating agent	Radiation type	NP uptake [# /cell]	SER 10%	Reference
Colorectal	HT-29	50	-	9 MV X-rays	$6 \cdot 10^5$	1.37	Saberi et al. [126]
	CT26	4.7	PEG	6 MV photons	$5 \cdot 10^5$	1.33	Liu et al. [127]
Liver	HepG2	16	Tirapazamine	50 kVp X-rays	$6.5 \cdot 10^2$	1.25	Liu et al. [128]
		14	PEG	660 keV X-rays	-	1.20	Guo et al. [129]
		30			-	1.30	
Lung	L132	1.9	Thiol	160 kVp X-rays	-	0.98 *	Butterworth et al. [116]
	A549	13	Glucose	6 MV photons	$1.4 \cdot 10^5$	1.49	Wang et al. [130]
		10	PEG	225 kV photons 25 keV/ μ m protons	$1.9 \cdot 10^5$	1.22 1.14	Penninckx et al. [131]
Ovarian	SK-OV-3	14	Glucose	90 kVp X-rays 6 MV photons	$1.5 \cdot 10^5$	1.44 1.30	Geng et al. [132]
Prostate	PC-3	1.9	Thiol	160 kVp X-rays	-	1.02 *	Butterworth et al. [116]
		-	PEG	6 MV X-rays	-	1.09	Wolfe et al. [133]
	DU-145	1.9	Thiol	160 kVp X-rays	-	1.03 *	Butterworth et al. [116]
		1.9	Thiol	225 kVp X-rays	-	1.08 *	Taggart et al. [115]
		10.8	Glucose	662 keV γ -rays	$6.3 \cdot 10^4$	1.30 *	Roa et al. [134]
		44	-	160 MeV proton	-	1.15	Polf et al. [135]
Vulvar	A431	5	PEG	25 keV/ μ m protons	$2.4 \cdot 10^5$	1.08	Li et al. [136]
		10			$7.7 \cdot 10^4$	1.14	

Table 5. Non-exhaustive list of *in vitro* studies of cell death enhancement by GNPs. The results are alphabetically listed for the cancer type. * = SER calculated enhancement from reported experimental data available in the corresponding publication.

However, it was reported that some cell lines, such as human prostate DU145, are not sensitized by this 1.9 nm GNPs even if significant gold uptake was observed (SER = 1.03 [116] or 1.08 [115]). Comparison of *in vitro* data from Table 5 enables to find some inconsistencies. For example, Chithrani et al. [113] reported a 1.18 SER when HeLa cells pre-incubated with 50 nm GNPs are exposed to 660 keV γ -rays, Zhang et al. [123] observed a huge 1.42 SER when the same cells pre-incubated with 47 nm GNPs are exposed to the same radiation. While some groups evidenced an increase in SER when cells are exposed to increasing energetic beam [115, 116], others reported the inverse behavior [113, 120, 124] without hypothesizing the origin of this inconsistency. Unfortunately, the differences in SER reported in Table 5 cannot be rationalized due to the diversity of parameters and conditions tested in literature as well as to a lack of data regarding key parameters. Indeed, the cellular gold content upon irradiation was pointed as a key parameter of GNP radiosensitization effect but this information is missing in the majority of studies (Table 5).

Although gold was the most studied material as metallic radiosensitizer, other metals were also investigated:

- **Platinum NPs:** A limited number of studies have investigated the radiosensitization effect of platinum NPs for ionizing radiations. Le Sech et al. [137] found that platinum NPs bound to DNA could increase the DSB amount in DNA under dry conditions exposed to X-rays with energies near the L edge of platinum. Moreover, Kobayashi et al. [138] demonstrated that X-ray irradiation of chloroterpyridine platinum NPs bound to plasmid DNA enhance the number of DNA damages in aqueous solutions. In another study, Porcel et al. evidenced an increase in DSB number within cells pre-incubated with platinum NPs and exposed to helium [139] and carbon ions [140].
- **Silver NPs:** Although AgNPs were extensively studied for their antimicrobial activity, some works investigated their potential anticancer therapeutic activity. Xu et al. [141] showed that 20 nm and 50 nm AgNPs can sensitize gliomas cells to X-ray irradiation. This observation was also reported by Lu et al. [142] in human breast adenocarcinoma MDA-MB-231 cells and by Huang et al. [143] in gastric MGC803 cells.
- **Gadolinium NPs:** Gadolinium is commonly used as a magnetic resonance imaging contrast agent but was also identified as a potential sensitizer. Mowat et al. [144] demonstrated the ability of Gd_2O_3 NPs to enhance U87 and SQ20B cell death after γ -ray exposition. Furthermore, Detappe et al. [145] showed that sub-5 nm polysiloxane shell coupled to gadolinium (called AGuIX) sensitized pancreatic cancer cell lines to X-ray clinical beam.
- **Iron NPs:** Despite its relatively low atomic number ($Z = 26$), FeNPs have shown the ability to sensitize cells to X-rays [146, 147]. Moreover, Kim et al. [148] demonstrated the added value of FeNPs as radiosensitizers for protontherapy treatment.

It must be noted that a huge number of other nano-objects were demonstrated as potential radiosensitizers including bismuth, titanium, cerium, germanium, hafnium and tantalum based NPs.

3.4.2. *In vivo* evidences, preclinical studies and clinical trials

In addition to *in vitro* studies, a limited number of *in vivo* works have demonstrated the potential use of GNPs as radiosensitizer to treat animals. These works are listed in Table 6. The first proof-of-concept was provided by Hainfeld et al. [149] in 2004. In this study, Balb/C mice bearing EMT-6 murine breast cancer tumors were exposed to a single dose of 30 Gy 250 kVp radiation alone or in combination with GNPs (1.35 g of Au/kg) injected intravenously 5 min prior to irradiation. The authors reported that the irradiation alone induced tumor growth delay while irradiation + GNPs led to a significant decrease in tumor growth when assessed 1 month after treatment [149]. Further experiments using the same experimental setup but with a higher gold concentration at injection site (1.3 g/kg to 2 g/kg) enabled to observe an increase in median survival time of mice bearing SCCVII cells, a highly radioresistant murine squamous cell carcinoma [150]. Using 68 keV photons, significant tumor growth delay and long-term tumor control were observed when GNPs were combined with 42 Gy radiation compared with radiation alone. Interestingly, this effect was not observed when 30 Gy of radiation was used. Similarly, using 157 keV photons, a higher effect was observed when a combination of GNPs and 50.6 Gy was used instead of 44 Gy. Unfortunately, no analysis of GNP tumor uptake or distribution was reported in this study. In another study, Zhang et al. [151] investigated the potential benefit of ultrasmall GNPs on radiotherapeutic treatment. After injection of 10 mg GNPs/kg in BALB/C mice, 10 μ g GNPs/g of tumor was measured and a clear decrease in tumor volume 28 days was observed after X-ray irradiation. This *in vivo* evidence was confirmed by Kim et al. for protontherapy treatment by showing tumor regression and an increase in long-term survival in mice bearing CT26 cancer cells. To achieve this effect, 1.9 nm and 14 nm GNPs were used in combination with huge doses of a 40 MeV proton beam (100 Gy and 41 Gy respectively) [148, 152].

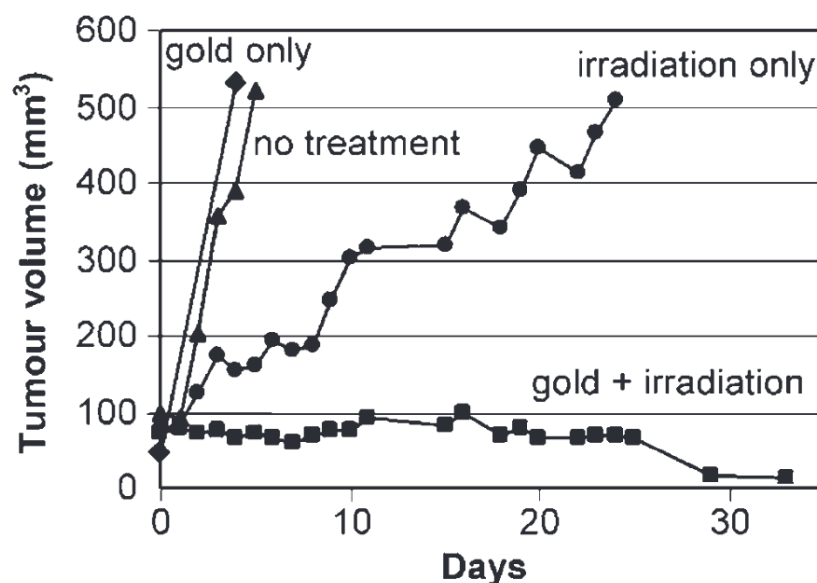


Figure 18. Average tumor volume assessed during 1 month after treatment: no treatment (▲, n = 12); gold only (◆, n = 4); irradiation only with 30 Gy of 250 kVp X-rays (●, n = 11); intravenous GNP injection followed by irradiation (■, n = 10). Balb/C mice bearing subcutaneous EMT-6 mammary carcinomas was used in this study. Adapted from [149].

Cell line	GNP size [nm]	Coating agent	Radiation type / total dose delivered	NP concentration and injection route	Observed effect	Reference
Tu-2449	1.9	Thiol	100 kVp 30 Gy	4 g Au/kg intravenous	Increase in long-term tumor free survival	Hainfeld et al. [153]
U251	12	PEG	175 kVp 20 Gy	1.25 g Au/kg intravenous	Increase in median survival (14 vs 28 days)	Joh et al. [119]
U87	18	BSA	160 kVp 5 Gy	325 µg intravenous	Tumor regression	Chen et al. [118]
EMT-6	1.9	Thiol	250 kVp 30 Gy	1.35 g Au/kg intravenous	Increase in long-term survival	Hainfeld et al. [149]
HeLa	4.8 12.1 27.3 46.6	PEG	662 keV 5 Gy	4 mg Au/kg intravenous	Tumor growth inhibition Most effect = 12.1 nm Lowest effect = 46.6 nm	Zhang et al. [123]
U14	< 2	BSA GSH	662 keV 5 Gy	10 mg Au / kg Intraperitoneal	Decrease in tumor volume (38 % for BSA and 55 % for GSH)	Zhang et al. [151, 154]
CT26	1.9	Thiol	40 MeV proton 100 Gy	300 mg Au/kg intravenous	Tumor regression	Kim et al. [148]
	14	citrate	40 MeV proton 41 Gy	300 mg Au/kg intravenous	Increase in long-term survival	Kim et al. [152]
SCCVII	1.9	Thiol	68 keV 42 Gy	1.9 g Au/kg intravenous	Increase in median survival (53 vs 76 days)	Hainfeld et al. [150]
	1.9	Thiol	157 keV 50.6 Gy	1.9 g Au/kg intravenous	Increase in median survival (31 vs 49 days)	Hainfeld et al. [150]

Table 6. *In vivo* studies of radiosensitization effect of GNPs.

Although research on high-Z NP application as radiosensitizer is a relatively immature scientific field, some products are subjected to preclinical studies and clinical trials:

- Nanobiotix Inc. is a French company that has been developing NBTXR3, a 50 nm HfO₂ NPs designed for direct intratumoral injection and subsequent radiosensitization. *In vivo* proof-of-efficiency was performed on A673 Ewing cells engrafted in nude mice as a sarcoma model. One intratumoral NBTXR3 injection performed 24 hours prior to irradiation increased the treatment efficiency when compared with radiotherapy alone. An approximately two-fold increase in tumor doubling time was demonstrated and a significant 82 % tumor growth inhibition was reported for NBTXR3 activated by 15 Gy X-rays compared to 72 % for 15 Gy X-rays alone [155]. The phase I trial of this nano-object started in 2011 and was completed in 2015. The report concluded that “human injection (22 sarcoma patients in France) was well tolerated until 10 % of tumor volume with preoperative external beam radiotherapy and did not result in leakage of these nanoparticles into the adjoining healthy tissues” [156]. Since this positive first phase, several phase 2 clinical trials are ongoing, recruiting participants for the treatment of head and neck, rectal, liver and prostate cancers. Moreover, the company has been conducting a prospective randomized phase III clinical trial (NCT02379845) for adult soft tissue sarcoma since March 2015. The latest news available on the company’s website (June 21st 2018) indicate that twice as many patients (16.1 % for NBTXR3 vs 7.9 % for radiation alone) achieved less than 5 % of residual viable cancer cells in the tumor post-treatment. (p=0.045).
- NH TherAGuIX is a French company that has been developing AGuIX, a 5 nm polysiloxane matrix with gadolinium cyclic chelates covalently grafted on the inorganic matrix for the treatment of brain metastases. *In vivo* proof-of-concept was performed using orthotopic 9L gliosarcoma cancer cells into rat. One intravenous injection of 40 mg AGuIX/g of rat performed 20 min before irradiation increased the median survival time by a factor of 4.5 and 2 compared with untreated animals and irradiated animals respectively. Since then, AGuIX is associated to two phase I clinical trials: NanoRAD (NCT02820454, started in June 2016) for the treatment of brain metastases by whole brain radiation therapy and NanoCOL (NCT03308604, started in May 2018) for the treatment of locally advanced cervical cancer [157]. First results of NanoRAD clinical trial showed a good tolerance of AGuIX and its ability to pass through the blood brain barrier selectively in brain metastases, paving the way to NanoRAD phase II trial which will start end of 2018 [157].

3.5. Confrontation between theoretical physical predictions and experimental evidences

In this last section, we will confront theory (theoretical physical predictions) with experimental observations (*dose enhancement reported in vitro*). To do that, we focus only on studies for which data about gold content at irradiation time is available. Observed *in vitro* radiosensitization effect was plotted according to the predicted physical dose enhancement on Figure 19. This figure highlights three main deviations from the dose enhancement physical predictions:

- First, several studies reported significant radiosensitization effects when GNPs were used at concentrations lower than the 0.1 to 1 WP that is typically associated with theoretical predictions of significant dose increases. For example, Liu et al. [128] investigated the effect of 16 nm tirapazamine conjugated GNPs on HepG2 liver cancer cell under X-ray irradiation. Authors reported a gold content of $6.5 \cdot 10^2$ GNPs/cell corresponding to 0.003 WP and a significant surviving fraction reduction (0.25 DEU) in these conditions. This observed radiosensitization effect is 83-fold higher than the predicted one ($= 0.003$ DEU).
- Second, although enhancements have widely been observed with kilovoltage X-rays, as predicted, various studies have reported significant radiosensitization effect with megavoltage X-rays [120, 122, 126, 127, 130] where little or no increase in overall dose deposition would be expected according to the theory.
- Finally, the observed enhancement values are generally higher than the predicted ones. Butterworth et al. [116] evidenced this inconsistency by comparing the responses of 9 different cell lines. Assuming that irradiation using 160 kVp X-rays leads to a $1 \text{ DEU} \cdot \text{WP}^{-1}$ and that all GNPs added to the medium are internalized by the cell, a maximal 0.01 DEU should be observed. However, they observed a cell-dependent radiosensitization effect ranging from 0.4 to 0.97 DEU. This inconsistency is also illustrated in Figure 19. For almost all experimental results, the observed enhancement is higher than the physical predicted dose increase (plotted as a dashed line). Moreover, the correlation between the predicted dose enhancement and observed radiosensitization is very weak (Pearson's $r = 0.08$). It is interesting to note that radiosensitization effects were reported using proton beam while physical enhancement calculation predicted only negligible dose enhancement [136].

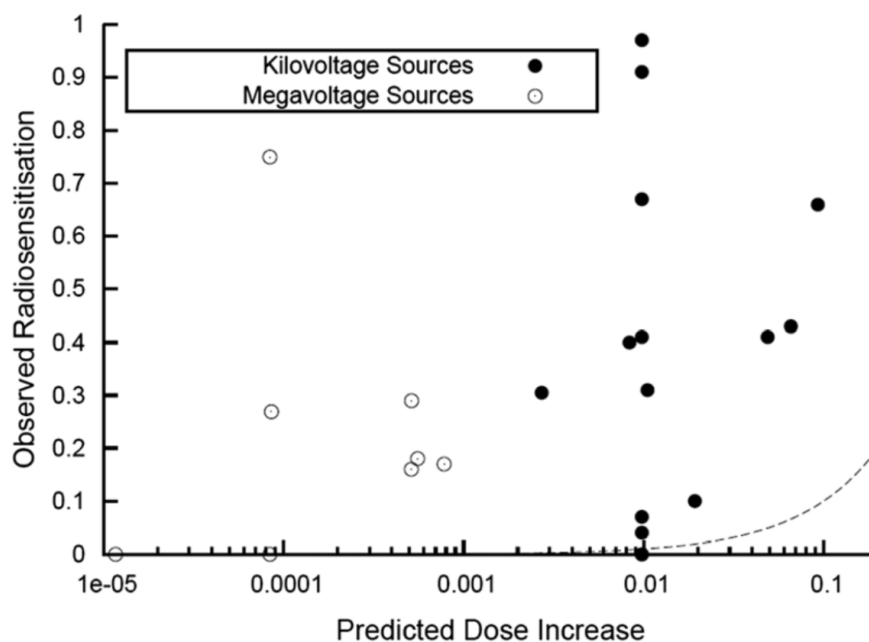


Figure 19. Comparison of observed *in vitro* experimental dose enhancement with predicted dose enhancement values for GNPs studies (kilovoltage and megavoltage radiation sources). Dashed line shows the trend which would be followed if the observed enhancement tracked with predicted increases in physical dose. This trend was calculated on a $1 \text{ DEU} \cdot \text{WP}^{-1}$ basis. Adapted from [158].

Furthermore, comparison between predicted physical enhancement and *in vivo* studies leads to the same conclusions. Indeed, Zhang et al. [154] demonstrated using gold clusters containing only 29–43 gold atoms covered with reduced glutathione ligands that a significant enhancement effect can be obtained even though the gold content was extremely low. In fact, the gold content in the tumor was a few micrograms per gram of tissue ($\approx 10^{-3}$ WP). Physical enhancement for such a small loading of gold would only be negligible. However, the authors observed almost no increase in tumor volume after 28 days with GNPs, whereas tumors in mice without GNPs and radiation grew five-fold over 28 days. Another example is the study of Hainfeld et al. [149], where a tumor gold content of 0.23 WP was reported. For the 250 kVp X-rays used in this study, the predicted physical enhancement using this tumor gold content was approximatively 0.2 DEU. Moreover, we can calculate the observed dose enhancement effect based on data presented in Figure 18. According to Guo et al. [99], if there is no toxicity from the nanomaterials and if the tumor growth follows an exponential function, the magnitude of the dose enhancement (DE) can be calculated using the following equation:

$$DE = \frac{\ln(\text{tumor size with no treatment}) - \ln(\text{tumor size with IR + GNPs})}{\ln(\text{tumor size for no treatment}) - \ln(\text{tumor size with IR alone})} - 1 \quad (23)$$

In the study of Hainfeld et al. [149], the calculated dose enhancement is 0.58 DEU which is higher than the predicted one.

All these findings raised questions concerning the mechanism(s) responsible for the radiosensitization effect of GNPs. Indeed, although many works reported the GNPs ability to enhance cell death upon irradiation, their sensitizing properties cannot be solely due to dose enhancement. Thereby, other mechanisms playing significant role in the observed radiosensitization need to be elucidated to fully understand the process.

PART II: Objectives

4. Objectives

Radiotherapy remains the main treatment modality to fight cancer, as half of all patients receive ionizing radiation during their treatment. Although the overall cancer death rate decreased year after year by an average of 1.5 %, it is not the case for all cancer types. Indeed, death rate for several cancers including nervous system and pancreas ones still increases due to inefficient treatment modalities for these ones up to now. Therefore, there is a real need of new treatment modalities discovery and/or current treatment improvement. The “Holy Grail” in radiotherapy is to find a technique, which enables to maximize the differential between the dose delivered to the tumor and to the healthy tissues surrounding it while enabling a reduction of the total dose delivered to the patient.

Since decades, tumor targeting in radiotherapy is constantly improving thanks to new modalities, including new imagery technologies or the use of charged particle therapy. Particle therapy offers the possibility to target tumors more precisely due to a spatial dose distribution that spare normal tissues as well as to increase treatment efficiency via its higher relative biological effectiveness. Although an increasing number of studies evidenced its efficiency *in vitro* and *in vivo*, additional works are still required to understand the fundamental effects caused by these radiations in cell.

In the meantime, development of nanomedicine offers the possibility to take advantage of nanoscale materials for therapeutic applications as radiosensitizer in oncology. Indeed, these materials have the ability to reach a given cancer cell killing using a reduced total dose delivered to the patient. Despite an increasing amount of data regarding high-Z NP – induced radiosensitization, it is still difficult to draw conclusions regarding this effect due to the diversity of parameters and conditions used in literature. This leads to important open questions such as the mechanism(s) responsible for the cell death enhancement, which remains a mandatory step towards the clinical use of metallic radiosensitizers.

Therefore, this thesis aims at improving radiotherapy treatment as the ultimate goal. The first part of this work consisted in the evaluation of a combination of charged particle therapy and GNPs in different cancer cell types. The aim was double: firstly, we characterized the response of this system by varying different parameters (physics ones such as LET, chemical ones such as GNP size and biological ones such as cell types) in order to better understand the impact of these parameters on the cell death enhancement effect. Secondly, we investigated the mechanism(s) responsible for the GNPs-induced radiosensitization effect. In the second part, we studied the DNA damage formation and repair responses after low and high-LET radiation exposition in a large *ex vivo* cohort of primary mouse fibroblasts. The goal was to progress in the fundamental understanding of biological consequences of charged particle irradiation as well as to probe if individual radiosensitivity is mediated by genetics.

Altogether, the results obtained during this thesis enabled to highlight the importance of personalized medicine approach for further cancer patient treatment taking into account the genetic background of the tumor for treatment using GNPs as well as the individual radiosensitivity of an organism to radiation.

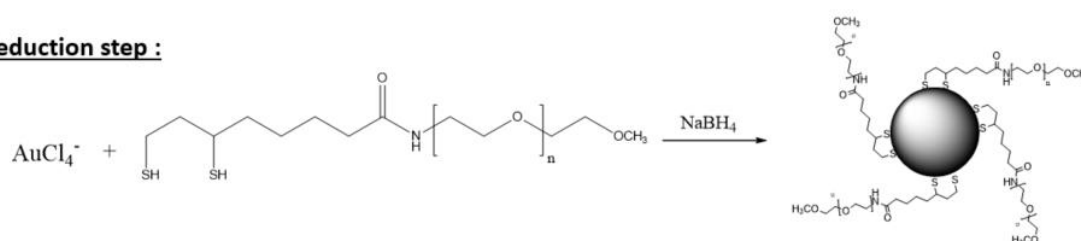
PART III: Results

5. Gold nanoparticle synthesis and characterization

5.1. Synthesis

Since the classic citrate reduction of aurate salt to prepare citrate-stabilized GNPs reported by Turkevich and Frens [159, 160], there has been a sustained effort aimed at developing new chemical routes to prepare stable GNPs that are easily dispersible in water. Based on [161], we developed a simple one-phase (aqueous) growth and passivation method to prepare a series of hydrophilic GNPs. The synthesis procedure is a three-step reaction consisting of (1) precursor formation by reacting an organic ligand with tetrachloroauric(III) acid (HAuCl_4), (2) growth of the GNP cores triggered by addition of a powerful reducing agent (NaBH_4) and (3) further passivation and functionalization of the cores by adding extra functional ligands.

Reduction step :



Passivation step :

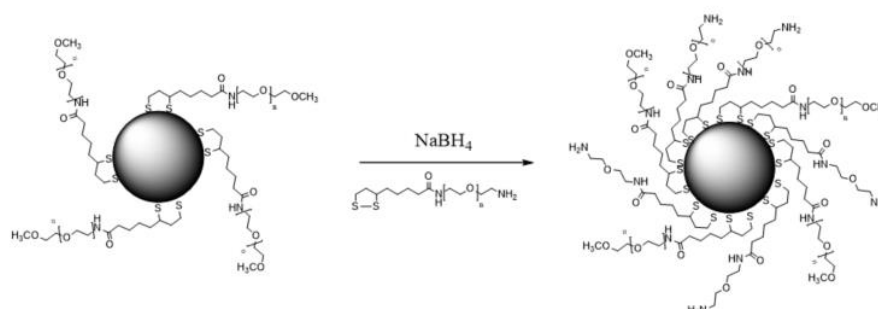


Figure 20. Schematic representation of the GNP synthesis method.

The ligands chosen for this synthesis are bifunctional polyethylene glycol (PEG) polymers with a thioctic acid (TA, which has a terminal disulphide) at one end and a given reactive group at another end. Since these NPs are stabilized with disulfide anchoring groups, they exhibit remarkable stability in the presence of excess counterions as evidenced by different groups [162, 163]. During the synthesis, HAuCl_4 and the ligands TA-PEG₅₅₀-OCH₃ were first mixed in water to promote the formation of a precursor underlined by a color change of the original yellow solution to colorless. Secondly, the addition of NaBH_4 initiated the gold ion reduction and the growth of the gold nanocrystals. Once the growth step was complete, TA-PEG₄₀₀-NH₂ ligands were further added to the solution (to a final Au/ligand molar ratio of 1:1). This last step provided an additional passivation (covering unoccupied site at the NP surface) and functionalization of GNPs with a positively charged reactive group. After 3 hours of stirring, the colloidal suspension was purified with a membrane filtration device. It must be noted that the two PEG ligands used in this study do not have the same role. While the second one

enables the functionalization of the coating, the first one enables to obtain a given GNP size. In fact, we are able to tune the GNP size by changing the molar ratio between gold and TA-PEG₅₅₀-OCH₃ ligand.

5.2. Characterization

5.2.1. Optical properties

UV-visible absorption spectra obtained from a set of GNP solutions prepared using increasing Au/PEG molar ratio are presented in Figure 21A. As shown, low Au-to-ligand molar ratios are associated to a weak surface plasmon band around 520 nm (not discernable for 1/1 Au/PEG ratio). For higher ratios, a well-defined plasmon band appears 525 nm indicating the presence of a narrow size distribution of GNPs. Moreover, this increase in Au/PEG ratio was associated to a color change from yellow to red, evidencing different GNP size (Figure 21B).

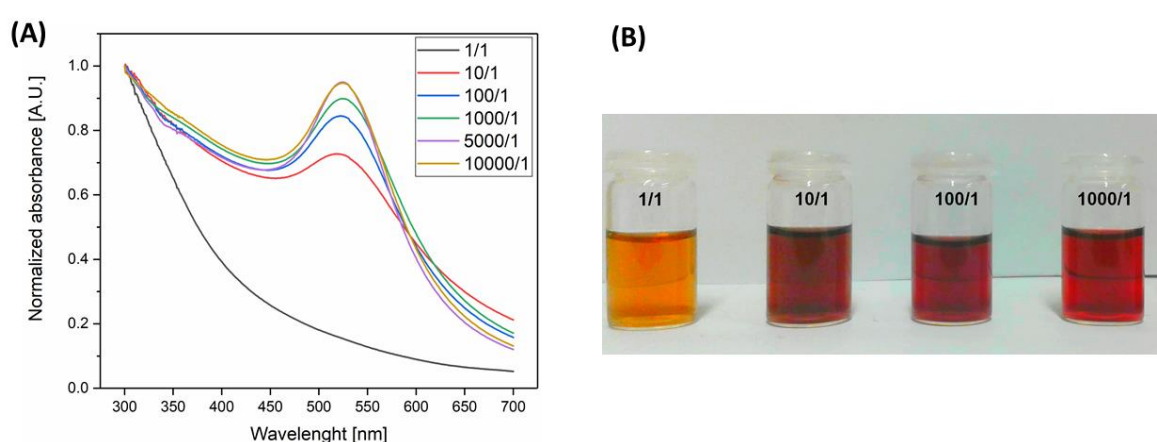


Figure 21. (A) Normalized UV-vis absorption spectra for several Au/PEG molar ratios. (B) Image collected from a series of GNP dispersions in deionized water. Changes in solution color from yellow (Au/PEG: 1/1) to red (Au/PEG: 1,000/1) reflect an increase in the nano-object size.

5.2.2. Size distribution and morphology

In order to investigate the size and the morphology of GNPs, transmission electron microscopy (TEM) images were taken. As shown in Figure 22, images evidenced that GNP size increased with Au/PEG ratio, as anticipated from the absorption spectra (Figure 21A). An average diameter was extracted from these images using Image J software. Results are listed in Figure 22. It is interesting to note that spherical shapes dominate the NP dispersion, even if slight inhomogeneities in shape were observed for the larger sizes (Au/PEG : 2,000/1 and 10,000/1).

A plot summarizing the progression of particle size (extracted from TEM) as a function of the Au/PEG ratio for the full set of solutions prepared is shown in Figure 23. This highlights a rapid increase in size at low ratios while this dependence becomes weak for large size (little changes in diameter from 2,000/1 to 10,000/1 ratios). This relation between size and Au-to-ligand ratio reflects the change in NP surface/volume ratios: After the nucleation step, two events occur simultaneously in the batch. On one hand, accumulation of gold atoms on the surface enables the growth of the NPs.

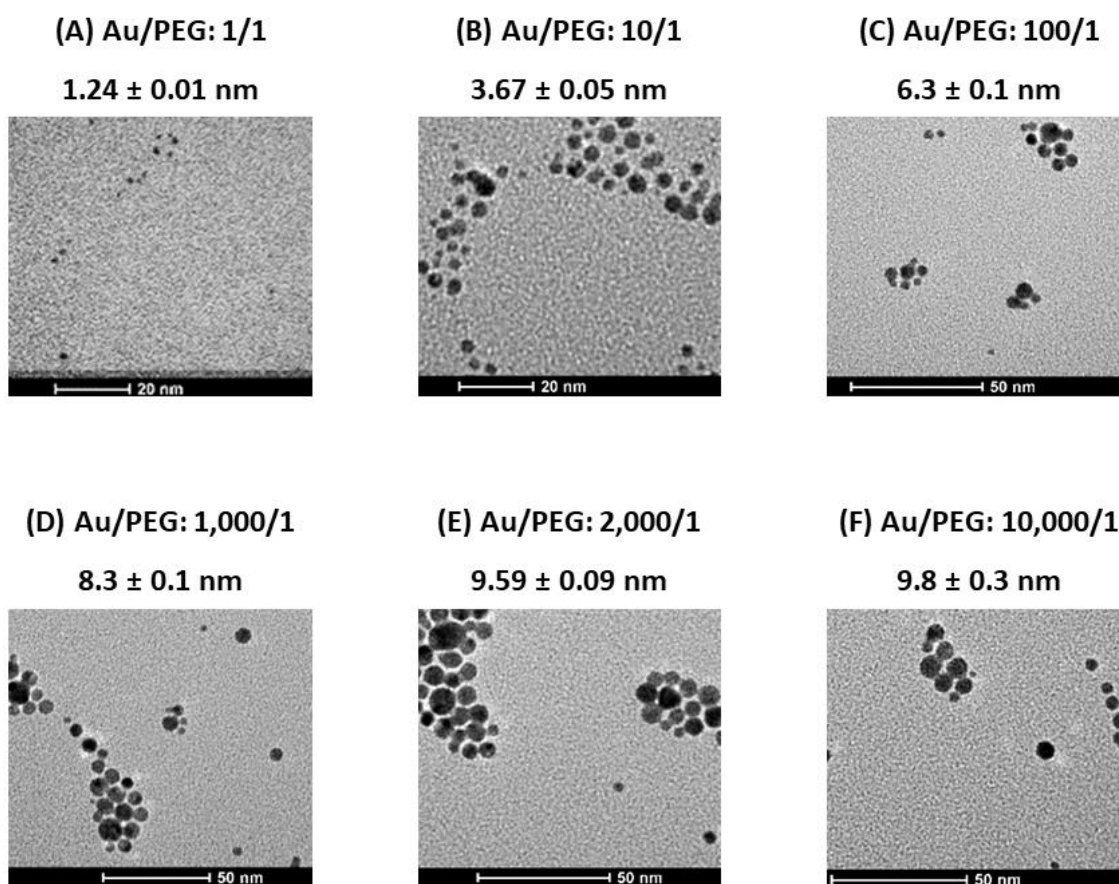


Figure 22. TEM images for several Au/PEG molar ratios ranging from 1/1 (A) to 10,000/1 (F). Average diameter and associated fit error are reported in each condition after analyzing at least 500 particles per condition using the ImageJ software.

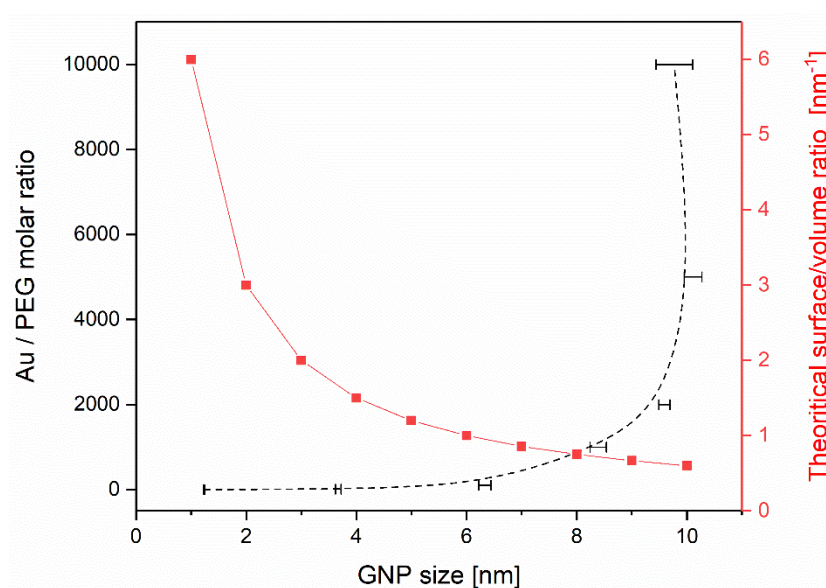


Figure 23. Relationship between Au/ TA-PEG₅₅₀-OCH₃ ratio and GNP size measured by TEM. The surface to volume ratio for each NP size (■) was plotted based on theoretical calculations.

On the other hand, disulphide terminal group of TA-PEG₅₅₀-OCH₃ links to GNP in formation. When the amount of ligand in solution is sufficient for covering the main part of the NP surface, the growth process is slowed down, stabilizing a given GNP size. The rapid size change measured at low Au/PEG ratios reflects the large decrease in surface-to-volume ratio when small size NPs grow (1 to 6 nm). As the surface-to-volume ratio decreases slower for larger particle (8 to 10 nm), the effect of ligand concentration becomes less dominant, which is translated into a weaker change in GNP size at higher Au-to-ligand ratios.

5.2.3. Colloidal stability

In order to assess the stability of the 10 nm GNPs produced by this synthesis, we performed zeta potential analyses. GNPs exhibited a zeta potential value of -19.3 ± 2.6 mV and -0.8 ± 2.5 mV when they are suspended in deionized water and culture medium respectively. This decrease in potential when GNPs were placed in culture medium is not surprising. In fact, proteins from the cell culture medium tend to adsorb at the NP surface through electrostatic interactions with positively charged amino groups from the coating. Usually, we consider that absolute zeta potential values above 30 mV provide a good colloidal stability, while values between + 5 mV and -5 mV indicate fast aggregation. However, these rules consider only a pure electric stabilization of colloids, which is not the case here due to the presence of a PEG coating which adds a steric stabilization. In the light of this, zeta potential values highlighted a relatively short-term stability in culture medium. To assess the kinetics of a potential aggregation process in solution, we performed UV-visible absorption measurements through time. GNPs were placed in Hank's Balanced Salt Solution (HBSS) medium supplemented with 10 % fetal bovine serum (FBS) and incubated at 37°C in order to mimic the usual incubation conditions of GNPs for cell experiments. By following the gold plasmon band across the time, we did not evidence any change in spectra until 7h of incubation (Figure 24A). From the 24h time point, a significant reduction in the absorption at 525 nm was observed as shown by the dashed line on Figure 24A. After a 48h and 72h incubation, an increase in the absorption at higher wavelength was observed, indicating an increase in particle size.

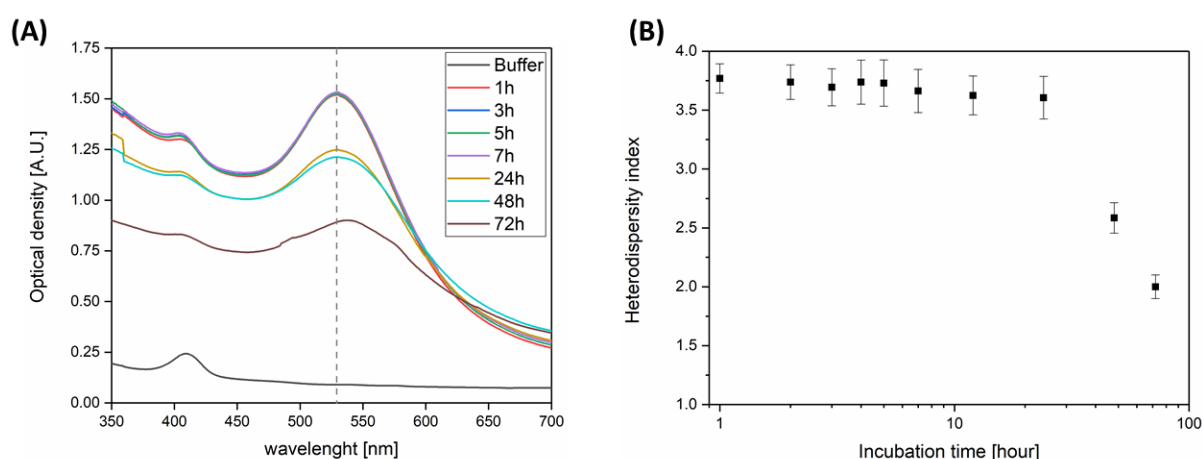


Figure 24. GNP stability in HBSS medium supplemented with 10 % FBS and incubated during 72h at 37°C. (A) UV-visible spectra at 1h (red curve), 3h (blue curve), 5 h (green curve), 7h (purple curve), 24h (yellow curve), 48h (cyan curve) and 72h (brown curve). Dashed line indicated the position of the maximal absorption wavelength ($\lambda_{max} = 525$ nm). (B) Heterodispersity index calculated from the spectrum for each time point ± 1 SD of three independent experiments.

This growth process is evidenced by a decrease in the heterodispersity index in Figure 24B. All together, these results suggest that GNPs are stable in culture medium during several hours prior to sediment (24h) and start an aggregation process (48h).

5.3. Scale-up

In order to probe the potential industrialization of the synthesis process, we performed two scale – up experiments, e.g. an extrapolation of the synthesis by multiplying all the reagent quantities by a same factor (2 and 5 in our case). As shown in Figure 25, scale-up did not alter the spherical morphology of GNPs. However, size distribution revealed a slight decrease in the average diameter with the scaling up, while full width at half-maximum remained unchanged. Lastly, a significant increase in the reaction yield was observed with scaling up due mainly to the decrease in GNP proportion lost on the membrane during the purification process.

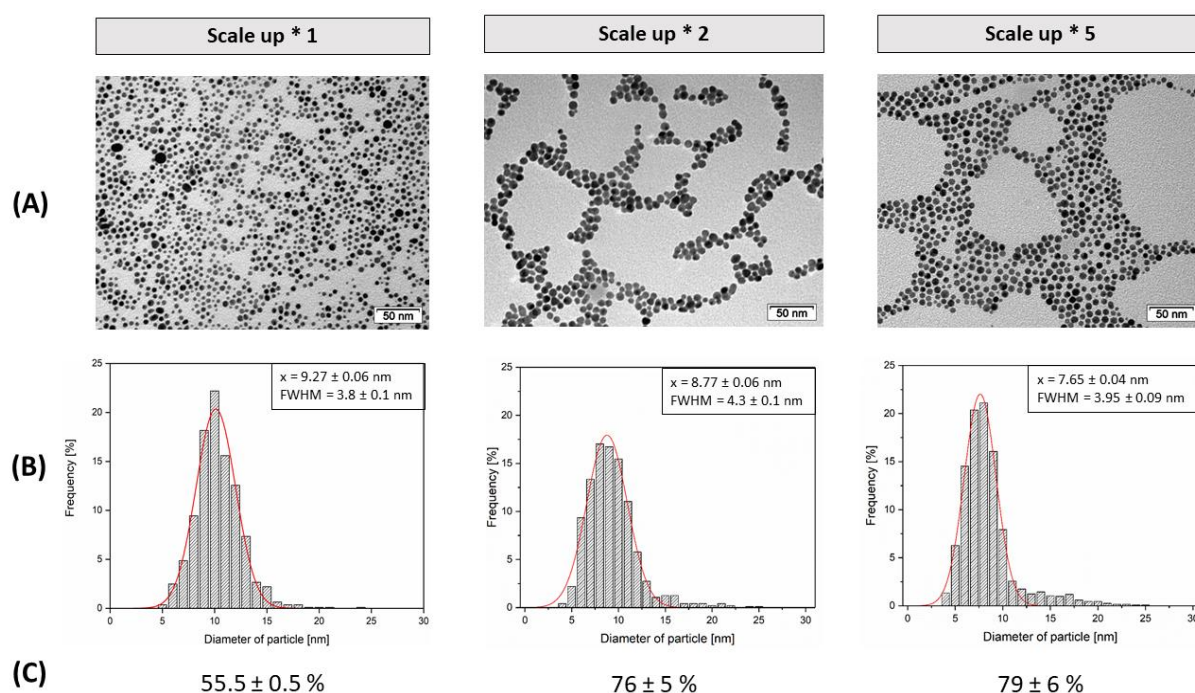


Figure 25. Scale-up of 10 nm GNPs synthesis (Au/PEG: 2000/1). (A) TEM images for each batch. (B) Size distribution analyzed using Image J software. Average diameter (x), full width at half-maximum (FWHM) and associated fit error are reported in each condition. (C) Average reaction yield obtained from at least 3 independent syntheses.

6. Gold nanoparticles as radiosensitizer for protontherapy: *in vitro* proof-of concept and key parameters

6.1. Context and goal of this study

When we started this study in 2015, the development of high-Z radiosensitizers was a hot topic leading to a plethora of new metallic nano-objects. Although many studies have shown their ability, when injected into the tumor, to amplify the X-ray radiation treatment efficiency, a very limited number of works have investigated this radiosensitization effect with charged particles. However, these studies led to contradictory results (cf. introduction). Jeynes et al. showed no significant enhancement effect when RT112 cells containing 50 nm GNPs were irradiated using a 3 MeV proton beam [103]. On the other hand, by exposing DU145 cells pre-incubated with 40 nm GNPs to a clinical 160 MeV proton beam, Polf et al. observed a 15 % enhancement in the relative biological effectiveness [135]. Unfortunately, comparison between studies did not improve the understanding of this GNP-induced radiosensitization due to the huge number of different experimental conditions used within studies that prevents to draw general conclusions.

To cope with these issues, we wanted to investigate the influence of physico-chemical parameters on this radiosensitization effect. Furthermore, we focused on proton irradiation due to the lack of data regarding GNP enhancing charged particle efficiency. In the meantime, the impact of the nano-object size was assessed using 5 and 10 nm GNPs. These nano-objects had the same spherical shape and PEG coating agent, two parameters reported in literature to influence the radiosensitization effect. Finally, the influence of these physico-chemical parameters was investigated using the same biological model, the epidermoid carcinoma A431 cell line.

In the first part of the article, we studied the interaction between cells and the GNPs. We determined a non-cytotoxic concentration of GNPs that enables an efficient cell internalization. Sub-cellular localization and cellular gold content were assessed in order to determine whether the GNP size influences the cell uptake process. In a second part, we irradiated cells pre-incubated or not with GNPs to study their ability to enhance the cell death after proton irradiation. The LET impact on the radiosensitization effect was highlighted and possible hypotheses were proposed to explain the observations.

6.2. First manuscript: “LET-dependent radiosensitization effects of gold nanoparticles for proton irradiation” – Nanotechnology (2016).

LET-dependent radiosensitization effects of gold nanoparticles for proton irradiation

Sha Li¹, Sébastien Penninckx¹, Linda Karmani², Anne-Catherine Heuskin¹,
Kassandra Watillon³, Riccardo Marega⁴, Jerome Zola³,
Valentina Corvaglia⁴, Geraldine Genard³, Bernard Gallez², Olivier Feron⁶,
Philippe Martinive⁵, Davide Bonifazi⁴, Carine Michiels³ and
Stéphane Lucas¹

¹ Research center for the Physics of Matter and Radiation (PMR-LARN), Namur Research Institute For Life Science (NARILIS), University of Namur, B-5000 Namur, Belgium

² Biomedical Magnetic Resonance Group (REMA), Louvain Drug Research Institute, Université Catholique de Louvain, B-1200 Woluwé Saint Lambert, Belgium

³ Unité de Recherche en Biologie Cellulaire (URBC), Namur Research Institute For Life Science (NARILIS), University of Namur, B-5000 Namur, Belgium

⁴ Namur Research College (NARC) and Department of Chemistry, University of Namur, B-5000 Namur, Belgium

⁵ Radiotherapy and Oncology Department, CHU and University of Liège, B-4000 Liège, Belgium

⁶ Pole of Pharmacology and Therapeutics (FATH), Institut de Recherche Expérimentale et Clinique (IREC), Université catholique de Louvain, B-1200 Brussels, Belgium

E-mail: carine.michiels@unamur.be

Received 2 May 2016, revised 19 June 2016

Accepted for publication 28 June 2016

Published 3 October 2016



CrossMark

Abstract

The development of new modalities and protocols is of major interest to improve the outcome of cancer treatment. Given the appealing physical properties of protons and the emerging evidence of biological relevance of the use of gold nanoparticles (GNPs), the radiosensitization effects of GNPs (5 or 10 nm) have been investigated *in vitro* in combination with a proton beam of different linear energy transfer (LET). After the incubation with GNPs for 24 h, nanoparticles were observed in the cytoplasm of A431 cells exposed to 10 nm GNPs, and in the cytoplasm as well as the nucleus of cells exposed to 5 nm GNPs. Cell uptake of 0.05 mg ml⁻¹ of GNPs led to 0.78 pg Au/cell and 0.30 pg Au/cell after 24 h incubation for 10 and 5 nm GNPs respectively. A marked radiosensitization effect of GNPs was observed with 25 keV μm^{-1} protons, but not with 10 keV μm^{-1} protons. This effect was more pronounced for 10 nm GNPs than for 5 nm GNPs. By using a radical scavenger, a major role of reactive oxygen species in the amplification of the death of irradiated cell was identified. All together, these results open up novel perspectives for using high-Z metallic NPs in protontherapy.

Online supplementary data available from stacks.iop.org/NANO/27/455101/mmedia

Keywords: gold nanoparticles, proton irradiation, A431 cells, radiosensitization, cell uptake

(Some figures may appear in colour only in the online journal)

1. Introduction

The development of nanomedicine offers the possibilities to take advantage of novel nanoscale materials to enhance the performance of current radiation-based therapeutic techniques. Numerous experimental and simulation studies have

evidenced the potential of high-Z nanoparticles (NPs) as radiosensitizing agents in combination with ionizing radiation [1–3]. The efficacy of NPs used as radiosensitizers was demonstrated by several groups *in vivo* and *in vitro* [4–6], and most of them have focused on conventional radiotherapy with photons. In the pioneering study of Hainfeld *et al* gold

nanoparticles (GNPs) with a diameter of 1.9 nm showed an efficiently increase in the survival of tumor-bearing mice in combination with 250 kVp x-rays compared to x-rays alone [7]. Another study showed that GNPs functionalized with cysteamine or thioglucose significantly enhanced breast cancer cell killing in conjunction with 200 kVp x-rays or gamma rays [8]. Jain *et al* showed that the enhancement effect of GNPs can also be observed with MeV photons [9].

At higher energies, the photon interaction with matter produces Compton electrons with a spectrum of energy which has higher probability of radiation interactions inside the cells [10]. GNPs are expected to improve the effects of the radiotherapy by their ability to increase dose deposition in the target volume. However, the major constrain of conventional radiation therapy using x-rays is the damage to the healthy tissue that surrounds the tumor being treated. To address this issue, the use of proton beams is actually increasing, driven by their attracting physical properties. Proton beams also transfer energy into healthy tissue in front of the tumor but much less compared to x-rays. Most of the energy is deposited at the end of the proton range (Bragg peak) in a targeted volume. Tissues behind the tumor lying in the direction of particle motion are—in contrast to conventional radiotherapy—nearly completely protected.

Radiotherapy with charged particles has become more prevalent in clinical practice over the past 20 years, and the possibility of radiosensitization using GNPs in the particle therapy (protons or carbons) is an attractive prospective. Recently, Porcel *et al* has reported 11.3% and 18.5% enhancement of D_{50} (irradiation doses for 50% cell survival) values for Chinese hamster ovary cells treated with gadolinium-based nanoparticles and irradiated by C^{6+} or He^{2+} respectively [11]. This study demonstrates the possibility to amplify the radiation effects of medical heavy ions using nanoagent [11]. A more recent study of Liu *et al* showed a sensitizer enhancement ratio of 1.44 at 50% surviving level when HeLa cells were pre-treated with $7.5 \mu\text{g ml}^{-1}$ GNPs and irradiated with carbon ions [12]. An *in vivo* study using a CT26 mouse tumor evidenced a 90% tumor volume reduction in GNPs pre-treated mice at 20 days post proton therapy compared to only 18% tumor volume reduction in the radiation-only group [13]. In addition to these experimental demonstrations, a recent simulation investigation indicated that a local radial dose enhancement of up to a factor of 2 for proton irradiation in the presence of metallic NPs could be observed for proton with energies of 2, 80 and 300 MeV. Moreover, the most beneficial materials in terms of local dose enhancement seem to be platinum and gold [14].

In this work, 5 and 10 nm amine-PEG functionalized GNPs were studied in parallel. First, the cell uptake of GNPs and their intracellular localization were investigated both qualitatively by transmission electron microscopy (TEM) and confocal microscopy and quantitatively by inductively coupled plasma mass spectrometry (ICP-MS). Secondly, we showed that this cell uptake of GNPs led to a significant enhancement of cell death under proton beam irradiation. The influence of different physicochemical parameters on the cell response after irradiation (GNPs size, energy, linear energy

transfer (LET), dose) was reported and discussed. Finally, the mechanism responsible for cell death enhancement was investigated using a reactive oxygen species (ROS) scavenger. In this work, we chose to use the human epidermoid carcinoma A431 cell line because these cells have previously been shown to be targeted by antibody-functionalized polymer-coated GNP both *in vitro* and *in vivo* without toxicity [15, 16].

2. Materials and methods

2.1. Cell culture

A431 cells were grown in a Dulbecco's modified Eagle's complete medium (DMEM; 4.5 g l^{-1} D-glucose; Gibco® by Life Technologies) supplemented with 10% (v:v) fetal bovine serum (FBS; Gibco® by Life Technologies) at 37°C in a humidified atmosphere incubator containing 5% CO_2 .

2.2. Proton beam irradiation

Detailed protocols can be found in [17]. Briefly, twenty-four hours before irradiation, the sterilized homemade irradiation chambers were pre-treated 20 min with $15 \mu\text{l}$ of bovine plasma fibronectin (Gibco® by Life Technologies) to allow cell adherence. Then, 40 000 cells were seeded as a $32 \mu\text{l}$ drop at the center of the irradiation chambers. These irradiation chambers were then closed with a plastic cap to avoid dehydration and contamination and were placed in an incubator at 37°C with 5% CO_2 . 2 h after seeding, the drop was rinsed twice with phosphate buffered saline pH = 7.4 (10 mM phosphate, 0.9% NaCl, PBS, Biowhittaker® by Lonza) to remove non adherent cells. The irradiation chambers were then filled with DMEM (control group) or with DMEM containing 0.05 mg ml^{-1} of GNPs (5 or 10 nm) and placed in the incubator for 24 h.

On the day of irradiation, the medium was discarded from the irradiation chamber, the plastic cap was removed and a sterile cotton swab was used to take away the cells, which may have diffused outside the irradiated field. The irradiated chamber was then closed with the plastic cap, rinsed with PBS and filled with a CO_2 -independent medium (Gibco® by Life Technologies).

The cell monolayer was irradiated with a homogenous proton beam over 1 cm^2 , produced by a 2 MV Tandem accelerator (High Voltage Engineering Europa). The reader is referred to [18] for a thorough description of the experimental set-up and the irradiation procedure. Briefly, the energy of the beam was tuned in order to deliver the desired LET within the cells to be irradiated. Pristine proton peaks were extracted in air through a $1 \mu\text{m}$ silicon nitride window and the irradiation chambers were placed on a sample holder fixed at the end of the beamline. Homogeneity was achieved by defocusing the beam and checked using a passivated implanted planar silicon detector moved along x and y directions (supplementary information figure S1). Dose rate was assessed every millimeter in a 1 cm^2 surface and errors were less than 5% in the

cell sample region. The LET at the cell sample location was computed using SRIM software [19]. In this study, a $25 \text{ keV } \mu\text{m}^{-1}$ LET value was chosen to obtain the maximum relative biological effectiveness (RBE) for a proton beam. Another LET of $10 \text{ keV } \mu\text{m}^{-1}$ was chosen in the plateau region for comparison. For both LETs, the dose rate was fixed to 1 Gy min^{-1} and the dose range was chosen to cover survival fraction down to 1%. All doses were calculated using the classic broad beam formula as shown below:

$$D = \frac{1.6 \times 10^{-9} \text{ LET } \Phi}{\rho} \quad (1)$$

Here the density ρ is taken as 1 g cm^{-3} and Φ is the proton beam fluence.

2.3. Other experimental procedures

The other experimental procedures are described in the supplementary information.

3. Results

3.1. Cell internalization of GNPs

In order to exert possible radiosensitization effects, GNPs need to be uptaken by the cells. To investigate whether GNPs were internalized by cells and to determine their intracellular location, A431 cells were incubated with a non-toxic concentration of well dispersed GNPs (0.05 mg ml^{-1} , figures S2 and S3) for 24 h and the cellular localization was analyzed by TEM and confocal microscopy.

As shown in figures 1(b) and (c), both 5 and 10 nm GNPs were localized within the cytoplasm of A431 cells. Moreover, we noticed that 5 nm GNPs were also found to be attached to the nuclear envelope (figure 1(b1)), which was not observed for 10 nm GNPs. Magnified TEM images show that GNPs are present as aggregates on the order of hundred nanometers which may or not be within vesicles.

In order to confirm the intracellular localization of the GNPs, the spatial distribution of GNPs was also investigated by scanning confocal microscopy. This technique was used to detect both the scattered light of label-free GNPs and the fluorescence of molecular dyes used for labeling cell components.

No GNPs were observed in the control cells (figure 2(a)). Cells incubated in the presence of 5 nm (figure 2(b)) or 10 nm GNPs (figure 2(c)) exhibited some green spots in addition to the fluorescence signals observed in the control cells. Each of the green spots is the fingerprint of the scattered light from a cluster of GNPs. These images show that GNP aggregates were mainly distributed in the cytoplasm. It is notable that a few 5 nm GNPs were also localized in close vicinity of the nucleus. These results are in agreement with the TEM analyses described here above.

In order to investigate whether GNPs were internalized into the cells or attached on the cell surface, scattered light and fluorescence images were taken at different depths, from the bottom to the top, inside one cell volume (figure 2(d)).

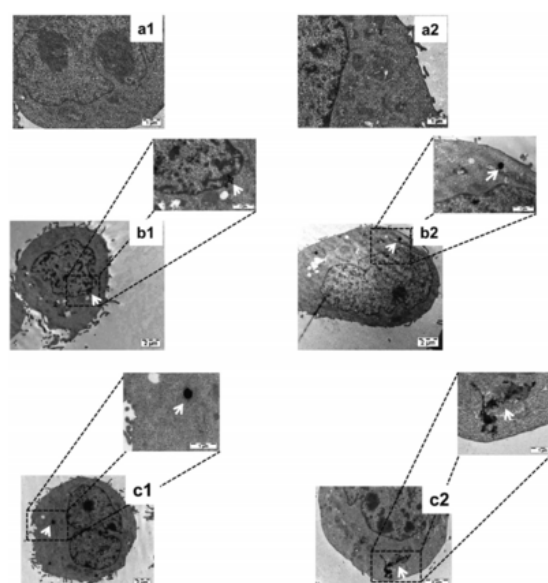


Figure 1. TEM images of A431 cells. Control A431 cells incubated without GNPs; scale bar: $1 \mu\text{m}$, (a1) and (a2); A431 cells incubated 24 h with 0.05 mg ml^{-1} of 5 nm GNPs (b1) and (b2) or 10 nm GNPs (c1) and (c2); scale bar $2 \mu\text{m}$. Arrows indicate GNPs within the cells. Images in the corners represent higher magnification images, scale bar: $1 \mu\text{m}$.

The Z-stacks of figures 2(e) and (f) show the entrapment of GNPs into a red area i.e., into the cytoplasm. This confirms the internalization of 5 and 10 nm GNPs into A431 cells. Moreover, the Z profiles through x and y axis show the presence of 5 nm GNPs in the nucleus. In addition to the intracellular localization of the GNPs, the analyses showed that the exposure to GNPs did not alter the cell morphology.

3.2. Quantification of the GNP cell uptake

To quantify the amount of GNPs internalized by A431 cells, ICP-MS assessments were also performed. After exposing cells to either 5 or 10 nm GNPs for 24 h, the entire cell population was detached and analyzed to determine the internalized gold quantity.

The GNP uptake was shown to be concentration dependent (figure 3). Indeed, as the GNPs concentration increased from 0.05 to 0.10 mg ml^{-1} , the ratio of gold quantity per cell ratios also increased by almost a factor of two. These results are in accordance with previously published results of different groups, which observed that efficient accumulation of GNPs into cancer cells can be achieved with longer incubation times and higher concentrations [20–22]. Furthermore, the A431 cells internalized a higher gold quantity of 10 nm GNPs than of 5 nm GNPs.

3.3. Radiosensitization effects of GNPs

In order to probe the potential radiosensitization effects of GNPs, A431 cells were incubated with a non-toxic concentration of

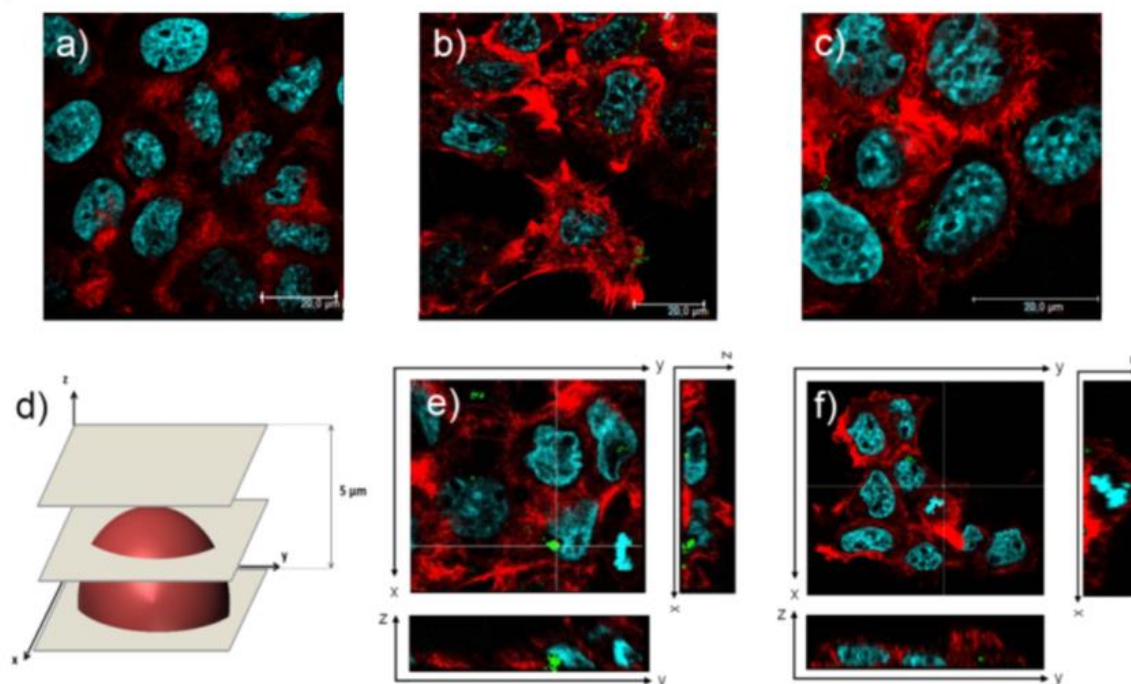


Figure 2. Confocal microscopy images of GNPs intracellular localization in A431 cells. Control A431 cells free of GNPs (a), A431 cells incubated 24 h with 0.05 mg ml^{-1} of 5 nm GNPs (b) or 10 nm GNPs (c), scale bar $20 \mu\text{m}$. Confocal optical stack from the bottom to the top of A431 cells (d) to show the intracellular localization of GNPs. The Z profiles of the cells (transversal view) were obtained after 24 h of incubation with 5 nm GNPs (e) or 10 nm GNPs (f). Blue and red areas respectively represent the signal of Hoechst dye from the nucleus and Alexa Fluor[®] Phalloidin 555 from the cytoplasm. Green areas represent the localization of the GNPs clusters. The white dashed lines indicate the axis studied in the Z-profile images.

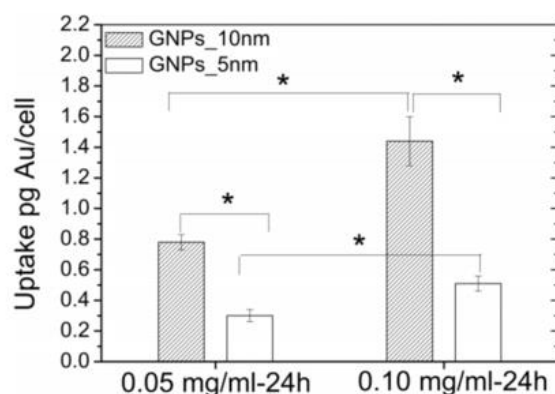


Figure 3. Determinations of the gold content in the cells exposed to GNPs. A431 cells were pre-incubated for 24 h with GNPs (5 or 10 nm) at a given concentration of 0.05 or 0.10 mg ml^{-1} . After the incubation, cells were washed, counted and lyophilized. The amount of gold was quantified by ICP-MS. Results are presented as means \pm SEM of three independent replicates. Results were statistically analyzed using a two-way ANOVA (turkey test, * $p < 0.05$).

0.05 mg ml^{-1} GNPs for 24 h and then irradiated by a proton beam. In these conditions, GNPs are internalized by A431 cells. In the present work, the effect of the nanoparticles was quantified by standard *in vitro* clonogenic assays. The survival

fractions of control A431 cells and cells pre-incubated with GNPs irradiated with 25 or $10 \text{ keV } \mu\text{m}^{-1}$ protons were measured for doses ranging from 0 to 3 Gy or 0 to 5 Gy respectively. The survival curves of A431 cells are presented in figure 4, with dose plotted on a linear scale and surviving fraction on a logarithmic scale.

The cell survival fraction decreased exponentially as a function of the radiation dose. More interestingly, this decrease was more pronounced in the presence of GNPs. To characterize the type of lesions amplified by the nanoparticles, we fitted the curves of cell survival (SF) with a linear quadratic (LQ) cell survival model as shown in equation (2) [23]

$$\text{SF} = e^{-(\alpha D + \beta D^2)} \quad (2)$$

In this model, the linear component [$\exp(-\alpha D)$] results from single-track events while the quadratic component [$\exp(-\beta D^2)$] arises from two-track events. The values of α and β as well as the ratio of α/β determined by the fitting procedure are reported in table 1.

These data showed a single exponential decrease in the survival fraction for the cells irradiated by a proton beam with LET of $25 \text{ keV } \mu\text{m}^{-1}$. This is evidenced by the disappearance of the characteristic low-dose curvature in the surviving curve (figure 4(a)), so that the β parameter is not applicable and the surviving curve appeared linear on the log-linear plot. The

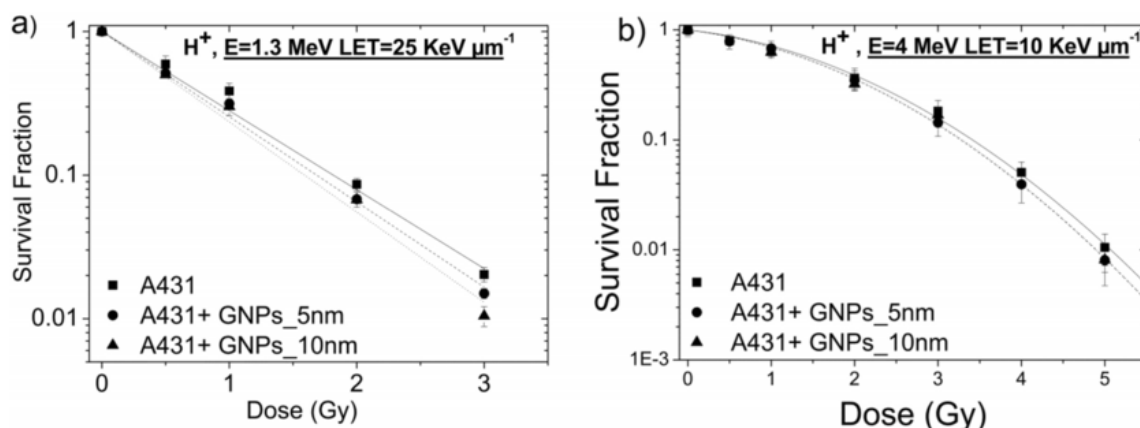


Figure 4. Survival curve of A431 cells without GNP (■, solid line), pre-incubated 24 h with 5 nm GNP (●, dash line) or 10 nm GNP (▲, dot line) and then irradiated by a proton beam (H^+) of (a) $LET = 25 \text{ keV } \mu\text{m}^{-1}$ and (b) $LET = 10 \text{ keV } \mu\text{m}^{-1}$. Results are expressed as means ± 1 S.D. ($n = 2-4$).

Table 1. Calculated α , β coefficients and the ratio of α/β for A431 cells irradiated by proton beam at different LET (25 or $10 \text{ keV } \mu\text{m}^{-1}$) after being pre-incubated during 24 h with 5 or 10 nm GNP (0.05 mg ml^{-1}) as well as in control cells (without GNP). The internalized GNP quantities in each condition measured by ICP-MS are reported in the last column.

LET of proton beam	Samples	$\alpha \text{ (Gy}^{-1}\text{)}$	$\beta \text{ (Gy}^{-2}\text{)}$	$\alpha/\beta \text{ (Gy)}$	GNP quantities (Au pg/cell)
$25 \text{ keV } \mu\text{m}^{-1}$	A431 (control)	$1.27(\pm 0.04)$	—	—	0
	GNPs 5 nm	$1.37(\pm 0.03)$	—	—	$0.30(\pm 0.04)$
	GNPs 10 nm	$1.45(\pm 0.05)$	—	—	$0.78(\pm 0.05)$
$10 \text{ keV } \mu\text{m}^{-1}$	A431 (control)	$0.19 (\pm 0.05)$	$0.14(\pm 0.01)$	$1.36(\pm 0.4)$	0
	GNPs 5 nm	$0.22 (\pm 0.03)$	$0.15(\pm 0.006)$	$1.47(\pm 0.2)$	$0.30(\pm 0.04)$
	GNPs 10 nm	$0.21(\pm 0.02)$	$0.15(\pm 0.02)$	$1.40(\pm 0.3)$	$0.78(\pm 0.05)$

straight exponential decrease is characteristic of surviving curves for densely ionization radiation [23]. While for cells irradiated with protons of $10 \text{ keV } \mu\text{m}^{-1}$, the surviving curves were better fitted by LQ curves on the log-linear plot. It has been reported that the shoulder in the survival curves, typical for sparsely ionizing radiation, is present for protons having LET up to $20 \text{ keV } \mu\text{m}^{-1}$ [24]. It has to be noted that in a previous work carried out by Wera *et al* that the surviving curve of A549 cells irradiated by protons of $10 \text{ keV } \mu\text{m}^{-1}$ showed a linear shape [18]. This is probably due to the difference in some biological characteristics of the cell lines. This data suggests that A431 epidermoid carcinoma cells might have different repair mechanisms than A549 lung carcinoma cells under proton irradiation.

The presence of 5 or 10 nm GNP induced an increase in the α parameter from 1.27 to 1.37 or 1.45 respectively, which indicates an enhancement of the lethality of the radiation when GNP were added. Corresponding sensitization enhancement ratios at 10% survival were calculated as being 1.08 and 1.14 respectively.

In this work, the potential radiosensitization effect of GNP irradiated by proton beam of different LET was also investigated. Within this context, a proton beam with LET of $10 \text{ keV } \mu\text{m}^{-1}$ was also applied. As demonstrated in figure 4(b), the survival curves of cells irradiated by protons

of $10 \text{ keV } \mu\text{m}^{-1}$ were characterized by a low-dose curvature. Compared to $25 \text{ keV } \mu\text{m}^{-1}$ proton irradiation, the survival curves of A431 cells pre-incubated with 5 or 10 nm GNP were not distinguishable from the one of the control cells. From the fitting parameters reported in table 1, we observed that the α and β parameters were similar for all experimental configurations (5, 10 nm GNP or control samples) after exposure to $10 \text{ keV } \mu\text{m}^{-1}$ protons.

The efficiency of GNP to amplify radiation-induced cell death was evaluated by calculating the amplification factor (AF) from the fitted surviving curves (equation (3)):

$$AF = \frac{SF_{\text{fitted curve control}} - SF_{\text{fitted curve GNP}}}{SF_{\text{fitted curve control}}} \times 100\%. \quad (3)$$

The AF indicates the enhanced proportion of dead cells in the presence of GNP compared to irradiation alone. The AFs of GNP of 10 or 5 nm were plotted as a function of the irradiation dose. Figure 5 shows that the AF increased with the irradiation dose. It is notable that the AF was higher for GNP of 10 nm in comparison to GNP of 5 nm. At 3 Gy, an AF of 25% or 40% was obtained with cells irradiated by protons of $25 \text{ keV } \mu\text{m}^{-1}$ after being pre-incubated with 5 or 10 nm GNP respectively. It must be noted that no AF was calculated for a LET of $10 \text{ keV } \mu\text{m}^{-1}$ because no statistical

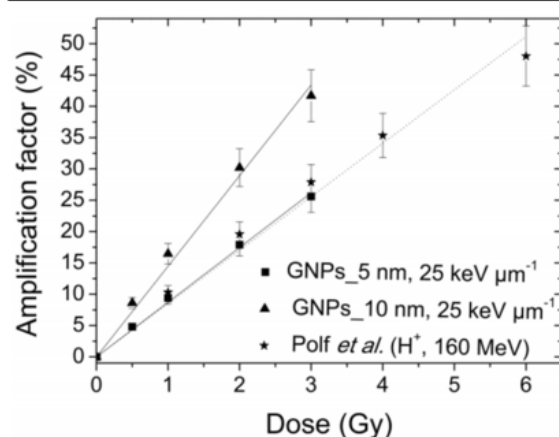


Figure 5. Amplification factors of radiation induced cell death obtained with A431 cells after being pre-incubated with GNPs of 10 or 5 nm and then irradiated by a proton beam ($\text{LET} = 25 \text{ keV } \mu\text{m}^{-1}$). The data of Polf *et al* are used for comparison [33].

significant differences were observed between survival curves of cells pre-incubated with 5 or 10 nm GNPs and control cells in our conditions. Overall, the highest cell death amplification was observed for cells pre-incubated with 10 nm GNPs and irradiated with $25 \text{ keV } \mu\text{m}^{-1}$ protons. It demonstrates that GNPs can produce a relevant increase in the cell death induced by the irradiation with high LET protons. However, we still need complementary data with x-ray irradiation in order to specify the RBE value of proton beam of different LETs as well as the potential RBE enhancement for GNPs-incubated cells [25].

3.4. Investigation of the radiosensitization mechanism using a radical scavenger

The induction of water radiolysis in biological system causes damage due to reactions of water radicals ($\cdot\text{OH}$, $\text{O}_2\cdot^-$) with cell constituents such as DNA, proteins and lipids. The contribution of this indirect action in cell killing can be estimated from the maximum degree of protection provided by dimethyl sulfoxide (DMSO), which can be used to efficiently scavenge $\cdot\text{OH}$ [26]. It has been shown that there is a maximum degree of protection around 1 M DMSO [27]. It must be noted that this concentration does not affect the cell capacity to divide (data not shown). In order to probe the role of water radicals in the radiosensitization effect of GNPs in combination with protons, irradiation experiments were conducted in the presence of the radical scavenger-DMSO.

Cells were irradiated with protons of $25 \text{ keV } \mu\text{m}^{-1}$ at 3 Gy, at which we observed a significant cell death enhancement by combining GNPs with proton beam. A431 cells were pre-incubated 24 h with or without 0.05 mg ml^{-1} of GNPs of 10 nm DMSO (1 M) was added just before the irradiation in some samples, kept during irradiation procedure and removed immediately after. The survival fractions of A431 cells were then assessed by conventional clonogenic assays in control medium (figure 6).

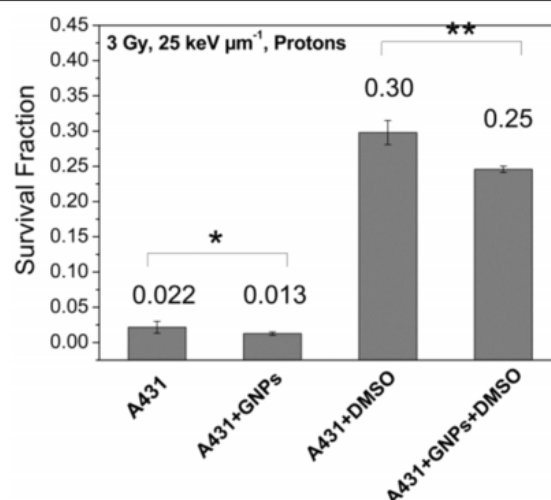


Figure 6. Survival fractions of A431 cells irradiated with $25 \text{ keV } \mu\text{m}^{-1}$ proton beam at 3 Gy. A431 cells were pre-incubated or not 24 h with 10 nm GNPs at 0.05 mg ml^{-1} . Cells were then irradiated in the presence or absence of DMSO that was added just before irradiation. Results were presented as mean \pm S.D. of three independent replicates. Results were statistically analyzed using a one-way ANOVA (turkey test, * $p < 0.05$, ** $p < 0.01$).

The results show that, in the absence of GNPs, when water radicals were scavenged by DMSO, the cell survival increased drastically from 2% to 30%. It is a clear indication that the cell death induced by proton irradiation is partially caused by the indirect action, i.e. production of free radicals by water radiolysis. The other 70% are probably due to direct effects, which cannot be prevented by the radical scavenger. It is in full agreement with the previous findings that showed that charged particles are densely ionizing and described a more significant contribution of the direct action to cell killing [26, 28]. In addition, we observed that GNPs contributed by about 40% to the decrease in cell survival when cells were irradiated by protons in the absence of DMSO. In the presence of DMSO, this contribution decreased to 17%. It is interesting to note that this value is similar to the augmentation ratio of the α parameter (15%) obtained from the cell survival curves (figure 6), which are both correlated with the direct effect of the interaction between protons and GNPs. In the other hand, the decrease in the radiosensitization contribution of GNPs (from 40% to 17%), when irradiated in the presence of the radical scavenger DMSO, highlights the major role of GNPs in enhancing the production of ROS in combination with protons.

4. Discussion

Given the emerging evidence of biological relevance of GNPs and the appealing physical properties of proton beams, the purpose of this *in vitro* study was to investigate the possible radiosensitization effects of GNPs for proton irradiation.

TEM and scanning confocal microscopy images confirm the internalization of both 5 and 10 nm GNPs in the cytoplasm of A431 cells. Moreover, the accumulation in the perinuclear region within A431 cells was observed only for 5 nm GNPs. Similar results have been reported by Liang *et al*. These authors have demonstrated that tiopronin-coated GNPs with size of 2–6 nm were found within the nucleus and the cytoplasm, while larger GNPs (15 nm) were only located in the cytoplasm of human breast cancer cells (MCF-7). They suggested that, due to the size of the ultrasmall particles (2–6 nm), the GNPs were able to enter the nuclei via the nuclear pores, while the larger particles were prevented from entering the nuclei [29]. In terms of GNPs numbers, it can be inferred from ICP-MS measurements that 7.7×10^4 and 24.0×10^4 nanoparticles were internalized per cell for 10 and 5 nm GNPs respectively. This result is consistent with confocal microscopy and TEM observations that showed the presence of slightly larger aggregates in cells incubated with 5 nm GNPs compared to the 10 nm ones. It must be noted that for a same aggregate size, the one consisting of 5 nm GNPs will contain more NPs than the one composed of 10 nm GNPs.

Our results on the cellular uptake of GNPs are in accordance with previous results obtained by different groups on different nano-objects. The group of Xiao postulated that the cell uptake of GNPs is driven by two processes: the penetration rate and the efflux rate [30]. They suggested that smaller GNPs can more easily penetrate into the cells. This suggestion is consistent with the result of Panyam *et al* which showed that a decrease in particle size leads to an increase in the surface area facilitating the diffusion of GNPs into cells [31]. In another study, Donkor and Tang observed the same results with 30 and 50 nm carbon nanotubes [32]. However, in addition to the penetration rate, Xiao suggested that smaller GNPs also have a higher efflux rate from cells [30].

A clear radiosensitization effect was evidenced with proton irradiation. These results are similar to the effects observed with GNPs activated by high-energy photons [2, 7, 33]. More interestingly, the effect was more pronounced for cells irradiated after being pre-incubated with 10 nm GNPs compared to 5 nm GNPs. This difference could be, at least partially, attributed to the different nanoparticle uptake. Indeed, the results from ICP-MS measurements indicated that A431 cells have internalized 3 times more 10 nm GNPs compared to 5 nm GNPs in total gold mass. However, when assessed as GNP number, 5 nm GNPs are three times more numerous than 10 nm GNPs. Nevertheless, the total section exposed by GNPs is proportional to the square of the particle radius. Even though the number of 5 nm GNPs internalized by the cells was higher, they exposed together a smaller total section. Thereby, the interaction probability between 5 nm GNPs and the proton beam is lower than for 10 nm GNPs. We hypothesized that these differences in the interaction probability could explain the GNP size effect observed in figure 4. Various studies have pointed out that for *in vivo* investigations as well as for potential biomedical applications in patients, it is of great importance to take into account both the

efficiency and the quantity of the uptake of the GNPs [34–36].

Our results demonstrated a marked effect of the LET on the radiosensitization effects of the GNPs. The interaction probability between GNPs and protons is driven by three different factors. The first one is related to GNP internalization, not necessarily as gold mass, but as total GNP section exposed to the beam, which in our case gives an advantage to 10 nm GNPs as stated above. The second factor is the number of projectiles: at high-LET, the number of protons that are necessary to achieve a given dose is lower than for low-LET protons. This reduces substantially the hit probability, and hence the interaction probability between gold and incident protons by a factor inversely proportional to the LET. Simulation calculation (Monte-Carlo track-structure simulations) and experiments indicate that the patterns and density of energy deposition substantially differs between low- and high-LET [37]. For high LET radiations, substantial energy transfer occurs through the deposition of relatively large quantities or packets of energy in a given volume. Comparatively, low-LET radiation gives rise to more sparsely energy deposition. GNPs localized on a proton track will thus interact more with high-LET protons. It must be noted that 1.3 MeV protons ($25 \text{ keV } \mu\text{m}^{-1}$ in cells) have a LET of $114 \text{ keV } \mu\text{m}^{-1}$ in gold, whereas 4 MeV protons ($10 \text{ keV } \mu\text{m}^{-1}$ in cells) reach only $62 \text{ keV } \mu\text{m}^{-1}$. Thus, 1.3 MeV protons have a higher probability of exciting GNPs. Nevertheless, the γ rays that can be produced by 4 MeV protons have a higher energy than 1.3 MeV protons (8.8 keV compared to 3.7 keV) and could more easily reach the GNP surface. Overall, there is a balance between the ballistic and energy factors as mentioned above and it is not trivial to determine in advance what experimental configuration will give rise to the most favorable conditions in term of radiosensitization. In this work, $25 \text{ keV } \mu\text{m}^{-1}$ protons in combination with 10 nm GNPs gave more significant contribution in term of additional cell death.

Although there is an extensive amount of data regarding GNPs-induced radiosensitivity, they were mainly obtained with X or γ ray irradiation. Only few data have been reported so far regarding proton irradiation. In the work of Polf *et al* DU145 human prostate carcinoma cells were irradiated by a proton beam (160 MeV) within the uniform clinical dose region of the spread out Bragg peak which contains a spectrum of proton beams with LET varying from 1 to $35 \text{ keV } \mu\text{m}^{-1}$ [38]. They observed an amplification of radiation-induced cell death with ~ 44 nm GNPs, which is similar to our results obtained with cells loaded with 5 nm GNPs and irradiated by proton of $25 \text{ keV } \mu\text{m}^{-1}$. They estimated that the concentration of gold in the GNPs-treated cells was approximately 1 ng cell^{-1} , which is 1000 times more than in our study. This higher cell uptake gives rise to a greater interaction surface between the beam and GNPs. On the other hand, Jeynes *et al* did not observe a significant radiosensitization effect of 50 nm GNPs in the RT112 bladder cancer cells irradiated by 3 MeV protons ($12 \text{ keV } \mu\text{m}^{-1}$ at the cell center) [39]. They measured a concentration of gold around 1 pg per cell (i.e. approximately 1000 GNPs per cell)

which is ~ 100 times lower than the concentration obtained in our experiments. Thereby, the total section of GNPs exposed to the beam is too low to enable an interaction with protons. Besides, the reported LET value is similar to $10 \text{ keV } \mu\text{m}^{-1}$ used in our study, at which we did not either observe a significant radiosensitization effect of GNPs.

Numerous studies showed evidence of radiosensitization effects when NPs are used in combination with irradiation. In order to rationalize these observations, Lacombe *et al* hypothesized that the interaction between charged particle beams and high-Z nanoparticles leads to the emission of secondary electrons [11]. These electrons may interact thereafter with their environment and increase the damage inside the cell. It must be noted that at higher proton energies, the interaction with GNPs can lead to proton-induced x-ray emission, which in turn produces secondary electrons [13]. In these models, the nanoparticle size and the intracellular concentration seem to be the major contributors to the radiosensitization effect. In fact, if the NPs are too small they do not provide enough volume from which additional electrons can be produced. Conversely, if they are too large, the electrons that are produced will be captured inside the nanoparticle and will not contribute to the enhancement of cell damage. Therefore it is likely that a GNP optimal size exists where a majority of secondary electrons can reach the GNP surface and the production of additional radiation is maximized. Moreover, the intracellular concentration of NPs needs to be high, since the more NPs the more electrons are generated, that will then produce damage in the cell. Nevertheless, an increase in NP concentration goes hand-in-hand with a potential higher cytotoxicity.

Finally, our results suggest that ROS partly explained the radiosensitization effects of the GNPs. A recent study carried out by Sicard-Roselli *et al* indicated that 1 nM ($\sim 210 \mu\text{g ml}^{-1}$) GNP induced a significant production of $\cdot\text{OH}$ radicals under x-ray irradiation [40]. This phenomenon has been explained by a multiple-step mechanism of activation of nanoparticles under irradiation [11, 41, 42]. Inner shells of gold atoms were first excited by irradiation, followed by the emission of abundant secondary electrons in the vicinity of NPs and finally the production of ROS in a local volume [42]. Our work hence suggests that ROS production is one way by which GNPs enhance lethal proton-induced damage to the cells.

5. Conclusions

We conclude that the specific internalization of GNPs into tumor cells could produce a clinically meaningful increase of proton therapy. Enhanced cell death observed by combining GNPs with $25 \text{ keV } \mu\text{m}^{-1}$ and not $10 \text{ keV } \mu\text{m}^{-1}$ proton beams suggests the amplifying radiation effect might be more pronounced with increasing LET and at the distal edge of irradiated tumor. The size of nanoparticles is one of the key parameters determining the efficiency of the nanoparticle-induced radiosensitization, notably by influencing cell uptake. From a clinical set-point, it provides the possibility to overcome the limitation of the tolerance dose in the surrounding

normal tissue as well as reducing the dose in upstream tissues. To develop future nanoagents in protontherapy applications, the capacity of nanoparticles to enter into cells and to emit secondary electrons under irradiation need to be considered. Hence, the addition of nanoparticles during the treatment by protons would allow a reduction of the total radiation dose given to the patient, ultimately reducing negative radiation effects in upstream healthy tissues.

The present findings demonstrate that this strategy can be used to improve the performances of other modalities than conventional radiotherapy, such as the protontherapy and the produced data may also be of interest for adapted treatment planning combining protons and nanoparticles as radiosensitizing agents.

Acknowledgments

We are grateful to Noëlle Ninane and Catherine Demazy for their skillful assistance with confocal microscopy. This research used resources of the electron microscopy service located at the University of Namur. This Service as well as the confocal microscope belongs to the technological platform 'morphology-imaging'. The authors also acknowledge the support of the SIAM platform. TheraPlus project is supported by the Walloon Region, grant n° 1318075. Sébastien Penninckx is a PhD fellow funded by the Belgian Fund for Scientific Research (FRS-FNRS, Belgium). Géraldine Genard is a recipient of a Télévie grant (FRS-FNRS, Belgium).

References

- [1] Butterworth K T, McMahon S J, Currell F J and Prise K M 2012 Physical basis and biological mechanisms of gold nanoparticle radiosensitization *Nanoscale* **4** 4830–8
- [2] Miladi I *et al* 2014 The in vivo radiosensitizing effect of gold nanoparticles based MRI contrast agents *Small* **10** 1116–24
- [3] Hainfeld J F, Smilowitz H M, O'Connor M J, Dilmanian F A and Slatkin D N 2013 Gold nanoparticle imaging and radiotherapy of brain tumors in mice *Nanomedicine* **8** 1601–9
- [4] Le Duc G *et al* 2011 Toward an image-guided microbeam radiation therapy using gadolinium-based nanoparticles *ACS Nano* **5** 9566–74
- [5] Al Zaki A, Joh D, Cheng Z, De Barros A L B, Kao G, Dorsey J and Tsourkas A 2013 Gold-loaded polymeric micelles for computed tomography-guided radiation therapy treatment and radiosensitization *ACS Nano* **8** 104–12
- [6] McMahon S J *et al* 2011 Energy dependence of gold nanoparticle radiosensitization in plasmid DNA *J. Phys. Chem. C* **115** 20160–7
- [7] Hainfeld J F, Slatkin D N and Smilowitz H M 2004 The use of gold nanoparticles to enhance radiotherapy in mice *Phys. Med. Biol.* **49** N309–15
- [8] Kong T, Zeng J, Wang X, Yang X, Yang J, McQuarrie S, McEwan A, Roa W, Chen J and Xing J Z 2008 Enhancement of radiation cytotoxicity in breast-cancer cells by localized attachment of gold nanoparticles *Small* **4** 1537–43

- [9] Jain S *et al* 2011 Cell-specific radiosensitization by gold nanoparticles at megavoltage radiation energies *Int. J. Radiat. Oncol. Biol. Phys.* **79** 531–9
- [10] Mesbahi A 2010 A review on gold nanoparticles radiosensitization effect in radiation therapy of cancer *Rep. Pract. Oncol. Radiother.* **15** 176–80
- [11] Porcel E, Tillement O, Lux F, Mowat P, Usami N, Kobayashi K, Furusawa Y, Le Sech C, Li S and Lacombe S 2014 Gadolinium-based nanoparticles to improve the hadrontherapy performances *Nanomed.: Nanotechnol. Biol. Med.* **10** 1601–8
- [12] Liu Y, Liu X, Jin X, He P, Zheng X, Dai Z, Ye F, Zhao T, Chen W and Li Q 2015 The dependence of radiation enhancement effect on the concentration of gold nanoparticles exposed to low- and high-LET radiations *Phys. Medica* **31** 210–8
- [13] Kim J K, Seo S J, Kim K H, Kim T J, Chung M H, Kim K R and Yang T K 2010 Therapeutic application of metallic nanoparticles combined with particle-induced x-ray emission effect *Nanotechnology* **21** 425102
- [14] Wälzlein C, Scifoni E, Krämer M and Durante M 2014 Simulations of dose enhancement for heavy atom nanoparticles irradiated by protons *Phys. Med. Biol.* **59** 1441
- [15] Karmani L *et al* 2013 Antibody-functionalized nanoparticles for imaging cancer: influence of conjugation to gold nanoparticles on the biodistribution of ⁸⁹Zr-labeled cetuximab in mice *Contrast Media Mol. Imaging* **8** 402–8
- [16] Marega R *et al* 2012 Antibody-functionalized polymer-coated gold nanoparticles targeting cancer cells: an in vitro and in vivo study *J. Mat. Chem.* **22** 21305
- [17] Heuskin A C, Wera A C, Riquier H, Michiels C and Lucas S 2013 Low-dose hypersensitivity and bystander effect are not mutually exclusive in A549 lung carcinoma cells after irradiation with charged particles *Radiat. Res.* **180** 491–8
- [18] Wéra A C, Riquier H, Heuskin A C, Michiels C and Lucas S 2011 In vitro irradiation station for broad beam radiobiological experiments *Nucl. Instrum. Methods Phys. Res. B* **269** 3120–4
- [19] Ziegler J F and Biersack J P 1985 *Treatise on Heavy-Ion Science: Volume 6: Astrophysics, Chemistry, and Condensed Matter* ed D A Bromley (Boston, MA: Springer US) pp 93–129
- [20] Chithrani B D, Ghazani A A and Chan W C W 2006 Determining the size and shape dependence of gold nanoparticle uptake into mammalian cells *Nano Lett.* **6** 662–8
- [21] Freese C, Gibson M I, Klok H-A, Unger R E and Kirkpatrick C J 2012 Size- and coating-dependent uptake of polymer-coated gold nanoparticles in primary human dermal microvascular endothelial cells *Biomacromolecules* **13** 1533–43
- [22] Trono J D, Mizuno K, Yusa N, Matsukawa T, Yokoyama K and Uesaka M 2011 Size, concentration and incubation time dependence of gold nanoparticle uptake into pancreas cancer cells and its future application to x-ray drug delivery system *J. Radiat. Res.* **52** 103–9
- [23] Hall E J and Giaccia A J 2006 *Radiobiology for the Radiologist* (Philadelphia, PA: Lippincott Williams & Wilkins)
- [24] Belli M *et al* 1998 RBE-LET relationships for cell inactivation and mutation induced by low energy protons in V79 cells: further results at the LNL facility *Int. J. Radiat. Biol.* **74** 501–9
- [25] Paganetti H, Niemierko A, Ancukiewicz M, Gerweck L E, Goitein M, Loeffler J S and Suit H D Relative biological effectiveness (RBE) values for proton beam therapy *Int. J. Radiat. Oncol. Biol. Phys.* **53** 407–21
- [26] Ito A, Nakano H, Kusano Y, Hirayama R, Furusawa Y, Murayama C, Mori T, Katsumura Y and Shinohara K 2006 Contribution of indirect action to radiation-induced mammalian cell inactivation: dependence on photon energy and heavy-ion LET *Radiat. Res.* **165** 703–12
- [27] Hirayama R *et al* 2014 Indirect action to cell killing by SOBP carbon-ion beams *J. Radiat. Res.* **55** i133–4
- [28] Hirayama R *et al* 2009 Contributions of direct and indirect actions in cell killing by high-LET radiations *Radiat. Res.* **171** 212–8
- [29] Huang K *et al* 2012 Size-dependent localization and penetration of ultrasmall gold nanoparticles in cancer cells, multicellular spheroids, and tumors in vivo *ACS Nano* **6** 4483–93
- [30] Yao M, He L, McClements D J and Xiao H 2015 Uptake of gold nanoparticles by intestinal epithelial cells: impact of particle size on their absorption, accumulation, and toxicity *J. Agric. Food Chem.* **63** 8044–9
- [31] Panyam J, Dali M M, Sahoo S K, Ma W, Chakravarthi S S, Amidon G L, Levy R J and Labhasetwar V 2003 Polymer degradation and in vitro release of a model protein from poly(D,L-lactide-co-glycolide) nano- and microparticles *J. Control. Release* **92** 173–87
- [32] Donkor D A and Tang X S 2014 Tube length and cell type-dependent cellular responses to ultra-short single-walled carbon nanotube *Biomaterials* **35** 3121–31
- [33] Hainfeld J F, Dilmanian F A, Slatkin D N and Smilowitz H M 2008 Radiotherapy enhancement with gold nanoparticles *J. Pharm. Pharmacol.* **60** 977–85
- [34] Freese C, Unger R E, Deller R C, Gibson M I, Brochhausen C, Klok H-A and Kirkpatrick C J 2013 Uptake of poly(2-hydroxypropylmethacrylamide)-coated gold nanoparticles in microvascular endothelial cells and transport across the blood–brain barrier *Biomater. Sci.* **1** 824–33
- [35] Cai W, Gao T, Hong H and Sun J 2008 Applications of gold nanoparticles in cancer nanotechnology *Nanotechnol. Sci. Appl.* **2008** 17–32
- [36] Alkilany A M and Murphy C J 2010 Toxicity and cellular uptake of gold nanoparticles: What we have learned so far? *J. Nanoparticle Res.* **12** 2313–33
- [37] Timlin C and Jones B 2010 Proton and charged particle radiotherapy *Br. J. Radiol.* **83** 87
- [38] Polf J C, Bronk L F, Driessen W H, Arap W, Pasqualini R and Gillin M 2011 Enhanced relative biological effectiveness of proton radiotherapy in tumor cells with internalized gold nanoparticles *Appl. Phys. Lett.* **98** 193702
- [39] Jaynes J C, Merchant M J, Spindler A, Wera A C and Kirkby K J 2014 Investigation of gold nanoparticle radiosensitization mechanisms using a free radical scavenger and protons of different energies *Phys. Med. Biol.* **59** 6431–43
- [40] Sicard-Roselli C, Brun E, Gilles M, Baldacchino G, Kelsey C, McQuaid H, Polin C, Wardlow N and Currell F 2014 A new mechanism for hydroxyl radical production in irradiated nanoparticle solutions *Small* **10** 3338–46
- [41] Štefančíková L *et al* 2014 Cell localisation of gadolinium-based nanoparticles and related radiosensitising efficacy in glioblastoma cells *Cancer Nanotechnol.* **5** 1–15
- [42] Porcel E, Liehn S, Remita H, Usami N, Kobayashi K, Furusawa Y, Le Sech C and Lacombe S 2010 Platinum nanoparticles: a promising material for future cancer therapy? *Nanotechnology* **21** 85103

LET-dependent Radiosensitization Effects of Gold Nanoparticles for Proton Irradiation

– Supplementary information –

1 . Materials and methods

1.1. Preparation of nanoparticle suspension

The GNPs (GNP, Amine functionalized Gold Colloid nanocrystal; AC Diagnostics Inc., USA) were lyophilized with a freeze-drying system (Alpha 2-4 LD Plus; Analis) and stored under inert atmosphere at 4°C for further utilization. Prior to being incubated with cells, the lyophilized nanoparticles were re-suspended in cell medium and sonicated for 15 min. The hydrodynamic size and the homogeneity of the nanoparticle suspension were analyzed by disc centrifuge (CPS Instruments Europe).

1.2. Cell viability assay

MTS assay was used to measure the viability of cells treated or not with GNPs at different concentrations. In this study, 4000 cells were seeded in a 96-well plate. 24 h later, culture medium containing different concentrations of GNP was added. After 24 h of incubation, the cells were washed with PBS and 120 µL of culture medium containing MTS (Cell Titer 96® Aqueous One Solution Reagent; Promega) in a 5:1 ratio was added in each well. After 1 hour of incubation with MTS tetrazolium compound, the optical density was determined at 490 nm using a spectrophotometer (X-Mark TM Microplate Spectrophotometer; Biorad).

1.3. Clonogenic assay

Immediately after irradiation, cells were detached using trypsin and the cell numbers were counted. In order to obtain countable colony numbers for different doses of irradiation, cells were seeded in 6-well plates containing DMEM medium supplemented with penicillin/streptomycin and incubated at 37 °C with 5% CO₂. In parallel, cells were also seeded in separate dishes at one density per dose. 2 hours after seeding, they were fixed with 4% paraformaldehyde (Merck Chemicals) for 10 min and washed 3 times with PBS. The number of cells attached to the dish is counted manually under an optical microscope to obtain the precise number of cells seeded for each cell density and dose. Eight days post irradiation, colonies were stained with violet crystal in 2% ethanol. The numbers of visible colonies (containing 50 or more cells) were considered to represent surviving cells and were manually counted. The plating efficiency (PE) was determined for each dose of irradiation and calculated by dividing the numbers of colonies by the initial numbers of seeded cells. The surviving fraction was obtained as the ratio of the PE for the irradiated cells to the PE for control cells. Note that the control cells underwent all procedures except the irradiation step. At least three independent experiments were performed for each irradiated condition and the errors were evaluated as standard deviation (S.D.).

1.4. DMSO treatment

Immediately prior to irradiation, medium was changed and the irradiation chambers were filled with CO₂-independent medium containing or not 1 M DMSO. Studies have shown that this concentration is non-toxic for short duration.^[1] Cells were irradiated with a proton beam of 25 keV μm^{-1} , at a dose rate of 1 Gy min^{-1} . Directly after the irradiation, cells were trypsinized for clonogenic assays.

1.5. Transmission electron microscopy

TEM was performed to precisely localize the position of intracellular nanoparticles. Cells were first fixed for 2 h at 4°C with 2.5% (w/v) glutaraldehyde (Agar Scientific) in 0.1 M cacodylate buffer (pH 7.4). Cells were washed with cacodylate buffer and subsequently post-fixed in 1% (v/w) osmium tetroxide (Merck Chemicals). Samples were dehydrated by successive passages in increasing concentration of ethanol (30%, 50%, 70%, 85% and 100%). After embedding in epon resin LX 112 (Ladd Research Industries), ultra-thin sections of cells were prepared for TEM analysis using an 8800 ultratome III (LKB). They were then colored with uranyl acetate and lead citrate. Observations were performed with a FEI Technai 10 TEM (Philips).

1.6. Confocal microscopy

60,000 cells were seeded in 24-well plates containing coverslips (13-mm Cover glasses; VWR). 2 h after seeding, these cells were incubated for 24 h with 0.05 mg ml^{-1} GNPs. Cells incubated without GNPs were used as control. After incubation, cells were fixed 10 min with 4% paraformaldehyde (Merck Chemicals) and washed three times with PBS. The nuclei and F-actin were stained with Hoechst 33258 (Molecular Probes™ by Life Technologies) and Alexa Fluor® 555 Phalloidin (Molecular Probes™ by Life Technologies) respectively. Cells were then washed three times with PBS. The coverslips were then mounted in Mowiol (Sigma) and observed with a Leica SP5 confocal inverted microscope.

The fluorescence signal of dyes associated to the nuclei and F-actin were detected using respectively a 405 nm UV-laser and a 561 nm laser. Additionally, a 514 nm laser was used to detect the presence of GNPs, using the surface plasmon resonance as described by Tsai *et al.*^[2] Optical stacks of 0.5 μm were taken through the cells in order to accurately localize the GNPs in the cytoplasm.

1.7. Inductively coupled plasma mass spectrometry (ICP-MS) measurement

After 24h incubation with GNPs, cells were washed twice with PBS at 37°C and then trypsinized. Detached cells were then washed with culture medium twice by successive centrifugation. The actual number of cells in each sample was then determined using a cell counter (Countess Automated Cell Counter, Invitrogen). After the third centrifugation, the medium was discarded, and the cells were transferred to a glass vial and lyophilized. The samples were hydrolyzed using 4 mL of pure 65% nitric acid (Merck chemicals, Belgium) in a water bath at 60 °C until complete solubilization. The analytical determination of gold (¹⁹⁷Au) in the samples was performed by ICP-MS (Agilent 7500cx, Agilent Technologies, Germany). The homogenized samples were diluted 100 times in basic diluent (2% butanol, 0.05% EDTA, 1% NH₄OH and 0.05% triton) containing iridium (¹⁹³Ir) as an internal standard. The gold content of the samples was quantified by plotting the calibration curve with known concentrations of a gold standard solution (Merck Chemicals, Belgium) used for external

calibration. The amount of gold detected into the cells was expressed as an internalized gold quantity per cell.

1.8 Experimental setup of *in vitro* irradiation for a broad beam

Experimental setup for the irradiation of A431 cells with proton beams of different LET is presented in Figure S1.

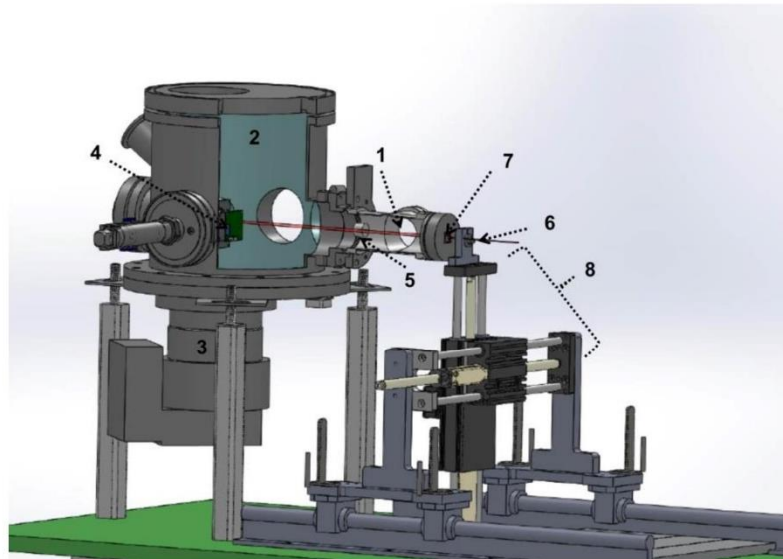


Figure S1. *In vitro* irradiation station for a broad beam (1) H⁺ broad beam; (2) vacuum chamber; (3) pumping system; (4) CCD camera fixed on a pneumatic jack; (5) & (6) internal and external PIPS detectors for the dose-rate monitoring; (7) Si₃N₄ window exit; (8) motorized XY table.

1.9. Statistical analysis

All of the experiments were repeated in triplicate on separate days. All curve fittings were performed with OriginLab® software (Northampton, USA). A linear-quadratic equation was used to fit clonogenic assay data:

$$SF = e^{-(\alpha D + \beta D^2)}$$

Where SF is the surviving fraction of the cells; α and β define the linear and the quadratic component, respectively and D is the deposited dose.

To evaluate the differences between the experimental and corresponding control samples, the data was analyzed using ANOVA for repeated measures (MTS assays). Turkey tests were used for survival curves of A431 cells and ICP-MS measurements. Survival fractions of A431 cells irradiated at 5 Gy by protons of 10 keV μm^{-1} were analyzed by one-way ANOVA. ICP-MS analysis measurements were analyzed by two-way ANOVA.

2. Results

2.1. GNPs preparation and characterization

5 nm and 10 nm amine-dihydrolipoic acid-PEGylated AuNPs (5 nm and 10 nm DHLA-PEG400-NH₂ AuNPs) were used in this study. Prior to cell treatment, the gold nanoparticle solutions were lyophilized and re-suspended in cell culture medium. The size distributions of GNPs before and after resuspension in cell medium were measured by analytical disc centrifuge as shown in Figure S2.

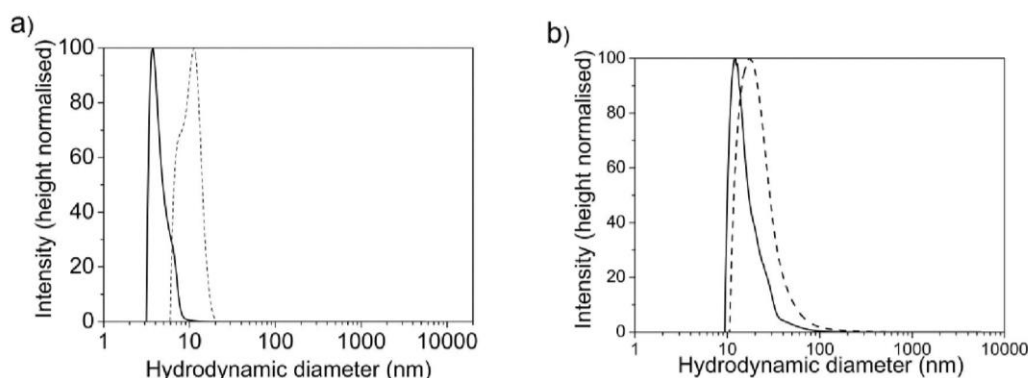


Figure S2. Size distribution data of 5 nm (a) and 10 nm (b) GNPs before (solid line) and after resuspension in cell culture medium (dash line), analyzed by analytical disc centrifuge.

Before lyophilization, 5 nm and 10 nm GNPs displayed a peak around 4 nm and 12 nm respectively, which corresponds to the indicated size. After lyophilization and resuspension in the cell culture medium, these two peaks were shifted to 7-12 nm and 14-18 nm, respectively. This slight shift to higher size of GNPs can be due to exposure to ions and proteins present in the cell culture media.^[3] However, these GNPs are coated with PEG groups and it has been described that such a ligand limits the impact of protein adsorption.^[4] Xie *et al.* have also observed that coating PEG on monodispersed Fe₃O₄ nanoparticles produced negligible aggregation in cell-culture conditions.^[5] Our studies demonstrated that GNPs coated with PEG-amine groups exhibited negligible aggregation in cell culture medium and the GNPs of the two different sizes were well distinguished.

2.2. Cytotoxicity of GNPs

The cytotoxicity measurements were aimed at determining the experimental conditions (GNPs concentration and incubation time) to perform microscopy and irradiation experiments with minimum toxicity. To investigate the toxicity of GNPs, the A431 cells were incubated 24 h with 5 nm and 10 nm GNPs at different concentrations (0 to 1 mg mL⁻¹ GNPs) and the cell viability was determined by a MTS assay. It must be noted that no significant absorption of GNPs in the culture medium was observed at 490 nm (data not shown). For both size of GNPs, a significant decrease in cell viability of A431 cells was observed for concentrations higher than 0.5 mg mL⁻¹ (Figure S3). The decrease was slightly more pronounced for 10 nm GNPs, which reduced cell viability by 40% at a concentration of 0.5 mg

mL^{-1} compared to the $\sim 10\%$ reduction induced by 5 nm GNPs at the same concentration. For the scope of our work, we established that incubation with 0.05 mg mL^{-1} GNPs during 24 h corresponds to toxicity lower than 5%. These conditions were used for the experiments described in the manuscript.

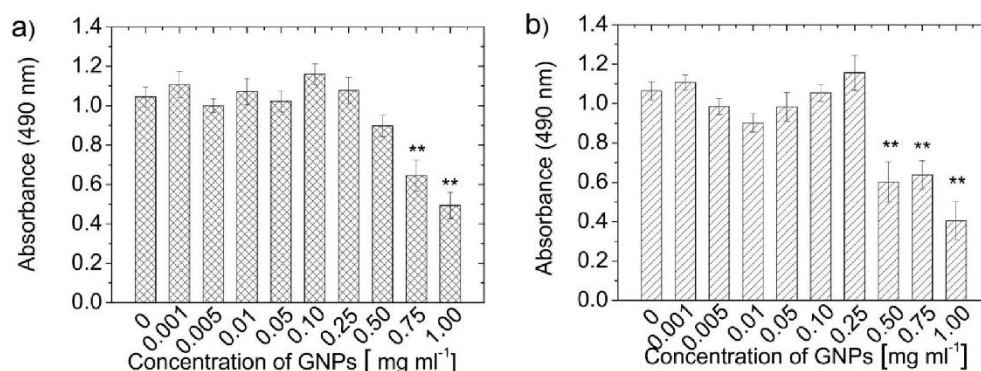


Figure S3. Cell viability of A431 cells incubated in the presence of different concentrations of GNPs for 24 h and assessed using a MTS assay. Data represent the mean absorbance ± 1 S.D. for three independent experiments of, a) 5 nm GNPs; b) 10 nm GNPs. Results were statistically analyzed using a one-way ANOVA (turkey test, ** $p < 0.01$).

3. References

- [1] Jeynes J C, Merchant M J, Spindler A, Wera A C and Kirkby K J 2014 Investigation of gold nanoparticle radiosensitization mechanisms using a free radical scavenger and protons of different energies *Phys Med Biol* 59 6431-43
- [2] Tsai S-W, Chen Y-Y and Liaw J-W 2008 Compound Cellular Imaging of Laser Scanning Confocal Microscopy by Using Gold Nanoparticles and Dyes *Sensors* 8 2306
- [3] Albanese A and Chan W C 2011 Effect of gold nanoparticle aggregation on cell uptake and toxicity *ACS Nano* 5 5478-89
- [4] Verma A and Stellacci F 2010 Effect of surface properties on nanoparticle-cell interactions *Small* 6 12-21
- [5] Xie J, Xu C, Kohler N, Hou Y and Sun S 2007 Controlled PEGylation of Monodisperse Fe_3O_4 Nanoparticles for Reduced Non-Specific Uptake by Macrophage Cells *Advanced Materials* 19 3163-6

7. Mechanistic investigations

As shown in the previous study, the GNPs produced at UNamur enhance the effectiveness of proton irradiation paving the way for a potential use as radiosensitizers in oncology. Although the influence of several parameters on this radiosensitization effect was investigated, the mechanism(s) responsible for it still remains unclear.

7.1. Physico-chemical insights

As claimed in the introduction section, the majority of published works attributed the origin of the measured enhancement to an increased absorption of ionizing radiations by nanomaterials. The difference in energy absorption between gold and the surrounding soft tissues enables a dose enhancement in cells containing GNPs. The interaction between the ionizing particles and high Z atoms leads to the emission of low-energy electrons from the nanoparticle. These electrons interact with the surrounding medium, producing ROS. Many groups have theoretically modelled this dose enhancement by dividing the process in three steps: X-ray absorption by the nanomaterial, the electron release, and the electron interaction with atoms in both nanomaterials and the surrounding medium. However, the number of experimental studies with an objective to demonstrate this remains extremely low in comparison to the number of theoretical studies. To cope with this, a chemical detection of ROS produced was used as an indirect measure of physical enhancement.

7.1.1. Investigation of ROS production upon irradiation using a radical scavenger

To assess the involvement of ROS in the radiosensitization effect, cells were pre-incubated with or without GNPs and irradiated in a medium containing 1M DMSO, a well-known hydroxyl radical scavenger. It must be noted that this high DMSO concentration does not affect the cell capacity to divide (plating efficiencies of A549 cells were 0.576 and 0.572 respectively in absence and in presence of DMSO). Results are presented in Figure 26 for lung carcinoma A549 and epidermoid carcinoma A431 cells. As already discussed in the previous manuscript, results showed the role of water radicals (indirect effect) in cell death evidenced by the increase in cell survival when DMSO was present (samples without GNPs). More interestingly, the death enhancement decreased in both cell types when DMSO was added during the irradiation (from 0.57 DEU to 0.24 DEU and from 0.69 DEU to 0.20 DEU for A549 and A431 cells respectively). This result shows that GNP enhancing effect is associated to the presence of ROS. To take this forward, we developed experimental protocols to determine which type(s) of ROS is/are produced during irradiation.

7.1.2. Determination of ROS produced during irradiation

The research in the ROS field is a challenging scientific area due to some characteristics of radicals that make them difficult to detect: their short lifetime (around μs) and the variety of antioxidants existing *in vivo*, able to scavenge these reactive species [164]. Consequently, a method for a direct ROS detection was not easy to develop, forcing us to consider an indirect detection method based on fluorescence measurements. The fluorescence methodology choice was motivated by its high sensitivity and simplicity in data collections compared to other potential techniques.

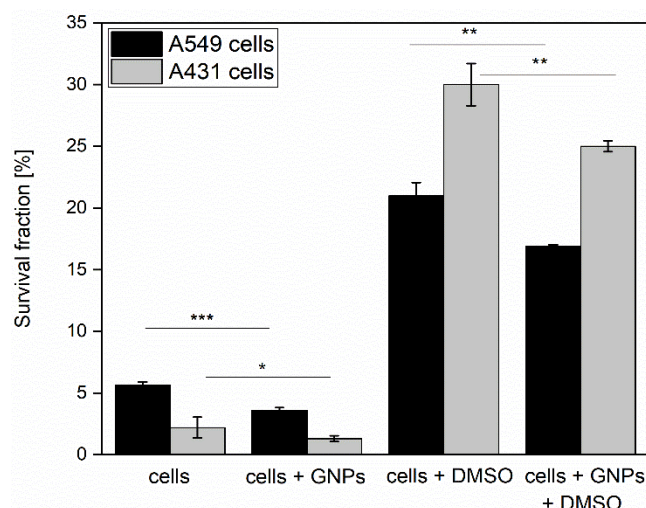


Figure 26. Survival fractions of A549 and A431 cells irradiated with $25 \text{ keV} \cdot \mu\text{m}^{-1}$ proton beam at 3 Gy. Cells were pre-incubated during 24 hours with or without 10 nm GNPs at $50 \mu\text{g} \cdot \text{ml}^{-1}$. Cells were then irradiated in the presence or absence of 1M DMSO that was added just before irradiation. Survival was assessed by conventional clonogenic assay. Results were presented as mean \pm S.D. of three independent replicates. Results were statistically analyzed using a one-way ANOVA (Tukey test, * $p < 0.05$, ** $p < 0.01$, *** $p < 0.001$).

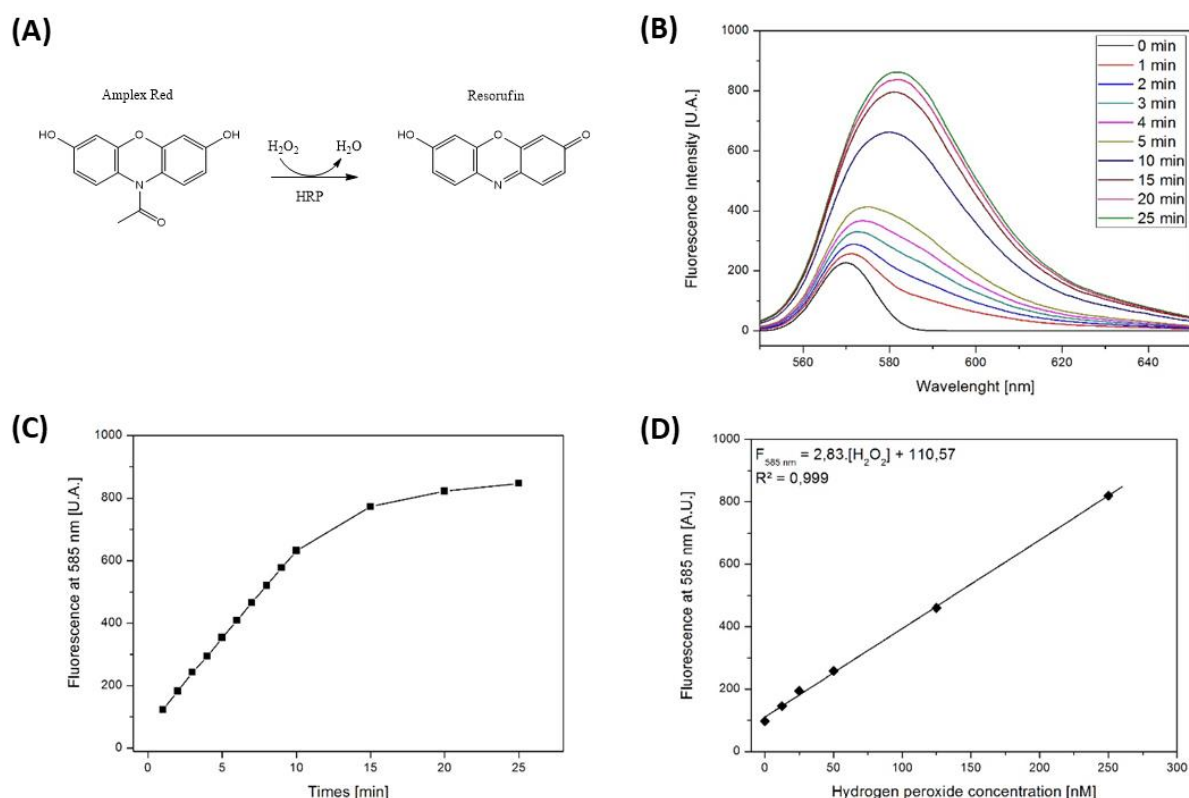


Figure 27. Validation of ThermoFisher's kit "Amplex Red Hydrogen Peroxide/Peroxidase Assay" according to manufacturer instructions (10 mM Amplex red and 10 U/mL of HRP). (A) Reaction between Amplex Red and hydrogen peroxide to form resorufin, a fluorescent molecule. (B) Fluorescence spectra obtained with 250 nM of hydrogen peroxide at different incubation times. (C) Kinetic measurement of fluorescence at 585 nm obtained with 250 nM of H_2O_2 . (D) Calibration curve of fluorescence at 585 nm over the hydrogen peroxide concentration after 30 min of incubation.

We used a non-fluorescent molecule (referred as “probe”) which has the ability to react specifically (or with a high selectivity) with a ROS of interest to form a stable, long-lived fluorescent product. Moreover, the detection was performed in a simple colloidal system instead of in biological environment to overcome constraints such as competition in ROS detection due to the presence of antioxidants or ROS generation via Fenton-type reactions. In practical terms, homemade irradiation chambers were filled with phosphate buffer pH 7 containing just the probe specific of the ROS of interest (control sample) or buffer containing this probe and GNPs (GNPs sample). After proton irradiation, fluorescence was assessed using a spectrophotometer. The influence of different physico-chemical parameters (such as dose⁸ and dose rate) on radical production was investigated. In the frame of this thesis, we evidenced the production of two different ROS during irradiation: hydrogen peroxide (H₂O₂) and hydroxyl radical (°OH).

Detection of hydrogen peroxide

N-Acetyl-3,7-dihydroxyphenoxazine (Amplex Red) is a non-fluorescent molecule that, when oxidized by hydrogen peroxide in the presence of horseradish peroxidase (HRP), produces resorufin, a fluorescent product (Figure 27A). Resorufin has excitation and emission maxima at 571 nm and 585 nm respectively, and a high extinction coefficient: $58,000 \pm 5,000 \text{ cm}^{-1}\text{M}^{-1}$. In order to detect hydrogen peroxide produced during the irradiation, we used the Amplex Red Hydrogen Peroxide/Peroxidase Assay kit from ThermoFisher Scientific. By following the protocol of the manufacturer, we determined the optimal conditions for the detection of H₂O₂ in colloidal system (GNPs suspension in buffer). In order to do that, the working reagent was mixed with 250 nM of standard H₂O₂ and a fluorescence spectra was registered every minute. As shown in Figure 27B, a bathochromic shift of the maximal emission to 585 nm was observed due to the increasing detection of H₂O₂. The kinetic of this detection system shows a linear behavior prior to reach a plateau after 30 minutes of incubation (Figure 27C). For the further irradiation experiments, we decided to fix the incubation time between Amplex Red dye and hydrogen peroxide at 30 minutes. This time lapse enables to perform multiple sample irradiations in a single run as well as to ensure reproducible measures since this timing corresponds to a plateau in the detection kinetic. Moreover, fluorescence spectra were also determined for increasing amounts of hydrogen peroxide, evidencing a linear behavior between fluorescence at 585 nm and hydrogen peroxide concentration in solution (Figure 27D). The method could detect concentration as little as 12 nM. Finally, the high selectivity of the method was demonstrated by the addition of sodium pyruvate 25 μM , a H₂O₂ scavenger, which completely prevented the increase in absorption at 525 nm when H₂O₂ at 250 nM was added (data not shown).

To determine whether hydrogen peroxide is produced during proton irradiation, we mixed a NP colloidal suspension with the reagent (50:50 v/v) and placed this solution in homemade irradiation chambers. As shown in Figure 28A-B, an increase in the fluorescence intensity at 585 nm ($F_{585 \text{ nm}}$), fingerprint of a H₂O₂ production, was observed after irradiation in control buffer and colloidal samples. These results demonstrated that proton-matter interaction led to water radiolysis and so to the production of hydrogen peroxide.

⁸ In these experiences, the dose reported is a “cell equivalent dose” in order to enable a comparison between these results and the ones obtained with cells.

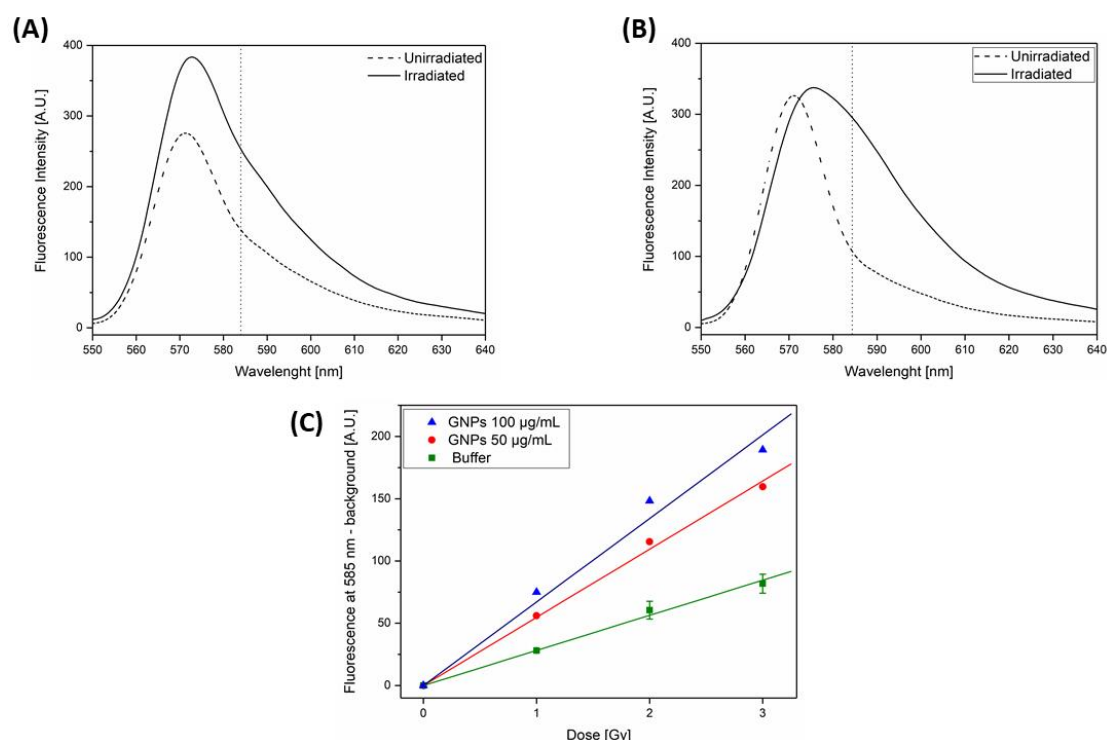


Figure 28. H_2O_2 production after 25 keV/ μm proton irradiation (3Gy/min). Fluorescence spectra of (A) buffer control sample and (B) GNP sample 30 minutes post-irradiation. Dashed and solid lines represent respectively non-irradiated control and irradiated samples. Dot lines indicate the 585 nm wavelength. (C) Fluorescence intensity depending on the radiation dose for 100 $\mu\text{g/mL}$ GNPs (\blacktriangle), 50 $\mu\text{g/mL}$ GNPs (\bullet) and buffer control samples (\blacksquare). Fluorescence intensity of unirradiated samples was subtracted from fluorescence of irradiated ones.

As shown in Figure 28C, the H_2O_2 production was dose- and concentration-dependent. These dependences could be explained by the increasing probability of the encounter between protons and nanoparticles when the GNP concentration and the number of projectiles increase. From these curves, we calculated a 0.94 and 1.38 DEU in the H_2O_2 production when 50 $\mu\text{g/mL}$ and 100 $\mu\text{g/mL}$ 10 nm GNPs are irradiated respectively. These results suggest that the hydrogen peroxide production was doubled during colloidal suspension irradiation in comparison to the same solution without GNPs.

Detection of hydroxyl radical

In the case of $^{\circ}\text{OH}$, no commercial detection kit was available. This forced us to develop our own method. It is well known that hydroxylation of aromatic rings produced phenolic moieties that possess fluorescent properties. A wide variety of aromatic compounds have been reported to react with $^{\circ}\text{OH}$ including terephthalate, benzoic acid, p-chlorobenzoic acid and benzene [165]. Among all these potential aromatic probes, we chose the coumarin backbone. Reaction of coumarin with $^{\circ}\text{OH}$ forms a set of hydroxylated products for which the fluorescence yield strongly depends on the site of hydroxylation on the aromatic ring. The major fluorescent product of hydroxylation of coumarin is the 7-hydroxycoumarin (umbelliferone), characterized by a high quantum yield [166]. To improve our chance to detect $^{\circ}\text{OH}$, we derivated coumarin by using the coumarin-3-carboxylic acid (3-CCA) as the probe. This substitution of hydrogen by a carboxylic group offers a double advantage. First, it avoids hydroxylation in position 3 and so the formation of a non-fluorescent product. Secondly, it increases the fluorescence of 7-hydroxylated coumarin derivative by two fold compared to umbelliferone [167].

The 7-hydroxy-3-CCA has excitation and emission maxima at 390 nm and 450 nm, respectively. In order to validate the detection method, a chemical induction of $^{\circ}\text{OH}$ was performed using a mixture of ascorbic acid (ASC) and Cu^{2+} ions as described in [168]. Without detailing all reactions, a mixture of ASC and Cu^{2+} can produce significant amount of $^{\circ}\text{OH}$ and H_2O_2 , after 9 successive chemical reactions. Fluorescence spectra were registered over the time, evidencing the apparition of a peak at 445 nm which corresponds to the fluorescence of hydroxylated coumarin products (Figure 29B). By evaluating this increase through the time, we observed a linear behavior prior to reach a plateau, as illustrated in Figure 29C. We observed that the time to reach it depends on the amount of radicals produced as suggested by the set of ASC concentrations tested. For the further irradiation experiments, we decided to fix the incubation time at 30 minutes. Finally, we evidenced that fluorescence intensity after a 30 min incubation was proportional to the $^{\circ}\text{OH}$ concentration in solution (Figure 29D). Selectivity of the detection method for hydroxyl radical was demonstrated by absence of signal when DMSO, a $^{\circ}\text{OH}$ scavenger, was present. Moreover, no significant increase in fluorescence was observed when the probe was oxidized by H_2O_2 instead of $^{\circ}\text{OH}$ (Figure 29D). To determine whether $^{\circ}\text{OH}$ is produced during proton irradiation, we mixed a NP colloidal suspension with 3-CCA (50:50 v: v) and placed this solution in homemade irradiation chambers. As shown in Figure 30A, an increase in the fluorescence intensity at 445 nm ($F_{445 \text{ nm}}$), fingerprint of a hydroxyl radical production, was observed after irradiation in control buffer and colloidal samples.

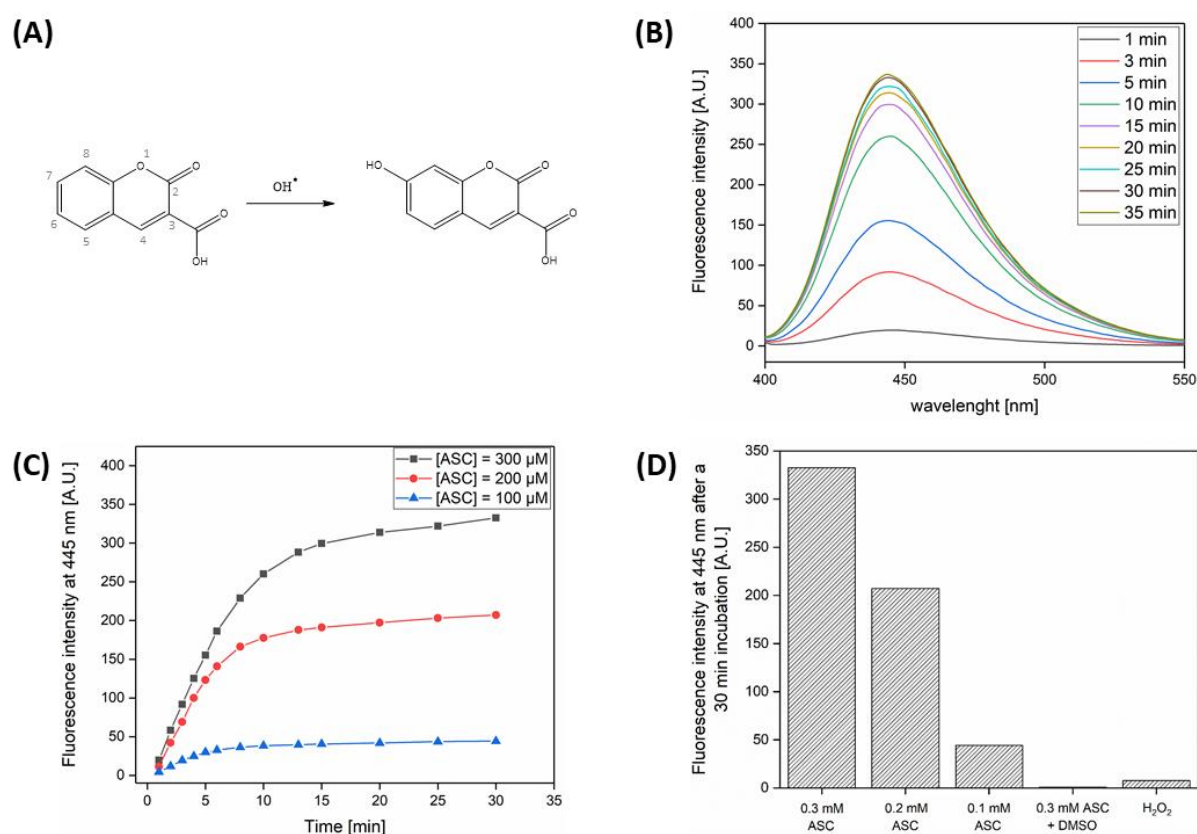


Figure 29. Validation of hydroxyl radical detection test. (A) Hydroxylation of 3-CCA leading to 7-hydroxy-3-CCA, one of the fluorescent products detected in the test. (B) Fluorescence spectra obtained by reaction of 0.1 mM 3-CCA with $^{\circ}\text{OH}$ inducer solution (0.3 mM ASC and 0.1 mM CuSO_4) at different incubation times. (C) Kinetic measurement of fluorescence intensity at 445 nm obtained with a set of ascorbic acid concentrations. (D) Fluorescence intensity at 445 nm in different experimental conditions after a 30 min incubation.

As reported for H_2O_2 measurement, we observed a linear relationship between the radical production and the radiation dose deposited in the solution. Moreover, we also observed that the presence of GNPs increased the water radiolysis compared to buffer sample (a 1.44 DEU in the $^{\circ}\text{OH}$ production was reported). The influence of dose rate on the radical production was also investigated, evidencing a decrease with dose rates over the range studied as illustrated in Figure 30C. However, this decrease was only significant ($p < 0.05$) for GNP samples irradiated at 3 and 6 Gy/min. Although this decrease in radical production when dose rate increased was previously reported by several groups working on X-ray irradiation [166, 169], we cannot exclude the possibility that it could result in an artefact caused by the experimental setup. When dose rate increases, the dose is delivered in short irradiation time. In an irradiation setup like the one used here, the proton energy is fixed which means that an increase in dose rate corresponds to a direct increase in the fluence. This induces an increase in the number of ROS formation area leading to a higher encounter probability between two ROS. This enables reactions between ROS to form other ones, which are not detected by the probe. It is the case for hydroxyl radicals that can react together to form hydrogen peroxide, which is not detected by this method. Thereby, the decrease in fluorescence that we observed when dose rate increased can be caused by a competitive reaction of $^{\circ}\text{OH}$ with the probe and with other radicals.

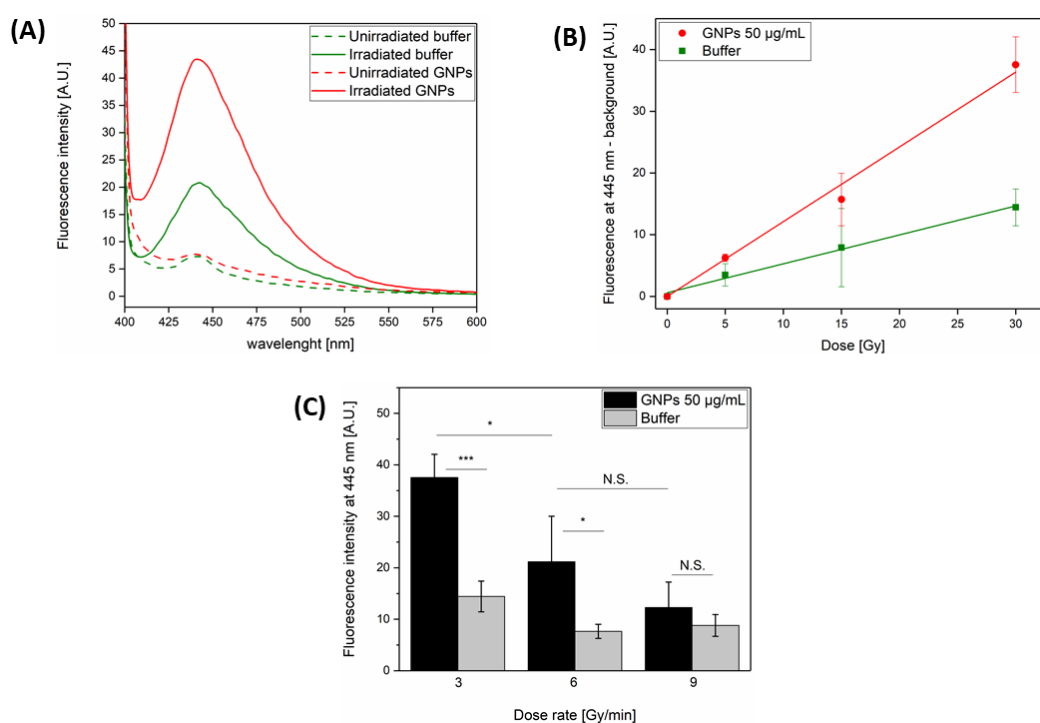


Figure 30. $^{\circ}\text{OH}$ production after 25 keV/ μm proton irradiation. (A) Fluorescence spectra of buffer control samples (green lines) and GNP samples (red lines) 30 minutes after irradiation. Dashed and solid lines represent respectively unirradiated controls and irradiated samples. (B) Fluorescence intensity depending on the radiation dose delivered at 3 Gy/min in solution containing 50 $\mu\text{g/mL}$ GNPs (●) or just buffer (■). Fluorescence intensity of unirradiated samples was subtracted from fluorescence of irradiated one. (C) Fluorescence intensity obtained in colloidal solution and buffer solution exposed to 30 Gy at different dose rates. Fluorescence intensity of unirradiated samples was subtracted from fluorescence of irradiated one. Results were analyzed via a one-way ANOVA (Tukey test, * $p < 0.05$, *** $p < 0.001$, N.S. not significant).

7.2. Biological insights

7.2.1. Context and goal of this study

When we started this study in 2016, mechanistic studies on radiosensitization effects focused on physico-chemical insights. This subject was approached from different angles by both experimental works (mainly via radical production [169, 170] and electron emission [171] measurements) and simulation studies (encounter probability estimation [104], microdosimetry calculation [172], ...). However, there are plenty of studies where an agreement was not reached between theoretically predicted and experimentally measured enhancement values, as discussed in the introduction. For example, Roa et al. [173] investigated the radiosensitization effect of GNPs in prostate cancer cells. Based on their uptake data, they predict a physical enhancement less than 0.07 DEU after irradiation with a 2 MeV X-rays. However, they reported an experimental enhancement between 0.5 and 1.0 DEU. This study is one of the various works which evidence that physical enhancement theory does not seem to be solely responsible for the measured enhancement. To cope with this issue, we wanted to investigate other ways to explain the GNP-induced radiosensitization process. A decision was made to focus on a potential biological response by studying the nanoparticle–cell interactions without any radiations. The aim of this work was to understand whether GNPs can disrupt the cell functioning making them more vulnerable to death. To do so, we only used the 10 nm GNPs due to their higher response to radiation (reported in the first manuscript) and the human lung carcinoma A549 cell line.

In the manuscript entitled “The role of thioredoxin reductase in radiosensitization effect of gold nanoparticles”, we demonstrated that experimental incubation conditions enable an efficient GNP internalization in this cell model as well as an enhancement of cell death using both X-ray and proton irradiation. In a second part, the impact of the GNP cell uptake on some biological pathways was assessed leading to the identification of a potential GNP target: the thioredoxin reductase (TrxR). The ability of GNPs to disrupt this enzyme activity was studied as well as the link between TrxR activity and response to radiation. All these results highlight a new biological mechanism responsible for the radiosensitization effect of GNPs

In the third manuscript entitled “Thioredoxin reductase activity predicts gold nanoparticle radiosensitization effect”, we checked whether the suggested mechanism has a “universal” character or not by studying it in a set of other cell lines. In practical terms, we assessed the gold content, the TrxR activity level and the radiosensitization effect in four other cell types. All these results demonstrated correlations between NP uptake, TrxR inhibition and radiosensitization effects.

7.2.2. Second manuscript: “The role of thioredoxin reductase in radiosensitization effect of gold nanoparticles” – Nanomedicine (2018)

Research Article

For reprint orders, please contact: reprints@futuremedicine.com

Nanomedicine



The role of thioredoxin reductase in gold nanoparticle radiosensitization effects

Sébastien Penninckx^{*1}, Anne-Catherine Heuskin¹, Carine Michiels² & Stéphane Lucas¹

¹Research Center for the Physics of Matter & Radiation (PMR-LARN), Namur Research Institute for Life Sciences (NARILIS), University of Namur, Rue de Bruxelles, 61, B-5000 Namur, Belgium

²Unité de Recherche en Biologie Cellulaire (URBC), Namur Research Institute for Life Sciences (NARILIS), University of Namur, Rue de Bruxelles 61, B-5000 Namur, Belgium

*Author for correspondence: sebastien.penninckx@unamur.be

Aim: To identify new mechanisms responsible for the radiosensitization effect of gold nanoparticles (GNPs). **Materials & methods:** A549 lung carcinoma cells were incubated with 10-nm GNPs during 6 or 24 h before to be exposed to 25 keV/μm protons or 225 kV x-rays. **Results:** GNP incubation led to a time-dependent mitochondria membrane depolarization, oxidative stress and to x-ray and proton radiosensitization. Moreover, a marked inhibition of thioredoxin reductase was observed. Irradiation of cells invalidated for thioredoxin reductase evidenced a radiosensitization effect, suggesting that this enzyme is a potential GNP target. **Conclusion:** We suggest that GNPs play a radiosensitizer role by weakening detoxification systems. Altogether, these results open up promising novel strategies for the development of nanotechnologies associated to radiotherapy.

First draft submitted: 15 May 2018; Accepted for publication: 5 September 2018; Published online: 14 November 2018

Keywords: biological mechanism • gold nanoparticles • proton irradiation • radiosensitization • thioredoxin reductase

Over the last decade, radiotherapy has been the main treatment modality used against cancer [1]. Although a great deal of effort has been devoted to this matter, radiotherapy is still limited by side effects caused to healthy tissues surrounding the tumor. One of the current challenges is to find new approaches that would maximize the differential response between the radiation dose deposited in the tumor and in normal healthy tissues (the so-called 'therapeutic ratio'). In this way, the research on optimized treatment modalities, such as intensity-modulated radiation therapy and hadrontherapy, is growing worldwide. Hadrontherapy is an emerging radiation treatment that uses charged particles like protons (as suggested by Wilson in 1946 [2]) instead of conventional x-ray photons. The major advantage of using these charged particles is a better spatial distribution of the absorbed dose. Indeed, the maximum energy deposition occurs at an adjustable selected depth (Bragg peak) and the beam can be scanned laterally to conform with the tumor 3D volume [3]. These unique properties ensure a more effective tumor targeting.

In the meantime, the development of nanomedicine offers the possibility to take advantage of nanoscale materials for diagnosis and therapeutic applications [4–7], including radiotherapy. In the pioneering work of Hainfeld *et al.*, injections of 1.9-nm gold nanoparticles (GNPs) showed an increase in the survival of tumor-bearing mice in combination with 250 kVp x-rays compared with x-rays alone [8]. Up to now, many *in vitro* [9–14] and *in vivo* studies [8,12–15] have evidenced the ability of high-atomic number nanoparticles, injected into the tumor, to amplify the x-ray radiation treatment efficiency. The potential use of these nano-objects enables to decrease the radiation dose, thereby reducing the risk to damage normal tissues. GNPs have been extensively studied due to their high absorption coefficient, good biocompatibility [16] and their ability to improve the performance of MRI diagnosis [17]. Their radiosensitization effect has been demonstrated for a variety of different cell lines [18] including colon [19,20], breast [21,22], prostate [23–25], brain [14,21,26] and bladder [9] cancer cell lines using radiation ranging from kV [23,24,26] to 9 MV [20] x-ray and charged particles [9,10,27]. Preclinical studies have reported that large GNP sizes (typically above 50 nm) could be trapped by the reticuloendothelial system leading to lower tumor uptake and accumulation in the liver and spleen [28,29]. To cope with this limitation, small size gold nanoclusters (GNCs) have been designed

Future
Medicine

Research Article Penninckx, Heuskin, Michiels & Lucas

to escape reticuloendothelial system absorption and the renal clearance barrier [15,30,31]. Indeed, Zhang *et al.* [15] demonstrated that intraperitoneal injection of sub-2-nm GNCs in mice enables a high selective tumor uptake. Moreover, they reported a strong radiosensitization effect after γ -ray irradiation even though the tumor uptake was at the ppm level, which is extremely low compared with *in vivo* GNP experiments [32].

Despite strong interest in these investigations, the mechanism(s) responsible for the radiosensitization effect of GNPs remains poorly understood, yet a mandatory step toward the clinical use of gold radiosensitizers. The present work aims at shedding light on mechanisms responsible for the radiosensitization effect of GNPs in combination with protons and x-rays. In this work, we focused on the effect of homemade 10-nm amino-PEG-functionalized GNPs on human lung carcinoma A549 cells. We evidenced cellular dysfunctions caused by the GNP internalization, suggesting a biological mechanism associated to the radiosensitization effect. The rationalization of these cellular dysfunctions enabled to identify a new potential biological target of GNPs: the thioredoxin reductase (TrxR) enzyme.

Materials & methods

Cell culture

Human lung carcinoma A549 cells were grown in Eagle's Minimum Essential Medium (MEM Glutamax; Gibco® by Life Technologies, MA, USA) supplemented with 10% (v/v) fetal bovine serum (FBS; Gibco by Life Technologies, MA, USA) at 37°C in a humidified atmosphere incubator containing 5% CO₂.

GNP synthesis & characterization

The 10 nm amine-PEG-functionalized GNPs were synthesized via a method described in [33]. Briefly, HAuCl₄ (Sigma-Aldrich, Overijse, Belgium) and TA-PEG₅₅₀-OCH₃ (Biochempeg Scientific, Inc., MA, USA) were mixed at a 2000:1 Au:PEG molar ratio in deionized water and stirred at room temperature for 1 h. NABH₄ (Sigma-Aldrich) was then added to the mixture under vigorous stirring and the solution was left stirring during 3 h. Then, TA-PEG₄₀₀-NH₂ (Biochempeg Scientific, Inc.) and NABH₄ were added to the solution for extra passivation. After 3 h of stirring, the colloidal suspension was purified with a membrane filtration device (Vivaspin, Millipore, Belgium).

GNPs were lyophilized with a freeze-drying system (Alpha 2–4 LD Plus; Analis, Belgium) and stored at 4°C for further use as in [10]. Prior to incubation with cells, the lyophilized GNPs were resuspended in cell medium and sonicated for 15 min. In all the experiments of this study, the cells were incubated with 50 μ g of gold per ml of medium, which corresponds to 8.22 nM of GNPs. The transmission electron microscopy (TEM) study was performed with an FEI Tecnai 10 instrument (100 kV). A drop of the sample was deposited on a holey carbon film-coated copper grid (Formvar/Carbon 200 mesh, Copper, TED Pella, CA, USA).

GNP localization using confocal microscopy

50,000 cells were seeded in 24-well plates containing coverslips (13-mm cover glasses; VWR, Belgium). After a 24-h incubation at 37°C, the medium was replaced for MEM supplemented with 10% FBS and 50 μ g Au.ml⁻¹ GNPs. Cells incubated without GNPs were used as a control. After a 24 h incubation, the cells were fixed for 10 min with 4% paraformaldehyde (Merck Chemicals, Belgium) and washed with phosphate-buffered saline (PBS) three-times. The nuclei and F-actin were stained with Hoechst 33258 (Molecular Probes™ by Life Technologies) and Alexa Fluor® 555 Phalloidin (Molecular Probes by Life Technologies), respectively. Cells were then washed three-times with PBS. After that, the coverslips were mounted in Mowiol (Sigma-Aldrich) and observed with a Leica SP5 confocal-inverted microscope. The fluorescence signal of dyes associated to the nuclei and F-actin were detected using, respectively, a 405-nm UV laser and a 561-nm laser. Additionally, a 514-nm laser was used to detect the presence of GNPs, using surface plasmon resonance as described in [34]. Optical stacks of 0.5 μ m were taken through the cells in order to accurately localize the GNPs in the cytoplasm.

GNP internalization

5×10^4 cells were seeded as 50 μ l drops in 24-well plates, in order to mimic the irradiation condition before to be placed in an incubator at 37°C with 5% CO₂. 2 h after seeding, the wells were filled with MEM + 10% FBS and placed in the incubator overnight. The medium was then removed, the wells were filled with MEM + 10% FBS without (control cells) or with 50 μ g Au.ml⁻¹ of GNPs and incubated at 37°C. After a given incubation time, the cells were detached using 0.25% trypsin. They were pelleted by centrifugation (1000 rpm, 5 min, 4°C) and the

media were discarded. The pellet was resuspended in 500 μl of PBS and side-scattered (SSC) light was analyzed immediately using a FACS Calibur flow Cytometer (BD Biosciences, NJ, USA). 20,000 cells were analyzed per sample using Cell Quest Pro Software (BD Biosciences).

Gold content quantification was performed by atomic absorption spectroscopy. After a 24-h incubation with GNPs, the cells were washed twice with PBS at 37°C and then trypsinized. Detached cells were then washed twice with culture medium by successive centrifugation. The actual number of cells in each sample was then determined using a cell counter (Countess Automated Cell Counter, Invitrogen, CA, USA). After the third centrifugation, the medium was discarded, and the pellets were digested using 2 ml of aqua regia (37% HCl, 65% HNO₃ Sigma–Aldrich) overnight. The samples' gold content was quantified using an atomic absorption spectrophotometer (AA-7000F from Shimadzu, Japan) by plotting the calibration curve with known concentrations of a gold standard solution (Merck Chemicals, Belgium) used for external calibration. Triplicate readings were analyzed for each sample. The amount of gold detected in the cells was expressed as an internalized gold quantity (pg) per cell.

Proton beam irradiation

The detailed protocols can be found in [35]. Briefly, 48 h before irradiation, 5×10^4 cells were seeded as 32- μl drops at the center of sterilized homemade irradiation chambers, closed with a plastic cap to avoid dehydration and infection and placed in an incubator at 37°C with 5% CO₂. 2 h after seeding, MEM was added and the chambers were placed in the incubator overnight. The medium was then removed, the wells were filled with MEM + 10% FBS without (control cells) or with 50 $\mu\text{g Au.ml}^{-1}$ of GNPs and incubated at 37°C until irradiation (6 or 24 h in our experiments). Prior to irradiation, the medium was discarded from the irradiation chamber, the plastic cap was removed and a sterile cotton swab was used to take away the cells, which might have diffused outside the irradiated field. The chamber was then closed again with the plastic cap, rinsed with PBS and filled with a CO₂-independent medium (Gibco by Life Technologies). The cell monolayer was irradiated with a homogenous proton beam over 1 cm^2 , produced by a 2-MV Tandem accelerator (High Voltage Engineering Europa). The reader is referred to [36] for a thorough description of the experimental setup and irradiation procedure. Briefly, the energy of the beam was tuned in order to deliver the desired LET within the cells to be irradiated. Pristine proton peaks were extracted in air through a 1- μm silicon nitride window and the irradiation chambers were placed on a sample holder fixed at the end of the beamline. Homogeneity was achieved by defocusing the beam and checked with a passivated implanted planar silicon detector moved along the x and y directions. The dose rate was assessed every millimeter in a 1 cm^2 surface and errors were less than 5% in the cell sample region. The LET at the cell sample location was computed with a SRIM software. In this study, a 25 $\text{keV } \mu\text{m}^{-1}$ LET value (beam energy: 1.3 MeV) was chosen to obtain the maximum relative biological effectiveness for a proton beam. The dose rate was fixed to 3 Gy.min^{-1} and the dose range was chosen to cover the survival fraction down to a few percent. All doses were calculated using the classic broad beam formula:

$$D = \frac{1.6 \cdot 10^{-9} \text{ LET } \Phi}{\rho}$$

Here, the density ρ is taken as 1 g/cm^3 and Φ is the proton beam fluence. All the experiments were repeated in triplicate on separate days. All curve fittings were performed with the OriginLab® software (MA, USA). A linear-quadratic equation was used to fit clonogenic assay data:

$$SF = e^{-(\alpha D + \beta D^2)}$$

Where SF is the surviving fraction of the cells; α and β define the linear and the quadratic components, respectively, and D is the deposited dose.

x-ray irradiation

48 h before irradiation, 50,000 cells were seeded as 50 μl drops in 24-well plates and placed in an incubator at 37°C with 5% CO₂. 2 h after seeding, the wells were filled with MEM supplemented with 10% FBS and placed in the incubator overnight. The medium was then removed, the wells were filled with MEM + 10% FBS without (control cells) or with 50 $\mu\text{g Au.ml}^{-1}$ of GNPs and incubated at 37°C until irradiation (6 or 24 h in our

Research Article Penninckx, Heuskin, Michiels & Lucas

experiments). Prior to irradiation, the medium was discarded from the wells, the plate was rinsed with PBS and filled with CO₂-independent medium (Gibco by Life Technologies). The cell monolayer was irradiated with a homogenous x-ray beam produced by a X-Rad 225 XL (PXi Precision x-ray, CT, USA) at 225 kV. The dose rate was fixed to 3 Gy.min⁻¹ and the dose range was chosen to cover the survival fraction down to a few percent.

Clonogenic assay

Immediately after irradiation, the cells were detached using 0.25% trypsin and they were counted. In order to obtain countable colony numbers for different radiation doses, the cells were seeded in 6-well plates containing MEM supplemented with 10% FBS, penicillin/streptomycin and incubated at 37°C. In parallel, cells were also seeded in separate dishes at one density per dose. 2 h after seeding, they were fixed with 4% paraformaldehyde (Merck Chemicals, Belgium) for 10 min and washed with PBS three-times. The cells attached to the dish were counted manually under an optical microscope to obtain the precise number of cells seeded for each cell density and dose. 11 days postirradiation, the colonies were stained with violet crystal in 2% ethanol. The amount of visible colonies (containing 50 or more cells) was considered to represent the surviving cells, which were counted manually. The plating efficiency (PE) was determined for each irradiation dose and calculated by dividing the amount of colonies by the initial numbers of seeded cells. The surviving fraction was obtained as the PE ratio for irradiated cells to the PE for control cells. The control cells underwent every procedure except the irradiation step. At least three independent experiments were performed and the errors were evaluated as standard deviation (SD). In order to quantify the GNPs ability to enhance cell death, we calculated two indicators, the amplification factor (AF) and the sensitization enhancement ratio (SER), from the fitted surviving curves:

$$AF[\%] = \left[\frac{SF_{control}^{fitted\ curve} - SF_{GNPs}^{fitted\ curve}}{SF_{control}^{fitted\ curve}} \right] \times 100$$

$$SER = \frac{\text{Radiation dose without GNPs}}{\text{Radiation dose with GNPs}}$$

The AF indicates the enhanced proportion of dead cells in the presence of GNPs compared with irradiation alone for a given dose. On the other hand, the SER is calculated for a given biological effect, usually a 10% survival fraction.

DNA damage study

50,000 cells were seeded in 24-well plates containing coverslips (13 mm cover glasses; VWR, Belgium). After a 24 h incubation at 37°C, the medium was replaced for MEM supplemented with 10% FBS and 50 µg Au.ml⁻¹ of GNPs. Cells incubated without GNPs were used as control. After a 6 h incubation, the cells were irradiated. After different incubation time after irradiation, cells were fixed for 10 min with 4% paraformaldehyde (Merck Chemicals) and washed with PBS three-times. The nuclei were stained with To-pro (Molecular Probes by Life Technologies). 53BP1 foci were labeled using an anti-53BP1 antibody coupled to Alexa Fluor 488 (Santa Cruz Biotechnology; sc-515841, TX, USA). The cells were then washed with PBS three-times. After that, the coverslips were mounted in Mowiol (Sigma-Aldrich) and observed with a Leica SP5 confocal-inverted microscope. In order to analyze the kinetics of the DNA repair process, we introduced a mathematical model based on the one described in [37]. Readers can refer to Supplementary information (S1) for further details on the mathematical model.

Mitochondrial membrane & oxidative stress measurement

5×10^4 cells were seeded as 50 µl drops in 24-well plates in order to mimic the irradiation condition before to be placed in an incubator at 37°C with 5% CO₂. 2 h after seeding, the wells were filled with MEM + 10% FBS and placed in the incubator overnight. The medium was then removed, the wells were filled with MEM + 10% FBS without (control cells) or with 50 µg Au.ml⁻¹ of GNPs and incubated at 37°C. After a given incubation time, the cells were detached using 0.25% trypsin. They were pelleted by centrifugation (1000 rpm, 5 min, 4°C) and the medium was discarded. The pellet was resuspended and incubated during 20 min at 37°C in 500 µl of 100 nM

tetramethylrhodamine ethyl ester perchlorate (Sigma–Aldrich) in MEM or in 10 μM 5-(6)-chloromethyl-2'-7'-dichlorodihydro-fluorescein diacetate (ThermoFisher, MA, USA) in HBSS (Gibco by Life Technologies, MA, USA) for, respectively, mitochondrial membrane potential and oxidative stress measurement. The cells were then pelleted by centrifugation (1000 rpm, 5 min, 4°C) and the medium was discarded. The pellet was resuspended in 500 μl of PBS and the fluorescence was analyzed immediately with a FACS Calibur flow Cytometer (BD Biosciences). 20,000 cells were analyzed per sample. The Cell Quest Pro Software (BD Biosciences, NJ, USA) was used to analyze the data.

Cell proliferation measurement

An MTS assay was used to measure the proliferation rate. 2×10^3 cells were seeded as 50 μl drops in 96-well plates and placed in an incubator at 37°C with 5% CO_2 . 2 h after seeding, the wells were filled with MEM + 10% FBS and placed in the incubator overnight. The medium was then removed, the wells were filled with MEM + 10% FBS without (control cells) or with 50 $\mu\text{g Au}\cdot\text{ml}^{-1}$ of GNPs and incubated at 37°C. After a given incubation time, the medium was discarded, the wells were rinsed with PBS and 120 μl of MEM + 10% FBS medium containing MTS (Cell Titer 96® Aqueous One Solution Reagent; Promega, WI, USA) in a 6:1 ratio was added in each well. After a 1-h incubation with an MTS tetrazolium compound, the optical density at 490 nm was determined using a spectrophotometer (X-Mark™ Microplate Spectrophotometer; Biorad, CA, USA).

TrxR activity assay

The TrxR activity was measured with a commercially available kit (Sigma–Aldrich). The kit is based on the catalytic reduction of 5,5'-dithiobis(2-nitrobenzoic) acid to 5-thio-2-nitrobenzoic acid by TrxR. This reduction generates a strong yellow colored product. Its absorbance is measurable by spectrophotometry. The cells were incubated 24 h with or without 50 $\mu\text{g Au}\cdot\text{ml}^{-1}$ of GNPs before to being detached with 0.25% trypsin. The cells were pelleted by centrifugation (1000 rpm, 5 min, 4°C) and the medium was discarded. The pellet was resuspended in a homemade lysis buffer (9% w/w sucrose; 5% v/v aprotinin [Sigma–Aldrich], in deionized water) and disrupted by a dounce homogenizer. Then, the TrxR activity was measured according to the manufacturer's instructions. The linear increase in absorbance at 412 nm was measured during 10 min using a spectrophotometer (Ultrospec 8000; GE Healthcare, IL, USA). The TrxR activity rate was calculated from the slope of absorbance at 412 nm versus time.

siRNA transfection

A549 cells were seeded at 50,000 cells/well in a 24-well plate and left 24 h in an incubator at 37°C with 5% CO_2 . The day after, the cells were transfected with 50-nM human TrxR siRNA (On-target plus Human TXNRD1 – Smart pool, Dharmacon, CO, USA) using a Dharmafect 1 (Dharmacon, CO, USA) transfection reagent according to the manufacturer's instructions. In the meantime, Risc-free siRNA (Dharmacon, CO, USA) was used as a negative control. The transfection medium was replaced after 24 h by fresh MEM culture medium supplemented with 10% FBS. The cells were then incubated for 24 h before irradiation.

Western blotting

A549 cells were scrapped in a Laemmli lysis buffer (1 M Tris-HCl pH 6.8, 10% SDS, 20% glycerol). The protein content per sample was evaluated using a nanodrop (Nanodrop 1000, ThermoScientific). The proteins were separated by electrophoresis on a 10% SDS-PAGE gel using a migration buffer (25 mM Tris-HCl, 192 mM glycine, 3.5 mM SDS) and then transferred onto a nitrocellulose membrane (Nitrocellulose membranes 0.2 μm ; BioRad, CA, USA). The membrane was blocked 1 h at room temperature in an Odyssey blocking buffer (BD Biosciences, MJ, USA) in PBS 50/50 v/v before an overnight incubation at 4°C in an Odyssey blocking buffer with 0.1% Tween containing a specific antibody: a mouse anti-TrxR monoclonal antibody (SC-28321; Santa Cruz Biotechnology, TX, USA) or a mouse anti- β -actin monoclonal antibody (A-5441; Sigma–Aldrich). After three washes of 5 min in PBS-0.1% Tween, a 1-h incubation with a goat antimouse IR Dye-labeled secondary antibody (Licor) was performed in an Odyssey blocking buffer with 0.1% Tween at room temperature. After three extra washes of 5 min in PBS-0.1% Tween and two washes in PBS, the membrane was dried at 37°C and scanned using an Odyssey infrared imaging system (Licor). Immunodetection of β -actin was used as loading control.

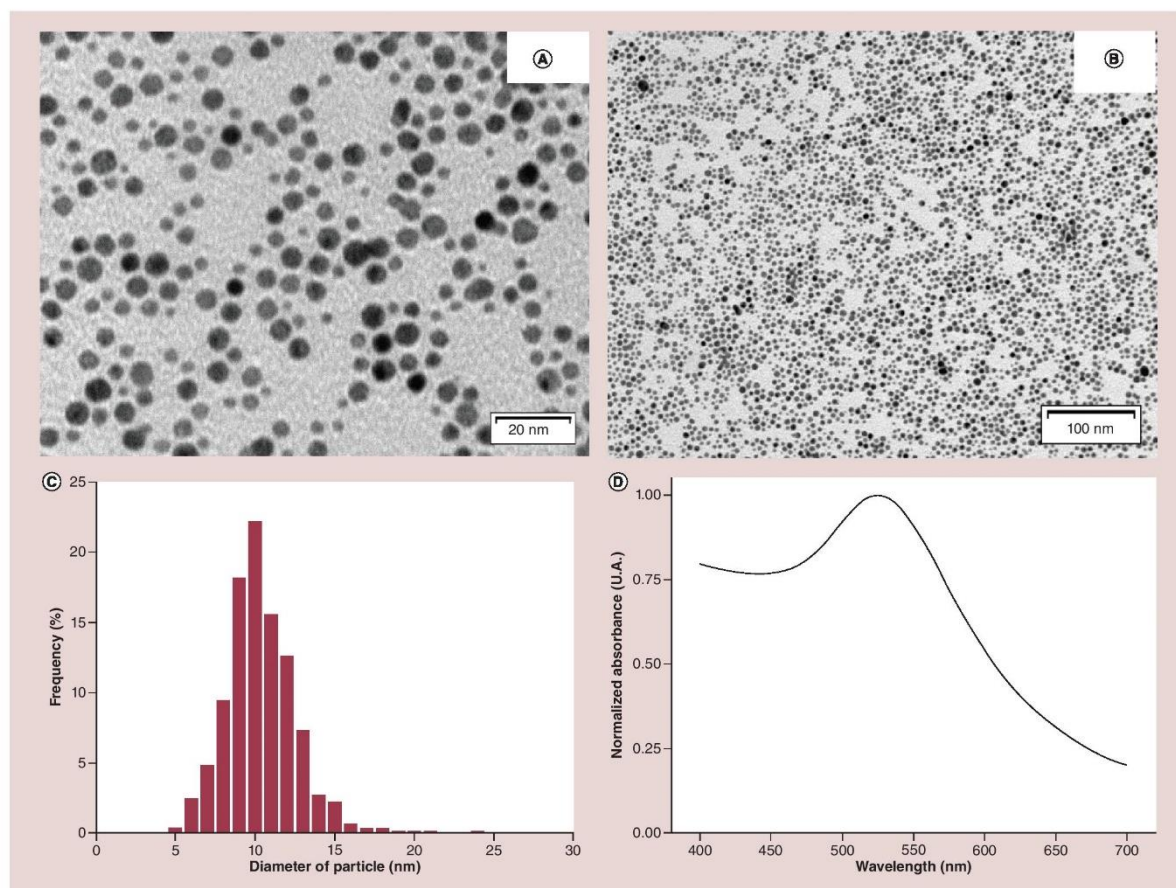


Figure 1. Characterization of amino-PEG functionalized gold nanoparticles. (A & B) Morphological images of gold nanoparticles obtained by transmission electron microscopy, scale bar: 20 (A) or 100 nm (B). **(C)** Size distribution histogram obtained by the analysis of 1000 particles on five transmission electron microscopy images taken at different magnifications. The mean diameter is 10.11 ± 0.06 nm. **(D)** UV-Vis absorption spectrum of gold nanoparticles evidencing a maximum absorption peak at 525 nm.

Statistical analysis

All experiments were repeated at least three-times on separate days. Results were reported as mean \pm corresponding SD. In addition, a one-way analysis of variance (ANOVA) was performed using Origin 8 in order to compare the differences between groups. The number of asterisks in the figures indicates the level of statistical significance as follows: * $p < 0.05$, ** $p < 0.01$, *** $p < 0.001$.

Results

GNP synthesis & characterization

The amino-PEG functionalized GNPs used in this study were prepared through a revisited Turkevich method, previously described in [33]. A ligand TA-PEG₄₀₀-NH₂ was chosen as the coating in order to increase the colloidal stability and prevent aggregation. The TEM images (Figure 1A & B) showed that the synthesized GNPs were spherical in shape and well-dispersed. An average diameter of 10.11 ± 0.06 nm was measured by analysis of 1000 particles on five TEM images taken at different magnifications (Figure 1C). Moreover, the UV-vis absorption spectrum (Figure 1D) showed a peak centered at 525 nm, corresponding to the plasmon resonance band of nanoparticles.

Cell internalization study

Preliminary cytotoxicity investigations of GNPs on A549 cells have shown no significant toxicity on a concentration range until $100 \mu\text{g} \cdot \text{ml}^{-1}$ (Supplementary Figure 2). In the frame of this work, we established that an incubation of $50 \mu\text{g} \cdot \text{Au} \cdot \text{ml}^{-1}$ of GNPs in the medium during 24 h did not generate any cytotoxicity and therefore allows internalization and irradiation experiments.

GNPs need to be internalized by cells in order to exert a potential radiosensitization effect. Hence, the intracellular localization of GNPs and their spatial distribution were investigated by confocal microscopy. This technique was used to detect both the scattered light of label-free GNPs and the fluorescence of molecular dyes used for labeling cell components. The control cells (Figure 2A) exhibited only blue and red areas corresponding, respectively, to the signal of Hoechst dye from the nucleus and Alexa Fluor Phalloidin 555 from the cytoplasm. No GNPs were observed in the control cells. The cells incubated in the presence of GNPs during 3 and 24 h exhibited some green spots in addition to the fluorescence signals from nucleus and cytoplasm (Figure 2B & C). Each of these green spots is the fingerprint of the scattered light from a GNP cluster. After a 3 h incubation (Figure 2B), GNP aggregates were mainly distributed in the close vicinity of the plasma membrane. After a 24 h incubation, GNP aggregates were localized in the cytoplasm close to the nucleus. It is notable that GNPs seem to self-agglomerate in bigger aggregates and move from the plasma membrane surface to the perinuclear region over time. In order to investigate whether GNPs were internalized into the cells or attached on the cell surface, scattered light and fluorescence images were taken at different depths, from the bottom to the top, inside one cell volume. The Z-stacks of Figure 2D show the entrapment of GNPs into red area (i.e., into the cytoplasm), confirming the internalization of GNPs into A549 cells.

In order to study the kinetic of GNP internalization, SSC light in flow cytometry was used to follow the nanoparticle uptake. As described by Toduka *et al.* [38], when nano-objects are taken up into cells, they increase the intracellular density changing the SSC intensity. As shown in Figure 2E, a quick cell uptake of GNPs was observed during the first 6 h of incubation. Afterward, a plateau was observed. One-way ANOVA analysis showed no significant difference upon longer incubation times, in other words, between 6 and 24 h of incubation ($p < 0.05$). The measured data points were fitted to one-phase exponential association curve, according to the formula:

$$Y = Y_{\max} [1 - \exp(-k \cdot t)]$$

Where Y is the SSC intensity (proportional to the uptake level), Y_{\max} is the maximal uptake level, k is the first-order rate constant in per hours and t is the incubation time of GNPs in hours. The first-order constant was determined from the fitted curve as $0.52 \pm 0.04 \text{ h}^{-1}$. These flow cytometry results are in agreement with the confocal fluorescence microscopy analyses (Figure 2) showing a larger GNP internalization after 24 h compared with a 3-h incubation.

Finally, the actual amount of GNPs internalized by A549 cells was determined by atomic absorption spectroscopy and reached $2.0 \pm 0.4 \text{ pg}$ of gold per cell after a 24-h incubation corresponding to 1.9×10^5 GNPs per cell.

Cellular impact of GNPs

In order to probe the cellular impact of GNPs, A549 cells were incubated with GNPs during varying incubation times (ranging from 0 to 24 h). At each defined incubation time, two cellular processes were investigated: oxidative stress and mitochondria homeostasis. As shown in Figure 3A and B, a significant decrease in mitochondrial membrane potential ($\Delta\psi_m$) and an increase in the reactive oxygen species (ROS) level were observed during the first 6 h of incubation in the presence of GNPs. At this time point, minimal $\Delta\psi_m$ ($77 \pm 2\%$ of control fluorescence) and the maximal ROS level (1.4 ± 0.1 -fold change) were observed. After this incubation time, a slow recovery leading to mitochondria membrane repolarization and reduction of the oxidative stress were detected until a 24-h GNP incubation. The kinetic process observed for $\Delta\psi_m$ was confirmed by ATP content measurements, which showed the same behavior according to the GNP incubation time (Supplementary Figure 3). It is interesting to note that the maximal cellular dysfunctions were measured when cell uptake reached a plateau (Figure 2E). In parallel, we observed the initiation of autophagy, which was markedly increased after a 12- and 18-h incubation but no longer after a 24 h incubation (Supplementary Figure 4). We hypothesized that the autophagy could be responsible for the elimination of dysfunctional mitochondria, hence for the cell recovery.

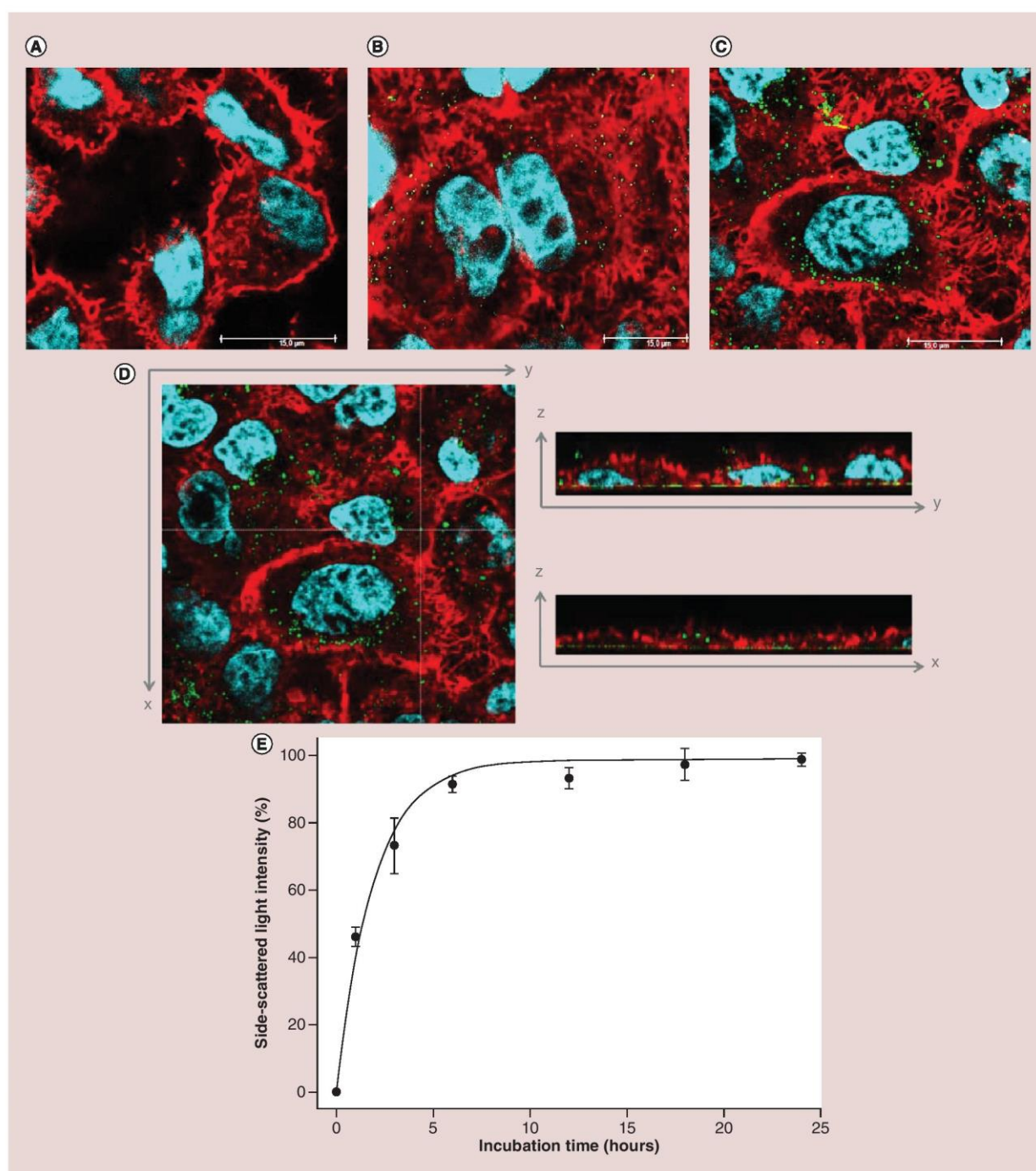


Figure 2. Gold nanoparticle uptake in A549 cells. Confocal microscopy images of gold nanoparticle intracellular localization (A) control cells free of GNPs; (B) cells preincubated with 50 $\mu\text{g Au.ml}^{-1}$ of gold nanoparticles during 3 h; (C) cells preincubated with 50 $\mu\text{g Au.ml}^{-1}$ of GNPs during 24 h, scale bar: 15 μm . (D) The Z profiles of cells (transversal view) were obtained after 24 h of incubation with 50 $\mu\text{g Au.ml}^{-1}$ of gold nanoparticles. Blue and red areas, respectively, represent the signal of Hoechst from the nucleus and Alexa Fluor® Phalloidin 555 from the cytoplasm. Green areas represent the localization of the gold nanoparticle clusters. The white dashed lines indicate the axes studied in the Z-profile images. (E) Kinetics of gold nanoparticle uptake for a concentration of 50- $\mu\text{g Au.ml}^{-1}$ of gold nanoparticles using flow cytometry. The curve is plotted as mean values relative to untreated control (sample after a 0 h incubation) \pm standard deviation of three independent experiments and nonlinear regression curve according to a one-phase exponential association curve.

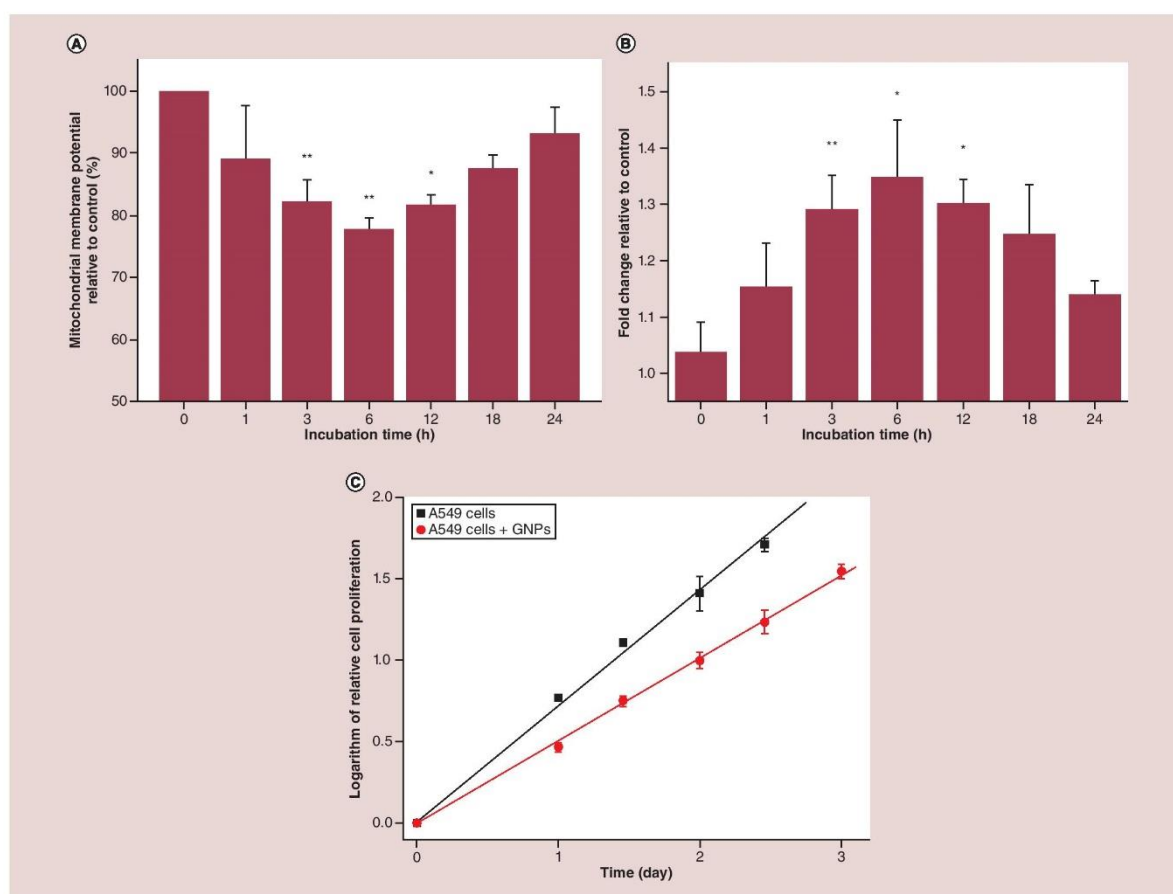


Figure 3. Gold nanoparticles cause dysfunctions in biological pathways. (A) Mitochondrial membrane potential assessed using TMRE fluorescent dye over incubation time in the presence of $50 \mu\text{g Au}\cdot\text{ml}^{-1}$ of GNPs. (B) Reactive oxygen species levels measured using the CM-H2DCFDA fluorescent dye over incubation time in the presence of $50 \mu\text{g Au}\cdot\text{ml}^{-1}$ of GNPs. TMRE (A) and CM-H2DCFDA (B) intensities are reported relative to the untreated control cells intensity (A549 cells without GNPs) for each given time post-incubation. (C) Cell proliferation of A549 cells pre-incubated during 24 h in the presence or not of $50 \mu\text{g Au}\cdot\text{ml}^{-1}$ of GNPs. All data are plotted as mean values \pm SD of at least three independent replicates. Results were statistically analyzed using a one-way ANOVA (Tukey test, * $p < 0.05$, ** $p < 0.01$).

ANOVA: Analysis of variance; CM-H2DCFDA: 5-(6)-chloromethyl-2',7'-dichlorodihydro-fluorescein diacetate; GNP: Gold nanoparticle; SD: Standard deviation; TMRE: Tetramethylrhodamine ethyl ester perchlorate.

An MTS assay was used in order to investigate the influence of GNPs on cell proliferation. It revealed that following a 24-h incubation, GNPs significantly reduced the cell proliferation rate (Figure 3C). Doubling times of $32.9 \text{ h} \pm 0.3$ and $23.2 \text{ h} \pm 0.4$ were measured in A549 cells incubated, respectively, in the presence and in the absence of GNPs.

Cell death enhancement by GNPs upon irradiation

A549 cells pre-incubated during 24 h with or without GNPs were irradiated using protons or x-rays. The cell survival was quantified by standard clonogenic assays. Dose–response curves are presented in Figure 4A. In both cases, the survival fraction exponentially decreased with increasing radiation dose. Moreover, this decrease was more pronounced when cells were pre-incubated with GNPs, evidencing a radiosensitization effect of GNPs. The cell survival (surviving fraction) curves were fitted with the linear quadratic model and the α and β values determined by the fitting procedure are reported in Table 1. Results indicated that the presence of GNPs in A549 cells induced

Research Article Penninckx, Heuskin, Michiels & Lucas

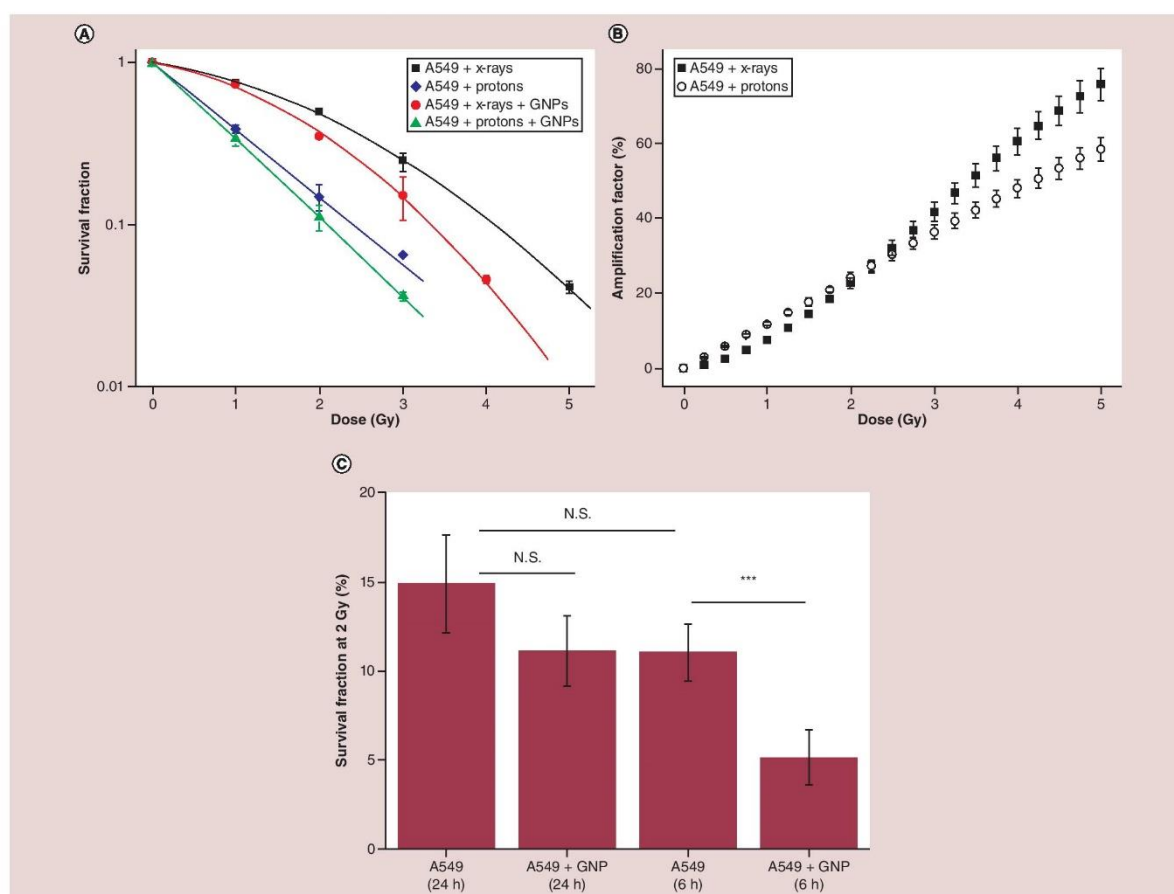


Figure 4. Irradiation experiments. (A) Survival curve of A549 cells incubated during 24 h in MEM without GNPs and irradiated by x-rays (■, black curve); without GNPs and irradiated by protons (◆, blue curve); with 50 $\mu\text{g Au.ml}^{-1}$ of GNPs and irradiated by x-rays (●, red curve); with 50 $\mu\text{g Au.ml}^{-1}$ of GNPs and irradiated by protons (▲, green curve). Results are expressed as mean values \pm SD of at least three independent experiments. (B) Amplification factors obtained from fits of survival fraction curves after 25 keV/ μm proton beam (○) or 225 kV x-rays (■). (C) Survival fraction of A549 cells incubated during 6 and 24 h with or without GNPs and exposed to 2 Gy of protons. Results are expressed as mean values \pm SD of three independent experiments. Results were statistically analyzed using a one-way ANOVA (Tukey test, N.S.: Not significant, *** $p < 0.01$).

ANOVA: Analysis of variance; GNP: Gold nanoparticle; MEM: Eagle's minimum essential medium; SD: Standard deviation.

Table 1. Calculated α , β coefficients and sensitization enhancement ratio at 10% survival for A549 cells irradiated by a 25 keV/ μm proton beam or 225 kV x-rays after being pre-incubated during 24 h with 50 $\mu\text{g Au.ml}^{-1}$ of GNPs as well as in untreated control cells (without GNPs). The α , β values are also reported for TrxR-invalidated A549.

Beam	Sample	α (Gy^{-1})	β (Gy^{-2})	SER 10%
Protons	A549	0.96 ± 0.03	–	1.14
	A549 + GNPs	1.071 ± 0.003	–	
x-ray	A549	0.18 ± 0.02	0.092 ± 0.006	1.22
	A549 + GNPs	0.21 ± 0.04	0.14 ± 0.01	
x-ray	A549 + siRF	0.22 ± 0.03	0.09 ± 0.01	1.24
	A549 + siTrxR	0.30 ± 0.06	0.13 ± 0.02	

GNP: Gold nanoparticle; RF: Risc-free; SER: Sensitization enhancement ratio; TrxR: Thioredoxin reductase.

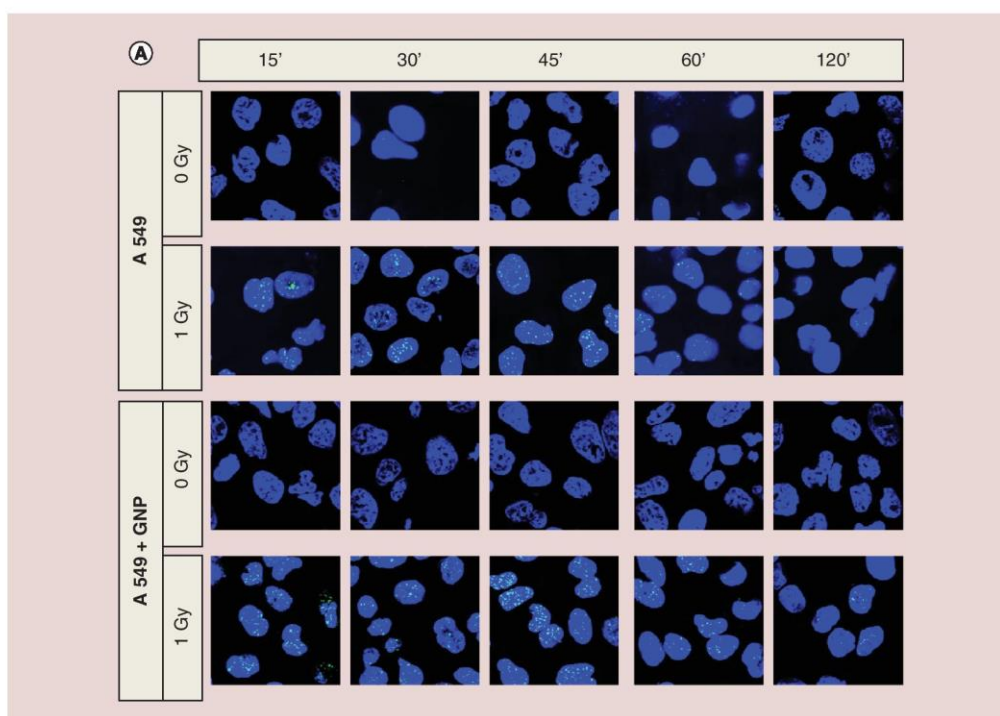


Figure 5. DNA damage study after irradiation. (A) Representative immunofluorescence labeling of 53BP1 for A549 cells pre-incubated with or without $50 \mu\text{g Au.ml}^{-1}$ GNPs. Cells were exposed to 1 Gy x-ray and fixed at different times after irradiation (0, 15, 30, 45, 60, 120, 240 min). Blue and green areas represent the signal of To-pro dye from the nucleus and 53BP1 labeling, respectively. **(B)** Quantification of the number of 53BP1 RIF in A549 without GNPs at different times after exposition. Results are plotted as mean values \pm SD. Quantification was performed on a minimum of 150 cells per condition; $n = 3$. **(C)** Quantification of the number of 53BP1 RIF in A549 cells containing GNPs at different times after exposition. Results are plotted as mean values \pm SD. Quantification was performed on a minimum of 150 cells per condition; $n = 3$. GNP: Gold nanoparticle; RIF: Radiation-induced foci; SD: Standard deviation.

a $16 \pm 3\%$ and $11.6 \pm 0.2\%$ increase in the α parameter after, respectively, x-rays and proton irradiation as well as a $52 \pm 4\%$ increase in the β parameter in case of x-rays.

The AF indicates the enhanced proportion of dead cells in the presence of GNPs compared with irradiation alone for a given dose [10]. This indicator was plotted as a function of the irradiation dose for both types of radiation (Figure 4B). This graph shows that the AF increased with the irradiation dose. At 2 Gy, a clinically relevant dose per fraction delivered to patients, a $22 \pm 1\%$ and $24 \pm 1\%$ AF was calculated from, respectively, x-rays and protons. No significant difference in the AF was reported for x-rays compared with proton irradiation at 2 Gy. Interestingly, Figure 4C shows a more pronounced radiosensitization effect, when A549 were pre-incubated with GNPs during 6 h ($\text{AF}_{2\text{Gy}} = 54\%$) compared with 24 h ($\text{AF}_{2\text{Gy}} = 24\%$). SER at 10% survival were calculated as 1.14 and 1.22 for proton and x-ray irradiation, respectively. These results demonstrate that GNPs can produce a significant increase in the cell death induced by radiation that is modulated according to the duration of the incubation time.

DNA damage repair after irradiation

In order to further examine the influence of GNPs when cells were irradiated, the level of 53BP1, a DNA double-strand break (DSBs) sensing protein [37,39] was evaluated by immunofluorescence labeling. Quantification of radiation-induced foci over post-irradiation time showed a similar profile for A549 cells pre-incubated in the presence (Figure 5C) or in the absence of GNPs (Figure 5B). Indeed, 53BP1 radiation-induced foci appeared during the first 15 min post-irradiation (1 Gy x-ray). Then, their number decreased with time. To analyze the kinetics of

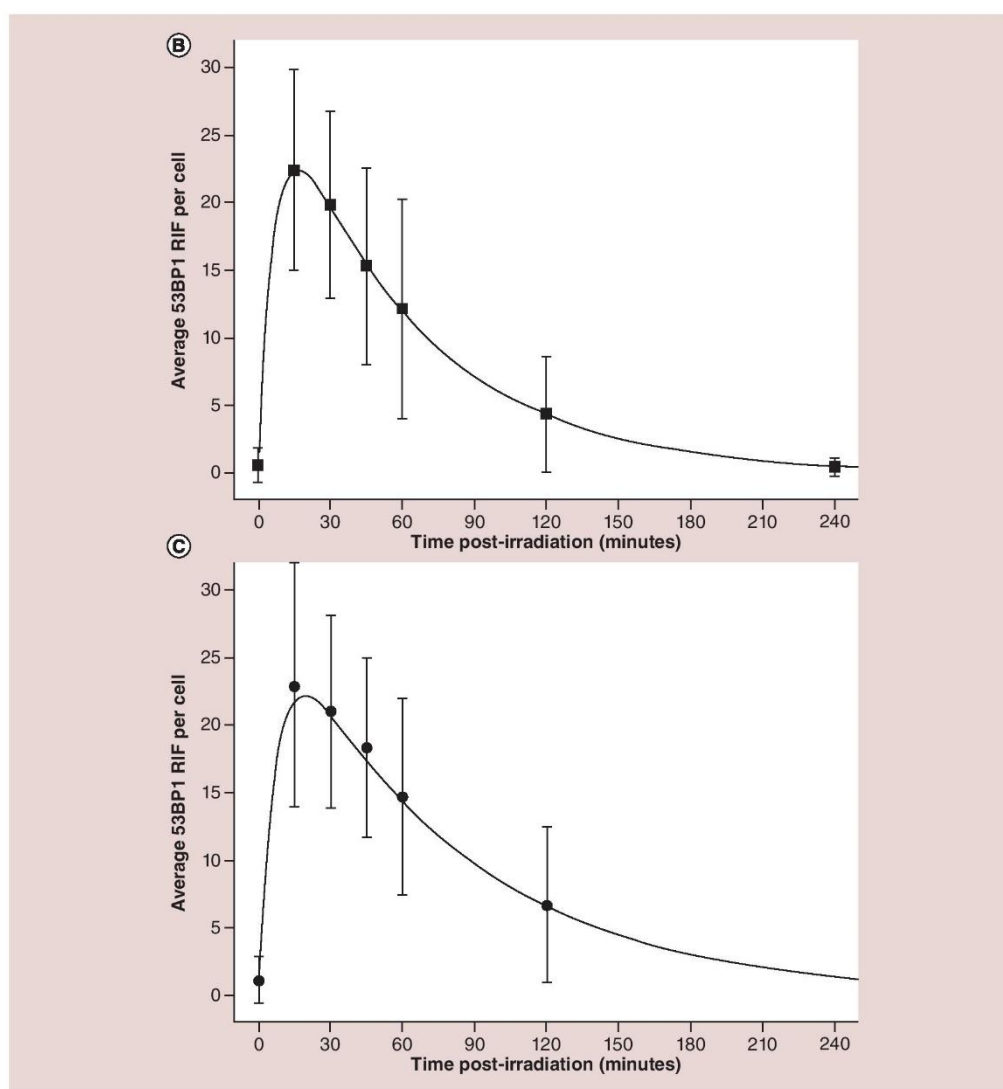


Figure 5. DNA damage study after irradiation (cont.). (A) Representative immunofluorescence labeling of 53BP1 for A549 cells pre-incubated with or without $50 \mu\text{g Au.ml}^{-1}$ GNPs. Cells were exposed to 1 Gy x-ray and fixed at different times after irradiation (0, 15, 30, 45, 60, 120, 240 min). Blue and green areas represent the signal of To-pro dye from the nucleus and 53BP1 labeling, respectively. (B) Quantification of the number of 53BP1 RIF in A549 cells without GNPs at different times after exposition. Results are plotted as mean values \pm SD. Quantification was performed on a minimum of 150 cells per condition; $n = 3$. (C) Quantification of the number of 53BP1 RIF in A549 cells containing GNPs at different times after exposition. Results are plotted as mean values \pm SD. Quantification was performed on a minimum of 150 cells per condition; $n = 3$. GNP: Gold nanoparticle; RIF: Radiation-induced foci; SD: Standard deviation.

this DNA damage repair process, experimental data were fitted using Equation 1 (see Supplementary data Equation 1) and coefficient values determined by the fitting procedure are reported in Table 2. Results indicated that the presence of GNPs in A549 cells did not influence the total number of DSBs per cell (29.4 ± 0.6 DSBs/Gy compared with 28.3 ± 0.6 DSBs/Gy for cells incubated without and with GNPs, respectively) but led to a 25% decrease in the repair process rate (k_2 coefficient).

Table 2. Fitted coefficients for A549 cells exposed to 1 Gy of 225 kV x-rays after pre-incubation during 6 h with or without 50 $\mu\text{g Au.ml}^{-1}$ of gold nanoparticles.

Sample	A (DSBs/Gy)	B (RIF)	k_1 (min^{-1})	k_2 (min^{-1})	R^2
A549	29.4 ± 0.6	0.51	0.146 ± 0.007	0.0172 ± 0.0004	0.9996
A549 + GNPs	28.3 ± 0.6	1.11	0.14 ± 0.01	0.0129 ± 0.0005	0.9990

A and B represent the total number of radiation-induced foci created per Gy of radiation and the number of radiation-induced foci detected in unirradiated control cells, respectively. k_1 and k_2 are kinetic parameters that reflect the time it takes to detect one DSB and the time it takes to repair the DSBs. R^2 is the coefficient of determination from the fitting procedure. DSB: Double-strand break; GNP: Gold nanoparticle; RIF: Radiation-induced foci.

Role of TrxR in the radiosensitization effect

In this study, TrxR was identified as a potential GNP target. The activity of this enzyme was assessed in A549 cells incubated with or without GNPs during 24 h. As shown in Figure 6A & B, a $71 \pm 2\%$ decrease in the TrxR activity was observed when cells were pre-incubated with GNPs. To distinguish whether GNPs were responsible for an enzymatic inhibition or whether they downregulated the protein expression, the amount of TrxR protein was evaluated in A549 cells after incubation with and without GNPs. As shown in Figure 6C, no significant change in the TrxR protein level was reported in these conditions.

To confirm that TrxR inhibition may lead to a radiosensitization effect, invalidation of the TrxR expression was performed using siRNA. It led to a significant decrease in the mRNA level and a residual 15% TrxR protein level, which was confirmed by an activity assay (Supplementary Figure 5). Invalidated A549 cells were irradiated without GNPs in the same aforementioned conditions, evidencing a significant radiosensitization of TrxR invalidation (Figure 6D). The α and β values were determined and are reported in Table 1. Results evidenced that cells harboring a decreased functional TrxR level underwent an increase in the β parameter upon x-ray exposure.

Discussion

Given the emerging need to improve current treatment modalities against cancer, this *in vitro* study was undertaken to investigate the impact of the combination of GNPs and proton therapy on human cancer A549 cells. The kinetics analyses of the cell uptake process showed a quick internalization of GNPs during the first 6 h of incubation followed by a plateau from a 6 to 24 h incubation. This observation was also reported by Chithrani's group where the plateau was reached at 4–7 h, depending on the particle size [40]. Moreover, these authors evidenced a size-dependent uptake half-life, with smaller GNPs taken up faster ($T_{1/2} = 2.1$ h for their 14-nm GNPs), which is in agreement with the uptake half-life calculated from our results ($T_{1/2} = 1.3$ h). This curve form suggests that the GNPs enter into cells via a receptor-mediated endocytosis mechanism due to a nonspecific adsorption of serum proteins at the nanoparticle surface. This hypothesis is supported by the presence of some protein-characteristic bands in the UV/visible spectrum of GNPs incubated in a serum-containing media [40]. On the other hand, Hühn *et al.* [41] showed differences in the internalization efficiency when incubating human umbilical vein endothelial cells with nanoparticles in a serum-free and serum-containing media. Moreover, TEM images of cells pre-incubated with GNPs evidenced the clustering of nano-objects in vesicles that could be endosomes [10].

Our work highlighted a clear radiosensitization effect with 225 kV x-ray photons and 25 keV/ μm protons enabling to eradicate about 25% more cells at 2 Gy compared with irradiation without GNPs. More interestingly, the proportion of extra dead cells reached $76 \pm 4\%$ when cells containing GNPs were exposed to 5 Gy x-ray photons. This result opens the door to clinical applications, especially in hypofractionation treatments or in stereotactic external-beam radiation therapy where high-radiation doses are used [42,43]. A limited number of works have investigated the radiosensitization effect with protons and showed contradictory results. Jaynes *et al.* showed no significant enhancement effect when RT112 cells containing 50-nm GNPs were irradiated using a 3-MeV proton beam [9]. On the other hand, by exposing DU145 cells pre-incubated with 40-nm GNPs to a clinical 160-MeV proton beam, Polf *et al.* observed a 15% enhancement in the relative biological effectiveness [25]. Furthermore, our group reported a LET-dependent radiosensitization effect when A431 cells containing 10-nm GNPs were irradiated using a 25-keV/ μm proton beam [10]. In this study, the authors reported a 10% SER of 1.14 as well as in the present study.

In spite of the growing amount of data regarding GNPs-induced radiosensitivity, the responsible mechanisms remain poorly understood. In recent years, evidences for a physicochemical mechanism are growing. The difference in energy absorption between gold and the surrounding soft tissues enables a dose enhancement in cells containing GNPs. The interaction between the ionizing particles and high Z atoms leads to the emission of low-energy electrons

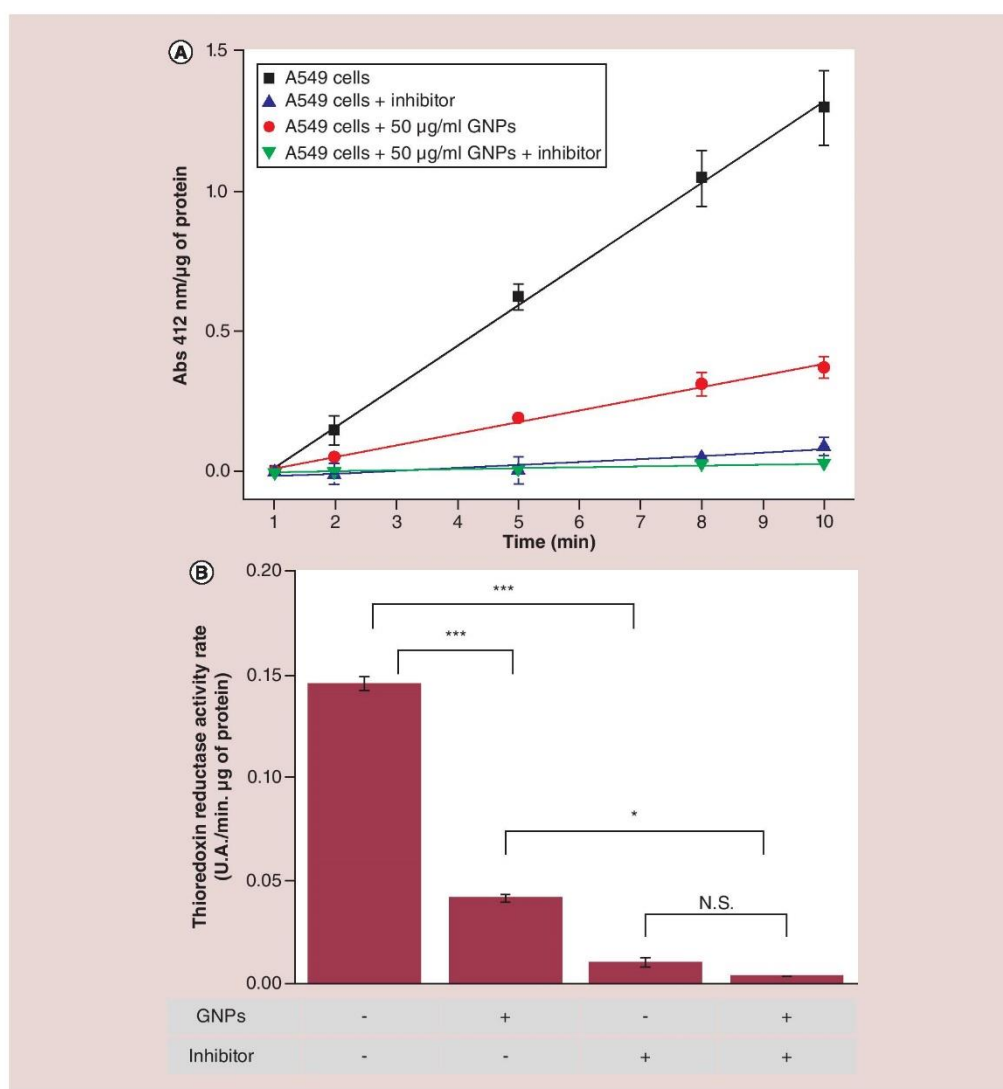


Figure 6. TrxR as a potential target of GNPs. (A) TrxR activity measurement in A549 cells pre-incubated with or without 50 $\mu\text{g Au.ml}^{-1}$ GNPs during 24 h. The activity is measured by the absorption at 412 nm over time. Data are plotted as mean values of absorbance normalized by the total protein content \pm SD of three independent experiments. **(B)** TrxR activity rate calculated from the slope of TrxR activity curves. Data are plotted as mean values \pm SD of three independent experiments. **(C)** The abundance of TrxR in A549 cells pre-incubated with or without 50 $\mu\text{g Au.ml}^{-1}$ GNPs during 24 h was detected by western blotting. β -actin was used as loading control. TrxR fluorescence intensity was quantified and normalized for β -actin. **(D)** Survival curve of invalidated A549 cells using siRF as control (■, black curve) and siTrxR (●, red curve) after 225 kV x-ray irradiation. Results are expressed as mean values \pm SD of three independent experiments. All results were statistically analyzed using a one-way ANOVA (Tukey test, * $p < 0.05$, *** $p < 0.001$, N.S.: Not significant). ANOVA: Analysis of variance; GNP: Gold nanoparticle; N.S.: Not significant; RF: Risc-free; TrxR: Thioredoxin reductase; SD: Standard deviation.

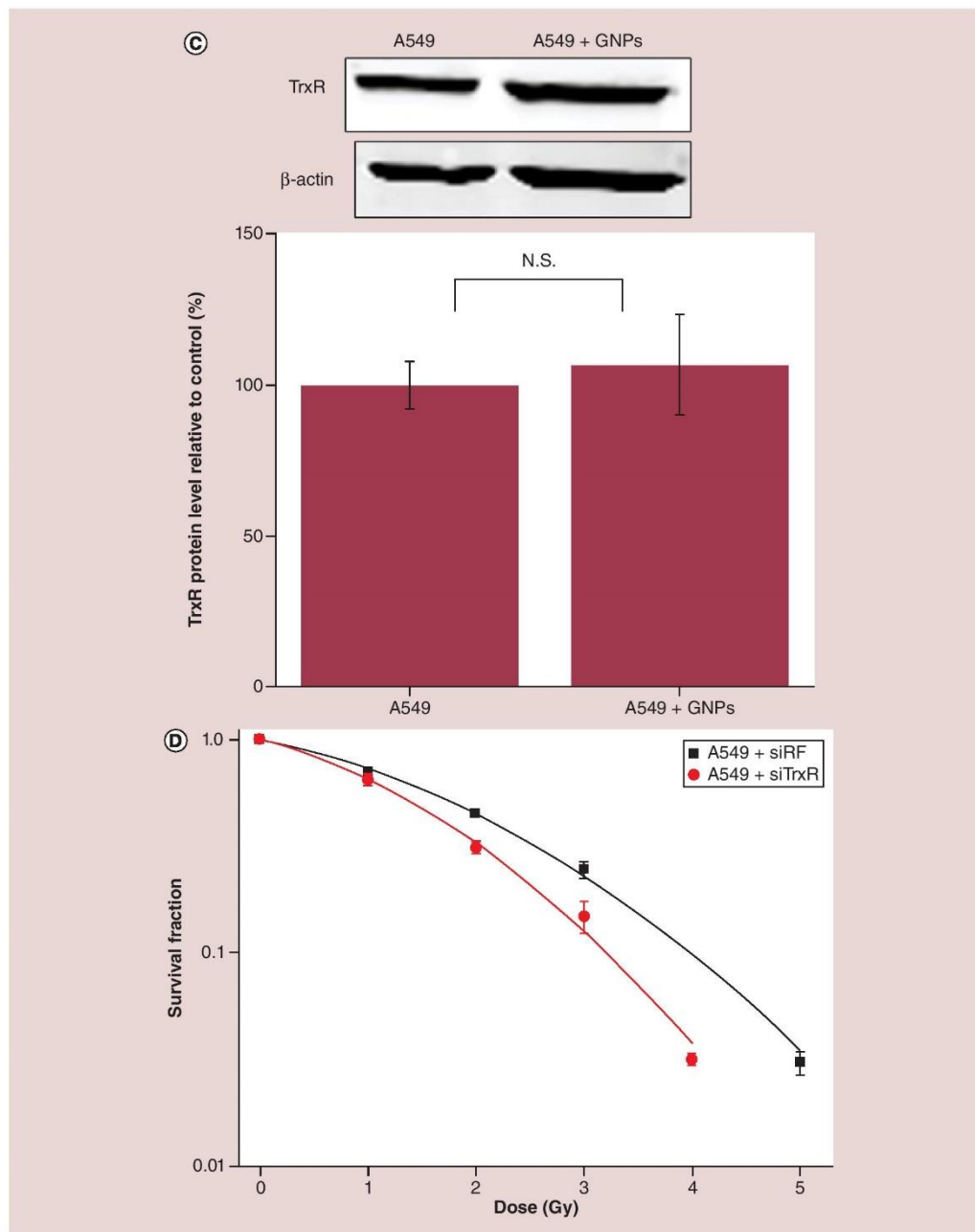


Figure 6. TrxR as a potential target of GNPs (cont.). (A) TrxR activity measurement in A549 cells pre-incubated with or without $50 \mu\text{g Au}\cdot\text{ml}^{-1}$ GNPs during 24 h. The activity is measured by the absorption at 412 nm over time. Data are plotted as mean values of absorbance normalized by the total protein content \pm SD of three independent experiments. (B) TrxR activity rate calculated from the slope of TrxR activity curves. Data are plotted as mean values \pm SD of three independent experiments. (C) The abundance of TrxR in A549 cells pre-incubated with or without $50 \mu\text{g Au}\cdot\text{ml}^{-1}$ GNPs during 24 h was detected by western blotting. β -actin was used as loading control. TrxR fluorescence intensity was quantified and normalized for β -actin. (D) Survival curve of invalidated A549 cells using siRF as control (■, black curve) and siTrxR (●, red curve) after 225 kV x-ray irradiation. Results are expressed as mean values \pm SD of three independent experiments. All results were statistically analyzed using a one-way ANOVA (Tukey test, * $p < 0.05$, *** $p < 0.001$, N.S.: Not significant). ANOVA: Analysis of variance; GNP: Gold nanoparticle; N.S.: Not significant; RF: Risc-free; TrxR: Thioredoxin reductase; SD: Standard deviation.

Research Article Penninckx, Heuskin, Michiels & Lucas

from the nanoparticle [44,45]. These electrons with an energy in the order of 100 eV interact with the surrounding medium, producing ROS. Several researchers have evidenced the production of these ROS in irradiated water solutions containing GNPs [46–48]. Misawa and Takahashi showed an increase in the production rate of hydroxyl radicals (1.46-fold) and superoxide anions (7.68-fold) in GNP solutions exposed to 100 kVp x-rays [46]. However, it seems unlikely that this mechanistic hypothesis can, on its own, explain the enhancement effect observed because it suffers from the need of a direct interaction between the incident beam and the nanoparticle. Indeed, Heuskin *et al.* recently demonstrated that the interaction probability of GNPs with the incident beam is very low when charged particles are considered [49]. Based on [10], they calculated a 10^{-6} – 10^{-5} fraction of the total nanoparticle content actually interacting per Gy of radiation. Moreover, their simulations showed no increase in neither the macroscopic nor the microscopic dose in cells. In the meantime, Sotiropoulos *et al.* [50] reached the same conclusions and suggested that other mechanisms have greater contribution than physical interaction to the radiosensitization effect. For the first time, the present study evidences a GNP incubation time-dependent radiosensitization effect. Indeed, the AF at 2 Gy was 54% after a 6 h GNP incubation compared with 24% after 24 h. This drop in GNP-induced radiosensitivity over time is not in agreement with the aforementioned physical mechanism because cell uptake measurements demonstrated no significant change in the gold content between a 6 and 24 h incubation.

All these works open the door to new mechanistic hypotheses such as a potential biochemical mechanism. This study clearly evidenced that GNPs exert significant impacts on various important biological pathways. Several groups have evidenced that exposure to nanoparticles results in the production of ROS, which is one of the main cytotoxicity mechanisms [21,23,51,52]. Moreover, oxidative stress is known to cause mitochondria dysfunction through a depolarization of the mitochondrial membrane potential [53]. Our study showed a 25% mitochondrial membrane potential depolarization leading to a significant decrease in the ATP content after 6 h of GNP incubation. These results are in agreement with the results of Prise's group who reported a cell-dependent mitochondrial oxidation after GNP incubation [21]. Moreover, surface-enhanced Raman scattering measurement of 13-nm GNPs preincubated with A549 cells revealed that GNPs are in contact with biomolecules, which can be originating from mitochondria [54]. Although this result suggests a direct physical interaction with the mitochondria, additional investigations are needed to understand the link between the GNPs inducing an increase in the ROS level and mitochondria dysfunction. An electrostatic interaction between the GNP-coating positive charge and the mitochondria lipid membrane could disrupt its membrane potential, a process known to induce cell oxidative stress. On the other hand, an increase in cytoplasmic oxidative stress could affect the mitochondria. It is interesting to note that the ROS level and the mitochondria potential are two well-known pathways implicated in the induction of cell death, especially by apoptosis [55]. Furthermore, the aforementioned biological dysfunctions are time-dependent, undergoing a partial recovery after a 24-h incubation. We propose that this could explain the difference in radiation enhancement at 6 h compared with 24 h of GNP incubation.

In view of its involvement in a variety of biological pathways, the TrxR system was suggested as an interesting target for clinical applications [56–58]. TrxR is the only known enzyme that catalyzes the reduction of oxidized thioredoxin by coupling with the oxidation of NADPH to NADP⁺ [59]. Thioredoxin (Trx) is a small protein found in all known organisms that is involved in the activity regulation of other proteins such as Trx peroxidase (which breaks down cytoplasmic H₂O₂ to H₂O) or ribonucleotide peroxidase (which allows DNA synthesis by the ribonucleotide reduction to deoxyribonucleotide) [57,59,60]. In this work, we highlighted TrxR inhibition in cells preincubated with GNPs and demonstrated that a decrease in TrxR activity radiosensitized cells. All together, these results suggest a new biological mechanism of action for the radiosensitization effect of GNPs (Figure 7). Following cellular uptake through a receptor-mediated endocytosis, endosomes containing GNPs fuse with lysosomes. The decrease in pH inside the vesicle could trigger an *in situ* degradation of the GNPs, leading to the release of gold ions [61]. These ions could interact with the TrxR through the formation of an Au-S bond with the thiol active site of the enzyme as demonstrated by various groups [56,62]. This chemical interaction inhibits the TrxR enzyme leading to a disruption in the oxidized–reduced Trx balance. Then, the decrease in the amount of reduced Trx further impacts the Trx peroxidase activity resulting in the accumulation of ROS in the cytoplasm, causing oxidative stress. These radicals could react with biomolecules and organelles such as mitochondria, leading to a mitochondrial depolarization and therefore a decrease in the ATP production. This drop in the energy source of cells could interfere with various biological pathways, especially the DNA damage repair leading to a decrease in the DNA repair process rate observed in this study. Moreover, the extra ROS produced by the interaction between biological matter and ionizing radiation will increase the oxidative stress in a cell with limited detoxification systems to counteract them due to TrxR inhibition. Overall, this new mechanism suggests that GNPs exert their radiosensitizer effect by

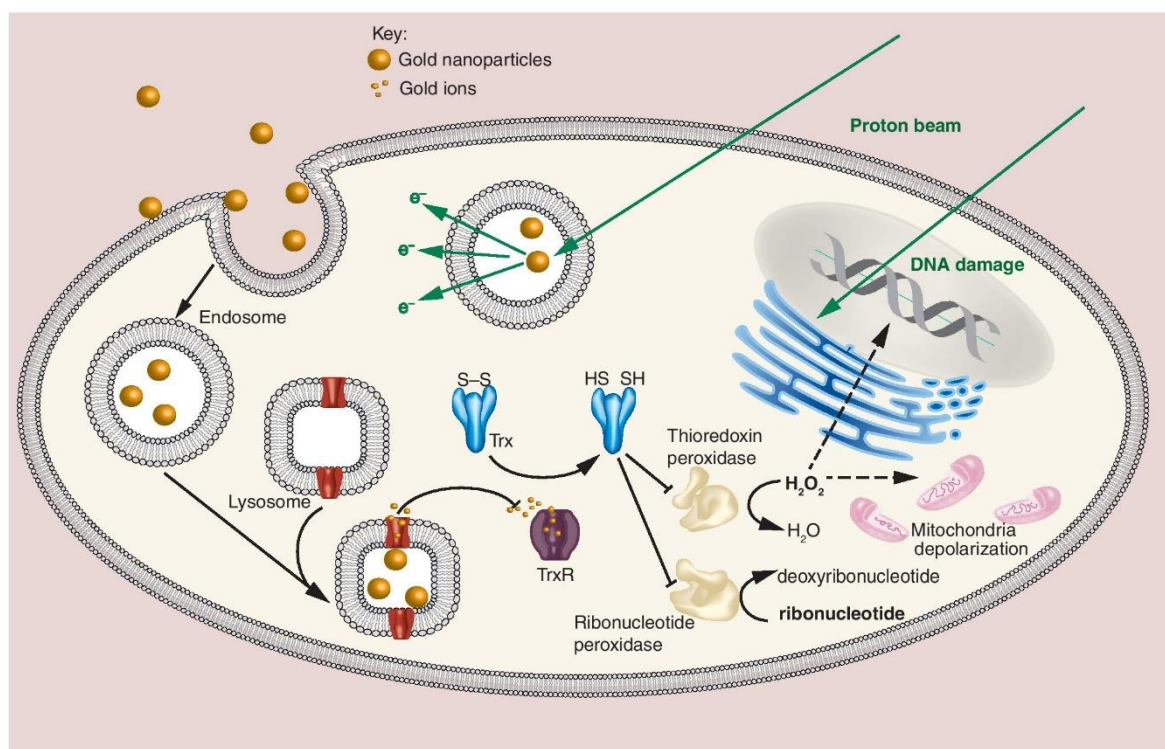


Figure 7. A549 cell exposed to 0.1 Gy of 25 keV/ μm proton beam. Following cell uptake through a receptor-mediated endocytosis, endosomes containing GNPs fuse with lysosomes. The decrease in pH inside the vesicle triggers a restricted *in situ* degradation of the GNPs leading to the release of gold ions. An Au-S bond is created between gold ions and the thiol-active site of TrxR, leading to a disruption in the oxidized – reduced Trx balance. Then, the decrease in the amount of reduced Trx further impacts the Trx peroxidase activity resulting in the accumulation of ROS in the cytoplasm generating an oxidative stress. These radicals could react with mitochondria leading to a mitochondrial depolarization and therefore a decrease in the ATP production. This drop in energy source could interfere with various biological pathways, especially DNA damage repair leading to a decrease in the DNA repair process rate. GNP: Gold nanoparticle; ROS: Reactive oxygen species; Trx: Thioredoxin; TrxR: Thioredoxin reductase.

weakening the detoxification systems in the cell before the irradiation rather than via a radioenhancement effect. Recently, protein disulfide isomerase was suspected to be a key mediator of the cellular response to GNPs [21]. The similarity between the enzyme active site and the TrxR one suggests that GNPs could interact with various other thiol-reductase proteins, widely present in oxidative stress response pathways or with antioxidants (such as glutathione).

In recent years, the pharmaceutical industry has tried to find new uses for old already the US FDA-approved drugs. In this context, auranofin [2,3,4,6-tetra-*o*-acetyl-L-thio- β -D-glycopyranosato-S-(triethylphosphine)-gold(I)], a TrxR inhibitor used for the treatment of rheumatoid arthritis, has attracted renewed attention as a prospective anticancer agent [63]. Numerous studies have evidenced the ability of auranofin to trigger ROS overproduction and apoptosis in various cancer cell lines [64–66] paving the way to lung cancer [67], leukemia [68] or ovarian cancer [69] clinical trials. In a recent work, Wang *et al.* [66] evidenced that TrxR inhibition greater than 50% could be obtained by incubating 4T1 and EMT6 cell lines with auranofin in a 5–10 μM concentration range. This TrxR inhibition radiosensitized both cell lines to x-ray irradiation. However, they also highlighted that the drug decreased cell viability in a dose-dependent manner with IC₅₀ values of 19 and 11 μM for 4T1 and EMT6 cells, respectively. These results demonstrate the toxicity associated to the use of auranofin and bring in light the potential added value of GNPs, for which a powerful TrxR inhibition can be reached without significant cytotoxicity.

Research Article Penninckx, Heuskin, Michiels & Lucas

Conclusion & future perspective

This work highlights the importance of the nanoparticle–cell interactions to fully understand the radiosensitization mechanism. Indeed, it constitutes the first proof-of-concept that GNP can radiosensitize cells by inhibiting detoxification enzymes. Nevertheless, *in vivo* studies are required to investigate metabolic changes in tumor when GNPs are injected into mice. Besides GNPs, other nanomaterials should be considered and their capacity to inhibit the thiol-reductases protein family (such as TrxR) or antioxidants needs to be assessed for the development of nanotechnologies associated to radiotherapy applications. Mechanistic studies still remain a mandatory step toward the clinical use of nanomaterials as radiosensitizers.

Summary points

- 10 nm amino-PEG functionalized gold nanoparticles (GNPs) were successfully internalized by A549 cells and exerted a marked radiosensitization effect when cells were irradiated with 25 keV/ μm protons or 225 kV x-rays.
- We evidenced a mitochondria membrane depolarization and an oxidative stress after a 6-h incubation in the presence of GNPs followed by a recovery at 24-h incubation. These observations are correlated with a more important radiosensitization effect at 6 h of incubation compared with 24 h, demonstrating for the first time that GNP-induced radiosensitivity was modulated overtime.
- We reported a marked inhibition of thioredoxin reductase (TrxR) in cells incubated with GNPs. Moreover, the irradiation of cells invalidated for TrxR evidenced a radiosensitization effect, suggesting that GNPs exert their radiosensitization effect via the inhibition of this enzyme.
- All together, the results suggest that the inhibition of TrxR can lead to an accumulation of reactive oxygen species in the cytoplasm, damaged mitochondria and therefore to a decrease in the ATP production. This drop in the ATP content could decrease the DNA repair rate after irradiation. Moreover, the extra reactive oxygen species produced by interaction between biological matter and ionizing radiation will increase the oxidative stress in cells, which have limited detoxification systems due to TrxR inhibition. Overall, this new mechanism suggests that GNPs exert their radiosensitizer effects by weakening detoxification systems in the cells before irradiation.

Supplementary data

To view the supplementary data that accompany this paper please visit the journal website at: www.futuremedicine.com/doi/full/10.2217/nmm-2018-0171

Financial & competing interests disclosure

The authors have no relevant affiliations or financial involvement with any organization or entity with a financial interest in or financial conflict with the subject matter or materials discussed in the manuscript. This includes employment, consultancies, honoraria, stock ownership or options, expert testimony, grants or patents received or pending or royalties.

No writing assistance was utilized in the production of this manuscript.

References

Papers of special note have been highlighted as: • of interest; •• of considerable interest

- 1 Delaney G, Jacob S, Featherstone C, Barton M. The role of radiotherapy in cancer treatment: estimating optimal utilization from a review of evidence-based clinical guidelines. *Cancer* 104(6), 1129–1137 (2005).
- 2 Wilson RR. Radiological use of fast protons. *Radiology* 47(5), 487–491 (1946).
- 3 Brown A, Suit H. The centenary of the discovery of the Bragg peak. *Radiother. Oncol.* 73(3), 265–268 (2004).
- 4 Boisselier E, Astruc D. Gold nanoparticles in nanomedicine: preparations, imaging, diagnostics, therapies and toxicity. *Chem. Soc. Rev.* 38(6), 1759–1782 (2009).
- 5 Ghosh P, Han G, De M, Kim CK, Rotello VM. Gold nanoparticles in delivery applications. *Adv. Drug Deliv. Rev.* 60(11), 1307–1315 (2008).
- 6 Mieszawska AJ, Mulder WJ, Fayad ZA, Cormode DP. Multifunctional gold nanoparticles for diagnosis and therapy of disease. *Mol. Pharma.* 10(3), 831–847 (2013).
- 7 Saha K, Agasti SS, Kim C, Li X, Rotello VM. Gold nanoparticles in chemical and biological sensing. *Chem. Rev.* 112(5), 2739–2779 (2012).
- 8 Hainfeld JF, Slatkin DN, Smilowitz HM. The use of gold nanoparticles to enhance radiotherapy in mice. *Phys. Med. Biol.* 49(18), N309–N315 (2004).

The role of thioredoxin reductase in gold nanoparticle radiosensitization effects Research Article

- 9 Jeynes JC, Merchant MJ, Spindler A, Wera AC, Kirkby KJ. Investigation of gold nanoparticle radiosensitization mechanisms using a free radical scavenger and protons of different energies. *Phys. Med. Biol.* 59(21), 6431–6443 (2014).
- 10 Li S, Penninckx S, Karmani L *et al.* LET-dependent radiosensitization effects of gold nanoparticles for proton irradiation. *Nanotechnology* 27(45), 455101 (2016).
- 11 Li S, Porcel E, Remita H *et al.* Platinum nanoparticles: an exquisite tool to overcome radioresistance. *Cancer Nanotechnol.* 8(1), 4 (2017).
- 12 Miladi I, Aloy MT, Armandy E *et al.* Combining ultrasmall gadolinium-based nanoparticles with photon irradiation overcomes radioresistance of head and neck squamous cell carcinoma. *Nanomedicine* 11(1), 247–257 (2015).
- 13 Zhang H, Patel N, Ding S, Xiong J, Wu P. Theranostics for hepatocellular carcinoma with Fe₃O₄@ZnO nanocomposites. *Biomater. Sci.* 4(2), 288–298 (2016).
- 14 Bhattarai SR, Derry PJ, Aziz K *et al.* Gold nanotriangles: scale up and X-ray radiosensitization effects in mice. *Nanoscale* 9(16), 5085–5093 (2017).
- 15 Zhang X-D, Luo Z, Chen J *et al.* Ultrasmall glutathione-protected gold nanoclusters as next generation radiotherapy sensitizers with high tumor uptake and high renal clearance. *Sci. Rep.* 5, 8669 (2015).
- 16 Currell F, Villagomez-Bernabe B. Physical and chemical processes for gold nanoparticles and ionising radiation in medical contexts. In: *Gold Nanoparticles for Physics, Chemistry and Biology*. Scientific W (Ed.). World Scientific, NJ, USA, 509–536 (2017).
- 17 Miladi I, Alric C, Dufort S *et al.* The *in vivo* radiosensitizing effect of gold nanoparticles based MRI contrast agents. *Small* 10(6), 1116–1124 (2014).
- 18 Rosa S, Connolly C, Schettino G, Butterworth KT, Prise KM. Biological mechanisms of gold nanoparticle radiosensitization. *Cancer Nanotechnol.* 8(1), (2017).
- **Review highlighting the potential underlying biological mechanisms in gold nanoparticle radiosensitization.**
- 19 Rezaee Z, Yadollahpour A, Bayati V, Negad Dehbashi F. Gold nanoparticles and electroporation impose both separate and synergistic radiosensitizing effects in HT-29 tumor cells: an in vitro study. *Int. J. Nanomedicine* 12, 1431–1439 (2017).
- 20 Arab-Bafarani Z, Saberi A, Tahmasebi Birgani MJ, Shahbazi-Gahrouei D, Abbasian M, Fesharaki M. Gold nanoparticle and mean inactivation dose of human intestinal colon cancer HT-29 cells. *Jundishapur J. Nat. Pharm. Prod.* 10(4), 29153 (2015).
- 21 Taggart LE, McMahon SJ, Butterworth KT, Currell FJ, Schettino G, Prise KM. Protein disulphide isomerase as a target for nanoparticle-mediated sensitisation of cancer cells to radiation. *Nanotechnology* 27(21), 215101 (2016).
- 22 Taggart LE, McMahon SJ, Currell FJ, Prise KM, Butterworth KT. The role of mitochondrial function in gold nanoparticle mediated radiosensitisation. *Cancer Nanotechnol.* 5(1), 5 (2014).
- 23 Coulter JA, Jain S, Butterworth KT *et al.* Cell type-dependent uptake, localization, and cytotoxicity of 1.9 nm gold nanoparticles. *Int. J. Nanomedicine* 7, 2673–2685 (2012).
- 24 Jain S, Coulter JA, Hounsell AR *et al.* Cell-specific radiosensitization by gold nanoparticles at megavoltage radiation energies. *Int. J. Radiat. Oncol. Biol. Phys.* 79(2), 531–539 (2011).
- 25 Polf JC, Bronk LF, Driessen WH, Arap W, Pasqualini R, Gillin M. Enhanced relative biological effectiveness of proton radiotherapy in tumor cells with internalized gold nanoparticles. *Appl. Phys. Lett.* 98(19), 193702 (2011).
- 26 Butterworth KT, Coulter JA, Jain S *et al.* Evaluation of cytotoxicity and radiation enhancement using 1.9 nm gold particles: potential application for cancer therapy. *Nanotechnology* 21(29), 295101 (2010).
- 27 Liu Y, Liu X, Jin X *et al.* The dependence of radiation enhancement effect on the concentration of gold nanoparticles exposed to low- and high-LET radiations. *Phys. Med.* 31(3), 210–218 (2015).
- 28 Huo S, Ma H, Huang K *et al.* Superior penetration and retention behavior of 50 nm gold nanoparticles in tumors. *Cancer Res.* 73(1), 319–330 (2013).
- 29 Zhang G, Yang Z, Lu W *et al.* Influence of anchoring ligands and particle size on the colloidal stability and in vivo biodistribution of polyethylene glycol-coated gold nanoparticles in tumor-xenografted mice. *Biomaterials* 30(10), 1928–1936 (2009).
- 30 Zhang XD, Luo Z, Chen J *et al.* Ultrasmall Au10–12 (SG) 10–12 nanomolecules for high tumor specificity and cancer radiotherapy. *Adv. Mater.* 26(26), 4565–4568 (2014).
- 31 Liang G, Jin X, Zhang S, Xing D. RGD peptide-modified fluorescent gold nanoclusters as highly efficient tumor-targeted radiotherapy sensitizers. *Biomaterials* 144, 95–104 (2017).
- 32 Guo T. *X-ray Nanochemistry: Concepts and Development*. Springer International Publishing, Cham, Switzerland (2018).
- **Extensive review of the potential of metallic nanoparticles for cancer therapy.**
- 33 Oh E, Susumu K, Goswami R, Matroussi H. One-phase synthesis of water-soluble gold nanoparticles with control over size and surface functionalities. *Langmuir* 26(10), 7604–7613 (2010).
- 34 Tsai SW, Chen YY, Liaw JW. Compound cellular imaging of laser scanning confocal microscopy by using gold nanoparticles and dyes. *Sensors* 8(4), 2306–2316 (2008).

Research Article Penninckx, Heuskin, Michiels & Lucas

- 35 Heuskin AC, Wera AC, Riquier H, Michiels C, Lucas S. Low-dose hypersensitivity and bystander effect are not mutually exclusive in A549 lung carcinoma cells after irradiation with charged particles. *Radiat. Res.* 180(5), 491–498 (2013).
 - 36 Wera AC, Riquier H, Heuskin AC, Michiels C, Lucas S. *In vitro* irradiation station for broad beam radiobiological experiments. *Nucl. Instrum. Methods Phys. Res.* 269(24), 3120–3124 (2011).
 - 37 Neumaier T, Swenson J, Pham C *et al.* Evidence for formation of DNA repair centers and dose–response nonlinearity in human cells. *Proc. Natl Acad. Sci. USA* 109(2), 443–448 (2012).
 - 38 Toduka Y, Toyooka T, Ibuki Y. Flow cytometric evaluation of nanoparticles using side-scattered light and reactive oxygen species-mediated fluorescence-correlation with genotoxicity. *Environment. Sci. Technol.* 46(14), 7629–7636 (2012).
 - 39 Schultz LB, Chehab NH, Malikzay A, Halazonetis TD. p53 binding protein 1 (53BP1) is an early participant in the cellular response to DNA double-strand breaks. *J. Cell Biol.* 151(7), 1381–1390 (2000).
 - 40 Chithrani BD, Ghazani AA, Chan WC. Determining the size and shape dependence of gold nanoparticle uptake into mammalian cells. *Nano Lett.* 6(4), 662–668 (2006).
 - 41 Hühn D, Kantner K, Geidel C *et al.* Polymer-coated nanoparticles interacting with proteins and cells: focusing on the sign of the net charge. *ACS Nano* 7(4), 3253–3263 (2013).
 - 42 Fogh SE, Andrews DW, Glass J *et al.* Hypofractionated stereotactic radiation therapy: an effective therapy for recurrent high-grade gliomas. *J. Clin. Oncol.* 28(18), 3048–3053 (2010).
 - 43 Timmerman R, Paulus R, Galvin J *et al.* Stereotactic body radiation therapy for inoperable early stage lung cancer. *JAMA* 303(11), 1070–1076 (2010).
 - 44 Hespels F, Heuskin AC, Scifoni E, Kraemer M, Lucas S. Backscattered electron emission after proton impact on carbon and gold films: experiments and simulations. *Nucl. Instrum. Methods Phys. Res.* 401(Suppl. C), 8–17 (2017).
 - 45 Porcel E, Tillement O, Lux F *et al.* Gadolinium-based nanoparticles to improve the hadrontherapy performances. *Nanomedicine* 10(8), 1601–1608 (2014).
 - 46 Misawa M, Takahashi J. Generation of reactive oxygen species induced by gold nanoparticles under x-ray and UV Irradiations. *Nanomedicine* 7(5), 604–614 (2011).
 - 47 Sicard-Roselli C, Brun E, Gilles M *et al.* A new mechanism for hydroxyl radical production in irradiated nanoparticle solutions. *Small* 10(16), 3338–3346 (2014).
 - 48 Minai L, Yeheskely-Hayon D, Yelin D. High levels of reactive oxygen species in gold nanoparticle-targeted cancer cells following femtosecond pulse irradiation. *Sci. Rep.* 3, 2146 (2013).
 - 49 Heuskin AC, Gallez B, Feron O, Martinive P, Michiels C, Lucas S. Metallic nanoparticles irradiated by low-energy protons for radiation therapy: Are there significant physical effects to enhance the dose delivery? *Med. Phys.* doi:10.1002/mp.12362 (2017) (Epub ahead of print).
 - 50 Sotiropoulos M, Henthorn NT, Warmenhoven JW, Mackay RI, Kirkby KJ, Merchant MJ. Modelling direct DNA damage for gold nanoparticle enhanced proton therapy. *Nanoscale* 9(46), 18413–18422 (2017).
 - 51 Piret JP, Jacques D, Audinot JN *et al.* Copper(II) oxide nanoparticles penetrate into HepG2 cells, exert cytotoxicity via oxidative stress and induce pro-inflammatory response. *Nanoscale* 4(22), 7168–7184 (2012).
 - 52 Wu H, Lin J, Liu P *et al.* Reactive oxygen species acts as executor in radiation enhancement and autophagy inducing by AgNPs. *Biomaterials* 101, 1–9 (2016).
 - 53 Wang Y, Nartiss Y, Steipe B, Mcquibban GA, Kim PK. ROS-induced mitochondrial depolarization initiates PARK2/PARKIN-dependent mitochondrial degradation by autophagy. *Autophagy* 8(10), 1462–1476 (2012).
 - 54 Karatas OF, Sezgin E, Aydin O, Culha M. Interaction of gold nanoparticles with mitochondria. *Colloids Surf. B, Biointerfaces* 71(2), 315–318 (2009).
 - 55 Heiskanen KM, Bhat MB, Wang HW, Ma J, Nieminen AL. Mitochondrial depolarization accompanies cytochrome c release during apoptosis in PC6 cells. *J. Biol. Chem.* 274(9), 5654–5658 (1999).
 - 56 Casini A, Messori L. Molecular mechanisms and proposed targets for selected anticancer gold compounds. *Curr. Topics Med. Chem.* 11(21), 2647–2660 (2011).
 - 57 Saccoccia F, Angelucci F, Boumis G *et al.* Thioredoxin reductase and its inhibitors. *Curr. Protein Peptide Sci.* 15(6), 621–646 (2014).
 - 58 Biaglow JE, Miller RA. The thioredoxin reductase/thioredoxin system: novel redox targets for cancer therapy. *Cancer Biol. Therap.* 4(1), 6–13 (2005).
 - 59 Arner ES, Holmgren A. The thioredoxin system in cancer. *Seminars Cancer Biol.* 16(6), 420–426 (2006).
 - 60 Dunn LL, Buckle AM, Cooke JP, Ng MK. The emerging role of the thioredoxin system in angiogenesis. *Arterioscler. Thromb. Vasc. Biol.* 30(11), 2089–2098 (2010).
 - 61 Sabella S, Carney RP, Brunetti V *et al.* A general mechanism for intracellular toxicity of metal-containing nanoparticles. *Nanoscale* 6(12), 7052–7061 (2014).
- First evidence of ion release from metallic nanoparticle elicited by the acidic conditions of the lysosome.

The role of thioredoxin reductase in gold nanoparticle radiosensitization effects Research Article

- 62 Cai W, Zhang L, Song Y *et al.* Small molecule inhibitors of mammalian thioredoxin reductase. *Free Radical Biol. Medicine* 52(2), 257–265 (2012).
- 63 Roder C, Thomson MJ. Auranofin: repurposing an old drug for a golden new age. *Drugs Res-D* 15(1), 13–20 (2015).
- 64 Fiskus W, Saba N, Shen M *et al.* Auranofin induces lethal oxidative and endoplasmic reticulum stress and exerts potent preclinical activity against chronic lymphocytic leukemia. *Cancer Res.* 74(9), 2520–2532 (2014).
- 65 Zou P, Chen M, Ji J *et al.* Auranofin induces apoptosis by ROS-mediated ER stress and mitochondrial dysfunction and displayed synergistic lethality with piperlongumine in gastric cancer. *Oncotarget* 6(34), 36505–36521 (2015).
- 66 Wang H, Bouzakoura S, De Mey S *et al.* Auranofin radiosensitizes tumor cells through targeting thioredoxin reductase and resulting overproduction of reactive oxygen species. *Oncotarget* 8(22), 35728–35742 (2017).
- 67 Sirolimus and auranofin in treating patients with advanced or recurrent non-small cell lung cancer or small cell lung cancer. ClinicalTrials.org
- 68 Phase I and II study of auranofin in chronic lymphocytic leukemia (CLL). ClinicalTrials.org
- 69 Auranofin in treating patients with recurrent epithelial ovarian, primary peritoneal, or fallopian tube cancer. ClinicalTrials.org

The role of thioredoxin reductase in gold nanoparticle radiosensitization effect - Supplementary information -

Supplementary data S1. Mathematical model of DSB detection and RIF formation. To analyze RIF kinetics, we introduced a basic mathematical model. One DSB is detected by the 53BP1 antibody used for immunostaining at a rate k_1 creating one RIF which will be observed by fluorescence. This RIF is called "RIF_{ON}". This one will be repaired at a rate k_2 leading to his disappearance ("RIF_{OFF}"). By assuming that both processes are irreversible, we can represent the model as followed:



The kinetic evolution of this model can be mathematically expressed as a system of differential equations:

$$\begin{cases} \frac{d DSB}{dt} = -k_1 \cdot DSB \\ \frac{d RIF_{ON}}{dt} = k_1 \cdot DSB - k_2 \cdot RIF_{ON} \end{cases}$$

To resolve this system, we have to fix two initial conditions. First, we decompose the number of DSB created by the irradiation in two parameters A et D corresponding to the number of DSB per Gy of radiation and the dose delivered to the cell respectively. Secondly, the number of RIF_{ON} observed at $t = 0$ is equal to B, the number of RIF_{ON} observed in unirradiated control cells:

$$\begin{cases} DSB(t = 0) = A \cdot D \\ RIF(t = 0) = B \end{cases}$$

By solving the system of differential equations with the two aforementioned initial conditions, we find two solutions describing the average number of DSB and RIF_{ON} at a given time post irradiation:

$$RIF_{ON}(t) = \frac{A \cdot D \cdot k_1}{k_2 - k_1} (e^{-k_1 \cdot t} - e^{-k_2 \cdot t}) + B \cdot e^{-k_2 \cdot t} \quad (\text{equation 1})$$

$$DSB(t) = A \cdot D \cdot e^{-k_1 \cdot t} \quad (\text{equation 2})$$

For the fitting procedure, we fixed the dose delivered to the cell ($D = 1$ Gy) and the coefficient B via experimental observations ($B_{A549} = 0.51$; $B_{GNP} = 1.11$).

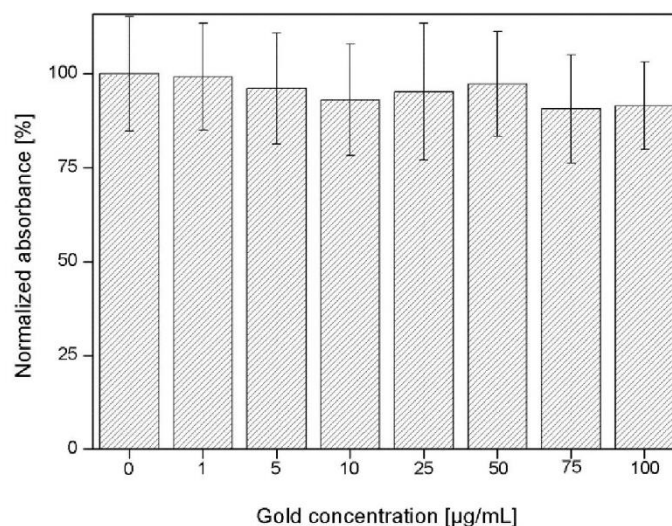


Figure S2. Cell viability of A549 cells incubated in the presence of different concentrations of gold for 24 h and assessed using a MTS assay. Data represent the mean absorbance relative to untreated control ± 1 S.D. for three independent experiments using 10 nm GNPs. Results were statistically analyzed using a one-way ANOVA evidencing no significant difference (Tukey test).

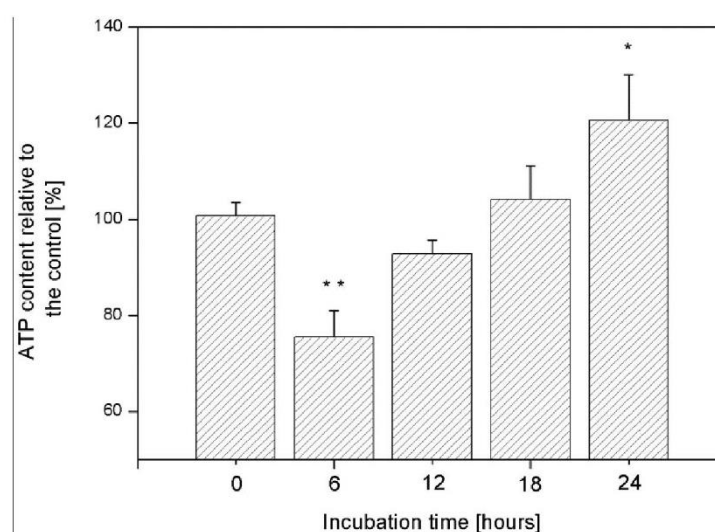


Figure S3. ATP content in cells incubated with GNPs overtime. A549 cells were incubated with 50 $\mu\text{g}\cdot\text{mL}^{-1}$ GNPs during various times. ATP content in cells were measured according the instructions from the Adenosine 5'-triphosphate Bioluminescent Assay Kit (Sigma-Aldrich). Data represent the mean values relative to untreated control ± 1 S.D. for three independent experiments. Mean values were normalized by the total protein content. Results were statistically analyzed using a one-way ANOVA (Tukey test, * $p < 0.05$, ** $p < 0.01$).

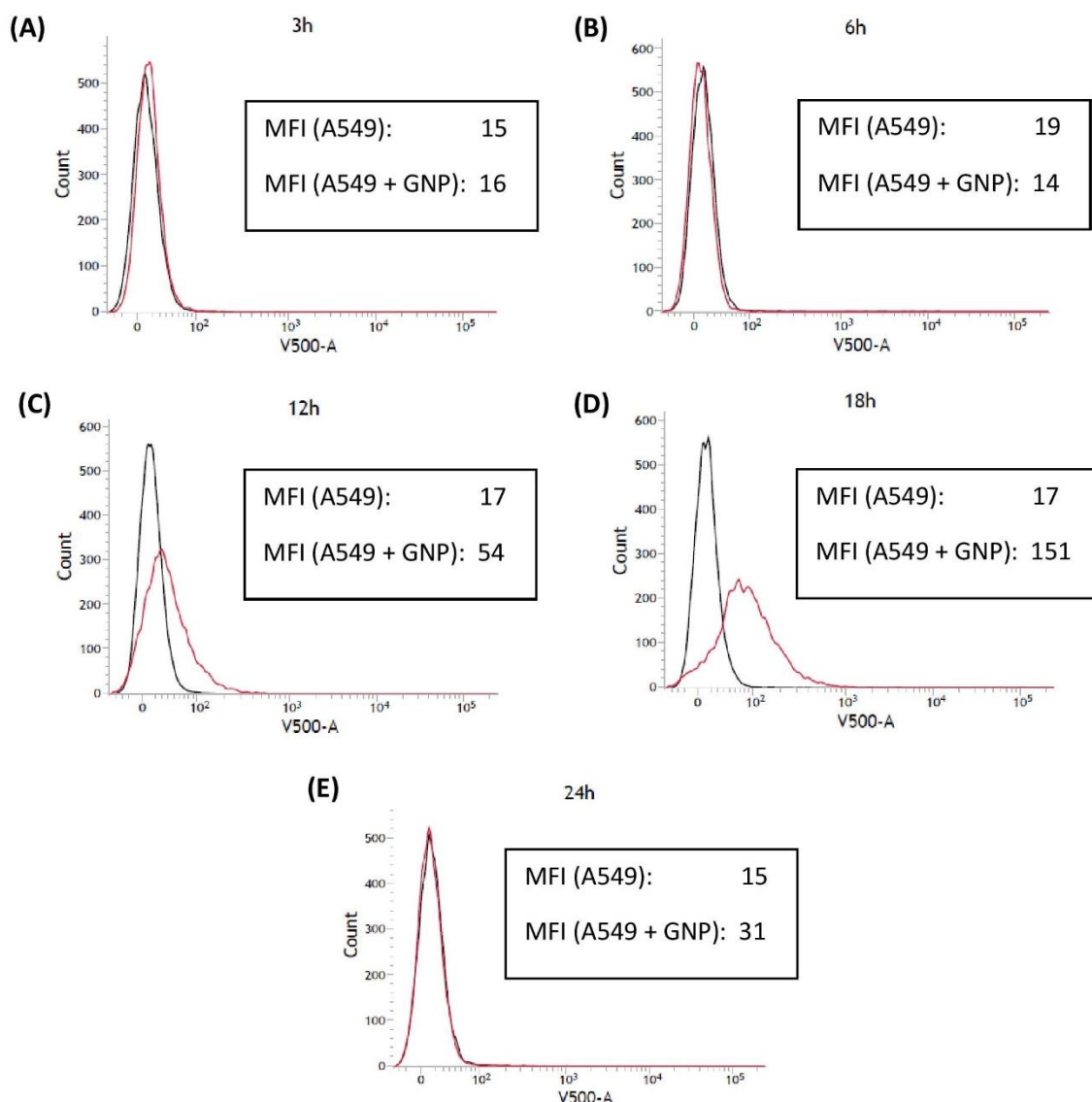


Figure S4. Autophagy process initiation in A549 cells incubated with GNPs. After a given incubation time with 50 $\mu\text{g/mL}$ GNPs (A: 3h, B: 6h, C: 12h, D: 18h, E: 24h), cells were labeled with monodansylcadaverine (MDC dye), a marker of autophagic vacuoles and the intensity of fluorescence was detected using flow cytometry (V500-A channel). For each sample, 10,000 cells were analyzed and mean fluorescence intensity (MFI) was recorded. Black and red curves represent control cells (without GNPs) and cells pre-incubated with GNPs respectively. Results showed the presence of autophagic vacuoles (increase in MDC fluorescence) after 12h and 18h of incubation.

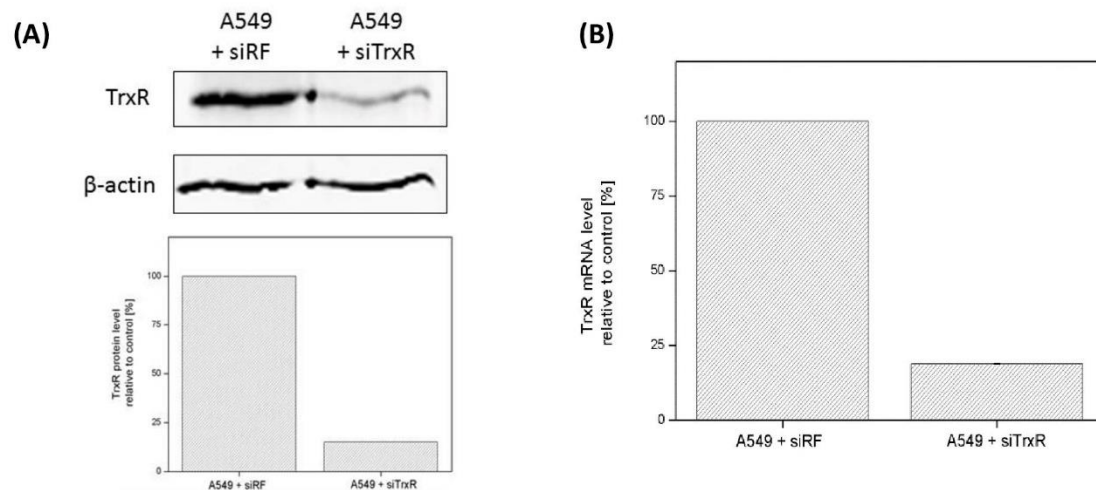


Figure S5. siTrxR invalidation in A549 cells. After 24 hours of incubation with siTrxR or siRF (Control), A549 cells were washed with PBS and the medium was replaced for MEM + 10% FBS for 24 hours. (A) The abundance of TrxR in A549 cells was analyzed by Western blotting. β -actin was used as loading control. The fluorescence intensity of TrxR was quantified and was normalized to the one of β -actin. (B) TrxR mRNA level was quantified using RT-qPCR.

7.2.3. Third manuscript: “Thioredoxin reductase activity predicts gold nanoparticle radiosensitization effect” – Nanomaterials (submitted in January 2019)

Thioredoxin reductase activity predicts gold nanoparticle radiosensitization effect

Sébastien PENNINCKX¹, Anne-Catherine HEUSKIN¹, Carine MICHIELS^{2} and Stéphane LUCAS¹*

1. Research center for the Physics of Matter and Radiation (PMR-LARN), Namur Research Institute For Life Sciences (NARILIS), University of Namur, Rue de Bruxelles 61, B-5000 Namur, Belgium
2. Unité de Recherche en Biologie Cellulaire (URBC), Namur Research Institute For Life Sciences (NARILIS), University of Namur, Rue de Bruxelles 61, B-5000 Namur, Belgium

* corresponding author: URBC-NARILIS, University of Namur, 61 rue de Bruxelles, 5000 NAMUR, Belgium. tel +32-81-724131, fax +32-81-724135 Email: carine.michiels@unamur.be

Abstract

Gold nanoparticles (GNPs) have been shown to be effective contrast agents for imaging and emerge as powerful radiosensitizers, constituting a promising theranostic agent for cancer. Although the radiosensitization effect was initially attributed to a physical mechanism, an increasing number of studies challenge this mechanistic hypothesis and evidence the importance of oxidative stress in this process. This work evidences the central role played by thioredoxin reductase (TrxR) in the GNP-induced radiosensitization. A cell type-dependent reduction in TrxR activity was measured in five different cell lines incubated with GNPs leading to differences in cell response to X-ray irradiation. Correlation analyses demonstrated that GNP uptake and TrxR activity inhibition are associated to GNP radiosensitization effect. Finally, Kaplan-Meier analyses suggested that high TrxR expression is correlated to low patient survival in four different types of cancer. Altogether, these results enable a better understanding of GNP radiosensitization mechanism which remains a mandatory step towards further use in clinic. Moreover, they highlight the potential application of this new treatment in a personalized medicine context.

Keywords: gold nanoparticles, radiosensitization, thioredoxin reductase, radiation, prognosis, biochemical mechanism

Introduction

Over the past century, radiotherapy has emerged as the main treatment modality for cancer (1). This powerful technique is based on the induction of lethal cellular damages caused by ionizing radiation delivered to tumors. Even if successful, this approach is still limited by dose distribution heterogeneity causing side effects to healthy tissues surrounding the tumor. In this way, the research on new strategies to achieve a better tumor targeting and enhance the biological effectiveness of radiation is growing (2, 3). Pushed by the development of nanotechnology, the scientific community takes advantage of nanoscale materials as sensitizers for therapeutic applications. It was suggested that the strong difference in energy absorption between high Z nanoparticles and water could be used to increase the local dose deposition in cells (4-6). The proof-of-concept was demonstrated by Hainfeld et al. (7) who evidenced that injections of 1.9 nm gold nanoparticles (GNPs) increased the survival of tumor-bearing mice in combination with 250 kVp X-rays compared to X-rays alone. Since this pioneering work, the development of new high-Z radiosensitizers (including silver (8, 9), gadolinium (10-12), hafnium (13, 14), platinum (15, 16), gold (6, 17, 18) or bismuth (19, 20) nanoparticles) has accelerated and many studies have shown their ability, when injected into the tumor, to amplify the X-ray radiation treatment efficacy. While evidencing this potential use as radiosensitizer, the large variations in all these experimental settings revealed the high variability of GNP effects according to different physico-chemical parameters including GNP size, shape and coating agent. Zhang et al. (21) performed radiosensitization experiments using four distinct polyethylene glycol (PEG)-coated GNP (5, 12, 27, 46 nm). Although they showed that all GNP sizes caused a decrease in cancer cell survival after irradiation, they reported a stronger effect using the 12 and 27 nm GNPs due to a more important tumor accumulation. Moreover, other groups demonstrated the influence of coating agent and GNP shape in the cell uptake process and so, in their involvement in the radiosensitization effect (22, 23).

Despite the increasing amount of data regarding GNP-induced radiosensitization, it is still difficult to draw conclusions regarding this radiosensitization effect due to the diversity of parameters and conditions (nanoparticle size, cell lines, radiation source, administration route, ...) used in literature (2). This leads to important open questions such as the mechanism(s) responsible for this effect which remains a mandatory step towards the clinical use of metallic radiosensitizers. In this context, the present work aims at shedding light on non-physical mechanisms responsible for the GNP-induced radiosensitization based on preliminary results described in our previous study (24). In the present work, we focused on the effect of homemade 10 nm amino-PEG functionalized GNPs in five different cell lines (A431 epidermoid carcinoma, A549 lung adenocarcinoma, MDA-MB-231 breast adenocarcinoma, PANC-1 pancreatic epithelioid carcinoma and T98G glioblastoma cell lines). We evidenced correlations between GNP uptake, residual thioredoxin reductase (TrxR) activity and radiosensitization effect.

Material & Methods

GNP synthesis. 10 nm amino-PEG functionalized GNPs were synthesized according to (24). Briefly, HAuCl₄ (Sigma Aldrich) and TA-PEG₅₅₀-OCH₃ (Biochempeg Scientific Inc., MA, USA) were mixed at a 2000:1 Au: PEG molar ratio in deionized water and stirred at room temperature for 1 hour. NaBH₄ (Sigma Aldrich) was then added to the mixture under vigorous stirring and the solution was left stirring during 3 hours. Then, TA-PEG₄₀₀-NH₂ (Biochempeg Scientific Inc., MA, USA) was added to the solution for extra passivation. After 3 hours of stirring, the colloidal suspension was purified using a membrane filtration device (Vivaspin, Millipore).

GNPs were lyophilized with a freeze-drying system (Alpha 2-4 LD Plus; Analis) and stored at 4°C for further use. In all experiments, cells were incubated with 50 µg of gold per mL of medium, which corresponds to 8.22 nM of GNPs.

Cell culture. Human lung carcinoma A549 cells were grown in Eagle's Minimum Essential Medium (MEM Glutamax; Gibco® by Life Technologies) supplemented with 10% (v/v) fetal bovine serum (FBS; Gibco® by Life Technologies). Epidermoid carcinoma A431 cells, mammary gland adenocarcinoma MDA-MB-231 cells, glioblastoma T98G cells and pancreas epithelioid carcinoma PANC-1 cells were grown in Dulbecco's Modified Eagle's medium (DMEM 4.5 g/L glucose; Gibco® by Life Technologies) supplemented with 10% (v/v) FBS. All cell lines were incubated at 37 °C in a humidified atmosphere incubator containing 5% CO₂.

GNP uptake. Gold content quantification was performed by atomic absorption spectroscopy (AAS). After a 24h incubation with GNPs, the cells were washed twice with PBS at 37°C and then harvested using trypsin. Detached cells were then washed twice with culture medium by successive centrifugation. The actual number of cells in each sample was determined using a cell counter (Countess Automated Cell Counter, Invitrogen). After the third centrifugation, the medium was discarded, and the pellets were digested using 2 ml of aqua regia (37% HCl, 65% HNO₃ Sigma-Aldrich) overnight. The gold content was quantified using an atomic absorption spectrophotometer (AA-7000F from Shimadzu) by plotting the calibration curve with known concentrations of a gold standard solution (Merck Chemicals, Belgium) used for external calibration. Triplicate readings were analyzed for each sample. The amount of gold detected in the cells was expressed as an internalized gold quantity (pg) per cell. Using the theoretical mass of a 10 nm GNP (= 1.01 10⁻¹⁷ g), results were expressed as a number of GNPs per cell.

X-ray irradiation. 48 hours before irradiation, 5 10⁴ cells were seeded as 50 µl drops in 24-well plates and placed in an incubator at 37°C with 5% CO₂. 2 hours after seeding, the wells were filled with corresponding medium and placed in the incubator overnight. The medium was then removed, the wells were filled with medium + 10% FBS without (control cells) or with 50 µg Au.ml⁻¹ of GNPs and incubated at 37°C until irradiation (24 hours of incubation). Prior to irradiation, the medium was discarded from the wells, the plate was rinsed with PBS and filled

with CO₂-independent medium (Gibco® by Life Technologies) without FBS. The cell monolayer was irradiated with a homogenous X-ray beam produced by an X-Rad 225 XL (PXi Precision X-ray) at 225 kV. The dose rate was fixed to 3 Gy.min⁻¹ and the dose to 2 Gy.

Clonogenic assay. Immediately after irradiation, the cells were detached using 0.25% trypsin and counted. In order to obtain countable colony numbers, the cells were seeded in 6-well plates containing medium supplemented with 10% FBS, penicillin/ streptomycin and incubated at 37°C. In parallel, cells were also seeded in separate dishes. 2 hours after seeding, they were fixed with 4% paraformaldehyde (Merck Chemicals) for 10 min and washed with PBS 3 times. The cells attached to the dish were counted manually under an optical microscope to obtain the precise number of cells seeded. Eleven days post-irradiation, the colonies were stained with violet crystal in 2% ethanol. The number of visible colonies (containing 50 or more cells) was considered to represent the surviving cells, which were counted manually. The plating efficiency (PE) was calculated by dividing the number of colonies by the initial numbers of seeded cells. The survival fraction was obtained as the PE ratio for irradiated cells to the PE for control cells. The control cells underwent the same procedure except the irradiation step. At least three independent experiments were performed and the errors were evaluated as standard error of mean (SEM). In order to quantify the GNP ability to enhance cell death, the amplification factor (AF) was calculated as previously described (6). **TrxR activity assay.** The TrxR activity was measured with a commercially available kit (Sigma Aldrich). The assay is based on the catalytic reduction of 5,5'-dithiobis(2-nitrobenzoic) acid to 5-thio-2-nitrobenzoic acid by TrxR. This reduction generates a yellow colored product. Its absorbance is measurable at 412 nm by spectrophotometry. The cells were incubated 24h with or without 50 µg Au.ml⁻¹ of GNPs before to being detached with 0.25% trypsin. The cells were pelleted by centrifugation (1000 rpm, 5 min, 4°C) and the medium was discarded. The pellet was resuspended in a homemade lysis buffer (9% w/w sucrose; 5% v/v aprotinin (Sigma-Aldrich), in deionized water) and disrupted by a dounce homogenizer. Then,

the TrxR activity was measured according to the manufacturer's instructions. The linear increase in absorbance at 412 nm was measured during 10 min using a spectrophotometer (Ultrospec 8000; GE Healthcare). The TrxR activity rate was calculated from the slope of absorbance at 412 nm versus time. Data are plotted as mean absorbance values normalized by the total protein in the sample.

Patient survival analysis. The online SurvExpress gene expression database (25) was used for the analysis of overall survival in different cancer types (1296 samples in total). Patients were classified into two risk groups according to their TXNRD1 gene expression. The median in gene expression was used as cutoff. The association between TXNRD1 expression and overall patient survival was assessed by using the Kaplan-Meier method and the significance was analyzed using the log-rank test. $P < 0.05$ was considered to indicate a statistically significant difference.

Statistical analysis. All experiments were repeated at least three times on separate days. A one-way analysis of variance (ANOVA) was performed using Origin 8 (OriginLab, USA) in order to compare the differences between groups. The number of asterisks in the figures indicates the level of statistical significance as follows: * $p < 0.05$, ** $p < 0.01$, *** $p < 0.001$.

Results

GNPs are successfully internalized in cancer cells.

To assess the GNP uptake in each cell type after a 24h incubation, AAS measurements were performed. As illustrated in Figure 1, a gold content of 0.51 ± 0.07 , 0.71 ± 0.18 , 0.84 ± 0.17 , 0.97 ± 0.08 and 2.0 ± 0.4 pg Au/cell was measured for PANC-1, A431, MDA-MB-231, T98G and A549 cells respectively, revealing a cell type-dependent uptake. Moreover, no significant toxicity was observed in any studied cell lines (Figure S1).

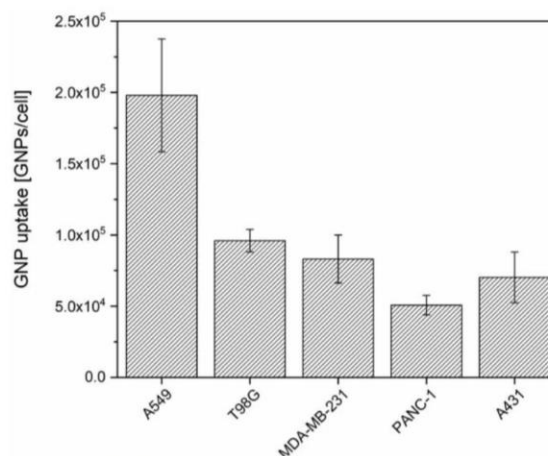


Figure 1. Cellular uptake of 10 nm GNPs in different cancer cell lines. Cells were incubated during 24 hours with $50 \mu\text{g} \cdot \text{mL}^{-1}$ of GNPs and the gold content was assessed by atomic absorption spectroscopy. Results are expressed as means \pm SD for three independent experiments.

GNPs decrease the TrxR activity in different cell lines.

The enzymatic activity of TrxR was evaluated in the different cell lines incubated with or without $50 \mu\text{g} \cdot \text{mL}^{-1}$ of GNPs during 24h. As shown in Figure 2, a decrease in TrxR activity was observed in all the cell lines when incubated with GNPs. Moreover, results demonstrated that the level of this enzymatic inhibition is cell type-dependent with a $49 \pm 7\%$, $64 \pm 5\%$, $75 \pm 4\%$ and $88 \pm 7\%$ of residual TrxR activity for A431, T98G, MDA-MB-231 and PANC-1 cells respectively. However, one-way ANOVA (Tukey test) evidenced that this inhibition was not significant for PANC-1 and MDA-MB-231 cells. It must be noted that a $28 \pm 3\%$ residual activity was previously measured in A549 cells incubated with the same GNPs (24).

GNPs enhance the cell death upon irradiation.

The five cancer cell lines were pre-incubated during 24h with or without $50 \mu\text{g} \cdot \text{mL}^{-1}$ of GNPs prior to be irradiated using 225 kVp X-rays. Cell survival fractions were assessed by standard clonogenic assays. As shown in **Error! Reference source not found.**, survival fraction decreased in all cell lines when they were pre-incubated with GNPs. To quantify this decrease in survival fraction, we calculated the amplification factor (AF) which indicates the enhanced proportion of dead cells in the presence of GNPs compared with irradiation alone for a given dose.

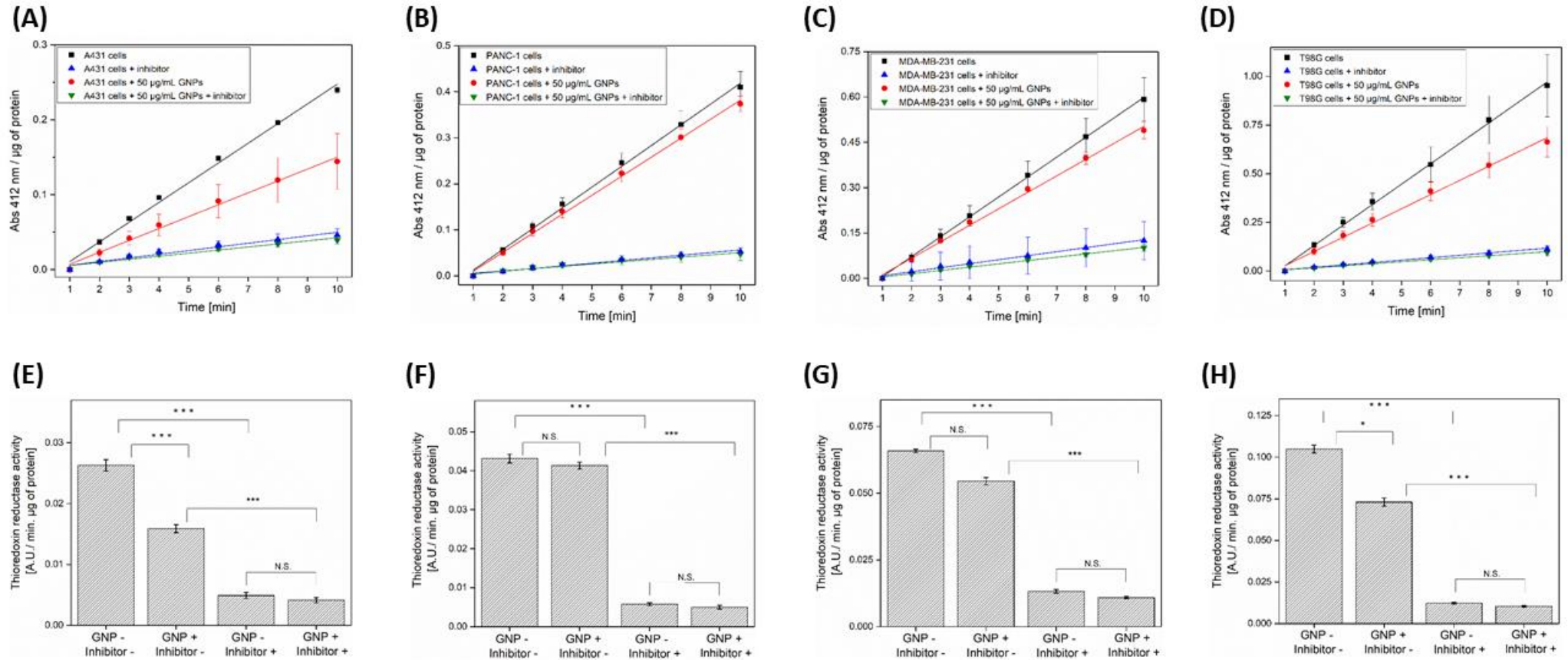


Figure 2. TrxR activity in cells incubated with or without 50 µg Au.mL⁻¹ GNPs during 24h. The activity was measured by the absorption at 412 nm over time in cell lysate of (A) A431, (B) PANC-1, (C) MDA-MB-231 and (D) T98G. Data are plotted as mean values of absorbance normalized by the total protein content \pm S.D. of 3 independent experiments. Slopes of these TrxR activity curves were used to calculate the TrxR activity rate in (E) A431, (F) PANC-1, (G) MDA-MB-231 and (H) T98G cell lines. Data are plotted as mean values \pm S.D. of 3 independent experiments. All results were statistically analyzed using a one-way ANOVA (Tukey test, * p < 0.05, *** p < 0.001, N.S. = not significant).

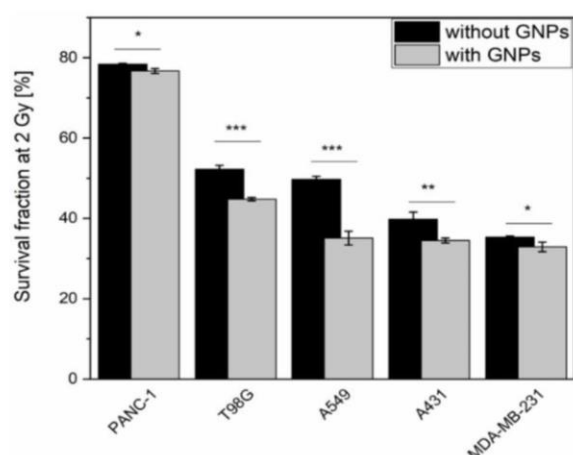


Figure 3. GNPs enhance cell death upon irradiation. Survival fractions were determined by colony forming assay for cells pre-incubated with $50 \mu\text{g}\cdot\text{mL}^{-1}$ GNPs. After a 24h incubation with GNPs, cells were irradiated with 225 kVp X-rays. Results are expressed as mean values of at least three independent experiments \pm SEM. Data were statistically analyzed using a one-way ANOVA (Tukey test, * $p < 0.05$, ** $p < 0.01$; *** $p < 0.001$)

At 2 Gy, a clinically relevant dose per fraction, a $13 \pm 4\%$, $23 \pm 1\%$, $7 \pm 4\%$, $14 \pm 3\%$ and $2 \pm 1\%$ AF was calculated for, respectively, A431, A549, MDA-MB-231, T98G and PANC-1 cells.

Correlation between cell response to radiation, TrxR activity and GNP uptake.

To better understand the relationship between survival fractions, gold content in cells and the GNP-induced TrxR inhibition, correlation studies were performed. Results highlighted a strong correlation between GNP uptake and the amount of inhibited TrxR (Figure 3A, Pearson's $r = 0.991$),

between the AF at 2 Gy and the residual level of TrxR activity (Figure 3B, Pearson's $r = -0.964$) and between the AF at 2 Gy and the GNP uptake (Figure 3C, Pearson's $r = 0.872$).

TXNRD1 is an unfavorable prognostic factor.

To investigate the possible involvement of TXNRD1 (gene coding for TrxR) expression in patient survival, we retrospectively analyzed microarray datasets of different types of cancer. A total of 1,296 samples with TXNRD1 status from five datasets were taken into account in this study. Five independent clinical cohort datasets were used: GSE-42669 (26) and GSE-30219 (27) cohorts for glioblastoma and lung adenocarcinoma respectively, TCGA-BRCA and TCGA-HNSC cohorts for invasive breast and squamous cell carcinomas respectively as well as PACA-AU for pancreatic ductal adenocarcinoma.

The characteristics of these different cohorts are described in Table 1. Using SurvExpress tools, overall patient survival was analyzed according to TXNRD1 mRNA expression. Figure 4 shows the Kaplan-Meier curves for different cancer types while a box plot across the groups is shown in Figure S2. The results showed that high expression of TXNRD1 gene was significantly associated with poor overall patient survival in brain, breast, lung and head & neck. The effect was the most pronounced for lung adenocarcinoma, for which the median survival time decreased from 102 months (low TXNRD1 expression) to 44 months (high TXNRD1 expression).

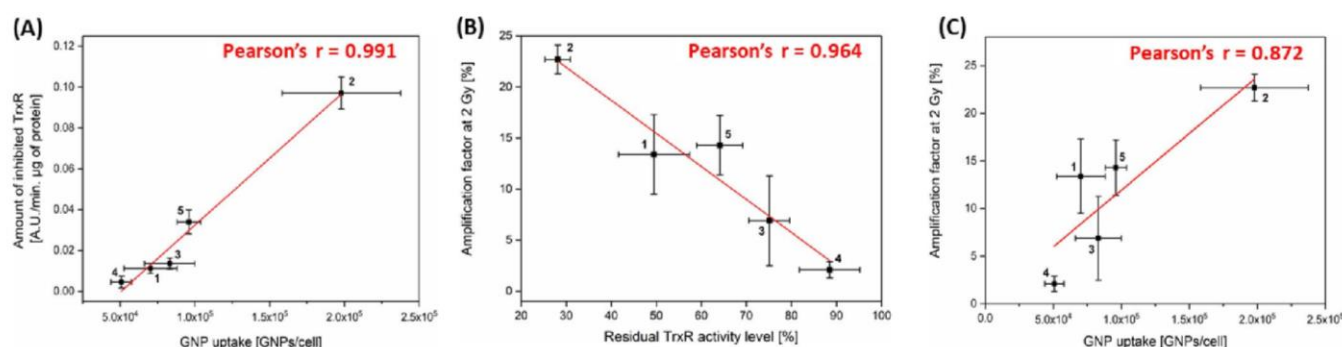


Figure 3. Correlation analysis showing the relation between (A) the amount of inhibited TrxR in cells and gold content; (B) the AF at 2 Gy and the residual TrxR activity level at irradiation time; (C) the AF at 2 Gy and the GNPs uptake. Data are presented as means of at least three independent experiments \pm SEM (for AF) or \pm SD (for TrxR activity and GNP uptake). 1 = A431 cells; 2 = A549 cells; 3 = MDA-MB-231 cells; 4 = PANC-1 cells; 5 = T98G cells

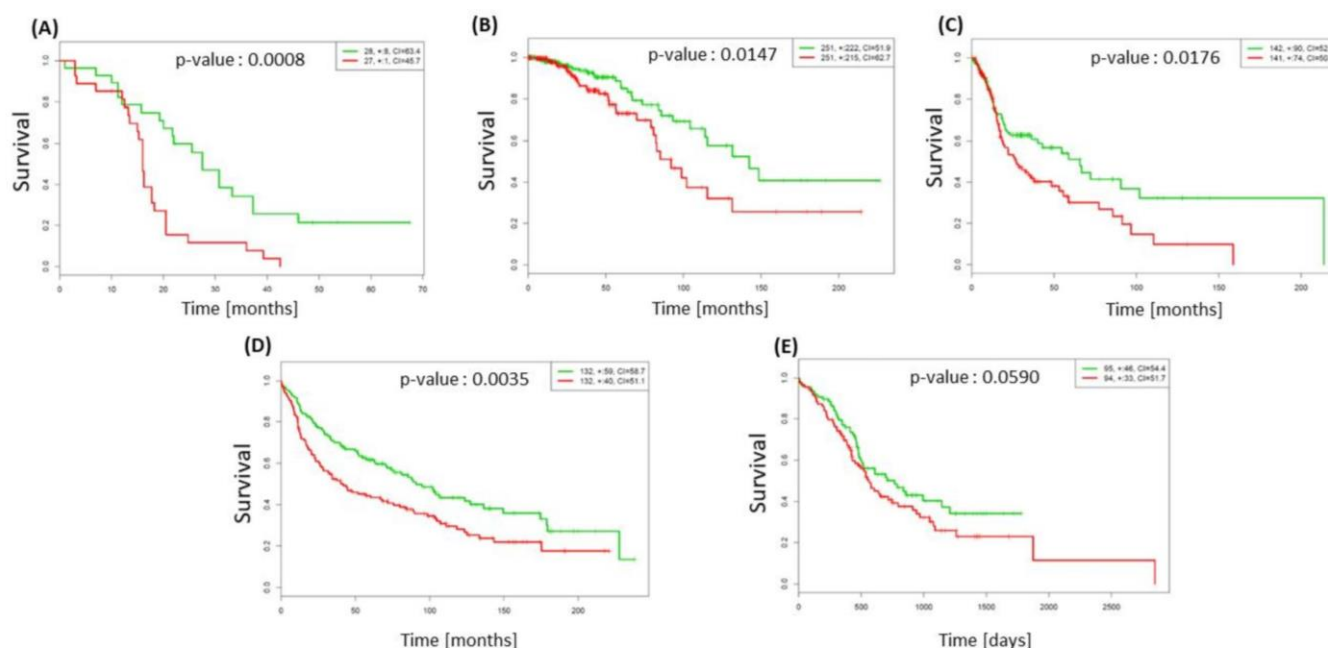


Figure 4. Kaplan-Meier analysis for overall patient survival according to TXNRD1 mRNA expression in (A) brain (GSE42669), (B) breast (TCGA-BRCA), (C) head & neck (TCGA-HNSC), (D) lung (GSE 30219) and (E) pancreas (PACA-AU) cancer datasets. Green and red curves mean low and high TXNRD1 expression groups respectively. Log-rank equal curves p-values were calculated using the SurvExpress tools and were considered as significant when $p < 0.05$.

Discussion

Since several decades, oncology is shifting towards a personalized medicine approach where the treatment selection for each cancer patient is becoming individualized (28).

This medical field is rapidly evolving driven by networks such as “The Cancer Genome Atlas” (TCGA) or “Gene Expression Omnibus” (GEO) that enable to catalogue genetic changes in key genes associated to cancer. These datasets permit scientific community to identify new potential biomarkers and therapeutic targets (28, 29). In this study, Kaplan-Meier survival plots generated from cohort data demonstrated that higher expression of TXNRD1 gene is significantly correlated with poor survival outcome, identifying this gene as an unfavorable prognostic factor for cancer patients. The protein encoded by TXNRD1 belongs to the pyridine nucleotide-disulfide oxidoreductase family and is a member of the thioredoxin (Trx) system. This system is a major redox regulator and comprises an oxido-reductase enzyme (TrxR) which catalyzes the reduction of oxidized Trx by coupling with the oxidation of NADPH to NADP⁺

(30). Since TrxR is also involved in tumor growth and DNA replication (31, 32), it is not surprising that TXNRD1 overexpression has been evidenced in many aggressive tumors (30, 33). Moreover, breast cancer resistance to docetaxel has been demonstrated in tumor expressing high mRNA TrxR level (34, 35).

In the context of personalized medicine, a therapeutic strategy to treat overexpressing TXNRD1 tumors could be to use Trx system inhibitors such as auranofin. Several studies have shown the ability of auranofin to trigger ROS overproduction and apoptosis in different cell lines (36-38) and to exert an antitumor activity in mice bearing breast or lung xenografts (38, 39). These works paved the way to ongoing lung cancer (40), leukemia (41) or ovarian cancer (42) clinical trials. Although auranofin was already FDA approved for the treatment of rheumatoid arthritis, its use is associated to cytotoxicity *in vitro* as demonstrated by Wang et al. (IC₅₀ values of 19 and 11 μ M for 4T1 and EMT6 cells respectively) (38). One less toxic alternative could be GNPs.

Organ	Cancer type	Number of patients	Median survival time [months]		Database
			Low TXNRD1	High TXNRD1	
Brain	Glioblastoma	58	27	16	GSE 42669 (26)
Breast	Invasive carcinoma	502	142	92	TCGA – BRCA
Head & Neck	Squamous cell carcinoma	283	66	27	TCGA – HNSC
Lung	Adenocarcinoma	264	102	44	GSE 30219 (27)
Pancreas	Ductal adenocarcinoma	189	26	19	PACA - AU

Table 1. Overall characteristics of the five datasets used in this study.

This study reported a cell type-dependent TrxR inhibition that may be explained by differences in cell capacity to internalize GNPs as well as in basal TrxR expression in each cell line. Indeed, we showed that even if we measured a similar gold content in A431 and MDA-MB-231 cells, we observed difference in TrxR inhibition (49 % of residual TrxR activity level in A431 cells versus 75 % in MDA-MB-231 cells). These differences may be due to a lower TrxR expression in A431 cells compared to MDA-MB-231 cells as suggested by activity measurement in Figure 2 (0.026 versus 0.066 A.U. /min. μg of protein for A431 and MDA-MB-231 cells respectively).

Our work highlighted a cell-dependent radiosensitization effect with 225 kVp X-ray photons enabling to eradicate up to 23% more cells (in case of A549 cells) at 2 Gy compared to irradiation without GNPs. Although various works evidenced the GNP ability to enhance the biological effectiveness of radiation (6, 24, 43, 44), the mechanism responsible for this effect remains poorly understood. Currently, two theories have been suggested. On one hand, a physico-chemical mechanism coming from the difference in energy absorption between gold and the surrounding soft tissues enables a dose enhancement in cells containing GNPs (5). The interaction between the ionizing particles and high Z atoms can lead to the emission of low-energy electrons (LEE) from the nanoparticle (11, 45) and the production of ROS (46, 47). This

“ballistic” approach which predicts that the cell response would be directly correlated to the gold content, requires a direct interaction between the incident beam and the GNPs. However, a growing amount of simulation works evidenced that the number of hits in a cell containing GNPs is very low, especially in case of charged particles (48, 49). Consequently, the calculated physical enhancement effects of GNPs are very low compared to the radiosensitization effect observed in *in vitro* studies. Moreover, various studies have reported significant radiosensitization effect with megavoltage X-rays where little or no increase in overall dose deposition would be expected according to the theory (50-52). This suggests that other mechanisms have greater contribution than physical interaction to the radiosensitization effect (48, 49, 53, 54). On the other hand, we previously demonstrated the involvement of the Trx system in GNP-induced radiosensitization suggesting a biological mechanism [24]. We performed an invalidation of the TrxR expression in A549 cells using siRNA technology leading to a residual 15% TrxR protein level. These invalidated A549 cells were irradiated without GNPs, evidencing a significant radiosensitization effect (AF of 30% at 2Gy) [24]. Therefore, we suggested a new mechanism: following cell uptake through a receptor-mediated endocytosis, endosomes containing GNPs fuse with lysosomes. By decreasing pH inside the vesicle, lysosomes trigger a GNP degradation leading to the release of gold ions, well-known TrxR inhibitors. This

inhibition induces various dysfunctions of pathways leading to a cytoplasmic ROS accumulation, a decrease in ATP production and DNA damage repair alterations. Irradiation of these weakened cells will cause DNA damage and an extra oxidative stress in cells with limited ATP stocks and detoxification systems (24). Although this link between TrxR and GNP-induced radiosensitization was previously hypothesized to explain lung carcinoma cells radiosensitization, the present study validated it in four other cell lines. Indeed, correlation analyses (Figure 3) demonstrated that the radiosensitization effect is strongly correlated to the residual TrxR level. The aforementioned suggested mechanism is in agreement with an increasing number of works that start to take into account nanoparticle impacts on cellular processes. By comparing a large amount of studies describing GNP-induced radiosensitization, Butterworth et al. (54) concluded that oxidative stress plays a central role in radiosensitization effect. This hypothesis was confirmed by various groups which evidenced a reduction in radiosensitization effect when DMSO, a ROS scavenger was present upon irradiation (6, 15, 55, 56). Recently, protein disulphide isomerase, an enzyme catalyzing the formation and breakage of disulfide bonds in cysteine residues, was suspected to be a key mediator of the cellular response to GNPs (57). Interestingly, some studies have showed that oxide nanoparticles have the ability to decrease DNA repair efficiency without any ROS

production enhancement, on the opposite to metallic NPs (58, 59). This highlights the need to consider biological impacts of nanoparticles in further studies in order to rationalize reported differences in literature and to progress in our global understanding of the phenomenon.

Conclusion

This work highlights the importance of nanoparticle - cell interactions to fully understand the radiosensitization mechanism. It evidences that the implication of TrxR, previously reported in GNP-induced lung cancer cell radiosensitization, is confirmed in other cancer types since a strong correlation between cell response to radiation and residual TrxR activity level is highlighted. Overall, this suggests that GNPs play a radiosensitizer role by weakening detoxification system in addition to the radioenhancer role widely described in literature. To progress in the development of nanotechnology for oncology applications, the capacity of nanomaterials to inhibit the thiol-reductases protein family (such as TrxR) and their impact on antioxidants need to be assessed. A deep understanding of the mechanism responsible for this enhancement effect still remains a mandatory step towards the optimized clinical use of nanomaterials as radiosensitizers.

Acknowledgments

We are grateful to Tijani Tabarrant for its skillful assistance with the irradiation facilities. The authors acknowledge the TCGA Research Network as well as the technical support of the SIAM technological platform of UNamur. The X-ray irradiator was purchased thanks to the financial support from Oncobeth ASBL and Fonds Anciaux of Solidarité-Espoir ASBL. Sébastien Penninckx is a PhD fellow funded by the Belgian Funds for Scientific Research (FRS-FNRS, Belgium).

References

1. Delaney G, Jacob S, Featherstone C, & Barton M (2005) The role of radiotherapy in cancer treatment: estimating optimal utilization from a review of evidence-based clinical guidelines. *Cancer* 104(6):1129-1137.
2. Laprise-Pelletier M, Simao T, & Fortin MA (2018) Gold Nanoparticles in Radiotherapy and Recent Progress in Nanobrachytherapy. *Adv Healthc Mater* 7(16):e1701460.
3. Genard G, et al. (2018) Proton irradiation orchestrates macrophage reprogramming through NFkappaB signaling. *Cell Death Dis* 9(7):728.
4. Kobayashi K, Usami N, Porcel E, Lacombe S, & Le Sech C (2010) Enhancement of radiation effect by heavy elements. *Mutat Res* 704(1-3):123-131.
5. Currell FV-B, Balder (2017) Physical and Chemical Processes for Gold Nanoparticles and Ionising Radiation in Medical Contexts. *Gold nanoparticles for physics, chemistry and biology*. ed Scientific W (World Scientific), pp 509-536.
6. Li S, et al. (2016) LET-dependent radiosensitization effects of gold nanoparticles for proton irradiation. *Nanotechnology* 27(45):455101.
7. Hainfeld JF, Slatkin DN, & Smilowitz HM (2004) The use of gold nanoparticles to enhance radiotherapy in mice. *Physics in medicine and biology* 49(18):N309-315.
8. Xu R, et al. (2009) Ag nanoparticles sensitize IR-induced killing of cancer cells. *Cell research* 19(8):1031-1034.
9. Liu P, et al. (2016) Silver nanoparticles outperform gold nanoparticles in radiosensitizing U251 cells in vitro and in an intracranial mouse model of glioma. *International journal of nanomedicine* 11:5003-5014.
10. Miladi I, et al. (2015) Combining ultrasmall gadolinium-based nanoparticles with photon irradiation overcomes radioresistance of head and neck squamous cell carcinoma. *Nanomedicine : nanotechnology, biology, and medicine* 11(1):247-257.
11. Porcel E, et al. (2014) Gadolinium-based nanoparticles to improve the hadrontherapy performances. *Nanomedicine: Nanotechnology, Biology and Medicine* 10(8):1601-1608.
12. Detappe A, et al. (2015) AGuIX nanoparticles as a promising platform for image-guided radiation therapy. *Cancer Nanotechnol* 6(1):4.
13. McGinnity TL, et al. (2016) Hafnia (HfO₂) nanoparticles as an X-ray contrast agent and mid-infrared biosensor. *Nanoscale* 8(28):13627-13637.
14. Pottier A, Borghi E, & Levy L (2014) New use of metals as nanosized radioenhancers. *Anticancer research* 34(1):443-453.
15. Li S, et al. (2017) Platinum nanoparticles: an exquisite tool to overcome radioresistance. *Cancer Nanotechnology* 8(1):4.
16. Porcel E, et al. (2010) Platinum nanoparticles: a promising material for future cancer therapy? *Nanotechnology* 21(8):085103.
17. Zhang X-D, et al. (2015) Ultrasmall glutathione-protected gold nanoclusters as next generation radiotherapy sensitizers with high tumor uptake and high renal clearance. *Scientific reports* 5:8669.
18. Liu Y, et al. (2015) The dependence of radiation enhancement effect on the concentration of gold nanoparticles exposed to low- and high-LET radiations. *Phys Med* 31(3):210-218.

19. Hossain M, *et al.* (2012) X-ray enabled detection and eradication of circulating tumor cells with nanoparticles. *Biosensors & bioelectronics* 38(1):348-354.
20. Huang Y, *et al.* (2014) Construction of multifunctional organic–inorganic hybrid Bi2S3–PLGA capsules for highly efficient ultrasound-guided radiosensitization of brachytherapy. *RSC Advances* 4(51):26861-26865.
21. Zhang XD, *et al.* (2012) Size-dependent radiosensitization of PEG-coated gold nanoparticles for cancer radiation therapy. *Biomaterials* 33(27):6408-6419.
22. Villanueva A, *et al.* (2009) The influence of surface functionalization on the enhanced internalization of magnetic nanoparticles in cancer cells. *Nanotechnology* 20(11):115103.
23. Ma N, *et al.* (2017) Shape-Dependent Radiosensitization Effect of Gold Nanostructures in Cancer Radiotherapy: Comparison of Gold Nanoparticles, Nanospikes, and Nanorods. *ACS Applied Materials & Interfaces* 9(15):13037-13048.
24. Penninckx S, Heuskin AC, Michiels C, & Lucas S (2018) The role of thioredoxin reductase in gold nanoparticle radiosensitization effects. *Nanomedicine (London, England)*.
25. Aguirre-Gamboa R, *et al.* (2013) SurvExpress: an online biomarker validation tool and database for cancer gene expression data using survival analysis. *PLoS One* 8(9):e74250.
26. Joo KM, *et al.* (2013) Patient-specific orthotopic glioblastoma xenograft models recapitulate the histopathology and biology of human glioblastomas in situ. *Cell Rep* 3(1):260-273.
27. Rousseaux S, *et al.* (2013) Ectopic activation of germline and placental genes identifies aggressive metastasis-prone lung cancers. *Sci Transl Med* 5(186):186ra166.
28. La Thangue NB & Kerr DJ (2011) Predictive biomarkers: a paradigm shift towards personalized cancer medicine. *Nat Rev Clin Oncol* 8(10):587-596.
29. Leone A, Roca MS, Ciardiello C, Costantini S, & Budillon A (2017) Oxidative Stress Gene Expression Profile Correlates with Cancer Patient Poor Prognosis: Identification of Crucial Pathways Might Select Novel Therapeutic Approaches. *Oxid Med Cell Longev* 2017:2597581.
30. Arner ES & Holmgren A (2006) The thioredoxin system in cancer. *Seminars in cancer biology* 16(6):420-426.
31. Dunn LL, Buckle AM, Cooke JP, & Ng MK (2010) The emerging role of the thioredoxin system in angiogenesis. *Arteriosclerosis, thrombosis, and vascular biology* 30(11):2089-2098.
32. Yoo MH, *et al.* (2007) Targeting thioredoxin reductase 1 reduction in cancer cells inhibits self-sufficient growth and DNA replication. *PLoS One* 2(10):e1112.
33. Yoo MH, Xu XM, Carlson BA, Gladyshev VN, & Hatfield DL (2006) Thioredoxin reductase 1 deficiency reverses tumor phenotype and tumorigenicity of lung carcinoma cells. *The Journal of biological chemistry* 281(19):13005-13008.
34. Kim SJ, *et al.* (2005) High thioredoxin expression is associated with resistance to docetaxel in primary breast cancer. *Clin Cancer Res* 11(23):8425-8430.
35. Iwao-Koizumi K, *et al.* (2005) Prediction of docetaxel response in human breast cancer by gene expression profiling. *Journal of clinical oncology : official journal of the American Society of Clinical Oncology* 23(3):422-431.
36. Fiskus W, *et al.* (2014) Auranofin induces lethal oxidative and endoplasmic reticulum stress and exerts potent preclinical activity against chronic lymphocytic leukemia. *Cancer research* 74(9):2520-2532.

37. Zou P, *et al.* (2015) Auranofin induces apoptosis by ROS-mediated ER stress and mitochondrial dysfunction and displayed synergistic lethality with piperlongumine in gastric cancer. *Oncotarget* 6(34):36505-36521.
38. Wang H, *et al.* (2017) Auranofin radiosensitizes tumor cells through targeting thioredoxin reductase and resulting overproduction of reactive oxygen species. *Oncotarget* 8(22):35728-35742.
39. Fan C, *et al.* (2014) Enhancement of auranofin-induced lung cancer cell apoptosis by selenocystine, a natural inhibitor of TrxR1 in vitro and in vivo. *Cell Death Dis* 5:e1191.
40. Anonymous (Sirolimus and Auranofin in Treating Patients With Advanced or Recurrent Non-Small Cell Lung Cancer or Small Cell Lung Cancer. (Clinicaltrials.org).
41. Anonymous (Phase I and II Study of Auranofin in Chronic Lymphocytic Leukemia (CLL). (Clinicaltrials.org).
42. Anonymous (Auranofin in Treating Patients With Recurrent Epithelial Ovarian, Primary Peritoneal, or Fallopian Tube Cancer. (Clinicaltrials.org).
43. Butterworth KT, *et al.* (2010) Evaluation of cytotoxicity and radiation enhancement using 1.9 nm gold particles: potential application for cancer therapy. *Nanotechnology* 21(29):295101.
44. Polf JC, *et al.* (2011) Enhanced relative biological effectiveness of proton radiotherapy in tumor cells with internalized gold nanoparticles. *Applied physics letters* 98(19):193702.
45. Hespeels F, Heuskin AC, Scifoni E, Kraemer M, & Lucas S (2017) Backscattered electron emission after proton impact on carbon and gold films: Experiments and simulations. *NIM B: Beam Interactions with Materials and Atoms* 401(Supplement C):8-17.
46. Misawa M & Takahashi J (2011) Generation of reactive oxygen species induced by gold nanoparticles under x-ray and UV Irradiations. *Nanomedicine : nanotechnology, biology, and medicine* 7(5):604-614.
47. Sicard-Roselli C, *et al.* (2014) A new mechanism for hydroxyl radical production in irradiated nanoparticle solutions. *Small* 10(16):3338-3346.
48. Sotiropoulos M, *et al.* (2017) Modelling direct DNA damage for gold nanoparticle enhanced proton therapy. *Nanoscale* 9(46):18413-18422.
49. Heuskin AC, *et al.* (2017) Metallic nanoparticles irradiated by low-energy protons for radiation therapy: Are there significant physical effects to enhance the dose delivery? *Medical physics*.
50. Wang C, *et al.* (2013) Enhancement of radiation effect and increase of apoptosis in lung cancer cells by thio-glucose-bound gold nanoparticles at megavoltage radiation energies. *Journal of Nanoparticle Research* 15(5):1642.
51. Saberi A, *et al.* (2017) Gold nanoparticles in combination with megavoltage radiation energy increased radiosensitization and apoptosis in colon cancer HT-29 cells. *International journal of radiation biology* 93(3):315-323.
52. Liu CJ, *et al.* (2008) Enhanced x-ray irradiation-induced cancer cell damage by gold nanoparticles treated by a new synthesis method of polyethylene glycol modification. *Nanotechnology* 19(29):295104.
53. Liu Y, *et al.* (2018) Metal-based NanoEnhancers for Future Radiotherapy: Radiosensitizing and Synergistic Effects on Tumor Cells. *Theranostics* 8(7):1824-1849.
54. Butterworth KT, McMahon SJ, Taggart LE, & Prise KM (2013) Radiosensitization by gold nanoparticles: effective at megavoltage energies and potential role of oxidative stress. *Translational Cancer Research* 2(4):269-279.

-
55. Jeynes JC, Merchant MJ, Spindler A, Wera AC, & Kirkby KJ (2014) Investigation of gold nanoparticle radiosensitization mechanisms using a free radical scavenger and protons of different energies. *Physics in medicine and biology* 59(21):6431-6443.
56. Schlathölter T, *et al.* (2016) Improving proton therapy by metal-containing nanoparticles: nanoscale insights. *International journal of nanomedicine* 11:1549-1556.
57. Taggart LE, *et al.* (2016) Protein disulphide isomerase as a target for nanoparticle-mediated sensitisation of cancer cells to radiation. *Nanotechnology* 27(21):215101.
58. Chiu SJ, Lee MY, Chou WG, & Lin LY (2003) Germanium oxide enhances the radiosensitivity of cells. *Radiation research* 159(3):391-400.
59. Mirjolet C, *et al.* (2013) The radiosensitization effect of titanate nanotubes as a new tool in radiation therapy for glioblastoma: A proof-of-concept. *Radiotherapy and Oncology* 108(1):136-142.

Thioredoxin reductase activity predicts gold
nanoparticle radiosensitization effect
- Supplementary information -

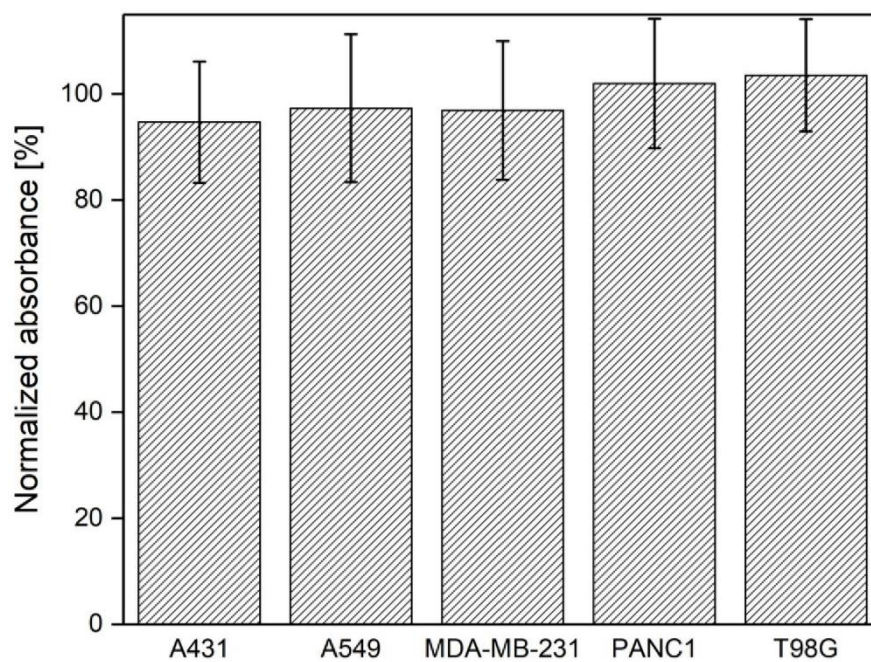


Figure S1. Cell viability of different cell lines incubated in the presence of $50 \mu\text{g}$ of gold.mL^{-1} for 24 h and assessed using a MTS assay. Data represent the mean absorbance relative to untreated control cells ± 1 S.D. for three independent experiments using 10 nm GNPs. Results were statistically analyzed using a one-way ANOVA evidencing no significant difference (Tukey test).

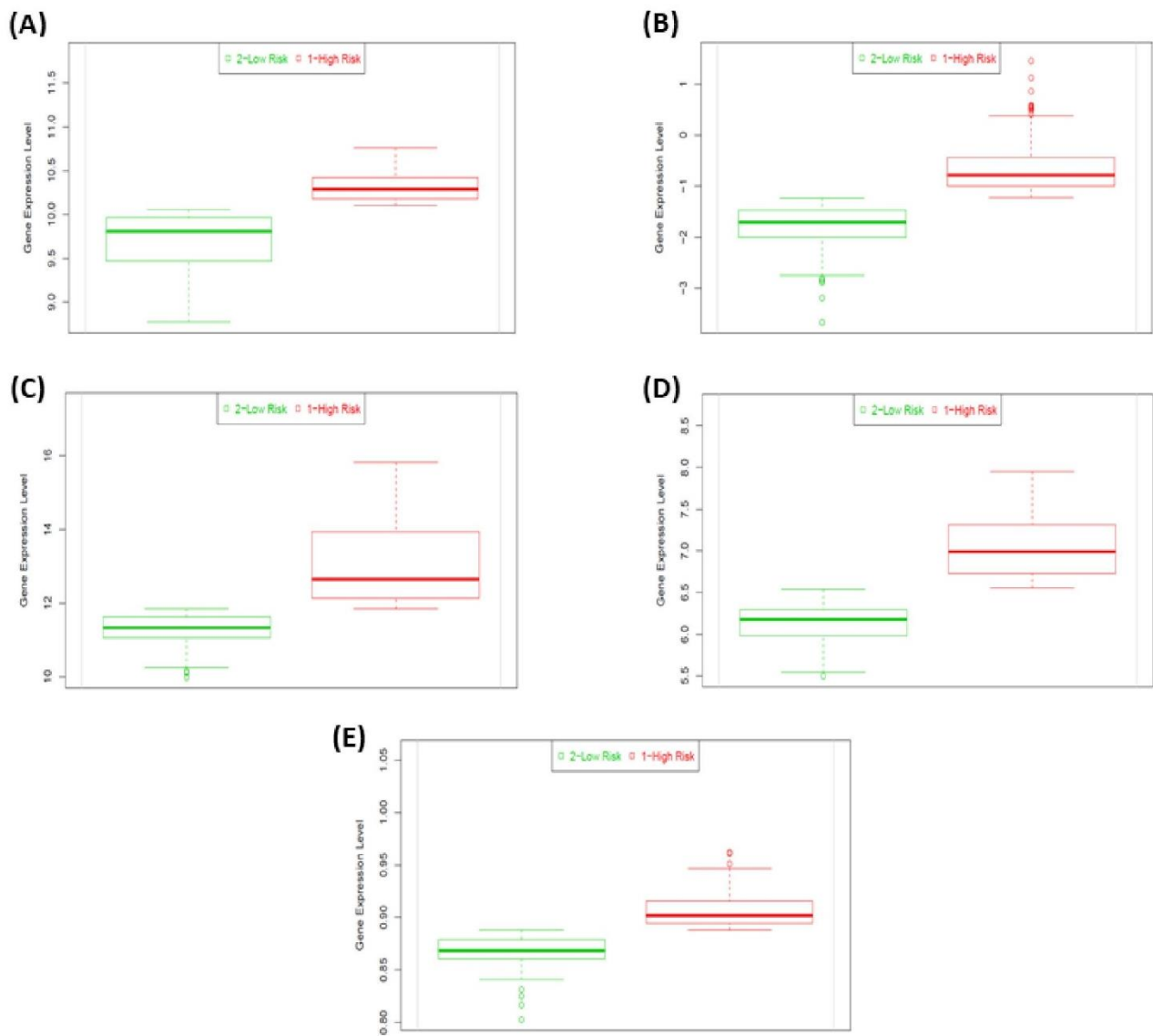


Fig S2. Box plot of TXRND1 mRNA expression across the two expression groups for (A) brain (GSE42669), (B) breast (TCGA-BRCA), (C) head & neck (TCGA-HNSC), (D) lung (GSE 30219) and (E) pancreas (PACA-AU) cancer datasets. P-values were calculated using t-test.

8. Towards a clinical use of GNPs as radiosensitizers

8.1. Context and goal of the study

Although we demonstrated the potential of GNPs as *in vitro* radiosensitizers, their use for *in vivo* biomedical applications still remains challenging. In fact, blood circulation times of GNPs as well as their biodistribution were found to be dependent on several factors including the NP size and the surface coating. Many groups reported that plasma proteins in blood can adsorb onto the surface of bare NPs leading to the formation of large aggregates that may alter their pharmacokinetics. To overcome this, PEG coating was found to minimize non-specific adsorption of proteins onto particles leading to a more stable formulation across time [174]. Several works highlighted an unequal distribution of GNPs depending on their size [175]. After intravenous injection into rats, De Jong et al. [176] demonstrated, using GNPs ranging from 10 to 250 nm, that GNPs have been taken up primarily by the liver and spleen but 10 nm GNPs was more broadly distributed in various organs compare to bigger ones. Moreover, they reported a higher amount of 10 nm GNPs in tumor. This NP ability to passively leak into a tumor is known as EPR phenomenon. As discussed in introduction section, due to their relatively smaller size compared to the typical cutoff size of tumor vasculature pores (up to 400 nm), NPs can leak into the tumor interstitium from blood vessels and enter into the tumor [177].

For an efficient treatment, NPs would have the ability to accumulate in the desired cell/tissue/organ in order to avoid side-effects to the healthy tissue. Thereby, the development of targeted NPs was growing e.g. NPs capable of overcoming the successive physiological barriers they will encounter and which can recognize the target cancer cells. To achieve it, many strategies were imagined including the conjugation of different moieties to NPs. These moieties can be low-molecular weight ligands (such as folic acid [178]), peptides [179], ...), polysaccharides (such as chitosan [180]) and so forth.

In this manuscript, the active targeting moiety used was the cetuximab, a monoclonal antibody that has a high affinity for epithelial growth factor receptor (EGFR, an overexpressed receptor in many types of carcinomas). We described the successful antibody conjugation to the GNPs surface as well as the chemical characterizations made on this new nano-objects. The affinity of the conjugated GNPs for the EGFR was assessed using two different cell lines: A431 cells – a human epidermoid carcinoma cell line overexpressing EGFR; and MDA-MB 453 cells - a human breast carcinoma cell line that does not express EGFR. Finally, we investigated whether this targeting influenced the radiosensitizing effect.

8.2. Fourth manuscript: “Antibody-functionalized gold nanoparticles as tumor targeting radiosensitizers for proton therapy” – Nanomedicine 2019.

Research Article

For reprint orders, please contact: reprints@futuremedicine.com

Nanomedicine



Antibody-functionalized gold nanoparticles as tumor targeting radiosensitizers for proton therapy

Sha Li^{‡,1}, Sandra Bouchy^{‡,2}, Sébastien Penninckx^{‡,1}, Riccardo Marega¹, Ornella Fichera¹, Bernard Gallez³, Olivier Feron⁴, Philippe Martinive⁵, Anne-Catherine Heuskin¹, Carine Michiels^{*,2} & Stéphane Lucas¹

¹Research Center for the Physics of Matter & Radiation (PMR-LARN), Namur Research Institute for Life Sciences (NARILIS), University of Namur, B-5000 Namur, Belgium

²Unité de Recherche en Biologie Cellulaire (URBC), Namur Research Institute for Life Sciences (NARILIS), University of Namur, B-5000 Namur, Belgium

³Biomedical Magnetic Resonance Group (REMA), Louvain Drug Research Institute, Université Catholique de Louvain, B-1200 Woluwé, Saint Lambert, Belgium

⁴Pole of Pharmacology & Therapeutics (FATH), Institut de Recherche Expérimentale et Clinique (IREC), UCL (Université Catholique de Louvain), B-1200 Brussels, Belgium

⁵Department of Radiotherapy & Oncology, CHU & University of Liège, B-4000 Liège, Belgium

*Author for correspondence: Tel.: +32 81 724 131; carine.michiels@unamur.be

[‡]Authors contributed equally

Aim: This study aimed at developing antibody-functionalized gold nanoparticles (AuNPs) to selectively target cancer cells and probing their potential radiosensitizing effects under proton irradiation. **Materials & methods:** AuNPs were conjugated with cetuximab (Ctxb–AuNPs). Ctxb–AuNP uptake was evaluated by transmission electron microscopy and atomic absorption spectroscopy. Radioenhancing effect was assessed using conventional clonogenic assay. **Results & conclusion:** Ctxb–AuNPs specifically bound to and accumulated in EGFR-overexpressing A431 cells, compared with EGFR-negative MDA-MB-453 cells. Ctxb–AuNPs enhanced the effect of proton irradiation in A431 cells but not in MDA-MB-453 cells. These data indicate, for the first time, that combining enhanced uptake by specific targeting and radioenhancing effect, using conjugated AuNPs, is a promising strategy to increase cell killing by protontherapy.

First draft submitted: 8 May 2018; Accepted for publication: 14 November 2018; Published online: 24 January 2019

Keywords: EGFR • gold nanoparticles • nanoparticle uptake • protontherapy • radiosensitizing effects

Radiotherapy is mainly limited by two factors: the tolerance to the irradiation of healthy tissues surrounding tumors and tumor radioresistance. One of the main strategies proposed to improve the selectivity of radiation effects is to use targeted nanoagents able to enhance the efficacy of tumor targeting and to amplify the effects of radiations. Experimental and simulation works have demonstrated that gold nanoparticles (AuNPs) enhance the effect of radiation in combination with kilovolt (kV) photons, megavolt (MV) photons, electrons and charged particles (H^+ , C^{6+}) [1–7]. AuNPs are expected to improve the effects of the radiation by their ability to increase the dose deposition in the target volume or to locally increase the temperature. Indeed, after activation by radiation, electron bursts are emitted in the close vicinity of the nanoparticles (NPs) leading to the production of water radical clusters [8,9]. These early-stage mechanisms (up to 1 s at most after interaction) are responsible for the induction of damage to biomolecules [9]. A pioneering study carried out by Hainfeld *et al.* has demonstrated the effect of AuNPs to amplify x-ray radiation effect, by using AuNP intravenous injection in mice bearing a subcutaneous mammary carcinoma: a 1-year survival of 86% with AuNPs + 250 kVp x-rays was observed compared to 20% with radiation alone [10].

Recently, great efforts have been devoted to the development of active targeting with nanoparticles, for example, through their conjugation to tumor-specific ligands [11]. The EGF receptor (EGFR) is an attractive candidate for anticancer therapy [12]. Indeed, overexpression of EGFR has been reported in many types of human carcinoma [13]

Future
Medicine

and has led to the development of various EGFR-targeted therapies [14–16]. Cetuximab (Ct**xb**; Erbitux®) is a mouse–human chimeric monoclonal antibody that binds the EGFR with high affinity. It has been approved as a first line of treatment for metastatic colorectal cancer [17] but also in non-small-cell lung cancers as well as in head and neck cancers [18]. Also, strategies to conjugate Ct**xb** to other therapeutic compounds or nanoobjects have been developed.

Several studies have, for instance, reported that Ct**xb**-conjugated AuNPs are able to target EGFR *in vitro* and *in vivo*, leading to enhanced cellular internalization of the targeted nanoparticles and therapeutic outcomes [19–22].

To date, very few studies have yet reported the effect of tumor-targeting nanoparticles in combination with heavy particle therapy. The use of heavy particle therapy (protons or carbon ions) in clinical practice has become more prevalent over the past 20 years, driven by their attracting physical properties. Proton beam deposits most of the proton energy at the end of the proton range (Bragg peak) in a targeted volume. Tissues behind the tumor, in contrast to conventional radiotherapy, are nearly completely protected. One of our previous studies has shown that amine–PEG-functionalized AuNPs successfully enhanced the effect of radiation of 25 keV μm^{-1} protons [23]. Simulation studies showed dose possible enhancement effect by AuNPs for protons. However, an intracellular AuNP concentration at least two orders of magnitude higher than what was achieved in the latter study is needed to generate these effects [1,24]. To increase the amount of gold accumulation inside the cancer cells but also with the aim of increasing their specificity, the major goal of this work was to develop EGFR-targeting AuNPs and to probe their effects in combination with protons.

Here, we describe the successful conjugation of Ct**xb** to the surface of AuNPs. The binding affinity of Ct**xb**–AuNPs to A431 cells – a human epidermoid carcinoma cell line expressing high levels of EGFR (EGFR⁺) – was much higher than the one to MDA-MB 453 cells – a human breast carcinoma cell line that does not express EGFR (EGFR[−]). Furthermore, a clear radiosensitizing effect was evidenced in combination with protons.

Materials & methods

Chemical materials

All chemicals were purchased from commercial sources and used without further purification except if explicitly mentioned. Allylamine and COMU (1-cyano-2-ethoxy-2-oxoethylidenaminooxy-dimethylamino-morpholinocarbenium hexafluorophosphate) were obtained from Sigma-Aldrich, Overijse, Belgium. Water was purified using a Millipore Milli-Q water production system. Commercially available Ct**xb** formulation (Erbitux 2 or 5 mg ml^{−1}, Merck & Co., Darmstadt, Germany) was purified by discontinuous diafiltration in centrifugal concentrators with a molecular weight cutoff (MWCO) of 10,000 g mol^{−1} (Sartorius Vivaspin, Goettingen, Germany) and the purified antibody (Ab) was freeze-dried.

Synthesis of AuNPs & antibody conjugation

Synthesis of AuNPs coated with plasma-polymerized allylamine by plasma vapor deposition has already been reported [25]. The resulting polyallylamine-coated nanoparticles were then dispersed in acetate buffer (pH 5) under 10 min of sonication and then purified from the plasma-polymerized allylamine and NaCl excess by discontinuous diafiltration in centrifugal concentrators with an MWCO of 10,000 g mol^{−1}. Ct**xb** (17 mg) was dissolved in 17 ml of 0.1 M phosphate-buffered saline (PBS; pH 7.4), and then a solution of COMU at 30.5 mg in 20.4 ml of 0.1 M PBS was added. The resulting mixture was stirred at 25°C for 15 min, after that 12.35 mg of AuNPs (Au amount) was then added by using a water solution of AuNPs (11 ml) with an Au concentration of 1.12 mg/ml. The reaction was stirred at 25°C for 4 h, after which it was purified by discontinuous diafiltration against H₂O in centrifugal concentrators with MWCO of 300,000 g mol^{−1}. Purification was completed when the electrical conductivity of the filtrate was less than four-times the conductivity of the deionized water used during the discontinuous diafiltration (around 1 $\mu\text{S}/\text{cm}$). This decrease of about 2000-times in the electrical conductivity is related to the progressive removal of the salts and excess reagents (antibody, coupling agent) from the reaction mixture thanks to the membrane-based separation (Supplementary Figure 1 & Table 1). Ct**xb**–AuNPs were lyophilized through freeze-drying system (Alpha 2–4 LD Plus, Analis, Namur, Belgium), providing a pinkish red powder (9.57 mg). Ct**xb**–AuNPs were stored under inert atmosphere at 4°C for further utilization. Prior to being incubated with cells, the lyophilized nanoparticles were resuspended in cell culture medium and sonicated for 15 min.

Characterization

The size distribution of the nanoparticles was first determined by disc centrifuge (CPS Instruments Europe, Oosterhout, The Netherlands). This method estimates the 'hydrodynamic size', as measured by dynamic light scattering, to be 'the size of a hypothetical hard sphere that diffuses in a liquid in the same fashion as that of the particle being measured. In practice though, particles or macromolecules in solution are nonspherical, dynamic (tumbling) and solvated, hence the terminology, hydrodynamic diameter' [26].

Transmission electron microscopy (TEM) images were acquired with a Philips Tecnai 10 transmission electron microscope operating at 80 keV and in bright-field mode. Samples for TEM analysis were obtained by deposition of AuNPs and Ctxb–AuNPs solutions onto carbon-coated Cu grids. UV–vis spectra were recorded on a UV/vis spectrophotometer SPECORD® 205, using 1-cm path quartz or optical glass cuvettes. To assess the proportion of Ctxb conjugated to AuNPs, a set of thermogravimetric measurements, atomic absorption spectroscopy (AAS) and protein quantification assays (Thermo Scientific Pierce 660-nm assay) were conducted. Thermogravimetric analysis (TGA) was carried out with a TGA 4000 apparatus from Perkin Elmer, by treating the samples placed in Pt pans with the following procedure: isotherm at 100°C for 20 min (to remove residual solvent, if any), ramp from 100 to 1000°C at 10°C·min⁻¹ air (flow rate on the sample of 90 ml·min⁻¹). The Ctxb content of the samples was quantified by plotting the calibration curve with known concentrations of Ctxb, desalted by discontinuous diafiltration of Erbitux 5 mg ml⁻¹ solutions in centrifugal concentrators of 10,000 Da cutoff (Millipore Amicon 15, Burlington, MA, USA), used for external calibration. Absorbance at 660 nm of wells containing defined amounts of Au (7–8 µg Au/well, as determined by AAS) of both AuNPs and Ctxb–AuNP were recorded before and after addition of the colorimetric reagent using a spectrophotometer (X-Mark™ Microplate Spectrophotometer, BioRad, Hercules, CA, USA). Linear regression of the calibration curve, and absorbance subtraction between Ctxb–AuNP and AuNPs allowed to estimate the Ctxb content. The detailed explanation of this experimental part is proposed in Supplementary Information 2.

Cell culture

A431 cells and MDA-MB-453 cells were grown, respectively, in a Dulbecco's modified Eagle's complete medium (DMEM; 4.5 g l⁻¹ D-glucose, Gibco® by Life Technologies, MA, USA) or Roswell Park Memorial Institute medium (RPMI 1640, Gibco by Life Technologies, MA, USA), containing 10% (v:v) fetal bovine serum (FBS, Gibco by Life Technologies) at 37°C in a humidified atmosphere incubator containing 5% CO₂. A431 cells are known to expressed very high level of EGFR compared with other cancer cell types [27]. It has been estimated that A431 cells display 1.2×10^6 molecules of EGFR per cell [28]. On the other hand, the literature reports that MDA-MB-453 cells are negative for this receptor [29]. In order to confirm these data, we assessed, by RT-qPCR, the mRNA level of the EGFR in the two cell lines cultivated in our laboratory and used for the experiments described in the manuscript. The cycle threshold was 18.5 for A431 cells and 31.5 for MDA-MB-453 cells, indicating a 8×10^6 -fold difference.

Cell viability assay

MTS (3-(4,5-dimethylthiazol-2-yl)-5-(3-carboxymethoxyphenyl)-2-(4-sulfophenyl)-2H-tetrazolium) assay was used to measure the viability of cells incubated (or not) with Ctxb–AuNPs at different concentrations. In this study, 10,000 cells were seeded in 96-well plate. 24 h later, culture medium containing different concentrations of Ctxb–AuNPs was added. After 30 min of incubation, the cells were washed with PBS and 120 µl of culture medium containing MTS (Cell Titer 96® Aqueous One Solution Reagent, Promega, Madison, WI, USA) in a 5:1 ratio was added in each well. After 1 h of incubation with MTS tetrazolium compound, the optical density was determined at 490 nm using a spectrophotometer (X-Mark Microplate Spectrophotometer, BioRad, Hercules, CA, USA).

Surface ELISA

A431 cells or MDA-MB-453 cells were seeded at 10,000 cells per well, in 96-well plates (Costar, Sigma–Aldrich, Overijse, Belgium) 24 h prior to the ELISA test. Cells were rinsed once with PBS and then fixed 10 min with PBS containing 4% para-formaldehyde. After one wash with PBS, wells were blocked with 5% of nonfat dry milk in PBS for 1 h at room temperature. Cells were rinsed one time with PBS and one time with BSA 1% in PBS for 5 min. Ctxb or Ctxb–AuNPs were added to the cells at various concentrations for 1 h at room temperature. Plates were washed three-times with PBS–BSA, and a mouse monoclonal antihuman IgG–biotin antibody (Sigma) diluted in

Research Article Li, Bouchy, Penninckx et al.

PBS-BSA at 1 mg ml⁻¹ was added for 1 h at room temperature. Cells were washed three-times and incubated with streptavidin-alkaline phosphatase (Sigma) for 30 min at room temperature. After three washing steps with PBS-BSA and one with PBS, alkaline phosphatase activity was revealed with 1 mg ml⁻¹ *p*-nitrophenylphosphate in 0.1 M diethanolamine pH 10.3 containing 1.5 mM levamisole hydrochloride. The reaction was stopped with NaOH 2 N and the surface expression was quantified spectrophotometrically, by reading the optical density (405 nm) 45 min after addition of the substrate. Since AuNPs do absorb at 405 nm, for each AuNP concentration interfaced with cells, corresponding wells without cells but with culture medium were also incubated in exactly the same experimental conditions. Afterwards, all the washing and incubation steps were performed exactly using the same procedure for wells containing cells and wells without cells. At the end, when the absorbance is measured, the absorbance of the wells without cells was subtracted from the one of the corresponding wells with cells [30].

Intracellular distribution of nanoparticles

TEM was performed to precisely localize the position of intracellular nanoparticles. Cells were first fixed for 2 h at 4°C with 2.5% (w/v) glutaraldehyde (Agar Scientific) in 0.1 M cacodylate buffer (pH 7.4). Cells were washed with cacodylate buffer and subsequently post-fixed in 1% (v/w) osmium tetroxide (Merck Chemicals, Darmstadt, Germany). Samples were dehydrated by successive passages in increasing concentration of ethanol (30, 50, 70, 85 and 100%). After embedding in epon resin LX 112 (Ladd Research Industries, Williston, VT, USA), ultrathin sections of cells were prepared for TEM analysis using an 8800 ultratome III (LKB, Thermo Fisher Scientific, Asse, Belgium). They were then stained with uranyl acetate and lead citrate. Observations were performed with an FEI Technai 10 TEM (Philips, FEI Inc., OR, USA) [31].

Cell uptake analysis by atomic absorption microscopy

To verify and quantify a possible time-dependent amount of Au internalization by the selected cell lines, a combination of cell incubation experiments, cell mineralization and mineralized samples analysis by AAS was carried out. To avoid possible interferences of serum components into the targeting properties of the materials, the incubations occurred under serum-free conditions.

Briefly, A431 and MDA-MB-453 cells were incubated with 5 µg Au ml⁻¹ of AuNPs (Au amount) in a FBS-free medium for 30 min at 37°C under 5% CO₂. After incubation, cells were first washed with cell medium, then with PBS and finally trypsinized at 37°C. Detached cells were resuspended in complete cell medium and centrifuged. The actual number of cells in each sample was then determined using a cell counter (Countess Automated Cell Counter, Invitrogen, Carlsbad, CA, USA). After the centrifugation, the medium was discarded, and the cells were digested using 1 ml of aqua regia (37 wt% HCl, 65 wt% HNO₃; Sigma-Aldrich) overnight. The Au content of the samples was quantified using an atomic absorption spectrophotometer (AA-7000F from Shimadzu) by plotting the calibration curve with known concentrations of an Au standard solution (Merck Chemicals, Belgium) used for external calibration. Triplicate readings were analyzed for each sample. The amount of Au detected into the cells was expressed as internalized Au quantity (pg) per cell.

Proton irradiation

Detailed protocols were described in our previous report [23]. Briefly, 24 h before irradiation, the sterilized home-made irradiation chambers were pretreated 20 min with 15 µl of human fibronectin (PHE0023, Gibco by Life Technologies, MA, USA) to allow cell adhesion. Then, 40,000 of either A431 or MDA-MB-453 cells were seeded as a 32-µl drop at the center of the irradiation chambers. These irradiation chambers were then closed with a plastic cap to avoid dehydration and contamination and were placed in an incubator at 37°C with 5% CO₂. 2 h after seeding, the drop was rinsed twice with PBS to remove nonadherent cells. For both cell lines, attached cells formed monolayers. The irradiation chambers were then filled with FBS-free medium (control group) or with FBS-free medium containing 5 µg Au ml⁻¹ of Ctxb-AuNPs and placed in the incubator for 30 min.

On the day of irradiation, the medium was discarded from the irradiation chamber, the plastic cap was removed and a sterile cotton swab was used to take away the cells, which may have diffused outside the irradiation field. The irradiated chamber was then closed with the plastic cap, rinsed with PBS and filled with CO₂-independent medium (Gibco by Life Technologies, MA, USA).

The cell monolayer was irradiated with a homogenous broad proton beam defocused over 1 cm² area, produced by a 2 MV Tandem accelerator (High Voltage Engineering Europa). The reader is referred to [32] for a thorough description of the experimental setup and the irradiation procedure. Briefly, 1.3 MeV pristine proton beam was

extracted in air through a 1- μm silicon nitride window. The linear energy transfer (LET) at the cell sample location was computed using SRIM software [33], using three stacked layers representing the setup: 1 μm Si_3N_4 exit window, a small 3 mm air gap between the exit window and the cell dish, and the 3 μm mylar foil constituting the bottom of the irradiation dish. The energy of transmitted particles was averaged and the LET was obtained for this average proton energy. In this study, a 25 $\text{keV } \mu\text{m}^{-1}$ LET value, corresponding to an energy of 1.3 MeV in vacuum, was chosen to obtain the maximum relative biological effectiveness for a proton beam for A431 cells as determined in Li *et al.* [23]. The irradiation chambers were placed vertically on a sample holder fixed at the end of the beamline. Cell samples were thus positioned perpendicularly to the incoming beam. Homogeneity was achieved by defocusing the beam and checked using a passivated implanted planar silicon detector moved along x and y directions. Dose rate was assessed every millimeter in a 1 cm^2 surface with errors less than 5% in the cell sample region. The dose rate was fixed to 2 Gy min^{-1} and the particle flux was accordingly adjusted using the classic broad beam formula [34] as shown below (Equation 1):

$$D = \frac{1.610^{-9} \text{ LET } \Phi}{\rho} \quad (\text{Equation 1})$$

Here, the density ρ is taken as 1 g cm^{-3} and Φ is the proton beam flux in $\text{part cm}^{-2} \text{ s}^{-1}$. The dose range was chosen to cover survival fraction down to 1%.

Clonogenic assay

Immediately after irradiation, cells were detached using trypsin and the cell numbers were counted. The cell numbers were counted by Moxi™ Z-automated cell counter (Orflow). It provides an assessment of cell culture viability to report the standardized Moxi Viability Index (MVI). MVI is a ratio of the cell population of interest relative to the entire particle distribution in that sample, factoring in dead cells that have shrunk or broken apart as well as other debris and contaminants in the sample. In this work, all the cell samples had a $\text{MVI} \geq 0.90$.

In order to obtain countable colony numbers for different doses of irradiation, different numbers of cells were seeded in six-well plates containing DMEM medium (A431) and RPMI (MDA-MB-453) supplemented with serum and penicillin/streptomycin and incubated at 37°C with 5% CO_2 . 8 (A431) and 11 (MDA-MB-453) days postirradiation, respectively, colonies were stained with violet crystal in 2% ethanol. The numbers of visible colonies (containing 50 or more cells) were considered to represent surviving cells and were manually counted. The plating efficiency (PE) was determined for each dose of irradiation and calculated by dividing the number of colonies by the initial number of seeded cells. The surviving fraction was obtained as the ratio of the PE for the irradiated cells to the PE for control cells. The control cells underwent the exact same procedure, including the trypsinization step, except the irradiation step. At least three independent experiments were performed for each condition and the errors were evaluated as standard deviation (S.D.).

The efficiency of Ctxb-AuNPs to amplify radiation-induced A431 cell death was evaluated by calculating the sensitization enhancement ratio (SER):

$$\text{SER(NPS)} = \frac{D_{10\%}^{\text{control}}}{D_{10\%}^{\text{NPs}}}$$

Here, the $D_{10\%}^{\text{NPS}}$ and $D_{10\%}^{\text{control}}$ represent the dose required to achieve 10% surviving fraction for cells preincubated with nanoparticles and without nanoparticles, respectively.

DMSO treatment

Immediately prior to irradiation, the irradiation chambers were filled with CO_2 -independent medium containing 1 M DMSO or just the medium for control samples. Studies have shown that this concentration is nontoxic for a short duration [4]. Cells were irradiated with a proton beam of 25 $\text{keV } \mu\text{m}^{-1}$, at a dose rate of 2 Gy min^{-1} . Directly after the irradiation, cells were trypsinized for clonogenic assays.

Statistical analysis

All of the experiments were repeated in triplicate on separate days. All curve fittings were performed with OriginLab® software (Northampton, USA). A linear-quadratic equation was used to fit clonogenic assay data:

$$SF = e^{-(\alpha D + \beta D^2)}$$

Where SF is the surviving fraction of the cells; α and β define the linear and the quadratic components, respectively, and D is the deposited dose.

To evaluate the differences between the experimental and corresponding control samples, the data were analyzed using analysis of variance (ANOVA) for repeated measures.

Results

AuNP synthesis & characterization

To determine both the morphology and the size distribution of the synthesized nanoparticles, AuNPs and Ctxb–AuNPs were directly deposited onto a TEM grid. The observations revealed the presence of spherical objects (the Au cores) with an average size between 3 and 5 nm and a maximum at 4 nm (Figure 1A & B, Supplementary Information 3).

Disc-centrifuge analysis showed that AuNPs display a peak centered at 4–5 nm (Figure 1C). This result is in complete agreement with the one obtained by TEM. After bioconjugation of Ctxb–AuNPs, the size distribution shows a peak at around 40 nm (Figure 1C). For the observation in TEM, the hydration layer is not present due to the sample preparation procedures involved that includes dehydration. Furthermore, the organic part can shrink during this preparation procedure. Finally, due to the low contrast of the organic moieties (essentially composed by low atomic numbers atoms: H, C, N, O, and S compared with Au) in TEM, this part could be underestimated. Hence, the hydrodynamic diameter estimated by disc centrifuge (Figure 1C) is greater than the size estimated by TEM (Figure 1B).

Zeta potential measurement of the colloidal solutions of AuNPs showed a decrease of around 9 mV after the bioconjugation step, and that the incubation of these colloids in serum-supplemented cell culture medium determines a ‘neutralization’ of the zeta potential value that shifts toward 0 mV (Supplementary Information 4). The absorption spectrum of Ctxb (Figure 2A) displayed the typical proteinic signature at 280 nm (aromatic amino acids), and the characteristic absorption peak of peptide at 220 nm. Such absorption features are further highlighted in the first derivative plot (dAbs/dλ). As expected, the AuNP absorption spectrum shows the surface plasmon feature at 525 nm, characteristic of small-sized AuNPs (Figure 2B) and obviously none of the ‘protein signatures’ found in the derivative plot of Ctxb. In the UV–vis traces of Ctxb–AuNP, one can notice the contemporaneous presence of the surface plasmon absorbance (at 535 nm) and the protein signatures of Ctxb, as previously described for similar Ctxb–AuNP bioconjugates [30]. The approximate 10-nm redshift in the SPR peak of Ctxb–AuNP can be due to a combination of the alterations in the local refractive index owing to the presence of a layer of antibody molecules on the surface of AuNPs, and the presence of some agglomerated AuNPs, as seen in the TEM images in Figure 1B.

To assess the proportion of Ctxb conjugated to AuNPs, a set of TGA, AAS and protein quantification assays were conducted (see the detailed procedure in Supplementary Information 2). As already shown for different Ctxb–nanomaterial bioconjugates [30,35,36], TGA is a useful tool to discriminate between the organic and inorganic moieties of nanomaterials. TGA of Ctxb shows a decomposition occurring in the range between 100 and 800°C, with a residual weight at 950°C close to 0%, while AuNPs typically show decomposition between 100 and 500°C, due to the polyallylamine moiety (around 30 wt%, thus ~5.0 μmol allylamine mg⁻¹ of AuNPs). Ctxb–AuNPs TGA plots clearly indicate an augmented weight loss (around 60%), which is thus also due to the Ctxb loading. Most importantly, the TGA provides direct estimation of the Au amount in each sample, which is related to the residual weight found in both AuNPs (around 70%) and Ctxb–AuNP (40–45 wt%, depending on the batches). Next, a colorimetric assay based on external calibration curve with Ctxb, and wells incubated with the same Au amounts for both AuNPs and Ctxb–AuNP, revealed very similar composition findings (Supplementary Information 2 & 5). By these assays, it was possible to estimate the average product composition of Ctxb–AuNPs as 32 wt% (± 9 wt%) Ctxb, 47 wt% (± 6 wt%) for gold and 21 wt% (± 3%) for polyallylamine (n = 6). It should be pointed out that all of the following biological studies rely on the use of aliquots originating from stock solutions where the exact Au amount was determined by AAS, for both AuNPs and Ctxb–AuNP. Nonetheless, these composition values can

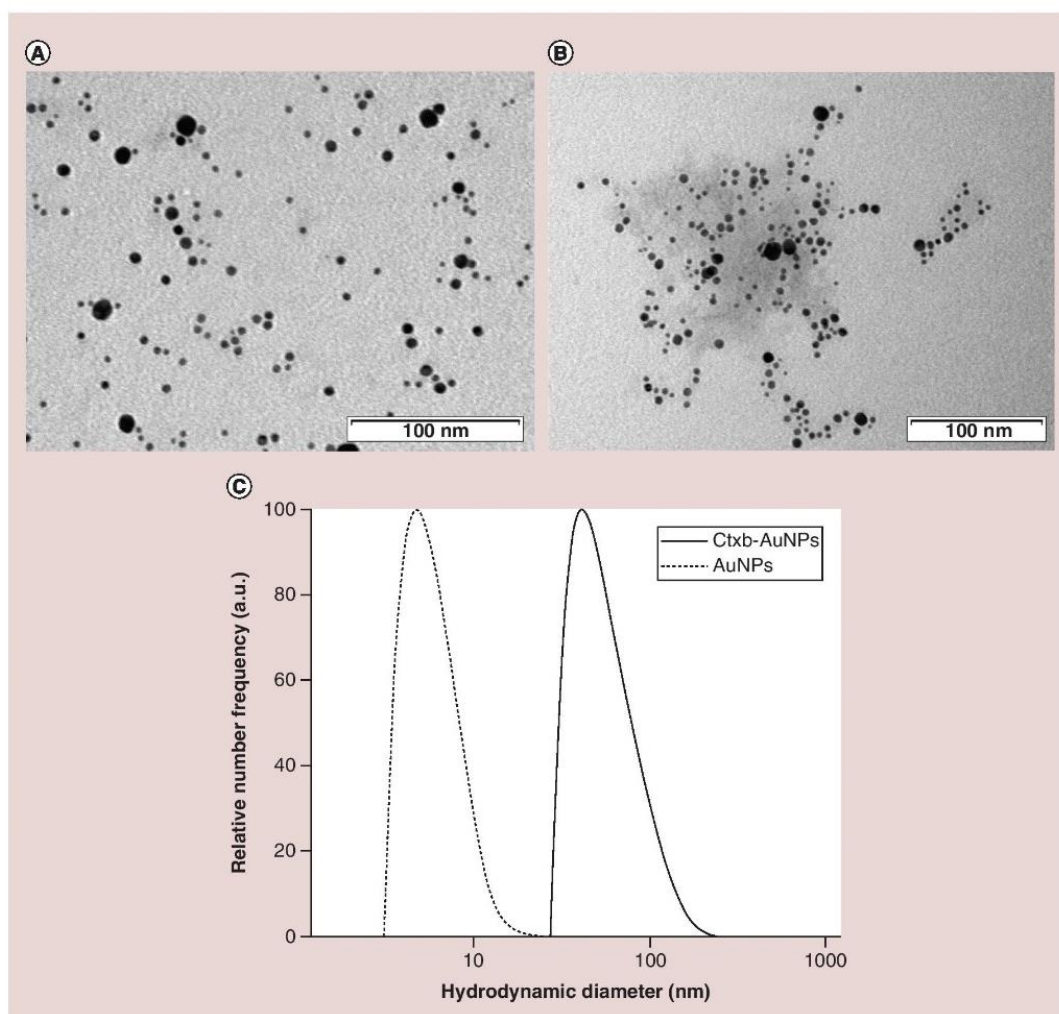


Figure 1. Characterization of gold nanoparticles and gold nanoparticles conjugated with cetuximab. TEM images of AuNPs (A) and Ctxb-AuNPs (B), scale bar: 100 nm. (C) Size distribution of AuNPs before bioconjugation and after bioconjugation analyzed by analytical disc centrifuge (a.u. = arbitrary units). AuNP: Gold nanoparticle; Ctxb: Cetuximab; TEM: Transmission electron microscopy.

be used to prepare solutions with equivalent Ctxb amounts to those determined in the Ctxb-AuNP ones, useful for the biological studies (ELISA, cytotoxicity, proton irradiation), and to estimate the number of Ctxb molecules per AuNPs. In this latter case, recent literature shows how, after performing site-oriented coupling procedures, it is possible to investigate at the microscopic scale (TEM imaging) the precise antibody loading and orientation [35]. In our case, we used the bulk composition values to estimate the average number of Ctxb molecules per particle (for a given AuNPs diameter), in line with the report by Kao *et al.* [22], who performed a similar quantification study.

It should be pointed out that this is an averaged (and thus only indicative) assessment, due to the nonoriented coupling procedure, the polydispersity of AuNPs and the probability of having a distribution also in terms of the actual number of Ctxb molecules coupled to AuNPs having the same size. By a series of assumptions and cross comparison between the compositional data, calculations, size distribution values and by comparison with literature findings, we estimate to have diameter-dependent loading of Ctxb/AuNPs that, for the most frequent sizes of 5 and 6 nm falls in the range of a theoretical ratio of 2–3 antibody molecules/nanoparticle (Supplementary Information 5).

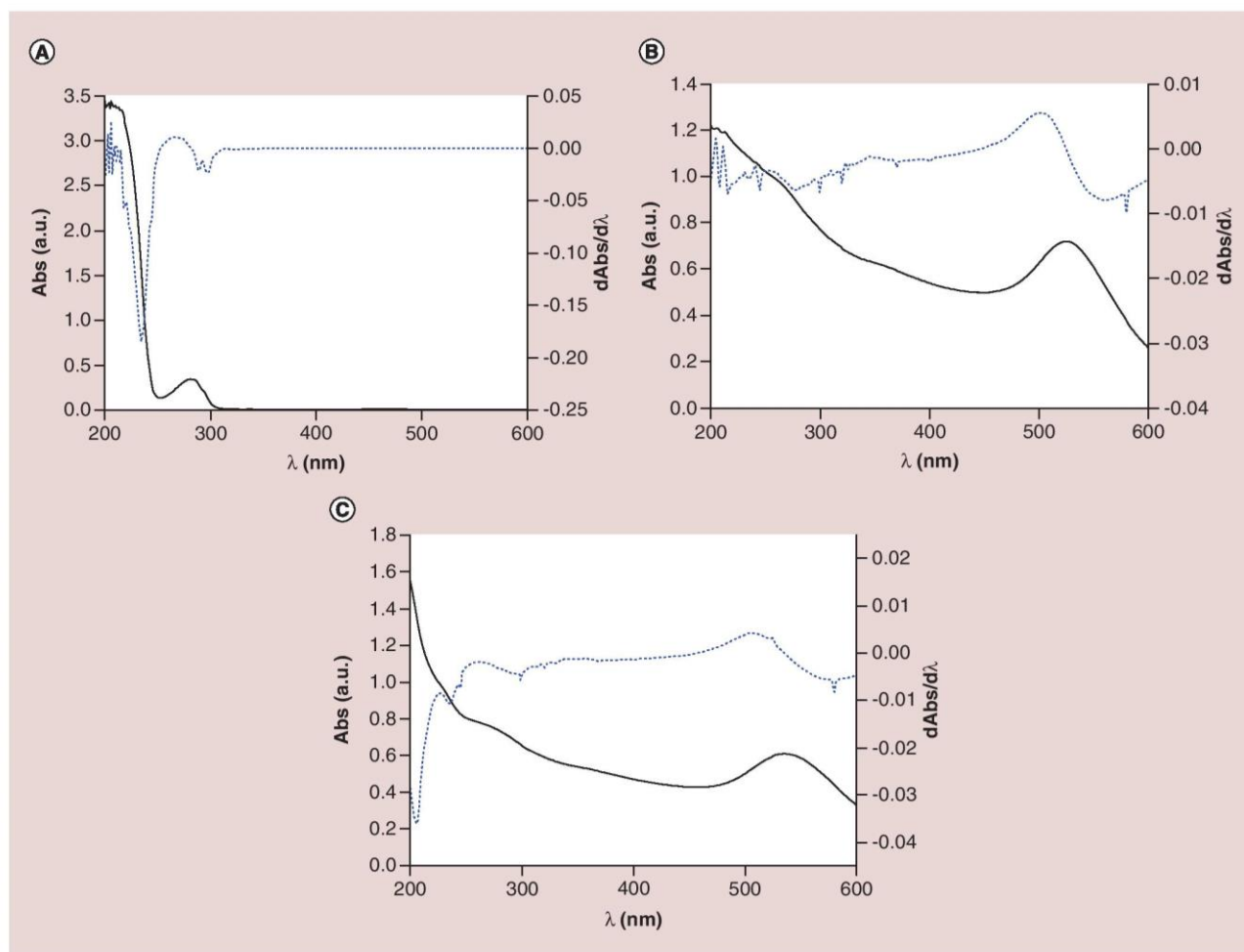


Figure 2. Characterization of AuNPs and Ctxb-AuNPs. Steady-state UV-vis absorption spectra (solid line) and derivative plots $d\text{Abs}/d\lambda$ (dot line) for cetuximab (A), AuNPs (B) and Ctxb-AuNPs (C). AuNP: Gold nanoparticle; Ctxb: Cetuximab.

In vitro evaluation of EGFR targeting

An ELISA was used to examine the relative binding affinity of Ctxb-AuNPs toward EGFR-overexpressing cells. To this end, different concentrations of Ctxb and of Ctxb-AuNPs were tested both on EGFR⁺ and EGFR⁻ cells (Figure 3).

As expected, Ctxb bound to EGFR⁺ cells in a concentration-dependent manner. On the other hand, there was no binding to EGFR⁻ cells. In our experimental setup, Ctxb binding saturated at a concentration of $0.32 \mu\text{g ml}^{-1}$ that corresponds to around 7×10^{14} Ctxb molecules per ml or 5×10^6 Ctxb molecules per A431 cell. Interestingly, Ctxb-AuNPs also bound to EGFR⁺ cells in a concentration-dependent way. Moreover, the binding increased almost linearly with the concentration of Ctxb without saturation in the studied concentration range, suggesting the retention of the correct antibody conformation for the epitope selection and interaction in Ctxb-AuNPs conjugates. A small portion of unspecific binding of Ctxb-AuNPs to EGFR⁻ cells was also observed. The washing process for removing NPs absorbed to the cell surface involved the step of centrifugation in order to replace the cell medium containing nanoparticles by fresh cell medium. However, during this step, some nanoparticles can be centrifuged together with the cells and thus absorbed to the cell surface by unspecific binding.

However, with the same concentration of Ctxb, a more important binding toward EGFR⁺ cells was observed with Ctxb molecules compared with Ctxb-AuNPs. Marega *et al.* hypothesized that the spatial distribution is

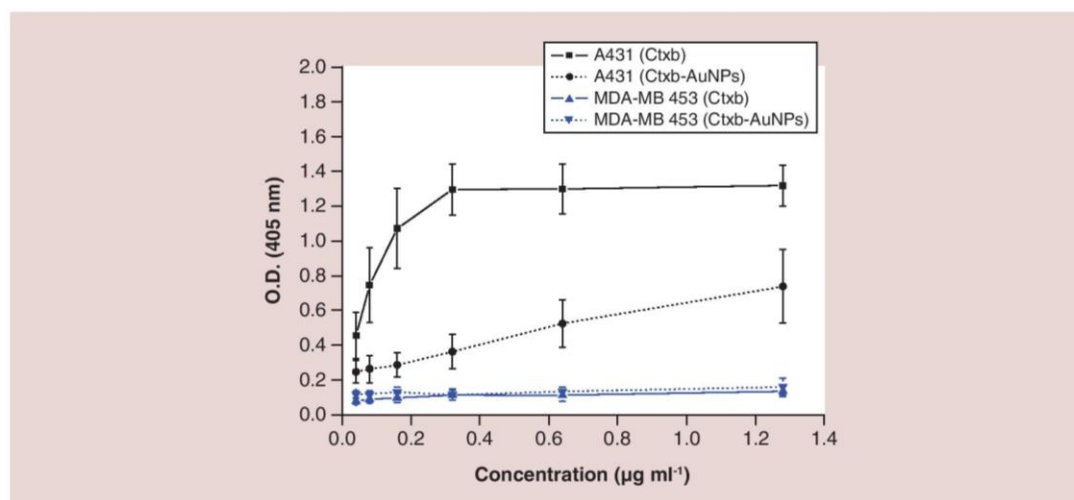


Figure 3. Surface ELISA for cetuximab and gold nanoparticles conjugated with cetuximab on EGFR⁺ (A431) and EGFR⁻ (MDA-MB-453) cells. The concentrations are expressed as microgram of Ctcb per milliliter. Results are presented as means \pm 1 S.D. for three independent experiments. Ctcb: Cetuximab; S.D.: Standard deviation.

constrained around nanoparticles for AuNPs conjugated with Ctcb in comparison to free Ctcb. Thus, it is possible that not all the Ctcb molecules are available to recognize the antigens that are distributed on the monolayer cell surface [30]. This could explain the apparent difference of binding affinity observed here, in other words, a lower binding of the Ctcb–AuNPs compared with free Ctcb.

Assessment of Ctcb–AuNP cytotoxicity

The cytotoxicity measurements were aimed at determining the experimental conditions to perform irradiation experiments with minimum toxicity. To investigate the toxicity of Ctcb–AuNPs, A431 cells or MDA-MB-453 cells were incubated for 30 min with Ctcb–AuNPs at different concentrations (0–100 µg Au/ml) and cell viability was assessed by a colorimetric test (MTS assay). In such an assay, viable cells produce a chromophore with absorption maxima at 490 nm, and thus absorption values are expected to decrease in case of reduction of cell viability. In principle, AuNPs may interfere with such a chromophore, generating additive absorption at 490 nm and hence, leading to an underestimation of the overall cytotoxicity. In the reality, the amount of Au internalized by the cells in each well (pg–ng range) is much lower than the amount of chromogenic substrate dispensed (hundreds of micrograms), thus it was easy to verify that the color generation was due to cell viability assessment rather than to the presence of AuNPs (Supplementary Information 6).

As shown in Figure 4, for both cell lines, Ctcb–AuNPs induced a small decrease in cell viability at a concentration of 100 µg Au ml⁻¹. This decrease was slightly more pronounced for A431 cells, which showed a 10% decrease when incubated with 25 µg Au ml⁻¹ of Ctcb–AuNPs. At the same concentration, the viability of MDA-MB 453 cells was not affected. The toxicity increased with longer incubation times. For the scope of our work, we established that incubation with 5 µg Au ml⁻¹ Ctcb–AuNPs during 30 min corresponds to a toxicity lower than 5%. These conditions were used for the experiments described in the manuscript. It must be noted that this concentration remained nontoxic for a longer incubation time (Supplementary Information 7).

Internalization & cell uptake of Ctcb–AuNPs

Chithrani *et al.* have shown that citrate-coated AuNPs might interact with serum proteins during incubation in cell culture medium and that nonspecific absorption of serum proteins onto bare AuNP may contribute to an appreciable AuNP cell uptake [37]. The cell uptake of the two different cell lines were analyzed by AAS for three different incubation conditions: cells incubated with Ctcb–AuNPs resuspended in cell culture medium (DMEM containing 10% FBS for 30 or 60 min); cells incubated with Ctcb–AuNPs resuspended in cell culture medium

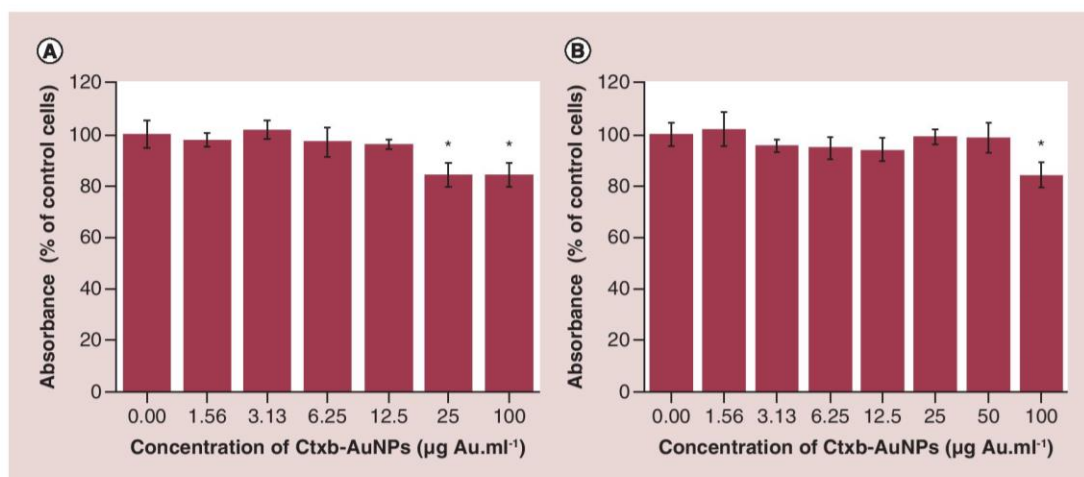


Figure 4. Cytotoxicity of AuNPs and Ctxb-AuNPs. A431 cells (A) or MDA-MB 453 cells (B) were incubated with different concentrations of Ctxb-AuNPs during 30 min and the number of viable cells was assessed by an MTS assay. Data are normalized to cells incubated in the same conditions without Ctxb-AuNPs and represent the mean absorbance ± 1 S.D. for $n = 5$ in one experiment. Results were statistically analyzed using a one-way ANOVA (Tukey test, * $p < 0.05$).

ANOVA: Analysis of variance; AuNP: Gold nanoparticle; Ctxb: Cetuximab; MTS:

(3-(4,5-Dimethylthiazol-2-yl)-5-(3-carboxymethoxyphenyl)-2-(4-sulfophenyl)-2H-tetrazolium); S.D.: Standard deviation.

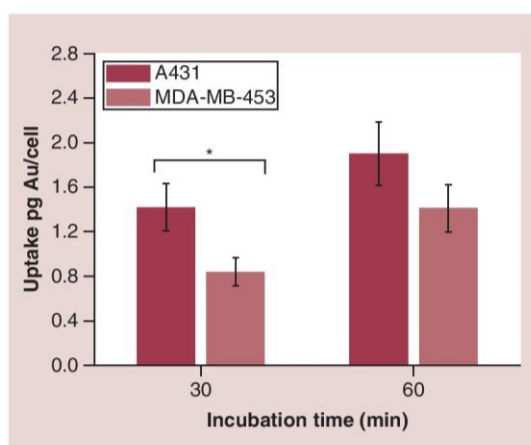


Figure 5. Determination of the gold content in cells exposed to gold nanoparticles conjugated with cetuximab. A431 and MDA-MB-453 cells were preincubated for 30 or 60 min with Ctxb-AuNPs at $5 \mu\text{g Au ml}^{-1}$. After incubation, cells were washed, counted and digested by aqua regia. The amount of gold was quantified by AAS. Results are presented as mean ± 1 S.D. of three independent experiments. Results were analyzed using a one-way ANOVA (Tukey test, * $p < 0.05$). AAS: Atomic absorption spectroscopy; ANOVA: Analysis of variance; AuNP: Gold nanoparticle; Ctxb: Cetuximab; S.D.: Standard deviation.

(DMEM containing 1% BSA for 15 or 30 min) and cells incubated with Ctxb-AuNPs resuspended in cell culture medium DMEM without any supplement (Supplementary Information 8).

Comparing these three conditions allows us to discriminate different NP-cell interactions. The analysis of AAS showed that there were three- to four-times higher cell internalization of the two cell lines for Ctxb-AuNPs resuspended in DMEM containing 10% FBS compared with DMEM alone. However, no marked difference regarding cell internalization between the two cell lines were observed for the media containing FBS or BSA. The GNP internalization in the presence of serum is mainly attributed to the presence of a protein corona surrounding the particles [38]. This serum protein-mediated internalization seems to be predominant compared with the specific receptor-mediated internalization. Thus, the cellular internalization of AuNPs was studied further by exposing Ctxb-AuNPs to A431 and MDA-MB-453 cells in the absence of serum proteins, followed by extensive washing to remove NPs adsorbed to the cell surface. AuNP uptake was quantified using AAS (Figure 5).

Receptor-mediated nanoparticle internalization is a rather rapid process compared with endocytic routes. Marega *et al.* have observed the cellular uptake of zeolite nanocrystals functionalized with Ctxb antibodies in the cells overexpressing the EGFR⁺ already begins 15 min after incubation, at a rate around tenfold faster than that

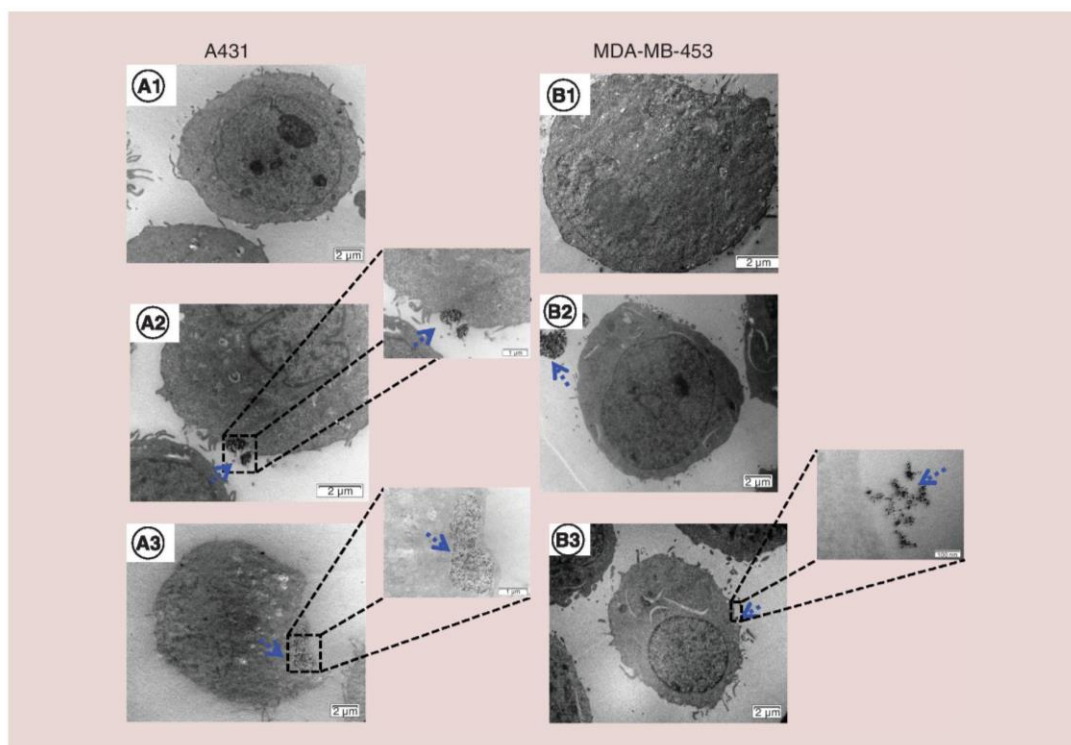


Figure 6. Transmission electron microscopy images of A431 and MDA-MB-453 cells. Control A431 cell (A1) or MDA-MB-453 cell (B1), 5 µg Au ml⁻¹ of Ctxb-AuNPs incubated 30 min with A431 cells (A2 & A3) or MDA-MB-453 cell (B2 & B3). The scale bars are 2, 1 µm and 100 nm. Blue arrows indicate the localization of AuNPs. Images in the corners represent higher magnification images. AuNP: Gold nanoparticle; Ctxb: Cetuximab.

observed in the negative control cells (EGFR⁻) [36]. Thus, the significant internalization of Ctxb-AuNP at 30 min can be mainly attributed to fast receptor-mediated nanoparticle internalization that is not the case for MDA-MB 453 cells. However, when the incubation time is longer, in other words, for 1 h incubation, more than one processes (physical membrane permeation, endocytosis) can be involved in the nanoparticle internalization, which considerably contribute to the cell internalization in MDA-MB 453 cells. The fast receptor-mediated nanoparticle internalization process might explain the apparent difference of NPs internalization of A431 (EGFR⁺) and MDA-MB 453 cells (EGFR⁻) at a rather shorter (30 min) compared with longer incubation times (1 h).

Ctxb-AuNPs displayed a higher uptake in A431 cells compared with MDA-MB-453 cells at each time interval. After 30 min of incubation, 1.42 pg Au corresponding to about 1.1×10^6 AuNPs was internalized in each A431 cell, on average. This result suggests a rapid and efficient cell uptake of Ctxb-AuNPs mediated by ligand-receptor interaction. Unspecific binding of the AuNPs on the cell surface may explain the gold detected for MDA-MB-453 cells. The Ctxb-AuNPs uptake increased with incubation time for both cell lines. Furthermore, the uptake was much higher for Ctxb-AuNPs than for AuNPs (Supplementary Information 7). These data demonstrate that Ctxb-AuNPs were efficiently taken up by the EGFR-overexpressing cells A431, due to the proper binding ability of Ctxb to EGFR.

To confirm these data, the uptake of the Ctxb-AuNPs in A431 and MDA-MB-453 cells was also qualitatively observed by TEM (Figure 6). TEM images are not useful to assess the number of GNPs per cell. Indeed, 'ultrathin' sections from 50 to 100 nm thick are able to be viewed in the TEM and only a few cells are visible on a TEM grid. Furthermore, the objects that are observed are clusters of NPs and not individual NPs, hence, it is not possible to estimate the number of GNPs per cell by this technique. However, it gives useful information regarding their intracellular localization.

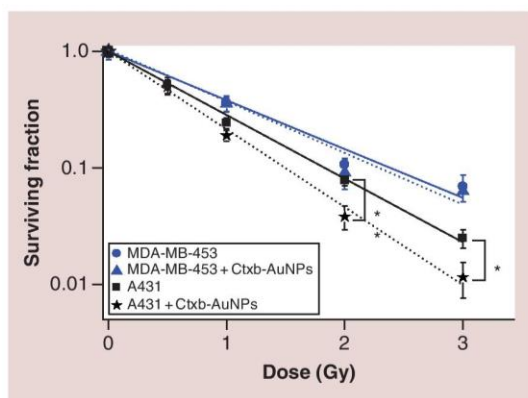


Figure 7. Survival curves of MDA-MB-453 cells and A431 cells incubated without gold nanoparticles conjugated with cetuximab (● solid line and ■ solid line, respectively) or preincubated 30 min with gold nanoparticles conjugated with cetuximab at $5 \mu\text{g Au ml}^{-1}$ (▲, dot line and ★ dot line, respectively). All the cells were then exposed to protons (LET = $25 \text{ keV } \mu\text{m}^{-1}$). Results are expressed as means \pm 1 S.D. for 2–4 independent experiments, each performed in triplicates. Results were analyzed using a one-way ANOVA (Welch test, * $p < 0.05$, ** $p < 0.01$). ANOVA: Analysis of variance; LET: Linear energy transfer; S.D.: Standard deviation.

After incubation with $5 \mu\text{g Au ml}^{-1}$ of Ctxb–AuNPs for 30 min, black spots were observed both for A431 cells or MDA-MB-453 cells, in cytoplasm and on the cell surface. However, A431 cells internalized a higher amount of Ctxb–AuNPs compared with MDA-MB-453 cells (Figure 6). Moreover, as shown in Figure 6 (a2), clusters of Ctxb–AuNPs were found around cellular extensions of A431 cell, which may indicate the recognition between the EGF receptors expressed in the plasma membrane of A431 cells and the Ctxb antibodies coupled to the AuNPs. The A431 cells seem to be bound on the cell surface and internalized probably by phagocytosis or receptor-mediated endocytosis since clusters of NPs are observed in membrane delineated vesicles (Supplementary Information 9). This recognition has not been observed neither for MDA-MB-453 cells, nor for A431 cells incubated with uncoupled AuNPs (Supplementary Information 9). The uptake, as measured by AAS, observed for MDA-MB-453 cells was thus probably due to unspecific binding of the AuNPs on the cell surface. For the TEM analysis, A431 cells and MDA-MB 453 cells were treated in parallel for comparison and incubated or not (control A1 and B1) with Ctxb–AuNPs for 30 min.

Altogether, these results suggest a specific internalization of Ctxb–AuNPs into A431 cells.

Radiosensitization effect of Ctxb–AuNPs

Irradiation experiment was performed to probe the possible radiosensitizing effects of Ctxb–AuNPs. For this purpose, A431 and MDA-MB-453 cells were incubated with a nontoxic concentration of $5 \mu\text{g Au ml}^{-1}$ Ctxb–AuNPs for 30 min and then irradiated by a proton beam. It should be noted that free Ctxb molecules (same concentration as in Ctxb–AuNPs) did not induce any change in cell survival upon irradiation at 2 Gy (data not shown). We chose to remove the NPs from the medium for the irradiation because we wanted to assess the effect of the NPs within the cells, without the interference of reactive oxygen species (ROS) that could be generated from the NPs in the culture medium. The radiosensitizing effect of Ctxb–AuNPs was quantified by standard *in vitro* clonogenic assays. The survival fractions were measured for doses ranging from 0 to 3 Gy upon irradiation with $25 \text{ keV } \mu\text{m}^{-1}$ protons.

An exponential decrease in survival fraction for the cells irradiated by a proton beam of $25 \text{ keV } \mu\text{m}^{-1}$ was observed (Figure 7). Survival fraction of MDA-MB-453 cells preincubated or not with Ctxb–AuNPs followed almost the same trend. However, the slope of the curve was higher for A431 cells preincubated with Ctxb–AuNPs compared with control A431 cells. A significant decrease in cell survival was already observed at 2 Gy, a clinically relevant radiation dose.

The efficiency of Ctxb–AuNPs to amplify radiation-induced A431 cell death was evaluated by calculating the SER at 10% survival. An SER value of 1.22 was obtained (Table 1). Our previous study demonstrated that 10-nm commercial amine-PEG-functionalized AuNPs amplified the cell death induced by $25 \text{ keV } \mu\text{m}^{-1}$ proton beam radiation (SER was 1.14) [23]. In comparison, the cancer cell-targeting Ctxb–AuNPs developed in this study provided a higher SER than AuNPs.

Cell survival curves were fitted with a linear quadratic model. The coefficient α corresponds to the contribution of lesions, which are directly lethal for the cell, whereas β is attributed to the contribution of additive sublethal lesions. This last one was null for all conditions (Table 1).

Table 1. Calculated α coefficients and sensitization enhancement ratios for A431 and MDA-MB 453 cells irradiated with a proton beam at $25 \text{ keV } \mu\text{m}^{-1}$ after being preincubated during 30 min with gold nanoparticles conjugated with cetuximab ($5 \text{ } \mu\text{g Au ml}^{-1}$) as well as in control cells (without gold nanoparticles conjugated with cetuximab). The internalized gold nanoparticle quantities in each condition are reported in the last column.

Samples	$\alpha \text{ (Gy}^{-1}\text{)}$	SER at 10% survival	AuNP quantities (Au pg/cell)
A431 (control)	1.26 (± 0.02)	–	0
A431 + Ctxb–AuNPs	1.54 (± 0.04)	1.22 (± 0.11)	1.42 (± 0.2)
MDA-MB-453 (control)	0.97 (± 0.06)	–	0
MDA-MB-453 + Ctxb–AuNPs	1.01 (± 0.07)	–	0.84 (± 0.1)

AuNP: Gold nanoparticle; Ctxb: Cetuximab; SER: Sensitization enhancement ratio.

This analysis showed that the presence of nanoparticles induced a 22% increase in the α parameter, indicating an enhancement of the lethality of the radiation treatment when Ctxb–AuNPs were added. This increase in cell killing is generally thought to be due to extra deposited dose from secondary electrons generated in the nanoparticles, subsequently giving rise to a local burst of ROS. *In silico* studies have demonstrated that this is indeed the case for spreadout Bragg peak (SBOP) protons, though to a lesser extent than when using kV photons. Using a modified Local Effect Model (LEM) approach, Lin *et al.* were able to predict SER for different nanoparticle distributions in a cell model and showed that AuNPs need to be close to a critical target, such as the cell nucleus, in order to get a significant effect when using a clinical proton beam [1]. Indeed, the range of secondary electrons produced in AuNPs is not sufficient to reach distant targets. This is even more relevant in this work, as the proton energy used (1.7 MeV) could only give rise to very low-energy electrons in AuNPs (hence nanometre-scale spike of ROS) and as the low number of these high-LET protons would limit the interaction probability with AuNPs. This issue questions the role of ROS in the radiosensitizing effect when using low-energy/high LET protons.

Hence, DMSO has been used to demonstrate the indirect effect of free radicals on cell killing with both photons and high LET particle radiation [4,23,39], a concentration of 1 M DMSO offering a maximal degree of protection, without having a toxic effect [40]. To address the role of ROS in the radiosensitizing effect of Ctxb–AuNPs in combination with protons, A431 cells were preincubated 30 min with or without $5 \text{ } \mu\text{g Au ml}^{-1}$ of Ctxb–AuNPs. DMSO (1 M) was added just before the irradiation in some samples, kept during irradiation procedure and removed immediately after the 30-min incubation.

In the absence of Ctxb–AuNPs, cell survival increased from 2 to 18% when DMSO was added during the irradiation (Figure 8). It is a clear indication that the cell death induced by proton irradiation is partially caused by indirect action, in other words, production of free radicals by water radiolysis. In addition, we observed that, in the absence of scavenger, Ctxb–AuNPs contributed to 54% of cell death at 3 Gy. It decreased to 16% in the presence of radical scavenger. This corresponded to a decrease of 70% in the contribution of Ctxb–NPs to radiosensitization, when irradiation was performed in the presence of the radical scavenger. This finding further highlighted the possible role of Ctxb–NPs in enhancing the production of ROS in combination with low-energy protons, although this radiation quality was not initially expected to produce secondary electrons able to markedly ionize AuNPs.

Discussion

Our results demonstrate that the radiosensitization effect of AuNPs in combination with protons could be amplified with active targeting. The amount and specificity of gold accumulation in cancer cells can be greatly increased by conjugating AuNPs to Ctxb, a specific monoclonal antibody directed against EGFR. The higher uptake gives rise to a higher hit probability between the gold and incident proton tracks, resulting in the production of great amounts of extremely localized Auger and/or secondary electrons (within a range $<100 \text{ nm}$) around nanoparticles. Due to the shorter-range secondary electrons produced for proton irradiation compared with x-rays, more action sites (internalized nanoparticles) are preferable in order to obtain a significant microscopic dose enhancement [41–43]. The dose enhancement, in principle, has two sources: direct ionization of critical cellular targets by the low-energy Auger electrons or secondary electrons (direct effects); ROS production generated by localized energy deposition (indirect effects).

While the exact mechanisms for AuNPs mediated radiosensitization with protons are yet to be fully elucidated, the ability of AuNPs to generate ROS along ion tracks and subsequent damage to critical cellular targets is worth to be investigated. An increased ROS production can be a direct consequence of a microscopic dose enhancement

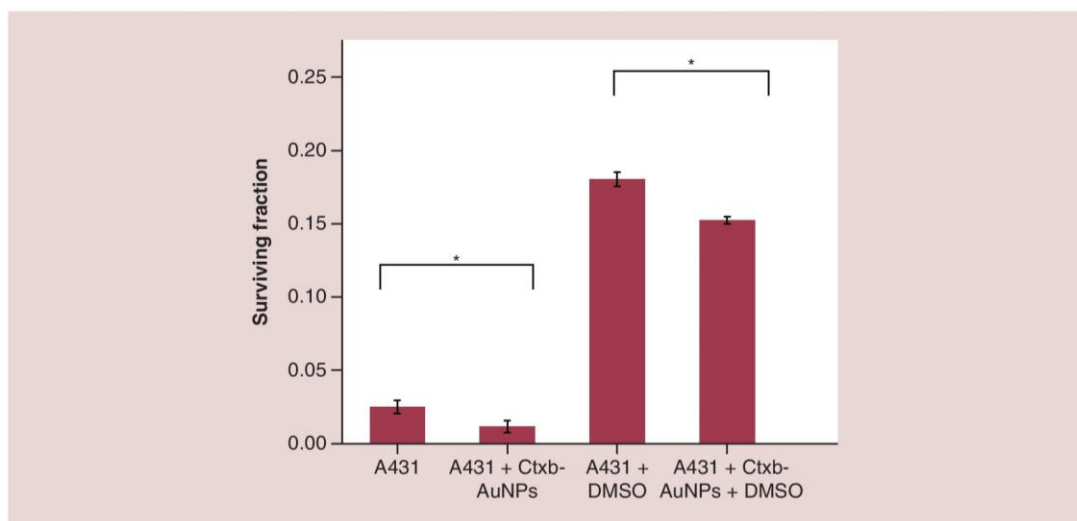


Figure 8. Survival fractions of A431 cells irradiated with $25 \text{ keV } \mu\text{m}^{-1}$ proton beam at 3 Gy. A431 cells were preincubated or not for 30 min with Ctxb-AuNPs at $5 \mu\text{g Au ml}^{-1}$. Cells were then irradiated in the presence or absence of DMSO that was added just before irradiation. Results are presented as mean \pm S.D. for two independent experiments, each performed in triplicates. Results were statistically analyzed using a one-way ANOVA (Tukey test; * $p < 0.05$).

ANOVA: Analysis of variance; AuNP: Gold nanoparticle; Ctxb: Cetuximab; S.D.: Standard deviation.

(Auger electrons and secondary electrons) around Ctxb-NPs, as shown by Monte Carlo simulation studies [43,44]. As we showed that Ctxb-AuNPs are not essentially located in the close vicinity of nucleus, it can be hypothesized that the triggered ROS attack DNA by traveling through the nuclear membrane, or alter other crucial cell components in the cytoplasm.

So far, there have been limited reports on the radiosensitizing effects of nanoparticles in combination with ions. Porcel *et al.* have reported 11.3 and 18.5% enhancement of D50 (irradiation doses for 50% cell survival) values for Chinese hamster ovary cells treated with gadolinium-based nanoparticles and irradiated by C^{6+} or He^{2+} , respectively [45]. In another *in vitro* study, a dose reduction of 29% for C^{6+} irradiation is demonstrated for glucose-capped AuNPs-treated Hela cells as compared with untreated cells [46]. Kim *et al.* showed that internalized AuNPs decreased CT26 tumor cell survival in combination with 45 MeV proton beam [47]. As shown by those studies, a significant radiosensitization effect was observed for relatively higher concentration of nanoparticles ($>0.1 \text{ mg ml}^{-1}$) and longer incubation time (few hours or overnight). Here, we showed a rapid and efficient cell uptake upon 30 min of incubation with $5 \mu\text{g ml}^{-1}$ of active targeting AuNPs. Moreover, the internalized Ctxb-AuNPs significantly enhanced the effect of proton radiation. In our previous report [23], the SER at 10% survival was 1.08 and 1.14 for A431 cells irradiated with protons of $25 \text{ keV } \mu\text{m}^{-1}$ after being preincubated, respectively, with bare untargeted 5 or 10 nm AuNPs at $50 \mu\text{g Au ml}^{-1}$ for 24 h. In the present study, the SER at 10% survival was 1.22 for targeted Ctxb-AuNPs at $5 \mu\text{g Au ml}^{-1}$ for 30 min, demonstrating the much higher effect due to active targeting. The active targeting of such Ctxb-coupled nanoparticles toward EGFR-expressing A431 cells has already been demonstrated *in vitro* and *in vivo* [30].

Low-energy protons used in this work ($25 \text{ keV } \mu\text{m}^{-1}$) are of interest clinically because a proportion of beam energy in the spread out Bragg peak will be below 10 MeV. The radiosensitization provided by AuNPs in the distal part of the tumor would be highly dependent on those low-energy protons. This is particularly important as different beam qualities do not provide the same effect (as shown in our previous work [23]). A variation of SER could potentially be observed along tumor depth *in vivo*. It is the first proof of concept that actively targeting nanoparticles may be used for proton therapy.

Conclusion & future perspective

Significant progress has been made in the development of new agents and new strategies against cancer. Yet, the major challenge remains in targeting and selectively killing cancer cells while affecting as few healthy cells as possible.

In this work, we demonstrate that AuNPs conjugated to tumor-targeting moieties can bind to cancer cells with high affinity and specificity. Moreover, they amplify cell death with proton ions used as ionizing radiations. It evidences the feasibility of adopting a novel protocol of combining protontherapy with tumor-targeting nanomedicine in cancer treatment. This finding impacts the strategy to develop targeted cancer nanotherapy and treatment planning aimed at improving proton ion treatments, ultimately, reducing negative radiation effects in healthy tissues in front of the tumor. This strategy is at its start and requires many more improvements. The efficacy and biodistribution of nanoparticles must be further optimized to be of clinical interest for radio-oncologists. Finally, the ideal combination (proton dose and sequence of treatment) still needs to be defined.

Summary points

- Approximately two to three cetuximab (Ct**x**b) molecules were conjugated to each gold nanoparticle (AuNP).
- Ct**x**b–AuNPs specifically bind to EGFR-overexpressing A431 cells, but not to EGFR-negative MDA-MB-453 cells.
- Transmission electron microscopy analysis evidenced the accumulation of Ct**x**b–AuNPs in the cell membrane region and cytoplasm of A431 cells.
- Uptake, quantified by atomic adsorption spectroscopy, showed higher gold quantity in A431 cells compared with MDA-MB-453 cells.
- Ct**x**b–AuNPs significantly enhanced the effect of proton irradiation in A431 cells but not in MDA-MB-453 cells.
- The radiosensitizing effect of Ct**x**b–AuNPs was higher than with unconjugated AuNPs.

Supplementary data

To view the supplementary data that accompany this paper please visit the journal website at: www.futuremedicine.com/doi/full/10.2217/nnm-2018-0161

Acknowledgments

The authors thank the 'Morphology-Imaging' technological platform of the University of Namur for the electron microscopy. The authors also acknowledge the support of the SIAM platform. Sébastien Penninckx is a PhD fellow funded by the Belgian Funds for Scientific Research (FRS-FNRS, Belgium).

Ethical conduct of research

The authors state that they have obtained appropriate institutional review board approval or have followed the principles outlined in the Declaration of Helsinki for all human or animal experimental investigations. In addition, for investigations involving human subjects, informed consent has been obtained from the participants involved.

Financial & competing interests disclosure

TheraPlus project was supported by the Walloon Region (grant 1318075). The authors have no other relevant affiliations or financial involvement with any organization or entity with a financial interest in or financial conflict with the subject matter or materials discussed in the manuscript apart from those disclosed.

No writing assistance was utilized in the production of this manuscript.

References

Papers of special note have been highlighted as: • of interest; •• of considerable interest

1. Lin Y, McMahon SJ, Scarpelli M, Paganetti H, Schuemann J. Comparing gold nano-particle enhanced radiotherapy with protons, megavoltage photons and kilovoltage photons: a Monte Carlo simulation. *Phys. Med. Biol.* 59(24), 7675–7689 (2014).
2. Lin Y, Paganetti H, McMahon SJ, Schuemann J. Gold nanoparticle induced vasculature damage in radiotherapy: comparing protons, megavoltage photons, and kilovoltage photons. *Med. Phys.* 42(10), 5890–5902 (2015).
3. Hainfeld JF, Dilmanian FA, Slatkin DN, Smilowitz HM. Radiotherapy enhancement with gold nanoparticles. *J. Pharm. Pharmacol.* 60(8), 977–985 (2008).
4. Jaynes JC, Merchant MJ, Spindler A, Wera AC, Kirkby KJ. Investigation of gold nanoparticle radiosensitization mechanisms using a free radical scavenger and protons of different energies. *Phys. Med. Biol.* 59(21), 6431–6443 (2014).
5. Polf JC, Bronk LF, Driessen WH *et al.* Enhanced relative biological effectiveness of proton radiotherapy in tumor cells with internalized gold nanoparticles. *Appl. Phys. Lett.* 98(19), 193702 (2011).

6. Shrestha S, Cooper LN, Andreev OA, Reshetnyal YK, Antosh MP. Gold nanoparticles for radiation enhancement *in vivo*. *J. Radiat. Oncol.* 7(8), 026 (2016).
7. Haume K, Rosa S, Grellet S *et al.* Gold nanoparticles for cancer radiotherapy: a review. *Cancer Nanotechnol.* 7(1), 8 (2016).
- **Extensive review of the potential of gold nanoparticles (AuNPs) for cancer therapy.**
8. Porcel E, Liehn S, Remita H *et al.* Platinum nanoparticles: a promising material for future cancer therapy? *Nanotechnology* 21(8), 85103 (2010).
9. McMahon SJ, Hyland WB, Muir MF *et al.* Biological consequences of nanoscale energy deposition near irradiated heavy atom nanoparticles. *Sci. Rep.* 1, 18 (2011).
10. Hainfeld JF, Slatkin DN, Smilowitz HM. The use of gold nanoparticles to enhance radiotherapy in mice. *Phys. Med. Biol.* 49(18), N309–15 (2004).
- **One of the first reports to evidence nanoparticle-mediated radiosensitization *in vivo*.**
11. Zhong Y, Meng F, Deng C, Zhong Z. Ligand-directed active tumor-targeting polymeric nanoparticles for cancer chemotherapy. *Biomacromolecules* 15(6), 1955–1969 (2014).
12. Arteaga C. Targeting HER1/EGFR: a molecular approach to cancer therapy. *Semin. Oncol.* 30(3 Suppl. 7), 3–14 (2003).
13. Grandis JR, Sok JC. Signaling through the epidermal growth factor receptor during the development of malignancy. *Pharmacol. Ther.* 102(1), 37–46 (2004).
14. Liu J, Liang Y, Liu T, Li D, Yang X. Anti-EGFR-conjugated hollow gold nanospheres enhance radiocytotoxic targeting of cervical cancer at megavoltage radiation energies. *Nanoscale Res. Lett.* 10, 218 (2015).
15. Zimmermann M, Zouhair A, Azria D, Ozsahin M. The epidermal growth factor receptor (EGFR) in head and neck cancer: its role and treatment implications. *Radiat. Oncol.* 1, 11 (2006).
16. Yewale C, Baradia D, Vhora I, Patil S, Misra A. Epidermal growth factor receptor targeting in cancer: a review of trends and strategies. *Biomaterials* 34(34), 8690–8707 (2013).
17. Galizia G, Lieto E, De Vita F *et al.* Cetuximab, a chimeric human mouse anti-epidermal growth factor receptor monoclonal antibody, in the treatment of human colorectal cancer. *Oncogene* 26(25), 3654–3660 (2007).
18. Martinelli E, De Palma R, Orditura M, De Vita F, Ciardiello F. Anti-epidermal growth factor receptor monoclonal antibodies in cancer therapy. *Clin. Exp. Immunol.* 158(1), 1–9 (2009).
19. Qian Y, Qiu M, Wu Q *et al.* Enhanced cytotoxic activity of cetuximab in EGFR-positive lung cancer by conjugating with gold nanoparticles. *Sci. Rep.* 4, 7490 (2014).
20. Kao HW, Lin YY, Chen CC *et al.* Biological characterization of cetuximab-conjugated gold nanoparticles in a tumor animal model. *Nanotechnology* 25(29), 295102 (2014).
21. Karmani L, Labar D, Valembois V *et al.* Antibody-functionalized nanoparticles for imaging cancer: influence of conjugation to gold nanoparticles on the biodistribution of ⁸⁹Zr-labeled cetuximab in mice. *Contrast Media Mol. Imaging* 8(5), 402–408 (2013).
- **Biodistribution and tumor accumulation of AuNPs conjugated with cetuximab.**
22. Kao HW, Lin YY, Chen CC *et al.* Evaluation of EGFR-targeted radioimmuno-gold-nanoparticles as a theranostic agent in a tumor animal model. *Bioorg. Med. Chem. Lett.* 23(11), 3180–3185 (2013).
23. Li S, Penninckx S, Karmani L *et al.* LET-dependent radiosensitization effects of gold nanoparticles for proton irradiation. *Nanotechnology* 27(45), 455101 (2016).
24. Walzlein C, Scifoni E, Kramer M, Durante M. Simulations of dose enhancement for heavy atom nanoparticles irradiated by protons. *Phys. Med. Biol.* 59(6), 1441–1458 (2014).
25. Moreau N, Michiels C, Masereel B *et al.* PVD synthesis and transfer into water-based solutions of functionalized gold nanoparticles. *Plasma Proc. Polym.* 6(S1), 5888–5892 (2009).
26. Dynamic light scattering – common terms defined Malvern Instruments
Worldwide <http://docplayer.net/15065673-Dynamic-light-scattering-common-terms-defined.html>
27. Janmaat ML, Kruijt FA, Rodriguez JA, Giaccone G. Response to epidermal growth factor receptor inhibitors in non-small cell lung cancer cells: limited antiproliferative effects and absence of apoptosis associated with persistent activity of extracellular signal-regulated kinase or Akt kinase pathways. *Clin. Cancer Res.* 9(6), 2316–2326 (2003).
28. Meira DD, Nobrega I, de Almeida VH *et al.* Different antiproliferative effects of matuzumab and cetuximab in A431 cells are associated with persistent activity of the MAPK pathway. *Eur. J. Cancer* 45(7), 1265–1273 (2009).
29. Subik K, Lee JF, Baxter L *et al.* The expression patterns of ER, PR, HER2, CK5/6, EGFR, Ki-67 and AR by immunohistochemical analysis in breast cancer cell lines. *Breast Cancer (Auckl.)* 435–441 (2010).
30. Marega R, Karmani L, Flamant L *et al.* Antibody-functionalized polymer-coated gold nanoparticles targeting cancer cells: an *in vitro* and *in vivo* study. *J. Mat. Chem.* 22(39), 21305–21312 (2012).
31. Piret JP, Jacques D, Audinot JN *et al.* Copper(II) oxide nanoparticles penetrate into HepG2 cells, exert cytotoxicity via oxidative stress and induce pro-inflammatory response. *Nanoscale* 4(22), 7168–7184 (2012).

32. Wera AC, Riquier H, Heuskin AC, Michiels C, Lucas S. *In vitro* irradiation station for broad beam radiobiological experiments. *Nucl. Instruments Phys. Res. B.* 269(24), 3120–3124 (2011).
33. Ziegler JF. *The Stopping and Range of Ions in Matter*. Springer, MA, USA (1985).
34. Turner J. *Atoms, Radiation, and Radiation Protection*. Wiley-VCH Verlag GmbH & Co., KGaA, Germany (1995).
35. Pineux F, Marega R, Stopin A *et al.* Biotechnological promises of Fe-filled CNTs for cell shepherding and magnetic fluid hyperthermia applications. *Nanoscale* 7(48), 20474–20488 (2015).
36. Marega R, Prasetyanto EA, Michiels C, De Cola L, Bonifazi D. Fast targeting and cancer cell uptake of luminescent antibody-nanozeolite bioconjugates. *Small* 12(39), 5431–5441 (2016).
37. Chithrani BD, Ghazani AA, Chan WC. Determining the size and shape dependence of gold nanoparticle uptake into mammalian cells. *Nano Lett.* 6(4), 662–668 (2006).
38. Safi M, Courtois J, Seigneuret M, Conjeaud H, Berret JF. The effects of aggregation and protein corona on the cellular internalization of iron oxide nanoparticles. *Biomaterials* 32(35), 9353–9363 (2011).
39. Porcel E, Li S, Usami N *et al.* Nano-sensitization under gamma rays and fast ion radiation. *J. Phys.: Conf. Series* 373(1), 012006 (2012).
40. Hirayama R, Matsumoto Y, Uzawa A *et al.* Indirect action to cell killing by SOBP carbon-ion beams. *J. Rad. Res.* 55(Suppl. 1), i133–i134 (2014).
41. Lin Y, McMahon SJ, Paganetti H, Schuemann J. Biological modeling of gold nanoparticle enhanced radiotherapy for proton therapy. *Phys. Med. Biol.* 60(10), 4149–4168 (2015).
- **Monte Carlo simulations suggest that vasculature damage can be induced and may participate to tumor eradication.**
42. Ahmad R, Royle G, Lourenço A *et al.* Investigation into the effects of high-Z nano materials in proton therapy. *Phys. Med. Biol.* 61(12), 4537–4550 (2016).
43. Cho J, Gonzalez-Lepera C, Manohar N *et al.* Quantitative investigation of physical factors contributing to gold nanoparticle-mediated proton dose enhancement. *Phys. Med. Biol.* 61(6), 2562–2581 (2016).
44. Heuskin AC, Gallez B, Feron O *et al.* Metallic nanoparticles irradiated by low-energy protons for radiation therapy: are there significant physical effects to enhance the dose delivery? *Med. Phys.* 44(8), 4299–4312 (2017).
45. Porcel E, Tillement O, Lux F *et al.* Gadolinium-based nanoparticles to improve the hadrontherapy performances. *Nanomedicine* 10(8), 1601–1608 (2014).
46. Kaur H, Pujari G, Semwal MK, Sarma A, Avasthi DK. *In vitro* studies on radiosensitization effect of glucose capped gold nanoparticles in photon and ion irradiation of HeLa cells. *Nucl. Instruments Phys. Res. B* 3017–3011 (2013).
47. Kim JK, Seo SJ, Kim KH *et al.* Therapeutic application of metallic nanoparticles combined with particle-induced x-ray emission effect. *Nanotechnology* 21(42), 425102 (2010).

Antibody-functionalized gold nanoparticles as tumor targeting radiosensitizers for proton therapy

- Supplementary information -

Supporting information S1: AuNPs-Ctxb purification by membrane-based separation techniques

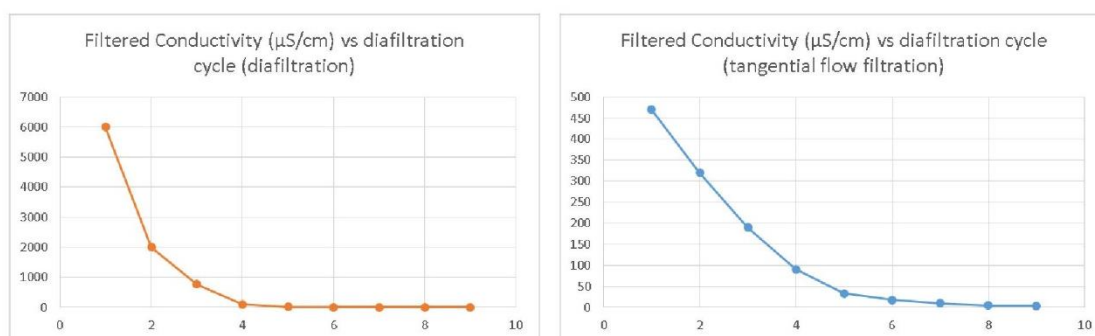


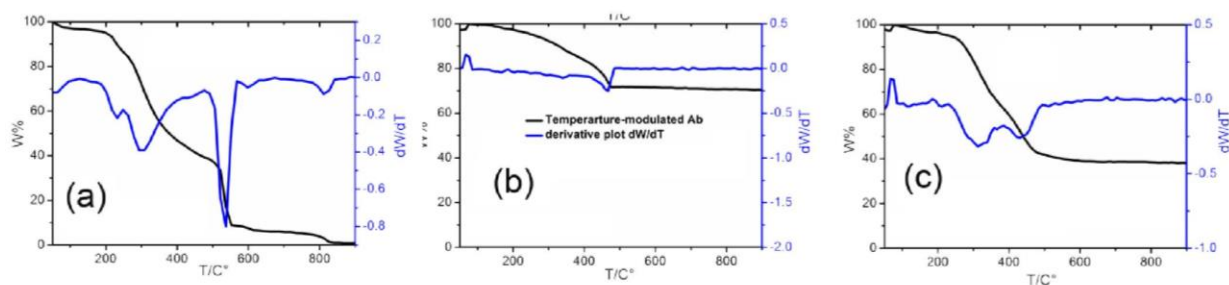
Figure S1. Evolution of filtered water conductivity as a function of the purification cycle during membrane-based purification of the AuNPs-Ctxb bioconjugates by discontinuous diafiltration (left) and tangential flow filtration (TFF, right). Membranes were 300,000 Da cut-off in both centrifugal concentrators (Vivaspin 20) and TFF (Pall). The difference in the absolute values between diafiltration and TFF is due to the different volume of the filtered solutions checked by their conductivity (around 5 mL for the diafiltration, around 50 mL for TFF).

Table S1. Filtered water conductivity as a function of the purification cycle during discontinuous diafiltration or tangential flow filtration of AuNPs-Ctxb reaction mixture purification.

	Diafiltration	TFF
Cycle	Filtered Conductivity (μS/cm)	
1	6000	470
2	2000	320
3	770	190
4	100	90
5	20	33
6	10	18
7	5	10
8	4	5
9	3	3.5

Supporting information S2: Estimation of AuNPs and AuNPs-Ctxb composition

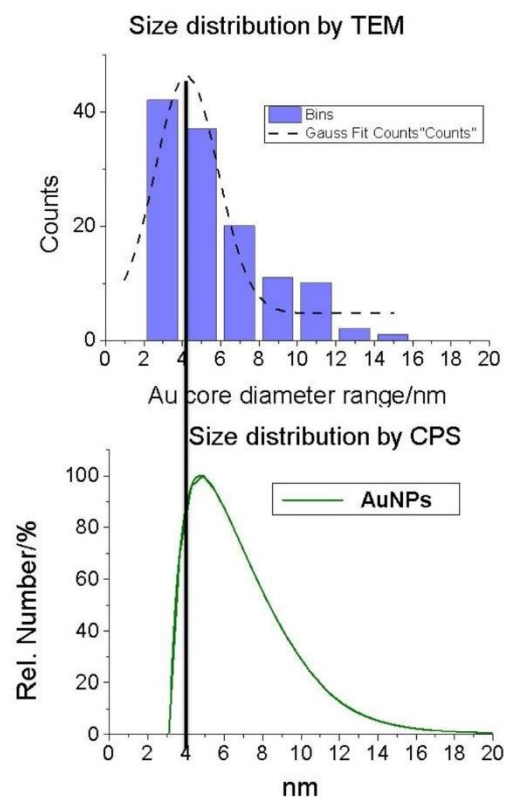
We report below the TGA assessment of Ctxb, AuNPs and AuNPs-Ctxb. One can notice that Ctxb shows the typical behaviour of proteins, by burning completely and leaving almost 0% residual weight at 800 °C (graph a). AuNPs also have an organic moiety (PAA), which decomposes leaving around 70 % of residual weight (graph b). AuNPs-Ctxb display an intermediate behaviour between Ctxb and AuNPs, which is a residual weight of around 40 wt% (up to 45 wt% in other samples) and the “thermal signature” of Ctxb in the first derivative plot (peaks between 200 °C and 500 °C, graph c, blue trace).



By this analysis we know the Au/PPAA weight ratio in AuNPs (70/30) and a first estimate of the Au amount in our AuNPs-Ctxb (40-45%).

Unfortunately, TGA analysis require high amounts of material (around 2 mg) and a dedicated instrumentation, reasons that pushed us to find an alternative that could be easier be adopted by other laboratories, and less demanding in terms of material loss. We have thus evaluated the composition of the bioconjugates by using a combination of atomic absorption spectroscopy (to determine the amounts of Au in the solutions of the samples) and a colorimetric protein quantification assay (the modified Coomassie blue method proposed by Thermo Scientific, the Pierce 660 nm Protein Assay). The use of a colorimetric assay to such purpose was already reported in the literature (e.g. Kao H-W et al., *Bioorg Med Chem Lett.* 2013; 23:3180-5).

We repeated these assessments to a series of bioconjugates, made during 2016, which led to the determination of an average and representative material composition of 32±8% Ctxb, 47±6% Au, 20±3% PPAA (n= 5 bioconjugates).

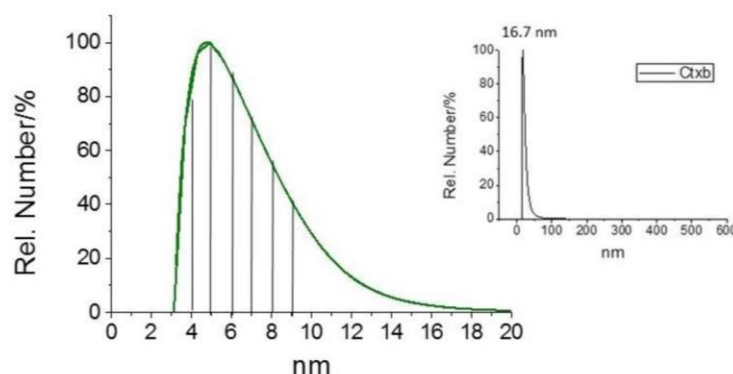
Supporting information S3: Size distribution of AuNPs cores and diameters by TEM and disk centrifuge**Supporting information S4:** Zeta potential measurement of AuNPs and AuNPs-Ctxb

	mV	SD (mV)	C mS/cm)
AuNPs	-29.1	0.4	0.1
AuNP-Ctxbs	-37.9	3.6	0.1
AuNPs serum	-1.9	1	14.9
AuNPs-Ctxb serum	-1.1	1.9	15.5

One can notice the changes occurring after bioconjugation (a change of around -9 mV) and upon incubation in serum supplemented media, which “equalizes” the zeta potential of both nanomaterials towards 0 mV.

Supporting information S5: Estimation of the number of cetuximab/particle

AuNPs are a size distribution of ranging from 4 – 16 nm, with the majority of the particles being 4 - 6 nm (see the image below). This distribution of particles is reacted with cetuximab, which shows a hydrodynamic diameter of around 17 nm, in agreement with other studies involving cetuximab analysis by DLS (see image below and Marega R et al., *Small*. 2016; 12:5431-41).



Being an unselective immobilization strategy based on amide bond formation, our procedure of functionalization is not amenable to the very elegant determination of cetuximab loading at the individual AuNPs level used to characterize site-oriented bioconjugates (Garcia-Fernandez L et al., *Nanoscale*. 2017; 9 :6111-21). We instead used a macroscopic approach, based on a modification of the procedure proposed by Kao H-W et al. (*Bioorg Med Chem Lett*. 2013; 23:3180-5), which used 14 nm AuNPs and reported a loading of 34 cetuximab/particle.

Thanks to the compositional assessment of each individual bioconjugate, one can calculate the number of molecules of cetuximab per mg of material (e.g. 32 wt% of cetuximab = 0.32 mg cetuximab/mg material = 2.2 nmol cetuximab/mg, 1.32×10^{15} molecules cetuximab/mg) and estimate the number of AuNPs per mg. This latter is indeed an estimation, since to convert the amount of Au in each bioconjugate we need geometric calculations (sphere volume), density values (unknown, we used the Au density, 19.3 g/cm^3 as in Kao, H-W et al., *Bioorg Med Chem Lett*. 2013; 23:3180-5) and a correction factor. We believe that a correction factor is needed to account for, on one hand, the presence of an organic layer spacing the AuNPs cores (AuNPs and AuNPs-Ctxb will most likely have a different density than pure Au). On the other hand, the fact that while the number of cetuximab molecules present in a defined amount of samples can be estimated with fair precision, the number of AuNPs in a defined amount of Au will be “forced” to fit one value, that is the most frequent hydrodynamic diameter (in our case 5-6 nm). By this, we exclude the huge contribution in the actual number of particles that small diameter AuNPs (3-4.9 nm).

An arbitrarily-determined correction factor of 0.4 seems reasonable because it attributes low cetuximab/AuNP for AuNPs having the smaller diameters (either 0 or 1 Ctxb/AuNP for 3 and 4 nm AuNPs), while for larger particles it determines values that are in line with other literature reports that used similar characterization methods (Kao, H.-W. et al., *Bioorg Med Chem Lett*. 2013; 23:3180-5 as well as Kao H-W et al., *Nanotechnology*. 2014; 25:295102). This leads to the possibility of estimating the theoretical number of cetuximab surrounding each AuNP, which is 2-3 for 5-6 nm AuNPs.

Supporting information S6: Cell viability assessment via a colorimetric test (MTS)

We have used a colorimetric test that base on the capability of viable cells of converting a chromogenic substrate thanks to their mitochondrial activity (MTS assay, the evolution of the MTT assay). The chromophore produced by the viable cells has a maximum of absorbance at 490 nm, and due to the low amount of AuNPs introduced in each well and internalized by the cells, no additive interference was observed between the nanoparticle absorption and the chromophore (see also the supporting information in Marega R et al. (Small. 2016; 12:5431-41). In a typical assay, cells are plated and the test compounds evaluated in quintuplicate. In this experiment, the incubation time was set to 3h. One can indeed notice that the absorbance readouts before AuNPs incubation range between 0.2 and 0.22 units, they obviously increase in a concentration dependent manner during the incubation step (0.2 – 1.1 units), to go back to the initial range of absorbance (0.2 – 0.27) after the washing steps prior to the addition of the colorimetric reagent. The latter is thus the key which determines the great changes in the absorbance as a function of cell viability (0.6-2 units).

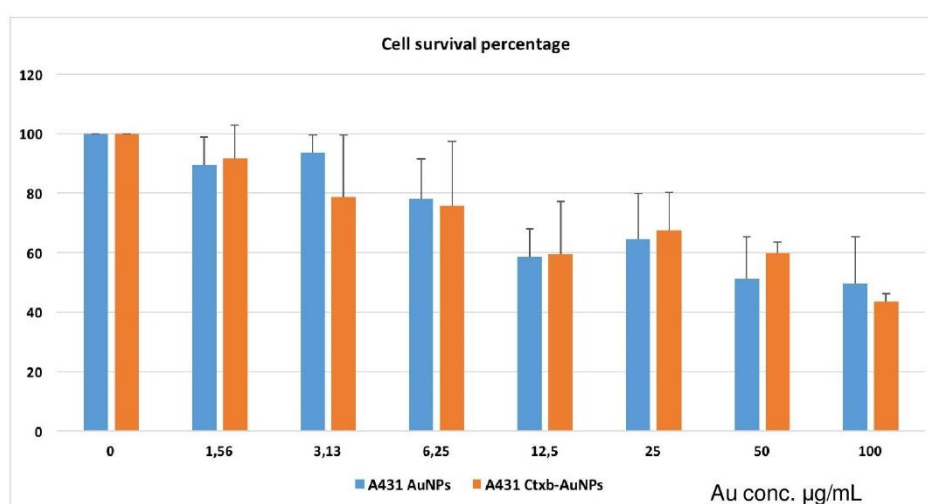
Supporting information S7: Cytotoxicity of AuNPs and Ctxb-AuNPs

Figure S7: A431 cells were incubated with different concentrations of Ctxb-AuNPs during 3 hours and the number of viable cells was assessed by a MTS assay. Data are normalized to cells incubated in the same conditions without Ctxb-AuNPs and represent the mean absorbance \pm 1 S.D. for 4 independent experiments.

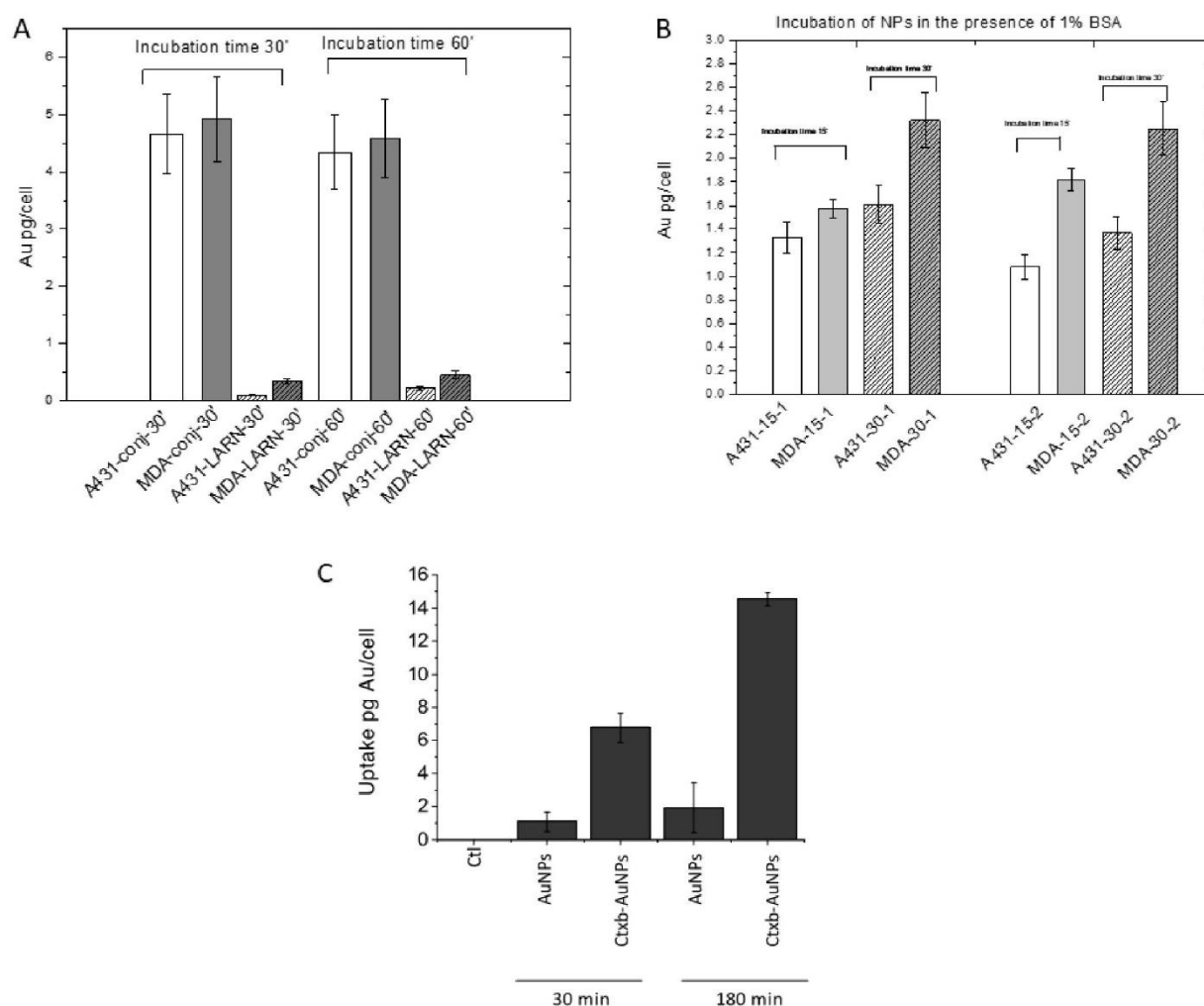
Supporting information S8: Determination of gold content by AAS

Figure S8. Determination of the gold content in cells exposed to Ctxb-AuNPs. A431 and MDA-MB-453 cells were pre-incubated for (A) 30 or 60 minutes with Ctxb-AuNPs at $5 \mu\text{g Au ml}^{-1}$ resuspended in DMEM containing 10 vol. % fetal bovine serum or (B) Duplicates of 15 or 30 minutes with Ctxb-AuNPs at $5 \mu\text{g Au ml}^{-1}$ resuspended in DMEM containing 1 vol. % 1% bovine serum albumin. After incubation, cells were washed, counted and digested by aqua regia. The amount of gold was quantified by AAS. Results are presented as mean \pm 1 S.D. of three independent experiments. (C) Determination of the gold content in cells exposed to AuNPs or Ctxb-AuNPs. A431 cells were pre-incubated for 30 or 180 minutes with AuNPs or Ctxb-AuNPs at $5 \mu\text{g Au ml}^{-1}$. After incubation, cells were washed, counted and digested by aqua regia. The amount of gold was quantified by AAS. Results are presented as mean \pm 1 S.D. (n=3).

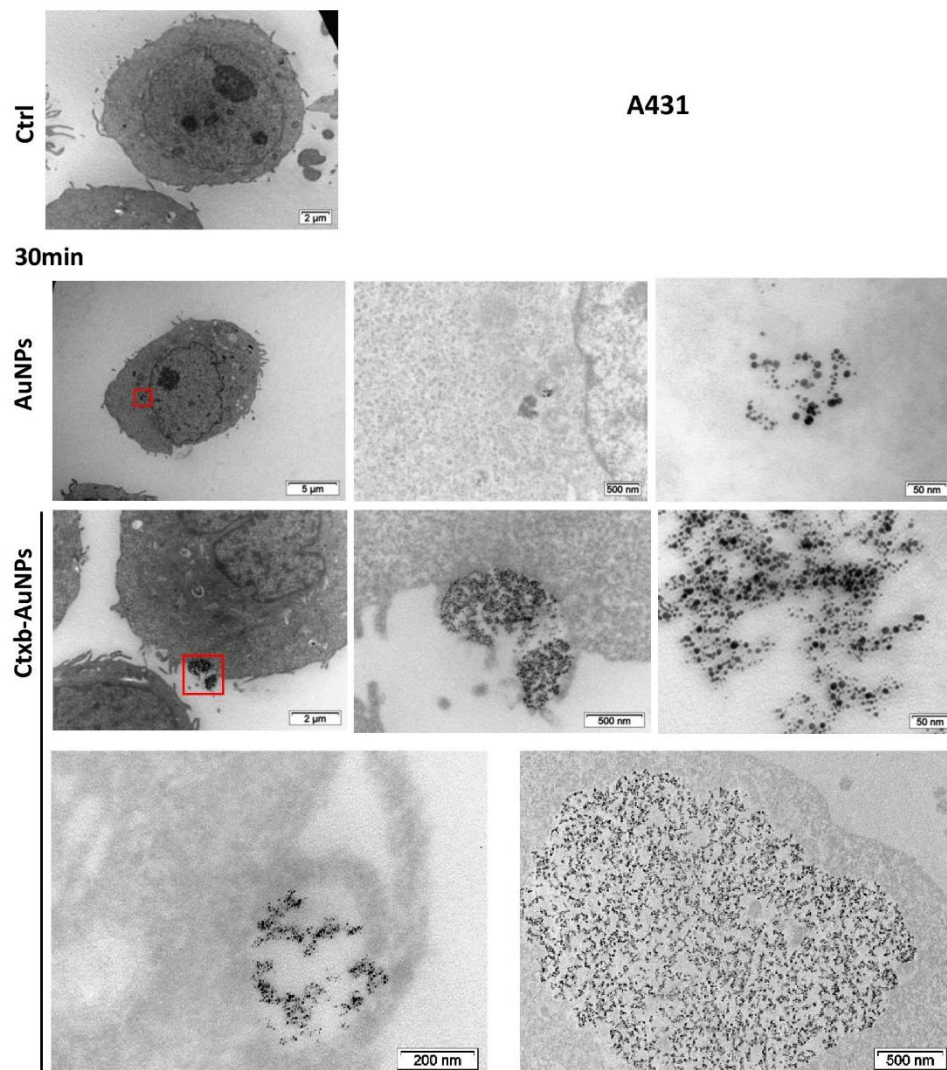
Supporting information S9: Internalization of Ctxb-AuNPs

Figure S9. TEM images for A431 cells incubated 30 minutes in culture medium without AuNPs (CTRL) or with $5 \mu\text{g Au mL}^{-1}$ of AuNPs or with $5 \mu\text{g Au mL}^{-1}$ of Ctxb-AuNPs. The size scale corresponds to 5 μm, 2 μm, 500 nm, 200 nm and 50 nm magnification. Red squares show the localization of gold nanoparticles in the low magnification images.

9. Towards a better understanding of DNA damage induced by high-Z particles

9.1. Context and goal of the study

As discussed in the introduction, individual radiosensitivity is a key factor which mediates the success of radiotherapy. The term “radiosensitivity” refers to either the extent of IR-induced biological responses or the susceptibility to IR-induced carcinogenesis. Nowadays, 15 genetic disorders associated to increased cellular radiosensitivity have been identified including ataxia telangiectasia (ATM mutation) and LIG4 syndrome (LIG4 mutation) [181]. Cells with ATM or LIG4 mutations are highly sensitive to radiation. Thereby, these mutations could drastically influence the treatment. On one hand, highly radiosensitive patients (such as homozygous patients of ATM or LIG4 mutations) develop huge side-effects associated to radiation. It was indeed reported that classical radiotherapy treatments may be fatal for these patients. On the other hand, radioresistant patients may receive an insufficient radiation dose to achieve a satisfactory tumor control. Nevertheless, these genetic disorders are very rare with occurrence in the population around 1 in 100,000 for ATM mutation and only one case reported for LIG4 mutation [181]. Currently, it has been evidenced that patient-related factors account for as much as 80 to 90 % of the variation observed in patient response to radiation [56]. Although the origin of this variability was attributed to genomic variations, scientific community failed to identify other genetic disorders associated to them.

In this context, we used genome-wide-association study (GWAS) to identify single nucleotide polymorphisms (SNP) associated to a radiosensitive phenotype in mice. SNP is a variation in a single nucleotide that occurs at a given position in the genome with a frequency within the population above 1 %. In the first part of this work, we focused on the study and quantification of inter-individual radiosensitivity variations by assessing DNA damage repair as a biomarker of irradiation exposure. Since the DNA damage repair may vary with the dose and the LET of the incident particles, the cells were exposed to X-rays as well as to charged particles of different LET. In addition to the interest in radiotherapy researches, these results can serve for the selection of spacecraft mission candidates that will be exposed to high-Z charged particles during their mission. Thereby, we carefully characterized the dose and LET dependence of radiation-induced foci after irradiation of 76 primary skin cells derived from 15 different strains of mice. The repair kinetics were analyzed through both radiation characteristics and mouse strains, suggesting a genetic component. In the second part of this study, we used GWAS to identify the SNPs responsible for the observed higher radiosensitivity.

9.2. Fifth manuscript: “Dose, LET and strain dependence of radiation-induced 53BP1+ foci in 15 mouse strains”

Dose, LET and strain dependence of radiation-induced 53BP1+ foci in 15 mouse strains

Sébastien Penninckx^{1, 2*}, Egle Cekanaviciute^{3, 4*}, Charlotte Degorre⁵, Elodie Guiet¹, Louise Viger¹, Stéphane Lucas², Sylvain V. Costes^{1, 4}

* Both authors contributed equally to this work

¹Biological Systems and Engineering Division, Lawrence Berkeley National Laboratory, 1 Cyclotron Rd, Berkeley, CA 94720, USA

²Namur Research Institute for Life Science, University of Namur, Rue de Bruxelles, 61, 5000 Namur, Belgium

³Universities Space Research Association (USRA)

⁴Space Biosciences Division, NASA Ames Research Center, Moffett Blvd, Mountain View, CA 94035, USA

⁵Université de Nantes, 1 Quai de Tourville, 44035 Nantes, France

Correspondence: sylvain.v.costes@nasa.gov

Abstract

Here we present a comprehensive comparative analysis of repair of radiation-induced DNA damage *ex vivo* in 15 strains of mice, including 5 inbred reference strains and 10 collaborative-cross strains, of both sexes, totaling 5 million skin fibroblast cells imaged by high-throughput conventional microscopy. The *ex vivo* samples were subjected to increasing doses of both low and high-LET radiation (X rays, 350MeV/n ⁴⁰Ar, 600 MeV/n ⁵⁶Fe), which are relevant to carcinogenesis and human space exploration. Automated image quantification of 53BP1 radiation-induced foci (RIF) formation and repair during the first 4 - 48 hours after irradiation was performed as a function of dose and LET. Our data indicate that multiple DNA double-stranded breaks are induced in a dose and LET-dependent manner, and coalesce into isolated RIFs when DSBs are formed within the same discrete nuclear region coined as “repair domain”. Furthermore, we observed that the number of RIF/Gy was lower for higher doses of X-ray or for higher LET particles (i.e. 600 MeV/n ⁵⁶Fe), suggesting there are more DSB/RIF when the local absorbed dose increases in the nucleus. All 15 strains showed the same dose and LET dependence, but strain differences were preserved under various experimental conditions, indicating the number and sizes of repair domains are modulated by the genetic of each strain. This is Part I of a two-part study, of which the second part will analyze RIF formation kinetics to define the radiation susceptibility of individual strains, as well as compare strain-dependent radiation responses both *ex vivo* and *in vivo*.

Introduction

The past few decades have witnessed a growing interest of space agencies for long-duration exploration beyond the low-earth orbit, including planned lunar and Mars missions. One of the predominant health risks associated with these long-term missions is the continuous exposure of astronauts to radiation transmitted by the Galactic Cosmic Rays (GCR), which is much higher than in the current missions to the International Space Station, where astronauts still benefit from the protection of the Earth's magnetic field (1, 2). The GCR spectrum is composed of 90% protons, 9% He ions and 1% heavier ions which are typically referred as HZE particles (i.e. particles with high charge Z and high energy E) with energies ranging mainly between 0.1 and 1 GeV/n (3) and high linear energy transfer (LET). Despite their relative low abundance in the GCR spectrum, exposure to HZE particles has important health effects due to their high relative biological effectiveness (RBE) for DNA damage and cancer induction (4-6).

Exposure to ionizing radiation, especially to high-LET HZE particles, causes DNA double-strand breaks (DSBs), which in seconds to minutes are recognized by DNA damage-sensing proteins that form immunofluorescently stainable nuclear domains called radiation-induced foci (RIF) (7-9). RIF measurements are routinely used to quantify DSB and evaluate repair kinetics after medical radiation exposure, e.g. during cancer treatment (10, 11). Previous results from our group have shown that RIFs form preferentially in euchromatic regions (12), interact and merge with each other within restricted areas of the nucleus as shown by time-lapse microscopy (13). We have also observed nonlinear dose dependence of RIF formation, which saturates as X-ray doses increase beyond 1 Gy, and hypothesized that it was caused by permanent merging of multiple DSBs into RIFs, leading to fewer total RIFs than total DSBs (14).

This concept that DSBs are not static, but are instead moved into restricted area of the nucleus for repair, changes our views about the response of cells to radiation-induced DNA damage, especially in the context of GCR exposures, where HZE particles deposit the majority of their energy along their tracks in the nucleus, leading to the majority of DSBs being formed along particle trajectories. When the distance between multiple DSBs is reduced due to DSB relocation, the probability for DNA misrepair and chromosomal rearrangements increases drastically (15), and could stimulate cell death and carcinogenesis (16, 17).

We have previously validated the multi-DSB RIF model *in silico* by computer modeling to simulate the saturation of RIF formation in response to increasing radiation doses. We divided the nucleus into discrete cubical repair domains and used them to predict RIF yield as a function of dose of both low and high-LET radiation (18). By assuming that two DSBs relocated within the same nuclear domain have a larger probability of leading to cell death than DSBs far apart, we could recapitulate the classic bell shape curve for the LET dependence of RBE for cell survival (18).

However, the experimental validation of our model had been minimal, limited to only one immortalized cell line (human breast cancer line MCF10A). Therefore, in this study we have investigated whether DSB coalescence is not just a computational construct, but also a biological phenomenon that occurs in non-immortalized primary cells. We have defined the range and variability of RIF formation in response to X-ray and HZE particle radiation in *ex vivo* fibroblast cultures isolated from 15 different mouse strains. Our results help characterize the dose and LET dependence of RIF formation, demonstrate that DSB clustering into RIFs is conserved across 76 *ex vivo* isolates derived from 15 different strains of mice, and show that the kinetics of RIF formation

are determined by both radiation characteristics and mouse strains, suggesting a genetic association.

Materials & Methods

Isolation of primary fibroblasts from mouse ears:

Collaborative Cross (CC) mice presents a multiparental recombinant inbred population of mice derived from generations of inbreeding from five classic inbred strains (A/J, C57BL/6, 129S1/SvImJ, NOD/ShiLtJ and NZO/H1LtJ) and three wild-derived substrains (CAST/EiJ, PWK/PhJ) and WSB/EiJ) (19). High level of genetic variation distributed randomly across the CC genomes causes each line to be genetically independent and prone to fewer spurious associations in mapping studies (20). We chose 10 strains from the CC panel: CC002, CC011, CC013, CC019, CC032, CC037, CC040, CC042, CC051, CC061. In addition, we used 5 reference strains that had previously been characterized for various radiation phenotypes: C57Bl/6, BALB/CByJ, B6C3, C3H and CBA/CaJ, for the total of 76 animals.

Mouse ears were decontaminated by soaking them in 70% ethanol for 15 seconds and were let dry. Ears were cut in small pieces with sterilized scissors and were transferred to a Falcon tube containing 3 mL of 50 U/mL collagenase (Gibco 17101-015-1g) in HBSS (Gibco, Thermo Fisher Scientific). Tubes were placed at 37°C in water bath for 1 hour and were vortexed for 5 seconds every 15 minutes during this incubation. After incubation, the tubes were filled with Minimum Essential Media (MEM, Gibco, Thermo Fisher Scientific) supplemented with 10% v:v fetal bovine serum (FBS, Gibco, Thermo Fisher Scientific) and 1% v:v

penicillin/streptomycin (Gibco, Thermo Fisher Scientific). Tubes were centrifuged at 1000 rpm for 5 minutes and the supernatant was discarded. The pellet was re-suspended in 2 mL of culture medium and transferred into a 6 well plate. Cells were incubated in a humidified incubator containing 5% CO₂ and 3% O₂. After 24 hours of incubation at 37°C, the wells were rinsed and 2 mL fresh medium was added. At passage 3, fibroblast cells were re-suspended in an appropriate freezing medium (90% FBS, 10% DMSO) at a concentration of 10⁶ cells/mL and stored at -80°C in a cryo 1°C freezing container. The next day, cryovials were transferred in liquid nitrogen tank until further use. This procedure was performed for each of the 76 different animals. On an average, cells from 3 males and 3 females for each strain were expanded and frozen for further characterization.

Irradiation:

Fibroblasts were thawed at BNL (Brookhaven National Laboratory; NY, USA) or LBNL (Lawrence Berkeley National Laboratory; CA, USA) and immediately aliquoted into 96 well plates, one well for each individual cell line (76 primary lines), with precise recording of each cell position in the plates. 10⁴ cells were seeded in 96 well plates (IBIDI microplate, IBIDI®, Germany) and incubated at 37°C in a humidified incubator containing 5% CO₂ and 3% O₂. Medium was replaced two hours before exposure of each plate. Figure 1 summarizes the experimental design.

Briefly, at BNL plates were exposed to two different HZE: 350 MeV/n Ar and 600 MeV/n Fe, which have 104 and 170 keV/μm LET respectively, using two fluences: 1.1 and 3 particles per cell, in duplicate for each condition including control.

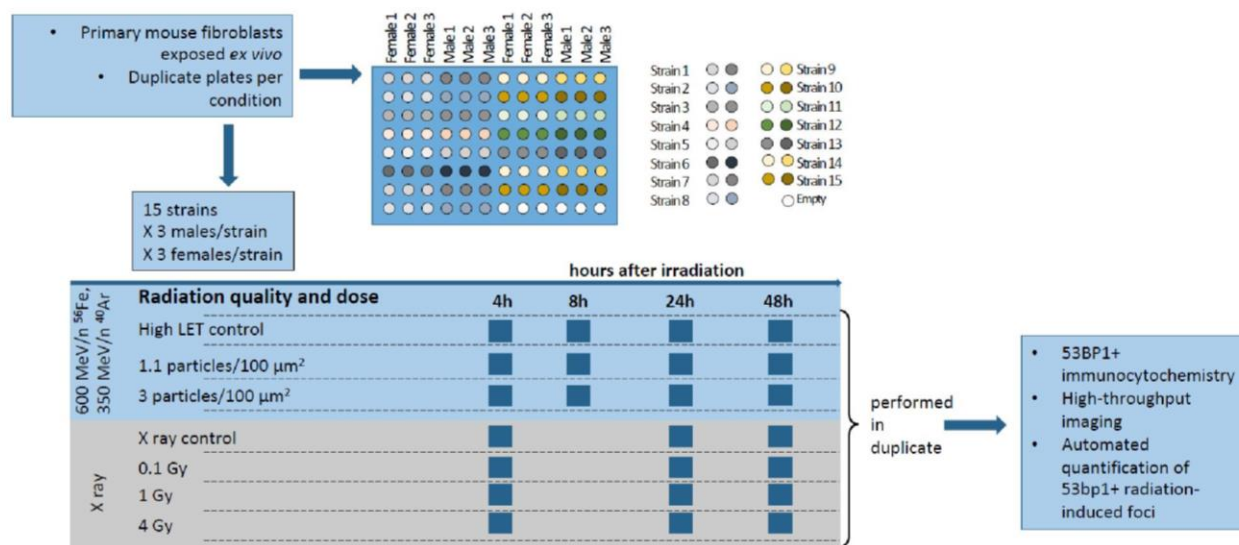


Figure 1. Experimental design. Primary skin fibroblasts isolated and cultured *ex vivo* from 15 strains of male and female mice were irradiated in duplicate either with HZE particles (600 MeV/n ^{56}Fe , 350 MeV/n ^{40}Ar) at 2 fluences (1.1 and 3 particles/100 μm^2) or with 3 doses (0.1, 1 and 4 Gy) of X-rays, or left unirradiated as controls. DNA repair was quantified by 53BP1+ foci immunocytochemistry at 4, 24 and 48 hours post-irradiation for both HZE particles and X-rays, and at additional 8 hours post-HZE particle irradiation.

HZE plates were thus exposed to 6 different doses given their different LETs (i.e. 0.30 Gy and 0.82 Gy for 600 MeV/n Fe; 0.18 Gy and 0.50 Gy for 350 MeV/n Ar). Cells were ~80% confluent for Ar and ~90% confluent for Fe irradiation, measured at the early time point (4 hours). Plates were exposed to radiation with the beam hitting below the plate, and the plate angled at less than 5 degree, generating clear distinct tracks in the nuclei visible at early time points. X-ray experiments were conducted at LBNL on a 160 kVp Faxitron X-ray machine. Dose rate for both X-ray and ion exposure was 1Gy/min.

At 4, 24 and 48 hours post-exposure for all radiation qualities and at an additional 8 hours post-exposure for HZE conditions, cells were fixed with 4% paraformaldehyde (Electron Microscopy Sciences, PA, USA) in PBS for 15 min at room temperature followed by three washes with PBS for 5 min each, sealed and kept at 4°C.

Immunostaining and imaging:

Cells were processed for immunostaining via programmed liquid handler (MultiFlo FX, BioTek). Detailed protocols can be found in our previous publications (8, 14). Briefly, cells were permeabilized with 0.1% Triton X-100 (Sigma Aldrich) in PBS for 20 min and blocked for 1 hour with 3% Bovine Serum Albumin (BSA; Thermo Fisher Scientific) in PBS at room temperature. Cells were then incubated at room temperature with rabbit polyclonal anti-53BP1 primary antibody 1:300 dilution (IHC-00001, Bethyl Laboratories) for 1 hour, and subsequently incubated with 5 $\mu\text{g}/\text{mL}$ AlexaFluor488 anti-rabbit secondary antibody (ThermoFisher). Nuclei were stained with 5 $\mu\text{g}/\text{mL}$ DAPI (Molecular Probes). Washing was performed between all incubations.

For high-throughput automated imaging and quantification, immunofluorescence data was consolidated and analyzed using commercial scanning microscope with Nikon objective (40X, 0.95 NA) and automated foci quantification

algorithm developed in lab, with a target of at least 800 cells per well, as previously described (14). A wavelet morphological filter was applied to enhance foci peaks while reducing non-specific signal noise. Nuclear area was identified by applying a constant threshold on the wavelet-filtered image and foci were identified using a background subtraction method. Touching foci were separated using a watershed algorithm (14, 18). All statistical analyses were done using R packages: least-square fits were done using ggplot2 (21, 22) and correlation plot were done with corrplot (23).

Results

1. DNA damage and repair kinetics indicate coalescence of multiple DSB into RIFs

We exposed 76 immortalized primary skin fibroblast cell lines from 15 different strains of mice to HZE particles using two LETs: 350 MeV/n ^{40}Ar (104 keV/ μm), 600 MeV/n ^{56}Fe (170 keV/ μm) and two ion fluences (1.1. and 3 particles/ $100\ \mu\text{m}^2$) at the NASA Space Research Laboratory in Brookhaven National Laboratory. In addition, the same cell lines were exposed to low-LET radiation: 0.1, 1 and 4 Gy 160 kVp X-rays at Lawrence Berkeley National Laboratory. We quantified RIF formation at 4-48 hours after irradiation using immunocytochemistry for a DNA repair protein 53BP1 followed by high-throughput automated detection of 53BP1+ intranuclear foci (see Materials and Methods and experimental setup in Figure 1).

Figure 2 depicts the formation of 53BP1 RIFs per cell at 4, 24 and 48 hours after X-ray irradiation in the 15 mouse strains used in the experiment, averaged across sex (N = 6 animals per dose per time point). In agreement with what we previously reported for human breast cell line

MCF10A (24), our early time point (4 hours) for the primary mouse fibroblast responses to X-rays show a dose response which is not linear, but instead reaches saturation between 1-4 Gy, and likely indicates multiple DSB coalescence into single RIF. DSB coalescence is illustrated in Fig. 2B showing representative images in CBA mice cells where 4 Gy X-rays elicit larger and brighter RIF 4 hours post-exposure than after 1 Gy, whereas number of RIF/cell are comparable for both doses. The concept of DSB coalescence is further schematized in Fig. 2C and one can read more about it in our previous work (24).

We chose 4 hours after irradiation as the earliest time point based on our prior experience with MCF10A cells and other studies that indicated earlier time points to be poorly reproducible, likely reflecting a comparatively large amount of noise generated by small differences in temperature and plate handling. By 4 hours these uncertainties are strongly reduced and RIFs are better established and clearly delimited, which facilitates automated detection. On the other hand, some RIFs by that time have already been resolved and thus differences of RIF levels between strains may also reflect differences in repair kinetic in the first 4 hours after irradiation. 24 hours post-exposure, most DSBs are repaired and the remaining RIF numbers increase linearly with dose. Interestingly, 48 hour time point shows departure from linearity again, this time showing a quadratic behavior with more RIF at 4 Gy against 0.1 and 1 Gy. This probably reflects a slower repair of the remaining RIFs combined with permanent RIFs induced by high doses.

Note that all RIF/cell were background corrected by subtracting the number of spontaneous foci that are constantly formed in the cells at baseline with no exposure to radiation.

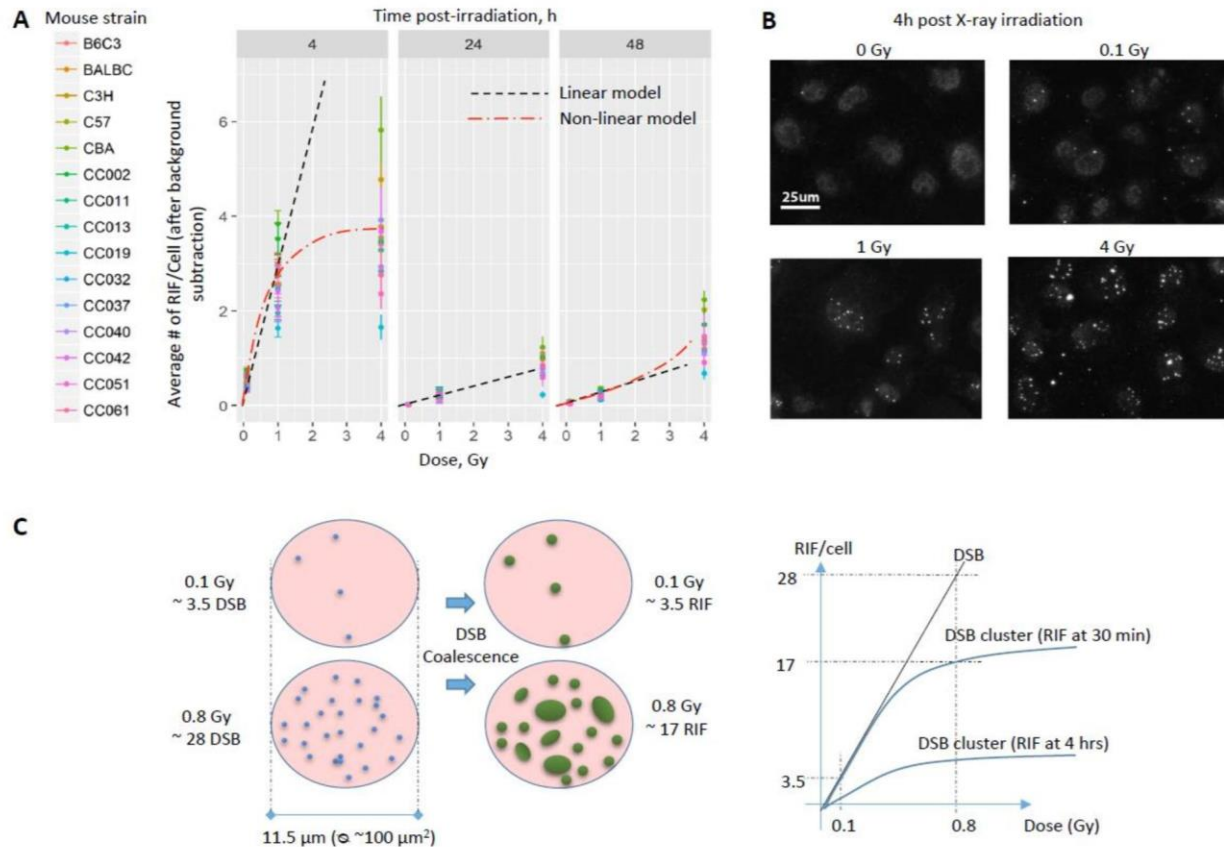


Figure 2. Dose and time dependence of RIF formation in response to X-ray irradiation. A. Average RIF per nucleus after X-ray irradiation in 15 mouse strains. Black dotted line, linear fit. Red dotted line, non-linear fit. **B.** Representative images of 53BP1+ RIFs 4 hours after irradiation with 0.1Gy, 1Gy and 4Gy doses of X-rays. CBA mouse strain. **C.** Schematic representation of RIF coalescence at high doses of X-ray irradiation.

In order to estimate the foci background, instead of averaging the number of foci in the 0 Gy group, we linearly fitted each individual strain dose response using a least square fit method (R statistics package, see Materials and Methods) for doses less than 4 Gy for both 4 and 48 hours (because at 4 Gy at those time points the responses become non-linear), and for all doses for 24 hour time point. The intercepts of these fits were used as an estimate of spontaneous foci formation at 0 Gy instead of simply using the average foci level of the control plates alone, due to stronger statistical value for correction.

Figure 3A and B show the dose response of RIF/cell corrected for background using the same approach for both 350 MeV/n ⁴⁰Ar and 600 MeV/n

⁵⁶Fe exposures. Even though both radiation qualities had the same two fluences, their corresponding doses are different due to the differences in LET with 600 MeV/n Fe exposures leading to a higher dose (see Figure 3C for a schematic representation). For all strains, the slope in RIF/Gy is higher at early time point for the lower LET (350 MeV/n Ar), but at later time point is lower compared to 600 MeV/n Fe. This difference cannot be explained by different number of DSBs, because the number of DSBs/Gy should be very similar between both LETs, which would cause slopes to overlap instead of diverging. Furthermore, it cannot be explained by a 1:1 correspondence between RIF and DSBs either.

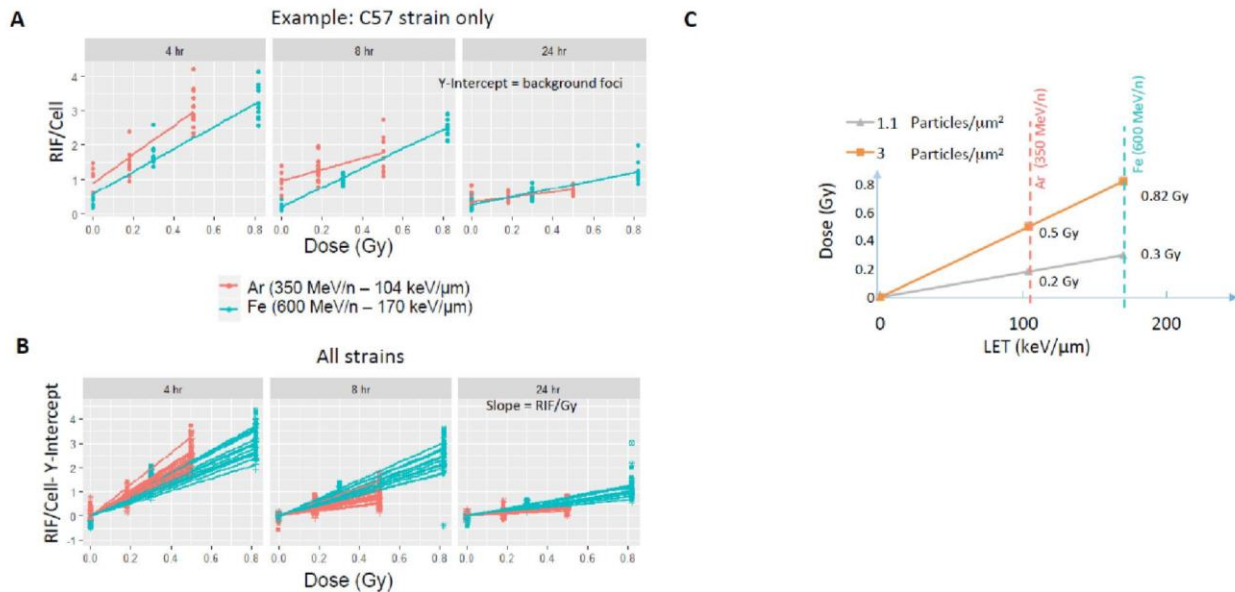


Figure 3. RIF number is linearly correlated with dose for both HZE particles. **A.** RIF number per cell in response to radiation dose at different time points after irradiation illustrated for one strain (C57), without distinguishing males and females. For each strain, a linear fit is applied and the Y-intercept is used to evaluate foci background. **B.** Number of RIF per cell normalized by background subtraction. In this second plot, all linear fits are forced through 0,0 since the data have already been corrected for the intercept. Each line represents a mouse strain. **C.** For HZE particles, the dose is determined by particle fluence and LET, with higher LET particles leading to higher dose for equal fluence. The corresponding doses are labeled and match the dose points displayed in **A** and **B**.

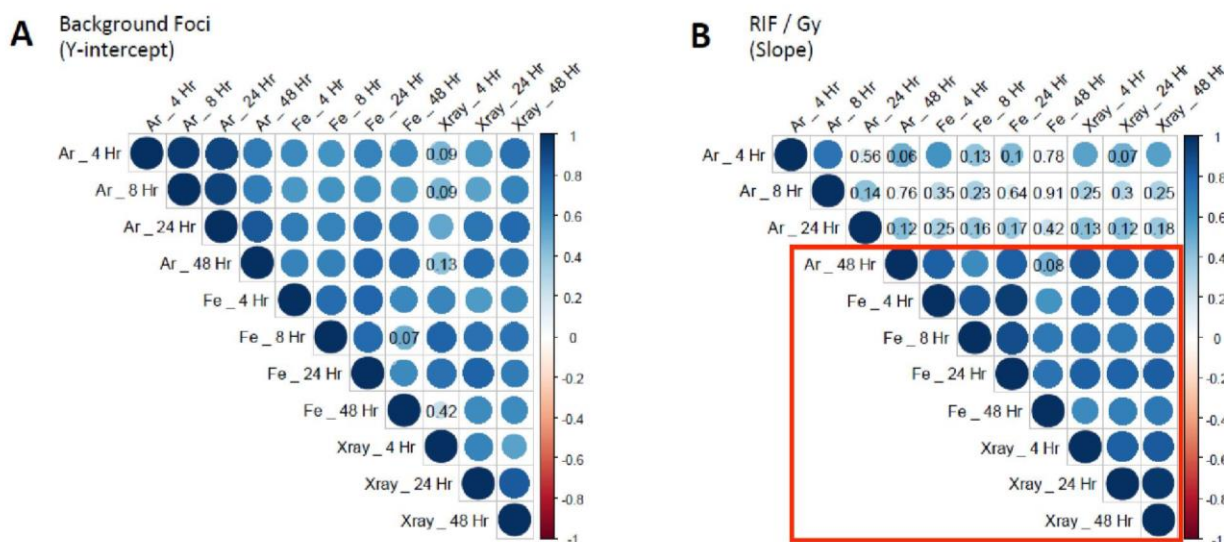


Figure 4. Background foci and dose dependence of radiation-induced foci formation are correlated between radiation qualities. **A.** Background foci (Y-intercept in Fig. 3A), per cell, averaged across all mouse samples from the same radiation quality and time point. **B.** Dose dependence of RIF formation (slope in Fig. 3A), per cell, averaged across all mouse samples of the same radiation quality and time point.

If that were the case, our data would indicate that cells repair faster after exposure to 600 MeV/n Fe, but the opposite has been shown to be true (25, 26). Therefore, we instead interpret these results as the evidence that as the LET increases, more DSBs are contained within one single RIF at early time points, with 600 MeV/n Fe producing more DSBs per RIF and fewer total RIFs/cell than 350 MeV/n Ar. Consequently, the increased number of DSB/RIF for higher LET leads to slower repair, as indicated by a steeper slope (RIF/Gy) for 600 MeV/n Fe at both 8 and 24 hours, reversing the position of Fe and Ar curves (Figure 3B).

2. Comparison of DSB formation at baseline and in response to increasing doses of X-ray and HZE radiation across 15 mouse strains

Figure 4 depicts the Pearson correlation coefficient (color coded between -1 for perfect anti-correlation to 1 for perfect correlation), for either the number of foci background (Y-intercept - Figure 4A) or RIF/Gy (slope - Figure 4B), combined across all 15 mouse strains. Pearson's coefficient > 0.52 for 15 potential pair of measurements leads to a P-value < 0.05 and thus a significant correlation between the measurements. The strong correlation for background foci computed here is evident as most circles are dark blue with P-value less than 0.05 (Figure 4A). Considering the fact that the various 96-well plates were seeded, irradiated and analyzed on different days and weeks, spanning over the course of a 3 month analysis and being conducted in two different sites for irradiation (BNL and LBNL) suggests a very strong association with genetics. This allows us to conclude that spontaneous DNA damage is a well conserved property across strains, with the same

strains always showing high background relative to other strains, independently of confluence or plating conditions. Similarly, the slope of RIF/Gy was well conserved for all time point for 600 MeV/n Fe and X-ray and at 48 hour for 350 MeV/n Ar (Figure 4B, red contour).

The 15 mouse strains can be ranked based on their background levels of DNA damage by computing the average foci background across all conditions corresponding to 11 independent measurements (4 time points x 2 LET and 3 time point for X-ray). Figure 5A shows representative 53BP1+ images of "high" and "low" responder strains in terms of RIF formation at baseline and at 4h and 24h following exposure to 3 particles/100 μm^2 of 600MeV/n ^{56}Fe irradiation. Figure 5B represents the quantification of background foci computed as the Y-intercept of the dose response (see Figure 3) for each strain. Similarly, mouse strains can be ranked based on RIF/Gy averaged between samples, in response to each radiation condition, at both 4 and 24 hours post-exposure (Figure 5C shows ranking for Fe at 24 hours).

Strain ranking is different between background and RIF/Gy at different time points. Interestingly, at 4 hours after irradiation, even though 350 MeV/n Ar causes more RIF/Gy than 600 MeV/n Fe (Figures 3B and 5C), the correlation for all 3 radiation type has a P-value less than 0.05 (Figure 4B). As observed in Figure 3B, Figure 5C show there are more DSB/RIF as the LET increases at 4 h while at later time point (24 h) this trend is completely reversed with more RIF/Gy for higher LET. On the other hand, the strain ranking remains very similar (as shown with low P-values) confirming again a strong genetics association with the actual clustering of DSB.

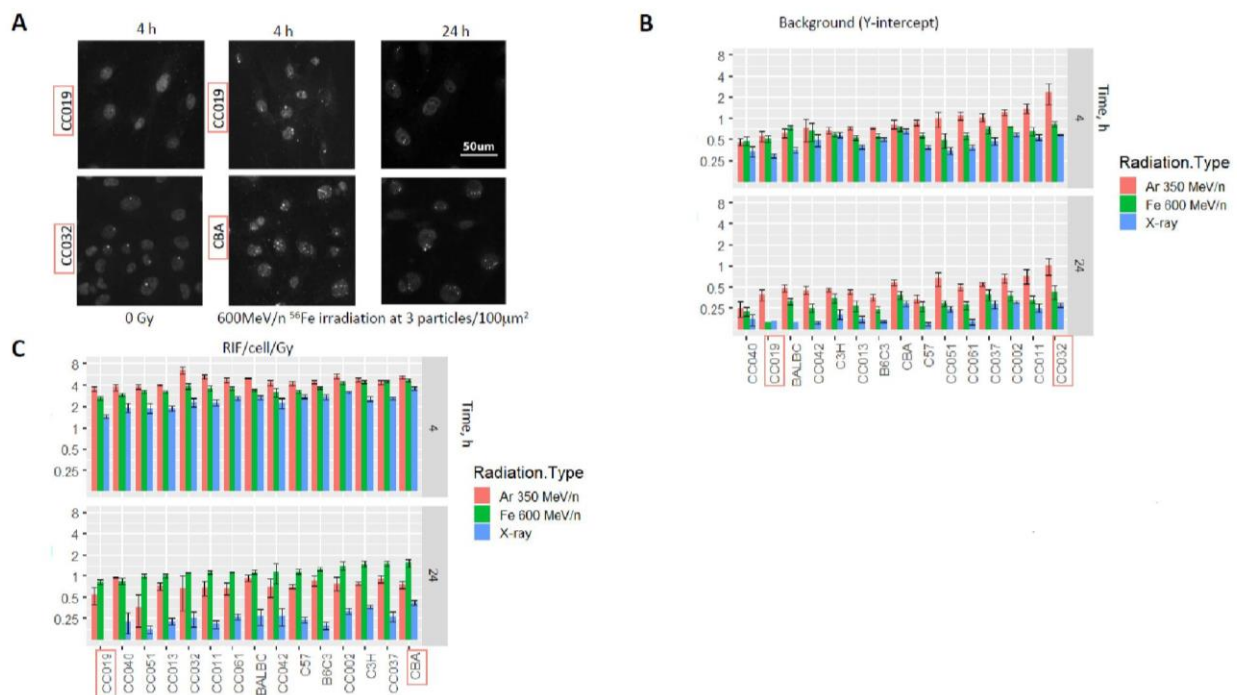


Figure 5. DSB clustering into RIFs is conserved across strains. Representative images (A) and quantification of background foci (B) and post-irradiation RIF formation at 4 hours and 24 hours (C) in all mouse lines in response to HZE particle and X-ray irradiation.

3. Introducing the metric of RIF number/track length in HZE-exposed cells for defining radiation sensitivity in each mouse strain

We have previously introduced the concept of another metric specifically for HZE RIF, which better reflects the LET of the particle: the average number of RIF per unit length along each track imaged by microscopy, with RIF/ μm as a unit (12). In order to make such measurement however, one needs cells which show visible tracks. This typically implies adherent cells which do not move over time. Such measurements are therefore limited to very early time-points and require sophisticated line detection algorithms for track identification. In this work, we approached our quantification by using high throughput microscopy (i.e. lower magnification 20X, high NA, 3D stacks without confocal imaging – see material and method). As such, track detection was not an

option and we propose an alternative method to estimate the average number of RIF/ μm using a simple normalization scheme as described below. Typically, the average number of RIF per cell (R_C) for HZE can be written as:

$$R_C = B + [\Phi \cdot V \cdot R_U] \quad (1)$$

where B is the foci background level measured without irradiation, Φ is the fluence, V is the average volume of the cell and R_U is the average number of RIF/ μm .

As we have shown in the past, the parameter R_U is LET dependent and typically starts showing saturation for LET larger than 150 KeV/ μm with maximum around 1 RIF/ μm for human breast epithelial cells MCF10A (18). We have interpreted this LET dependence as the fact that nearby DSBs clusters into single RIF along a track. Based on what we have shown in the previous figures, one would expect this factor to be strain dependent. In order

to estimate R_U parameter, we can rewrite equation (1) as followed:

$$R_U = \frac{R_C - B}{\Phi \cdot V} \quad (2)$$

The volume of cells can be estimated by measuring the nuclear area of each cell. The height of each cell was not computed in this work due to the high-throughput nature of imaging, but it has not been shown to strongly vary between skin fibroblasts of different mouse lines, and thus we assume constant cell height for all plates being imaged. We noted that nuclear area varied consistently across strains and was also a function of time with later

time point having smaller nuclear area due to the higher confluence.

Taking data from Figure 3 and normalizing them with equation (2), we computed a surrogate measurement of $R_U/\mu\text{m}$. Figure 6 A-B, illustrate these results as a function of LET for both fluences, separating female and male data. Both low and high fluence normalized data overlap, suggesting that equation (2) leads to a metric that is independent of fluence and truly reflects the intrinsic property of the mouse strain to form DSB clusters and repair them. We therefore proposed to average both low and high fluence normalized data as well as male and female for each strain as shown in Figure 6C as a function of LET.

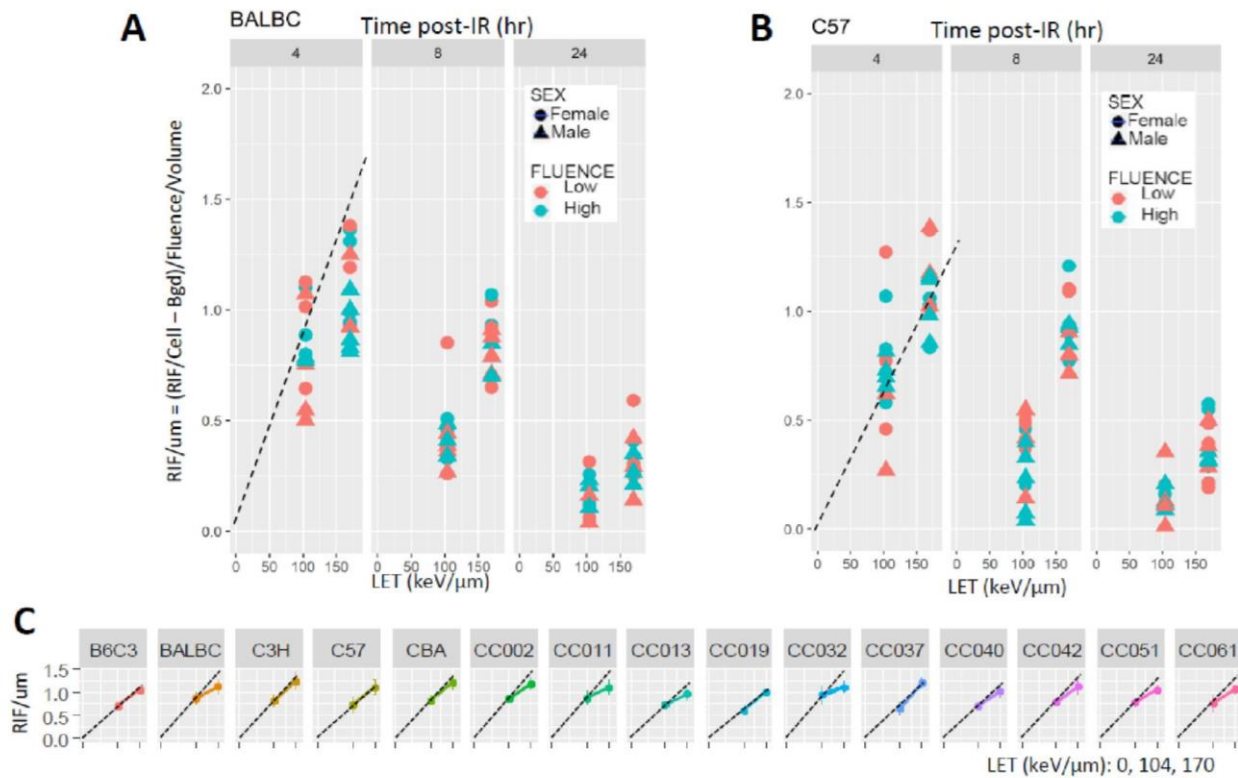


Figure 6. RIF/ μm dependence on LET, but not fluence, in different mouse lines. A-B. Surrogate estimation of R_U (RIF/ μm) at different time points (columns: 4h, 8h, 24h) post irradiation, with low-dose (1.1 particle/ $100\mu\text{m}^2$ fluence) and high-dose (3 particles/ $100\mu\text{m}^2$ fluence), low-LET (350MeV/n Ar) and high-LET (600MeV/n ^{56}Fe) irradiation in representative mouse lines (A, BALBc and B, C57). C. R_U (RIF/ μm) dependence on LET in all mouse lines, both doses and genders combined, at 4h post-irradiation. Dotted line, linear dependence. Note the difference in linearity between lines with e.g. BALB/C, CC032 and CC011 being non-linear (i.e. showing saturation) and C57 and CC019 being the most linear (i.e. no saturation).

Surprisingly, saturation for normalized HZE RIF was not as striking as it is for the X-ray response at 4 Gy, possibly due to the difference between doses: none of HZE doses reached 1 Gy. It is interesting to note that most strains have similar yield for RIF/ μm , but the LET dependence is highly driven by genetics with some strains showing no sign of saturation up to 170 keV/ μm (e.g. C57 and CC019), whereas other show significant saturation (e.g. BALB/C, CC032 and CC011).

To compare mouse lines based on RIF saturation in response to both X-ray and HZE particle irradiation, we introduce a metric for saturation in Figure 7, as described below:

$$Sat = 1 - \frac{Slope2}{Slope1} \quad (3)$$

Where *Sat* is the saturation coefficient (0 if no saturation and 1 if fully saturated), *Slope1* is the

linear parts of the curve for the dose or LET, and *Slope2* fits the saturated part of the curve (Figure 7A). For X-ray, this can be done by fitting a line for RIF/Cell-Bgd for 1 and 4 Gy points as the saturated part of the curve (*Slope 2*) and for 0.1 and 1 Gy for the linear part (*Slope 1*). For HZE, we can fit R_U for 104 and 170 keV/ μm (i.e. Ar and Fe) as the saturated part of the curve (*Slope2*) and assuming Ar data point alone stands on the linear part of the curve, which assumes no significant saturation below 100 keV/ μm (i.e. *Slope1*). *Slope2* is typically always lower than *Slope1*, except when there is no obvious saturation.

Figure 7B reports the saturation coefficient for all 15 strains.

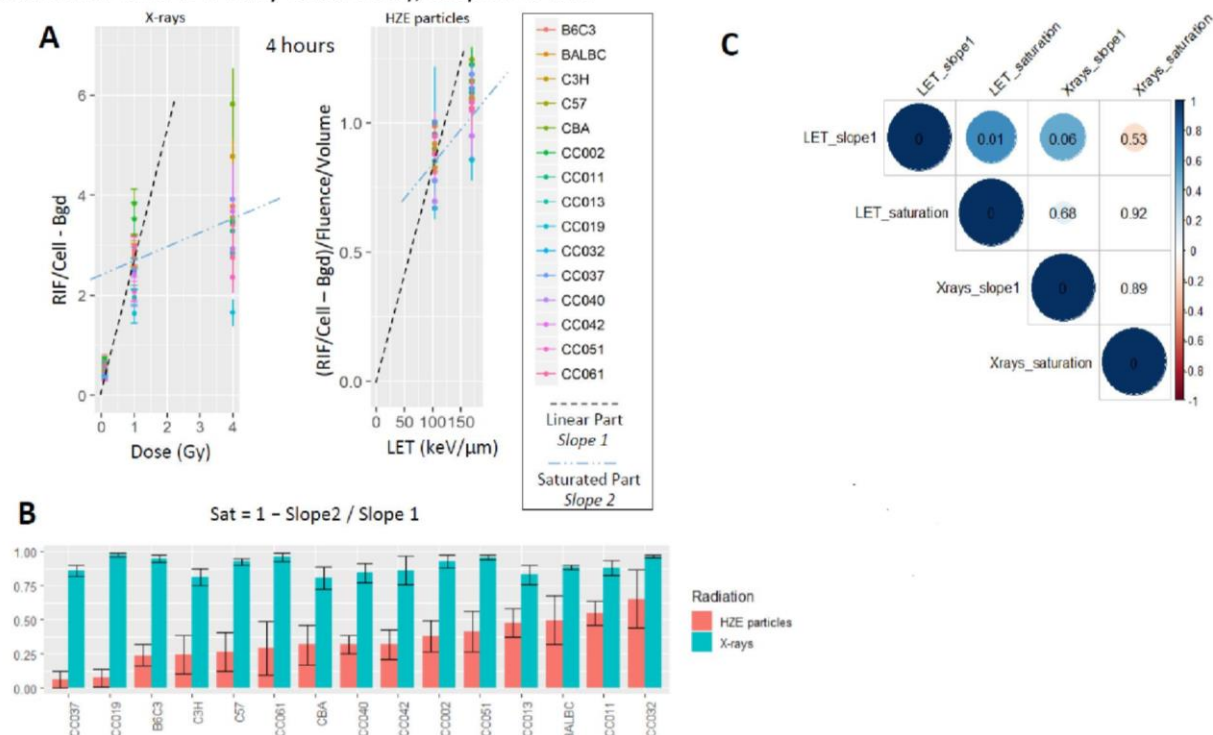


Figure 7. Comparison of early saturation parameters between mouse strains and radiation qualities. A. RIFs per cell as function of dose for X-rays or RIFs per μm as a function of LET for the two HZE particles, normalized to background. **B.** Mouse strain ranking based on Saturation coefficient defined as $1 - \text{Slope2} / \text{Slope1}$ (see A)). Note that the Saturation coefficient is 0 if *Slope1* and *Slope2* are identical (i.e. no saturation) and this coefficient is equal to 1

if the curve is fully saturated (i.e. Slope2=0). **C.** Correlation between saturation parameters between strains in response to X-ray and HZE radiation.

The first striking difference between HZE and X-rays is the latter shows extremely high saturation (between 80 to 100%), suggesting 4Gy dose may have been too high and remove our ability to distinguish the clustering properties of the strains. In contrast, the HZE response show saturation between 0 to 60%, with large differences between strains, suggesting that this metric is probably more accurate for HZE at doses analyzed in this experiment. As expected, no significant correlation was observed (p -value = 0.92) between X-rays and HZE saturation, suggesting a lower dose should be used in the future for better strain discrimination in response to X-rays (Figure 7C).

Discussion

This work is one of the most extensive studies on the possible genetic underpinnings of radiation-induced DNA damage and repair. We characterized 53BP1 radiation induced foci (RIF) in 76 clones of primary skin fibroblasts isolated from 15 different strains of Collaborative Cross and reference mice, using equal number of females and males. This work resulted in the analysis of more than 3000 wells being imaged with a target of 800 cells/well, in duplicate, leading to the analysis of ~5 million cells. In this first part of the work, we validated our previous computational model of DSB clustering patterns by characterizing the dose and LET dependence of 53BP1+ foci formation after exposure to two different HZE particles (350MeV/n Ar and 600 MeV/n Fe) and X-rays.

RIF quantification after low-LET X-ray exposure showed an asymptotic dependence on doses for early time points post-irradiation across all 15 strains, similar to what we had previously reported for immortalized human cell lines (14), with close to full saturation 4 hours following 4 Gy of X-rays, against partial saturation (up to 60% for one strain) 4 hours following 170 keV/ μ m HZE

irradiation. The clustering of DSB could also be witnessed across all strains, with the HZE response showing that the yield of RIF/Gy was LET dependent with more RIF/Gy for lower LET (X-ray and 350 MeV/n Ar) at 4 hours post-exposure compared to 600 MeV/n Fe. Assuming the number of DSB/Gy is fairly similar across all 3 LET considered here, this means that the average number of DSB/RIF increases with LET as we had previously hypothesized in one immortalized human breast cell line (8). In addition, at later time points (24 hours and above), the trend was inverted with more RIF/Gy for higher LET (by 600 MeV/n Fe), suggesting more difficulty for the cells to repair the larger clusters of DSBs per RIF. Finally, we observed that the RIF/Gy metric was strain-dependent and varied consistently across time points and radiation qualities, indicating that this phenotype is at least partially driven by genetics.

We have hypothesized that the nucleus of mammalian cells is divided into discrete regions which contain the movement of DSBs after irradiation, and that DSBs occurring in the same domain have a tendency to coalesce into single RIF for repair (18). Previous data suggest that repair domains are preferentially located in the euchromatin (12, 27) with a width of ~1 to 1.5 μ m in human cells (13, 18). We have also extensively discussed in the past how chromatin architecture modulates repair domains and thus how cell cycle and cell type, by having distinct chromatin structures, inherently have also distinct repair properties (10). In this new work, we now show how genetics also modulates repair domain and we summarize our results in an elaborate scheme describing the relationship between LET, dose, fluence and repair domains in Figure 8, showing how the LET and dose dependence observed in this work are in complete agreement with our hypothesis.

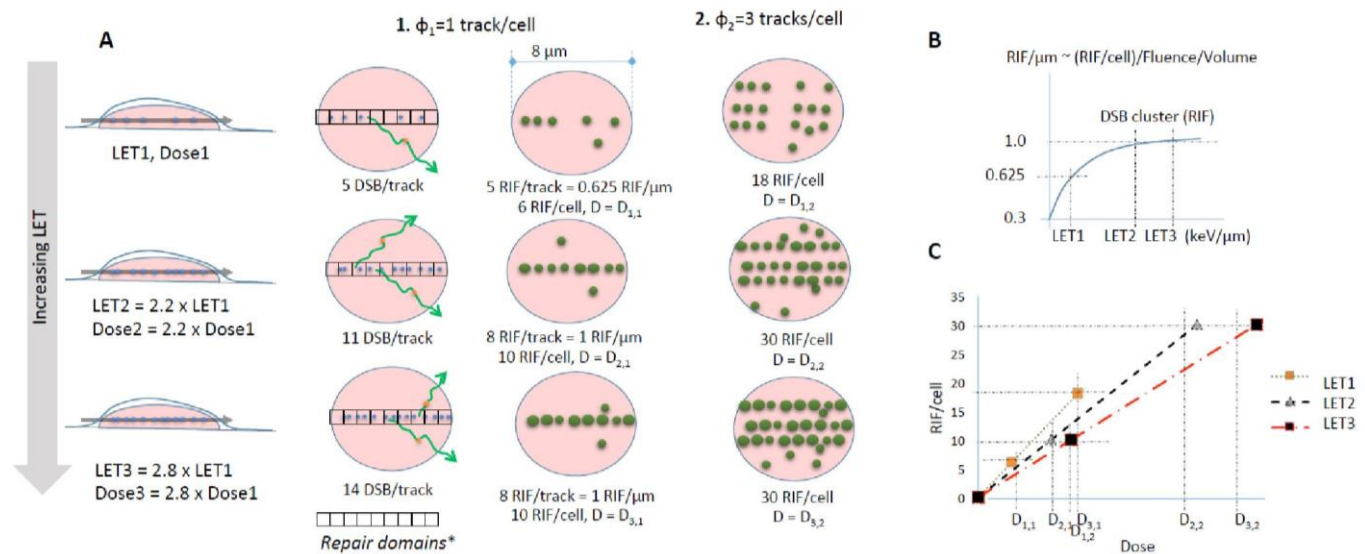


Figure 8. RIF formation is determined by particle LET and fluence and is modulated by nuclear organization of repair domains. A. Schematic representations. **1.** Increasing LET of particles at the same fluence (ϕ_1) increases the number of DSB/track. As the LET keeps increasing the number of DSB/track increases linearly with it, but not the number of RIF/track. This is because multiple DSBs start coalescing into isolate RIFs. **2.** Increasing the fluence (ϕ_2) increases the number of tracks per cell, but does not change the number of DSB/track or RIF/track with increasing LET. This results in a number of RIF/cell that is proportional to dose, while the number of RIF/track and thus RIF/ μ m saturate at higher LET as plotted in **B** and **C**. **B.** RIFs per track length (i.e. RIF/ μ m) plateau at high LET. **C.** Dose dependence of RIFs per cell.

The existence of repair domain and the concept that DSB are constrained to be repaired together when occurring at the same time and within the same domain is contrary to the classic “contact-first” hypothesis where DSBs are assumed to be immobile and repaired at the lesion site (28, 29). Aten et al. were first to show that RIF do cluster rapidly after exposure to ionizing radiation (30), and we recently confirmed using time-lapse fluorescent microscopy of 53BP1 fused to GFP that RIF are constrained in localized regions of the nucleus after exposure to X-ray (13).

Active movement of DSB to specific area of the nucleus for repair has the advantage of being much more efficient molecularly and could explain the previously published unexpected high frequencies of complex exchanges being revealed by FISH painting, as hypothesized by Savage et al (31). By assuming repair domains, the spatial distribution

of DSBs becomes a critical factor, which can explain large differences in chromosomal aberration observed between high and low-LET. Specifically, high-LET HZE generate several nearby DSBs along their linear track, increasing significantly the probability of them clustering into the same. As the linear density of DSB increases with LET, so does the probability of having more DSB per RIF (12, 32) RIF (as illustrated in Figure 8). Meanwhile, low doses of low-LET radiation, such as X-rays, generate DSB randomly in the nucleus and do not cause DSB clustering, thus keeping the number of DSB/RIF close to 1 for doses below 1 Gy (24). With such hypothesis, one can explain the hypersensitivity to high-LET radiation (and thus, the fact that mutation, cell death and cancer is much more prevalent following cosmic radiation) despite a low number of RIFs, by the fact that these RIFs contain a large number of DSBs. In this way our

model represents a paradigm shift where increased spatial proximity of DSB is an alternate explanation for hypersensitivity to high-LET in contrast to the classical DNA damage complexity as the primary mechanism (26, 33, 34).

We have observed significant differences in background RIFs, irradiation-dependent RIF formation and saturation of RIF numbers at higher radiation doses among mouse strains, which indicate a strong strain-dependent genetic component in radiation-induced DNA damage responses. In particular, the differences in the number of background RIFs, representing a baseline state without irradiation, were significantly correlated among all experiments, and thus likely represent an inherent, strain-specific characteristic. Mouse strain differences in susceptibility to radiation-induced cancers had been reported previously (35, 36) *in vivo* in 3-4 mouse strains. Here we expand that knowledge including 15 strains and focusing on a wide range of radiation response parameters *ex vivo* at a cellular level. Notably, some inbred mouse strains, such as CBA and C3H, are highly susceptible to cancers and have 12% rate of spontaneous carcinoma (37), which is consistent with our results that CBA and C3H have some of the highest rates of persistent radiation-induced foci out of all investigated strains. The high susceptibility to radiation and cancer prevalence in these strains is likely associated with genomic instability, which increases radiation-induced DNA damage and carcinogenesis at least in part due to non-targeted effects of reactive oxygen species released by neighboring cells (38, 39).

When interpreting metrics which precisely quantify the amount of DSB clustering in this work, we were challenged by two competing events taking place at the same time: DNA repair and DSB clustering. In other words, the numbers of RIF/Gy for X-ray and of RIF/ μm for HZE do not only reflect the initial clustering of DSBs into RIFs, but they are

also modulated by ongoing DNA repair processes. These metrics cannot distinguish between a strain with proper DNA repair genes with strong DSB clustering leading to persistent damage (indicated by a high number of RIFs at 24 hours), and a strain with deficient repair mechanisms that also lead to more persistent damage at 24 hours. In the second part of our study, we will present strategies to distinguish DNA repair processes from DSB clustering and we will associate the various phenotypes to *in vivo* endpoints related to radiation sensitivity across all 15 different strains, with an emphasis on identifying potential genetic loci associated to radiation sensitivity. Meanwhile, this part provides a phenotypic basis for comparing mouse strains and gives us a better understanding of the spectrum of differences for DNA repair and DSB clustering within the same mammalian species.

Significance Statement

Our study indicates that radiation-induced foci are composed of multiple double-stranded DNA breaks in each of the 15 mouse strains in response to both low and high-LET radiation. These results allow developing more accurate models that extrapolate absorbed radiation dose and associated damage from radiation-induced foci. In addition, we present mouse strain-dependent differences in radiation responses, which is a useful source for analyzing experimental results and investigating the genomic factors that mediate radiation sensitivity.

Acknowledgments

This work was supported by NASA grant #NNL15AA08I to S.V.C. (principle investigator) S.P. is a PhD fellow funded by the Belgian Fund for Scientific Research (FRS-FNRS, Belgium). We would like to thank Dr. Afshin Beheshti for comments, suggestions and discussion during preparation of manuscript.

References

1. Barratt MR, Pool SL, *Principles of clinical medicine for space flight*. New York: Springer; 2008.
2. Durante M, Cucinotta FA, Heavy ion carcinogenesis and human space exploration. *Nat Rev Cancer* 2008; 8, 465-72.
3. Mewaldt RA, Galactic cosmic ray composition and energy spectra. *Adv Space Res* 1994; 14, 737-47.
4. Alpen EL, Powers-Risius P, Curtis SB, DeGuzman R, Tumorigenic potential of high-Z, high-LET charged-particle radiations. *Radiat Res* 1993; 136, 382-91.
5. Cucinotta FA, Durante M, Cancer risk from exposure to galactic cosmic rays: implications for space exploration by human beings. *Lancet Oncol* 2006; 7, 431-5.
6. Asaithamby A, Uematsu N, Chatterjee A, Story MD, Burma S, Chen DJ, Repair of HZE-particle-induced DNA double-strand breaks in normal human fibroblasts. *Radiat Res* 2008; 169, 437-46.
7. Rogakou EP, Pilch DR, Orr AH, Ivanova VS, Bonner WM, DNA double-stranded breaks induce histone H2AX phosphorylation on serine 139. *J Biol Chem* 1998; 273, 5858-68.
8. Costes SV, Boissiere A, Ravani S, Romano R, Parvin B, Barcellos-Hoff MH, Imaging features that discriminate between foci induced by high- and low-LET radiation in human fibroblasts. *Radiat Res* 2006; 165, 505-15.
9. Rodier F, Coppe JP, Patil CK, Hoeijmakers WA, Munoz DP, Raza SR, et al., Persistent DNA damage signalling triggers senescence-associated inflammatory cytokine secretion. *Nat Cell Biol* 2009; 11, 973-9.
10. Costes SV, Chiolo I, Pluth JM, Barcellos-Hoff MH, Jakob B, Spatiotemporal characterization of ionizing radiation induced DNA damage foci and their relation to chromatin organization. *Mutat Res* 2010; 704, 78-87.
11. Roos WP, Thomas AD, Kaina B, DNA damage and the balance between survival and death in cancer biology. *Nat Rev Cancer* 2016; 16, 20-33.
12. Costes SV, Ponomarev A, Chen JL, Nguyen D, Cucinotta FA, Barcellos-Hoff MH, Image-based modeling reveals dynamic redistribution of DNA damage into nuclear sub-domains. *PLoS Comput Biol* 2007; 3, e155.
13. Georgescu W, Osseiran A, Rojec M, Liu Y, Bombrun M, Tang J, et al., Characterizing the DNA Damage Response by Cell Tracking Algorithms and Cell Features Classification Using High-Content Time-Lapse Analysis. *PLoS One* 2015; 10, e0129438.
14. Neumaier T, Swenson J, Pham C, Polyzos A, Lo AT, Yang P, et al., Evidence for formation of DNA repair centers and dose-response nonlinearity in human cells. *Proc Natl Acad Sci U S A* 2012; 109, 443-8.
15. Sachs RK, Chen AM, Brenner DJ, Review: proximity effects in the production of chromosome aberrations by ionizing radiation. *Int J Radiat Biol* 1997; 71, 1-19.
16. Rothkamm K, Lobrich M, Misrepair of radiation-induced DNA double-strand breaks and its relevance for tumorigenesis and cancer treatment (review). *Int J Oncol* 2002; 21, 433-40.
17. Li Z, Jella KK, Jaafar L, Li S, Park S, Story MD, et al., Exposure to galactic cosmic radiation compromises DNA repair and increases the potential for oncogenic chromosomal rearrangement in bronchial epithelial cells. *Sci Rep* 2018; 8, 11038.
18. Vadhavkar N, Pham C, Georgescu W, Deschamps T, Heuskin AC, Tang J, et al., Combinatorial DNA damage pairing model based on X-ray-induced foci predicts the dose and LET dependence of cell death in human breast cells. *Radiat Res* 2014; 182, 273-81.
19. Churchill GA, Airey DC, Allayee H, Angel JM, Attie AD, Beatty J, et al., The Collaborative Cross, a community resource for the genetic analysis of complex traits. *Nat Genet* 2004; 36, 1133-7.

20. Collaborative Cross C, The genome architecture of the Collaborative Cross mouse genetic reference population. *Genetics* 2012; 190, 389-401.
21. Wickham H, *ggplot2: elegant graphics for data analysis*: Springer; 2016.
22. Venables B, Hornik K, Maechler M, A collection of functions to implement a class for univariate polynomial manipulations. 2009.
23. Friendly M, Corrgams. *The American Statistician* 2002; 56, 316-24.
24. Neumaier T, Swenson J, Pham C, Polyzos A, Lo AT, Yang P, et al., Evidence for formation of DNA repair centers and dose-response nonlinearity in human cells. *Proceedings of the National Academy of Sciences of the United States of America* 2012; 109, 443-48.
25. Leatherbarrow EL, Harper JV, Cucinotta FA, O'Neill P, Induction and quantification of gamma-H2AX foci following low and high LET-irradiation. *Int J Radiat Biol* 2006; 82, 111-8.
26. Nikitaki Z, Nikolov V, Mavragani IV, Mladenov E, Mangelis A, Laskaratou DA, et al., Measurement of complex DNA damage induction and repair in human cellular systems after exposure to ionizing radiations of varying linear energy transfer (LET). *Free Radic Res* 2016; 50, S64-S78.
27. Chiolo I, Minoda A, Colmenares SU, Polyzos A, Costes SV, Karpen GH, Double-strand breaks in heterochromatin move outside of a dynamic HP1a domain to complete recombinational repair. *Cell* 2011; 144, 732-44.
28. Nikiforova MN, Stringer JR, Blough R, Medvedovic M, Fagin JA, Nikiforov YE, Proximity of chromosomal loci that participate in radiation-induced rearrangements in human cells. *Science* 2000; 290, 138-41.
29. Soutoglou E, Dorn JF, Sengupta K, Jasin M, Nussenzweig A, Ried T, et al., Positional stability of single double-strand breaks in mammalian cells. *Nat Cell Biol* 2007; 9, 675-82.
30. Aten JA, Stap J, Krawczyk PM, van Oven CH, Hoebe RA, Essers J, et al., Dynamics of DNA double-strand breaks revealed by clustering of damaged chromosome domains. *Science* 2004; 303, 92-5.
31. Savage JR, Insight into sites. *Mutat Res* 1996; 366, 81-95.
32. Ponomarev AL, Costes SV, Cucinotta FA, Stochastic properties of radiation-induced DSB: DSB distributions in large scale chromatin loops, the HPRT gene and within the visible volumes of DNA repair foci. *Int J Radiat Biol* 2008; 84, 916-29.
33. Rydberg B, , Holley WR, Chatterjee A, Dose-dependent misrejoining of radiation-induced DNA double-strand breaks in human fibroblasts: experimental and theoretical study for high- and low-LET radiation. *RadRes* 2005; 163, 526-34.
34. Asaithamby A, Hu B, Chen DJ, Unrepaired clustered DNA lesions induce chromosome breakage in human cells. *Proc Natl Acad Sci U S A* 2011; 108, 8293-8.
35. Kaplan HS, Hirsch BB, Brown MB, Indirect induction of lymphomas in irradiated mice. IV. Genetic evidence of the origin of the tumor cells from the thymic grafts. *Cancer Res* 1956; 16, 434-6.
36. Storer JB, Mitchell TJ, Fry RJ, Extrapolation of the relative risk of radiogenic neoplasms across mouse strains and to man. *Radiat Res* 1988; 114, 331-53.
37. Barcellos-Hoff MH, Blakely EA, Burma S, Fornace AJ, Jr., Gerson S, Hlatky L, et al., Concepts and challenges in cancer risk prediction for the space radiation environment. *Life Sci Space Res (Amst)* 2015; 6, 92-103.
38. Maxwell CA, Fleisch MC, Costes SV, Erickson AC, Boissiere A, Gupta R, et al., Targeted and nontargeted effects of ionizing radiation that impact genomic instability. *Cancer Res* 2008; 68, 8304-11.
39. Lorimore SA, Coates PJ, Wright EG, Radiation-induced genomic instability and bystander effects: nontargeted effects of exposure to ionizing radiation. *Oncogene* 2003; 22, 7058-69.

9.3. The 15-strain irradiation study Part II

9.3.1. Kinetic of DNA repair process

We propose to compute the track repair kinetic by measuring the rate of change in RIF/ μm as a function of time, according to the equation:

$$\frac{RIF}{\mu\text{m}} = \left(\frac{RIF}{\mu\text{m}} \right)_0 \cdot \exp\left(-\frac{t}{\tau}\right) \quad (24)$$

Where $(RIF/\mu\text{m})_0$ is the number of RIF/ μm directly after irradiation, t is the time [hours] and τ is a kinetic parameter depending on the strain [hours^{-1}]. As shown in Figure 31A, the number of RFI/ μm decrease through the time, evidencing a repair process. In order to quantify the kinetic of this process, the Tau parameters were calculated for each mice strain and summarized in Figure 31B. It must be noted that τ parameters were calculated by pooling the data obtained for male and female, characterizing the repair kinetic after high-LET exposition. Animals characterized by a fast repair kinetic are associated to a low τ parameter while a high τ parameter indicates a low repair kinetic. It is interesting to note that the five reference mice strains known to be radiation-induced cancer sensitive are associated to high tau parameters, as illustrated in Figure 31B.

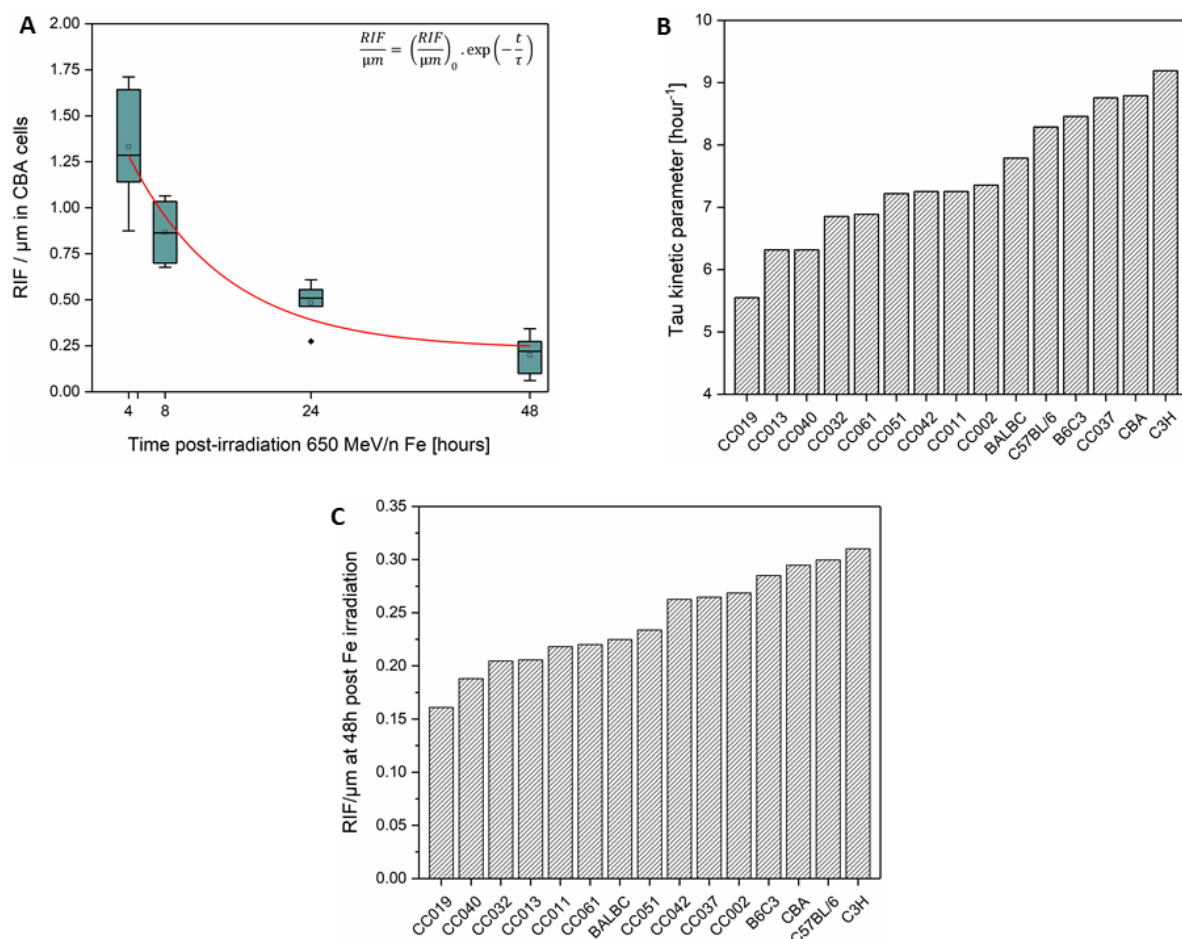


Figure 31. DNA damage repair kinetics and Persistent RIF/ μm at 48h compared across different mouse strains. (A) Representative example of the exponential decrease of RIF/ μm observed in CBA cells over the time post-irradiation. (B) Tau parameter calculated from an exponential fit across the different strains. Results are presented for 650 MeV/n Fe irradiation. (C) Persistent RIF/ μm observed across the different strain 48h post exposition to 650 MeV/n Fe.

9.3.2. Genome-wide association analysis of HZE particle induced RIF formation in inbred-mice skin derived fibroblasts

This cell-dependent DNA repair kinetic suggests that this phenotype is driven by genetics. Therefore, we sought to associate phenotype RIF/ μm averaged from males and female mice for each strain, at 48 hour time-point post radiation (Figure 31C) with the genotype of the CC and reference strains of inbred mice. To identify genomic loci responsible for the variation in DNA damage response, we performed a mouse genome wide association analysis with genome-wide significance threshold of 4.1×10^{-6} [182] and identified three potential associations on chromosomes 10 and 13 corresponding to 600 MeV/n Fe (Figure 32, Table 7). Analysis performed for 350 MeV/n Ar identified seven potential loci located at chromosome 2,3,7,10,11 and 19 (data not shown). Interestingly, for both high Z radiations, a common locus on chromosome 10 was identified, with peak SNP as UNC18214722 (p value = 7.22×10^{-7} for Fe and 4.24×10^{-6} for Ar) yielding to the identification of fourteen genes related to DNA damage response (Table 7).

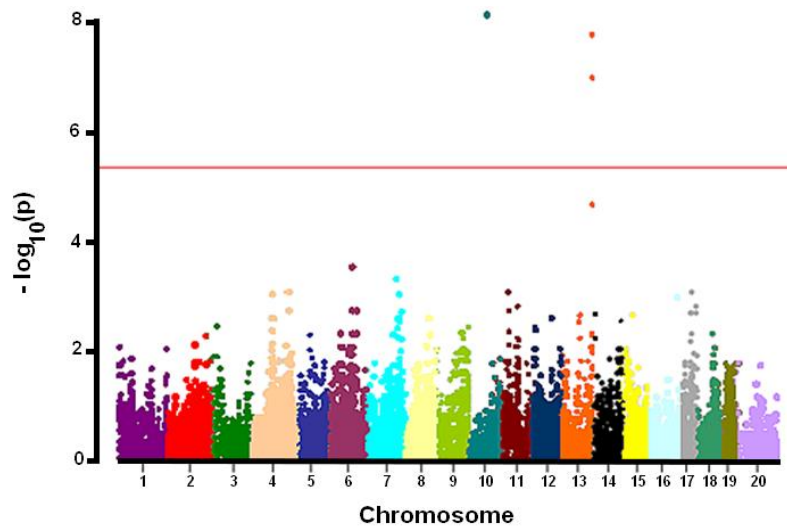


Figure 32. Manhattan plot for GWAS analysis of persistent DNA damage observed across the mouse strains after 650 MeV exposition.

Among the genes identified, SUMO3 and PIAS4 have been known to accumulate at sites of DNA damage [183]. SUMO3 acts in a mechanistically similar fashion to ubiquitin [183, 184] and Pias4 is required for the productive association of 53BP1 and BRCA1 [185]. BRCA1, also identified as one of the high LET response genes, has been studied extensively in relation to breast and ovarian cancer. Several lines of evidence have suggested recruitment of BRCA1 as a large complex into the sites of double stranded breaks and has been implicated in the maintenance of G1/S, S-phase and G2/M checkpoints. Interestingly, BRCA1 has been shown to participate in both main DNA repair processes, the homologous recombination and the non-homologous end joining [186]. HDAC5 was also identified and this class IIA lysine deacetylase is known to play a role in DNA repair involving base excision (BER), nucleotide excision and mismatch repair [187]. TDG, also a gene candidate in this loci, is a thymine DNA glycosylase contributing to BER pathways through transcriptional regulation and demethylation [188]. Of interest, DNMT3L which was also identified, acts as methylation regulator and interacts with HDAC1, repressing transcription during DNA damage response [189]. SIRT6, an histone deacetylase was found to activate PARP1, indicating a role in both BER and DSB repair [190]. Others DDR proteins

identified in the high LET associations support chromatin architecture, including Mum1 and ATXN7I3 [191].

This analysis was also performed with X-ray induced phenotype for high and low doses but no significant hits ($p > 4.1 \times 10^{-6}$) were obtained. This can be attributed to several factors but we strongly believe that the number of strains used in this study is too low to obtained significant hits. To cope with this limitation, additional experiments are ongoing by associating phenotype RIF/ μ m 48 hour post irradiation with the genotype of inbred mice without averaging male and female of a same strain. Thereby, we will have 76 different animal samples instead of 15 strain samples.

Table 7. List of genes identified by the GWAS analysis to be associated to DNA damage phenotype observed after 650 MeV/n Fe exposition.

SNP	Gene Symbol	Function
UNC18214722	Cdc34	Initiation of DNA replication
	Dnmt3l	DNA methyltransferase (genomic integrity, DNA repair)
	Fzr1	Required for the G2 DNA damage checkpoint
	Mcm3ap	Initiation of DNA replication
	Mum1	Maintenance of chromatin architecture after DNA damage
	Nfic	DNA-binding proteins that activates transcription and replication
	Pias4	DNA double-strand break repair
	Polr2e	RNA Polymerase II (transcription of DNA)
	Rrp1	Ribosomal RNA Processing (DNA repair)
	Sirt6	DNA double-strand break repair (genomic stability, aging)
	Smarb1	Tumor suppressor, relieves repressive chromatin structures
	Stk11	Serine-Threonine Kinase 11 (tumor suppressor)
	Sumo3	Sumoylation – DNA replication and repair
	Tdg	Thymine-DNA glycolase that removes thymine through base-excision repair
JAX00021248	Btg1	Anti-proliferative signal
UNC20271233	Atxn7I3	Chromatin organization
	Hdac5	Alters chromosome structure – transcriptional regulation
	Brca1	DNA damage sensor
	Rdm1	Homologous recombination DDR protein

PART IV: Discussion & further directions

10. The mechanisms responsible for the radiosensitization effect of GNPs

10.1. Physical enhancement

Prior to the publication of the majority of the studies regarding the use of nanomaterials to increase the radiation effectiveness, one of the earliest accounts related to this process was the increase in radiation dose observed around metal implants by Castilo et al [192]. They reported that a 6 MV irradiation delivered a 17 to 23 % higher dose in tissue around metal implants than in tissue without metal implants in proximity. This observation initiated the speculation that metallic materials may be used to enhance the photon absorption and so, to increase the cell death. As mentioned in the introduction, this physical enhancement can be obtained due to the difference in photon absorption between high-Z elements and water. In the same way, a higher stopping power was predicted when a charged particle passes through high-Z elements rather than in water. These phenomena can be translated into a significant increase in local dose deposition when even a small amount of high-Z element is present in the medium. This extra dose is associated to electron emission from NPs depositing their energy in the surrounding medium, resulting in ROS overproduction and thus, potential extra DNA damages. Although this physical enhancement was rapidly suggested as the mechanism responsible for this GNP-induced radiosensitization effect, its validity was difficult to be verified since complex indirect measurements using chemical or biological reactions are needed. Experimental works focused on the different parts of this mechanism to validate it. Alkhatib et al. [193] demonstrated an increased energy deposition near lead foils embedded in a phantom. They placed a radiographic film between two lead foils separated by 4 nm of water. After irradiation with an 18 MV X-ray beam, a dose of 140 cGy without the lead foils and 210 cGy with them was measured. This represents an enhancement of 0.5 DEU when lead foils were present. Although this experience was the most direct way to visualize the energy deposition enhancement, it was performed using a bulk material but not with nanomaterials. The importance of using NPs instead of bulk materials was evidenced by Casta et al. [194]. They measured the electron emission from 6 nm GNPs and gold plane surface in vacuum after X-ray irradiation. The authors demonstrated that the ratio of emitted electrons from GNPs to gold surface is around 2.3 and displayed a prominent peak below 100 eV. They reported a maximal ratio of 5.1 for electrons below 10 eV. Since it has been demonstrated that low-energy electrons could be very efficient at causing damage to DNA molecules through dissociative electron attachment [195], these findings are in agreement with the suggested mechanism hypothesis. Another experimental evidence of this mechanism was the work of Brun et al. [196] which studied the influence of GNPs on DNA damage generation under irradiation. Supercoiled plasmid DNA and GNPs were mixed together prior to be exposed to kV X-rays. Subsequently, a gel electrophoresis was performed to determine the DNA damage. Indeed, when damages occur in supercoiled plasmid DNA, its spatial conformation change leading to a difference in its ability to migrate in a gel electrophoresis. The authors reported an enhancement of 0.48 DEU for an equivalent gold in water of 0.4 WP, giving rise to a 1.2 DEU.WP⁻¹.

Furthermore, theoretical simulations have been performed to progress in the understanding of this physical enhancement. Early models investigated the macroscopic dose enhancement induced by the presence of GNPs randomly distributed in a volume. Several authors evidenced an energy

dependent physical enhancement. Cho et al. [100] have observed a 1.5, 0.9 and 0.01 DEU.WP⁻¹ when GNPs were exposed to 140 kVp, 250 kVp and 6 MV X-ray respectively. Despite the experimental data of Brun et al. [196] matching the theoretically physical enhancement predicted by Cho et al. [100], all these results are not in agreement with *in vitro* and *in vivo* results, as discussed in section 3.5 of the introduction. This may be partly explained by the fact that theoretical works are performed in conditions that did not reflect the *in vitro* and *in vivo* experimental conditions. In fact, GNPs are known to be distributed heterogeneously throughout the tumor volume under both passive and active targeting [136, 149, 197]. Moreover, it was reported that NPs typically aggregate and form clusters within cells [136, 198] increasing the heterogeneity of the NP distribution. In the light of this, the short ranges of electrons ejected from the NPs imply an energy deposition mostly in the vicinity of GNPs themselves, where the probability to find another GNPs is high. This may result in a non-uniform spatial distribution of the dose enhancement within cells.

Thereby, more recent studies considered microscopic dose distributions to obtain information of dose enhancement in area close to the GNP surface. McMahon et al. [199] performed an energy deposition study under 40 keV X-ray irradiation by comparing the macroscopic and microscopic approaches. They found that macroscopic enhancement was 0.075 DEU for a loading of 0.05 WP (1.5 DEU.WP⁻¹) while they reported a 1.05 DEU (21 DEU.WP⁻¹) at 2 nm away from the gold-filled region. This led them to suggest that the GNP radiosensitization effect is caused by several huge dose enhancement peaks located in close vicinity of the nano-objects. Although the microscopic approach enables to find higher physical dose enhancement than macroscopic one, all the deviations reported in section 3.5 of the introduction are not solved. Indeed, the absorption of megavoltage X-rays is negligible and microscopic physical enhancement predictions are still not in agreement with *in vitro* and *in vivo* works. Moreover, this theory does not seem to explain charged particle irradiation results. In fact, Heuskin et al. [104] recently demonstrated that the interaction probability of GNPs with the incident beam is very low. Based on [136] which reported a significant 0.14 DEU, they calculated that a 10⁻⁶-10⁻⁵ fraction of the total nanoparticle content interacts per Gy of radiation. Moreover, their simulations showed no increase in neither the macroscopic, nor the microscopic dose in cells. In the meantime, Sotiropoulos et al. [200] reached the same conclusions by studying another system for which a significant radiosensitization effect was measured experimentally.

Finally, the issue of GNP location is still unresolved. In fact, simulation studies performed by Carter et al. [201] demonstrated that GNPs need to be located in close proximity of DNA to maximize the tumor death. This conclusion was confirmed by Cho et al. who showed that GNPs have to be internalized inside the nucleus to produce an increase in cell death. However, only a few works have described a nuclear localization of GNPs while the large majority of studies evidenced a localization in the cytoplasm.

All these works evidenced that while a physical dose enhancement occur under GNPs irradiation, it could not explain on its own the enhancement effect observed. Therefore other mechanisms have to be involved to explain the radiosensitization effect. In the light of the results obtained during this thesis, two main other types of enhancement can be suggested: a chemical enhancement and a biological one.

10.2. Chemical enhancement

We reported that the presence of radical scavengers during the irradiation significantly reduce the radiosensitization effect in A549 and A431 cells. Moreover, enhancements of 0.94 DEU (H_2O_2) and 1.44 DEU ($^{\circ}\text{OH}$) were measured when 0.005 WP of 10 nm GNPs were irradiated. According to the previous section, physical enhancement due to this gold content should only give a negligible value. In addition, we observed a dose rate dependency of the enhancement effect which is not in agreement with the physical hypothesis. In fact, physical enhancement is independent of dose rate because the dose rate does not affect how photons are absorbed by GNPs or how charged particles lose their energy in GNPs. These results support a non-physical enhancement processes. One of them could be through ROS production. In contrast to the widely accepted theory that GNPs are chemically inert materials, increasing evidences showed that GNP surface is electronically active and is capable of catalyzing chemical reactions. It was demonstrated that the alteration in the electronic configuration of surface atoms enables a radical production at the GNP surface [202]. This could explain the observed enhanced ROS production that we reported when A549 cells were incubated with GNPs in the absence of radiation. Indeed, some studies claimed that GNPs catalyze the formation of ROS through a surface interaction with molecular oxygen, which facilitates surface-mediated transfer of electrons [202, 203]. In combination with ionizing radiation, the catalytic properties of GNPs can be enhanced by interacting with the highly reactive environment formed by the irradiation.

Misawa et al. [170] studied the enhancement effect of five different GNP sizes in terms of superoxide radical production. They used solutions of 10 to 1000 ppm (0.001 to 0.1 WP), at concentrations too low to cause any physical enhancement. However, they reported up to a 7.86-fold increase in superoxide anions production upon irradiation with 100 kVp X-rays. The authors attributed the observed enhancement to secondary X-ray fluorescence and Auger electron emission which suggested the enhancement was of a physical origin. However, evaluation of the relationship between ROS production and GNP size highlighted that smaller GNPs yielded higher levels of ROS compared to bigger ones. This suggested a catalytic role of the GNP surface since smaller GNPs have larger surface/volume ratios. In another experiment, Cheng et al. [204] showed a 4 DEU using 0.5 WP of 7 nm GNPs, which is higher than the predicted physical enhancement. They evidenced the importance of the GNP surface since no enhancement was detected when the GNP surface was covered using a silica layer. Furthermore, Gilles et al. [205] reported that GNP functionalization notably decreases the radiosensitization effect through hydroxyl radical production under X-rays. They observed a decrease in ROS production with the increase in number of atoms in the coating. They suggested two different explanations: first, the physical enhancement is expected to be responsible for electron emission from the GNPs at low X-ray energy. If these electrons are scavenged by the coating before they can react with water to produce ROS, hydroxyl radicals should be less abundant in solution. Secondly, they proposed that, at the nanoparticle-water interface, some H-OH bonds could be more easily broken by radiolytic processes. Then, ligands grafted at the GNP surface could disrupt the chemistry at the interface leading to a lower hydroxyl radical production. In the same way, we investigated this enhanced ROS production upon proton irradiation. When a solution containing 0.5 WP GNPs was exposed to 25 keV/ μm protons, we reported a 0.94 and 1.44 DEU in the H_2O_2 and $^{\circ}\text{OH}$ production. Here also, concentrations were too low to cause any physical enhancement evidencing the importance of chemical enhancement.

Further investigations have to be performed by exploring others ROS produced upon irradiation to fully understand the influence of GNPs in radiolysis process. Although this catalytic ROS production can explain the higher dose enhancement reported in *in vitro* and *in vivo* studies compared to the physical enhancement prediction, these radicals will be created in cancer cells which exhibit a high redox status. In fact, it was reported that cancer cells exhibited higher reduced glutathione and detoxification enzyme contents leading to a resistance to oxidative stress [206]. Thereby, the GNP-induced radiosensitization effect have also to be studied from a biological point of view to fully understanding it.

10.3. Biological enhancement

As discussed in the introduction, the success of modern radiotherapy is based on the “5 R” rules. At the molecular and cellular levels, if GNPs can modify pathways involved in this 5 R, they could modify the cellular response to radiation. Although a potential impact of NPs on biological pathways has been recognized, only a relatively small number of groups have investigated it. Evidences obtained to date for a “biological enhancement” can be classed according to the 5 R:

- **Repair:** It is widely recognized that the number of unrepaired DNA damage is directly correlated to cell death [38]. There is a few evidence of DNA repair inhibition by GNPs. In fact, Cui et al. [121] reported a delay in DNA damage repair after irradiation of MDA-MB-231 cells containing tiopronin-coated GNPs. In the same way, residual DNA damage has been found when HepG2 cells were irradiated in the presence of GNPs [207]. The authors concluded that their nano-objects influenced the DNA repair pathways without hypothesizing how. Contrastingly, no significant difference in residual DNA damage at 24h was reported in U87 cells pre-incubated with BSA-capped GNPs compared to cells that were not incubated with NPs [118]. Although other groups attributed these increases in residual DNA damage to a higher DNA damage induction caused by physical and chemical enhancement, the reality seems to be more complex. In fact, Cui et al. [121] did not observe any significant difference in DNA damage at 30 min post-irradiation suggesting that GNPs had no influence on their induction. Jain et al. [120] reached the same conclusion by reporting no impact of 1.9 nm GNPs on the DSB formation in MDA-MB-231 cells. In the same way, we reported a 25 % decrease in DSB repair when A549 cells containing GNPs were exposed to X-rays while no significant change in DNA damage formation was reported at 15 and 30 minutes post-irradiation. Interestingly, Schaeublin et al. [208] observed that GNP incubation is associated to a down-regulation of various genes involved in DNA repair including ATM and RAD51.
- **Reoxygenation:** It is well known that oxygen plays a major role in radiation therapy (cf. introduction). However, the impact of GNPs on reoxygenation was poorly investigated. It was reported that radiosensitization effect is greater under normoxia than hypoxia evidencing the importance of oxygen [209]. The authors suggested that this observation can be related to the chemical enhancement discussed before or to changes in cellular capacity to internalize the GNPs.

- **Redistribution:** The sensitivity of cells to ionizing radiation is influenced by their position in the cell cycle phases. It was reported that cells in G₂ and M phases are the most radiosensitive. Although several groups reported an impact of GNPs on cell cycle distribution, results are controversial. Roa et al. [134] demonstrated a G₀/G₁ phase acceleration and a G₂/M phase arrest when DU-145 cells are incubated with GNPs. Moreover, an increase in cyclin B1 and E expression was reported as well as a decreased expression of cyclin A. This G₂/M cell cycle arrest was evidenced in melanoma cells [210] and SK-OV-3 ovarian cells [132] incubated with 44 nm and 14 nm GNPs respectively. Using 30 nm GNPs coated with a nuclear localization sequence, Mackey et al. observed an increase in S-phase and a decrease in G₂/M phase in HSC-3 cells after a 24h incubation [211]. In contrast, several groups demonstrated no significant changes in cell cycle distribution when GNPs are incubated with cells [120, 121].
- **Repopulation:** Subpopulation of repopulating cells have been identified as the main cause of radiotherapy failure. GNP ability to inhibit or to slow down the cell proliferation has been demonstrated by different groups both *in vitro* and *in vivo*. We reported a 1.42 fold increase in doubling time when 10 nm GNPs are incubated during 24h with A549 cells. Recently, Zhang et al. [123] have reported a partial growth inhibition of U14 cervical cells 24 days after intraperitoneal injection of GNPs. Contrastingly, Connor et al. [212] did not observe difference in growth rates between untreated cells and cells exposed to 18 nm GNPs.
- **Intrinsic radiosensitivity:** A central issue in radiobiology is the marked difference in response to radiation observed between different cells. Since cancer cells result from the accumulation of genetic alterations, it is not surprising to observe gene expression changes in cancer cells that could modify their intrinsic radiosensitivity compared to normal tissue. For example, it was reported that cancer cells exhibited higher reduced glutathione and detoxification enzyme contents leading to a resistance to oxidative stress [206]. In this context, Butterworth et al. [116, 158] suggested that disruption of the cellular redox balance by using GNPs can modify the radiosensitivity. Taggart et al. [213] suspected that protein disulfide isomerase was a key mediator of the cellular response of GNPs. In the same way, we demonstrated that GNPs have the ability to inhibit TrxR, a regulator of redox reactions, in five different cell lines. We evidenced that overexpression of TXNRD1 (gene coding for TrxR) in tumor is associated to treatment resistance leading to a poor patient survival prognosis. To the best of our knowledge, no additional study identified a link between GNPs and a specific cellular target. In a recent article, Jaffray's lab regretted that no research describing links between intrinsic radiosensitivity of cells and radiosensitization effect of GNPs has been conducted [214]. It could be a key step towards the mechanism understanding. In fact, the only study which suggested a positive correlation between GNP enhancement and cell line radiosensitivity was undertaken by Marill et al. [215] using hafnium oxide NPs. However, they did not investigate the underlying mechanism(s).

All these studies highlight that GNPs might have different biological impacts across different cell lines. However, the lack of consistency in the parameters (cell lines, radiation types, NPs ...) used in literature does not allow to draw clear conclusions about the GNP effects. However, in this thesis, we evidenced the role played by TrxR and suggested a new mechanism responsible for the GNP

enhancement effect: first, GNPs enter into the cells through a receptor-mediated endocytosis leading to their sequestration in endosomes prior to the fusion with the lysosome. Second, the decrease in pH inside the vesicle triggers a partial GNP degradation leading to the release of gold ions that are well known TrxR inhibitor. This inhibition leads to a disruption in the oxidized - reduced Trx balance. Then, the decrease in the amount of reduced Trx further impacts the Trx peroxidase activity resulting in the accumulation of ROS in the cytoplasm, causing oxidative stress. These radicals could react with biomolecules and organelles such as mitochondria leading to a mitochondrial depolarization and therefore a decrease in the ATP production. The smaller amount of reduced Trx also impacts the ribonucleotide peroxidase which transforms ribonucleotides into deoxyribonucleotides, the building blocks of DNA. A set of the reported “biological dysfunctions” in literature could be a consequence of this suggested mechanism. In fact, the drop in ATP content could interfere with various biological pathways requiring a lot of energy such as DNA damage repair and cell division. Thereby, delay in DNA repair (Repair) and cell cycle arrest (Redistribution) observed by several groups can potentially be originated from the TrxR inhibition. Moreover, the decreased activity of ribonucleotide peroxidase subsequent to the TrxR inhibition can explain the observed decrease in cell proliferation (Repopulation). Finally, the reported decreased radiosensitization effect in hypoxia compared to normoxia (Reoxygenation) could be partially explained by a down-regulation of membrane protein involved in endocytosis [216]. This decrease in membrane protein expression in hypoxia leads to a lower GNP internalization which is directly correlated to the amount of TrxR inhibited, as evidenced in this thesis.

At the beginning of this thesis, the accepted theory was that GNPs play a radioenhancer role. However, this thesis suggests that GNPs play also a radiosensitizer role by weakening the detoxification potential of cells. Although more experimental works have to be performed to validate our findings, this thesis highlights the importance of considering NP – cell interaction in further studies. To go further in our understanding of the GNP enhancement effect, we need a harmonization of the experimental conditions relating to these studies [217]. In fact, we have to (i) precisely characterize the NPs used in the studies including at least NP size, coating agent, shape and NP loading in the cell/tumor which are frequently lacking information in the literature; (ii) establish a set of cell lines to benchmark *in vitro* data; (iii) investigate the influence of the time between NP injection and radiation response, a key parameter totally neglected so far in literature.

11. Design of the ideal NPs for an optimized enhancement effect

The better understanding of the mechanisms involved in NP-induced radiosensitization allows to suggest a design for an optimized NP.

The size of the nanoparticle is a key factor regarding the successful application of metallic nanoparticle in radiotherapy treatment. Since it influences the biological response as well as the GNP biodistribution, the size has to be optimized to achieve the highest therapeutic effectiveness. When the size of GNPs increases, the probability that the ejected secondary electrons lose their energy within the GNP increases, reducing the potential physical enhancement effect [218]. However, the increase in size can also increase this physical effect due to a higher interaction cross-section.

Contrastingly, the decrease in GNP size increases the surface to volume ratio resulting in a higher chemical and biological enhancement. Chemical enhancement is based on the ability of GNPs to catalyze the formation of ROS through a surface interaction with molecular oxygen. In the same way, the biological enhancement originating from the digestion of GNPs in lysosome is a surface process which will be higher for GNPs with a large surface to volume ratio. Although size affects differently the enhancement mechanisms, these trends should be put into perspective in light of the number of GNP internalized by cells, which is also size-dependent. This parameter influences the GNP biodistribution and its accumulation in the tumor matrix, its diffusion in tumor tissue and the cell uptake as well as the GNP excretion from the body [218]. By compiling data regarding size-dependent cell uptake, we observed that NPs between 20 and 60 nm exhibit the maximum cell uptake *in vitro* [219-222], but the exact diameter value appears to be coating- and cell line-dependent. However, it has been reported that *in vivo* biodistribution of these large GNPs is problematic. In fact, macrophages in the reticuloendothelial system (RES) play the role of filters to eliminate NPs from the body rapidly after intravenous GNP injection. It has been reported that large GNPs (50 – 100 nm) tend to be captured more easily by this system leading to an accumulation in liver, spleen and lymph nodes instead of in the tumor [219, 223]. Contrastingly, small GNPs (< 5 nm) tend to be eliminated through renal excretion [224, 225]. These differences in clearance system influence the GNP circulation time in blood as well as their accumulation in tumor. Huang et al. [226] compared the biodistribution of GNPs ranging from 2 to 15 nm. Twenty-four hours post NP injection in mice, they evidenced a higher tumor uptake and a reduced normal tissue accumulation of 2 nm GNPs compared to bigger ones. They also reported a longer circulation time in the blood for the smaller GNPs. In another studies, researchers demonstrated that the use of smaller NPs leads to homogeneous distribution in the tumor matrix while larger NPs have shown to be localized in the tumor periphery [226, 227]. In a recent article, Chou reported a continuous increase in tumor uptake for the 15 nm GNPs [228] while a maximum accumulation in the 4 to 8 hours post-injection was observed for the 100 nm GNPs. This peak was followed by a rapid decrease in gold content into the tumor over 24 hours. However, this elimination of GNPs seems to be tissue-dependent. Sadauskas et al. [229] reported a slow hepatic elimination of GNPs since more than 90 % of the gold loading in liver was still present in this organ 6 months post-injection. It was demonstrated that this long-term GNP retention in liver is associated to side-effects including histological alterations [230] and inflammatory cytokine secretion [231]. Overall, small NPs appear to be better to enable a high tumor accumulation *in vivo*. However, many studies have reported their higher toxicity in mammalian cells compared to bigger NPs due to a higher surface to volume ratio [232]. To overcome this issue, an adequate surface coating has to be chosen.

The coating agent is an essential element of the nano-object design since it fulfills multiple roles. First, it enables an increased stability of the GNP in a medium preventing aggregation and all the issues which are associated to a potential change in NP size. Second, it influences the cell uptake through its surface properties, amongst which is the charge. Indeed, it was reported *in vitro* that positively-charged GNPs promote cell internalization driven by electrostatic interactions with the negatively-charged phospholipid constituting cell membrane [219, 233]. Moreover, cancer cell membranes are more negatively charged than normal cell membranes due to an increased glycoprotein content [234], reinforcing this electrostatic interaction with positively charged GNPs. In *in vivo* studies, these positively-charged NPs have been reported to be more accumulated in liver and spleen than in tumor [235]. In contrast, a higher tumor loading was observed with neutral NPs due to a prolonged circulation time [236]. This could be explained by the third role played by the coating

agent: preventing the opsonization⁹ process. It was demonstrated that surface coating with large amount of PEG (a biocompatible neutral coating agent) enables to reduce the amount of opsonin attached to the GNPs resulting in a stronger protection against clearance through the RES [222]. While the grafting of increasing PEG molecules amount enables to gain in NPs stability, it also decreases the chemical enhancement effectiveness. In fact, Sicard-Roselli et al. [205] observed a lower hydroxyl radical production upon X-ray irradiation when GNPs are coated by PEG compared to naked GNPs. This phenomenon could be explained by (i) an energy deposition of emitted electrons in the coating instead of the surrounding medium; (ii) reaction of °OH radicals with the coating, especially if it contains alcohol or thiol reactive groups; (iii) a reduced catalysis generation of °OH due to the disruption of GNP-water interface by the coating. However, in our study on radiosensitization effect of GNPs conjugated to EGFR antibody, a significant cell death enhancement was observed even if the coating thickness was high.

Another parameter is the administration route of the nano-objects. In this thesis, we focused on the intravenous route, which is the most common one since it yields to a high systemic distribution. Thanks to EPR effect, GNPs accumulate within the tumor perivascular regions. However, *in vivo* studies reported that only 1 % of the injected GNPs are able to reach the tumor [237, 238]. The authors claimed that high NP clearance from the blood and the relatively high intratumoral pressure limit the passive GNP entry into the tumor. To overcome this, we designed a GNP coupled to EGFR antibody enabling a better tumor targeting. In addition to the significant cell death enhancement that we reported *in vitro*, literature showed an increase in the tumor targeting (up to 7 % of the injected dose) with this kind of active targeting GNPs *in vivo* [237]. However, an optimal radioenhancement effect could only be obtained through the maximization of the tumor gold loading. Based on the reported *in vivo* data of Hainfeld with which a significant increase in the median survival was observed, we have to inject between 1.35 to 1.9 g/kg [149, 150, 153]. For a human of 70 kg, this corresponds to 94 to 133 g of gold. This highlights the need for administration of high GNP doses in order to achieve a satisfactory radiosensitizing effect. A suggested alternative to the intravenous administration route was the intraperitoneal one, a route used to achieve high concentrations of therapeutic agents in the peritoneal cavity especially in the case of ovarian and gastric cancers [214]. However, no significant increase in the tumor gold loading was observed and a high undesirable heterogeneous distribution in liver, lungs and heart was reported [239]. To reduce the systemic toxicity associated to intravenous and intraperitoneal injection, intratumoral administration route was proposed. It consists to inject the therapeutic agent directly at the tumor site in order to achieve a high local dose of it into the tumor. Lin et al. [240] demonstrated the success of this administration route by observing that, 2 weeks post-injection, half of the administrated GNPs were still present in the tumor.

⁹ Opsonization is a term that refers to an immune process where foreign objects are identified and targeted for destruction by the immune system. This process is triggered by the binding of given molecules, called opsonin, at the object surface.

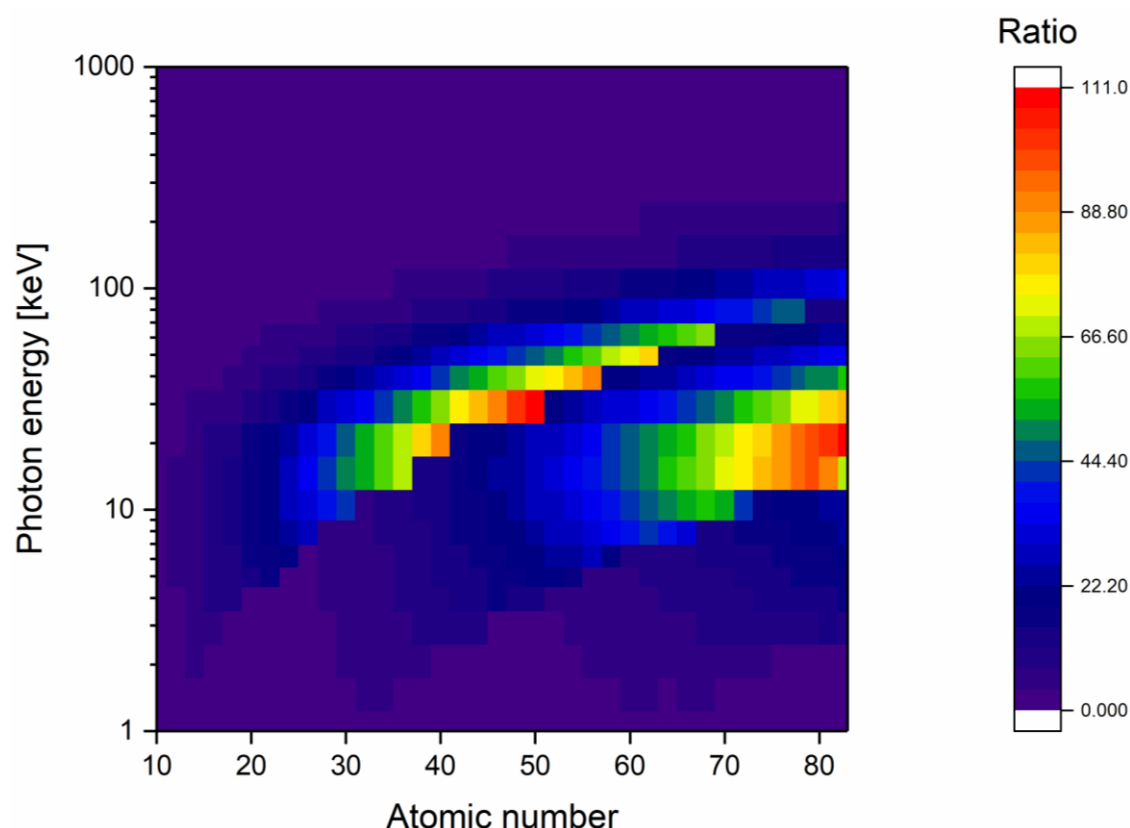


Figure 33. Comparison between photon cross section in water and in different materials. The ratio of absorption cross section in a NP on absorption cross section in water was plotted according to the incident photon energy and atomic number of the material of interest. Red areas indicate high dose deposition areas while purple ones correspond to no significant increase in photon absorption.

Finally, the metallic nature of the NP is the last parameter that can be optimized. The ideal NP should maximize the photon absorption (to optimize the physical enhancement) and release ions that have the ability to bind the thiol active site of TrxR (to achieve the biological enhancement). Firstly, we focused on physical enhancement. We analyzed the photon absorption in elements of the periodic table and compared it to the photon absorption in water. As illustrated in Figure 33, the photon absorption increases with atomic number of NP. This explains the focus of metallic radiosensitizer studies on high-Z materials such as hafnium ($Z = 72$), platinum ($Z = 78$), gold ($Z = 79$) or bismuth ($Z = 83$). However, a second interesting high photon absorption area appears in Figure 33 for atomic number ranging from 47 to 50. This could justify the significant radiosensitization effect observed with silver NPs ($Z = 47$) although its atomic number is lower compared to the aforementioned ones. In addition to these elements which absorb photons around 20 and 30 keV, the lanthanides ($Z = 60$ to 70) seem to be interesting materials since they absorb photons in a wider range of photon energies. Amongst these lanthanides, gadolinium ($Z = 64$) appears to be a good candidate due to an absorption window ranging from 9 to 70 keV.

Additionally, the ideal NPs need to have the ability to release ions that can bind the thiol-active site of TrxR. To predict the reactivity of metallic ions for thiol groups, we used the hard soft acid base (HSAB) theory. This theory uses Lewis acid-base and classifies them on the basis of their relatively

“hard” or “soft” character, a concept associated to polarizability¹⁰. Hard character will be associated to low polarizability elements while highly polarizable elements will be defined as soft. This chemical hardness as a quantitative definition enabling to classify every chemical element as a hard or soft acid or base [241]. The theory states that soft acids react faster and form stronger bonds with soft bases, whereas hard acids react faster and form stronger bonds with hard bases. Thiol groups constituting the active site of TrxR are Lewis bases which have a low hardness parameter, i.e. are soft bases in HSAB theory. Thereby, the ideal NPs have to release metallic ions which are soft acids in the HSAB theory. According to [241, 242], the potential candidates are Cu^+ , Ag^+ , Au^+ , Tl^+ , Pd^{2+} , Cd^{2+} , Pt^{2+} , Hg^{2+} , Ti^{2+} , Fe^{2+} , Pb^{2+} and metal atoms at zero oxidation state. Amongst these elements, cadmium and silver NPs grab our attention because literature reports an important ion release from these NPs at pH 4 [243], a mandatory step for the TrxR inhibition. Moreover, in these elements are found gold, silver and platinum, the most studied metallic NPs in radiosensitization experiments. It will be interesting to investigate if the biological mechanism that we proposed to explain GNP enhancement effect could be extended to these other NPs. If it is the case, further experiments evaluating the ability of these soft acid candidates to release ions in acidic conditions have to be performed. At that time, the potential use of these NPs as radiosensitizer should be evaluated while taking account to toxicity data that are missing for the moment.

Taken together all these data and by assuming that metallic nature of NPs did not influence data regarding impacts of GNP size, coating agent and biodistribution, the ideal NPs should have the following characteristics:

- Small size (< 5 nm): This will enable a better biodistribution as well as a high tumor accumulation. Moreover, the high surface/volume ratio of these NPs will maximize the chemical and biological enhancement.
- Surface coating: Neutral coating agent such as PEG will enable a long circulation half-life, a high tumor accumulation and a low cytotoxicity. An alternative could be squalene, a natural lipid which is an intermediate metabolite in the cholesterol synthesis. Recently, it has been evidenced that squalene binds lipoproteins present in the blood [244]. Due to an enhancing need of lipids to tumor growth, cancer cells exhibit high expression of lipoprotein receptors [245] enabling to take advantage of the squalene-lipoprotein association to indirectly target cancer cells.
- Silver or Cadmium NPs: These nano-objects exhibit a high photon absorption compared to water enabling a maximization in the local dose deposition after irradiation (physical enhancement). Moreover, their ability to release high amount of ions that can bind TrxR active site suggesting a potential strong biological enhancement. Moreover, these elements have to advantage to be cheaper (0.40 €/g and 0.01€/g for Ag and Cd respectively) than classical high-Z elements (34 €/g and 23€/g for Au and Pt respectively).

¹⁰ The ease with which electron density can be displaced or delocalized to form new covalent bonds.

Besides the design of an ideal NPs, the better understanding of the mechanisms responsible for the GNP radiosensitization effect opens the question of the clinical indications in which GNPs can be used. From the physical enhancement point of view, an optimized photon absorption will be obtained when low kilovoltage X-rays encounter NPs, as illustrated in Figure 33. These radiations are clinically used in two cases:

- Intra-operative radiotherapy (IORT): IORT is a radiation mobile radiotherapy technique consisting to delivered an X-ray boost between 30 and 50 keV to the tumor and the tumor bed (tissues surrounding the tumor up to 10 mm depth), at the time of surgical resection [246]. This technique reduces the need for post-surgical radiotherapy as well as the risk of recurrence in breast cancer patients [247]. In this context, an intratumoral injection of NPs prior to radiation exposition could significantly increase the effectiveness of IORT by enhancing the local dose deposition. Moreover, we reported a proportional relationship between the amplification factor and the dose delivered *in vitro* [131]. This feature could be interesting in the case of IORT with delivers a large single dose.
- Brachytherapy: Permanent brachytherapy is a radiation technique that consists in the insertion of radiative millimeter-sized seeds into the tumor. These seeds contain radioactive elements which emit low-energy photons that are attenuated by a few micrometers of biological tissue. This enables to constrain the radiation inside of the tumor, sparing healthy tissues. The main radioactive elements used in brachytherapy seeds are ^{125}I (59.4 days half-life, photon emission peak at 27.5 keV), ^{103}Pd (16.9 days half-life, photon emission peak at 20.7 keV) and ^{131}Cs (9.7 days half-life, photon emission peak at 30.4 keV) [248]. As in the case of IORT, the presence of NPs near the radioactive seeds could significantly increase the local dose deposition in the tumor.

From the biological enhancement point of view, GNPs can be useful in the treatment of overexpressing TrxR tumors which were reported to be more aggressive and associated to treatment resistance [249, 250]. Thereby, overexpression of TXNRD1 (gene coding for TrxR) is associated to a poor overall patient survival, as reported in this thesis. In this context, we investigated the mRNA expression of TrxR in various cancer types using 15 different TCGA datasets. Although TXNRD1 was expressed in all cancer types, higher expression was found in testicular (median at 32 FPKM) and lung (median at 27 FPKM) cancers compared to other ones (average median 13 FPKM), as illustrated in Figure 34B. Testicular cancers are mainly treated by chemotherapy. However, radiation therapy is the main treatment for lung cancer (77 % of the patients receive radiation during their treatment according to [9]). As a result of the reported higher TXNRD1 expression in this cancer type, injection of GNPs prior to radiotherapy sessions could result in the improvement of the treatment. In fact, median survival time of lung cancer patients decreased from 102 months to 44 months when tumors have high TXNRD1 expression (cf. our 3rd manuscript). Thereby, a GNP injection prior the radiotherapy treatment will inhibit TrxR inside the tumors which could increase the efficiency of treatment as well as the median patient survival time. However, a TrxR inhibition sufficient to allow a radiosensitization can be reached only with a huge gold loading in the tumor. This suggests the use of intratumoral administration route which could give rise to some technical issues for moving tumors such as lung ones.

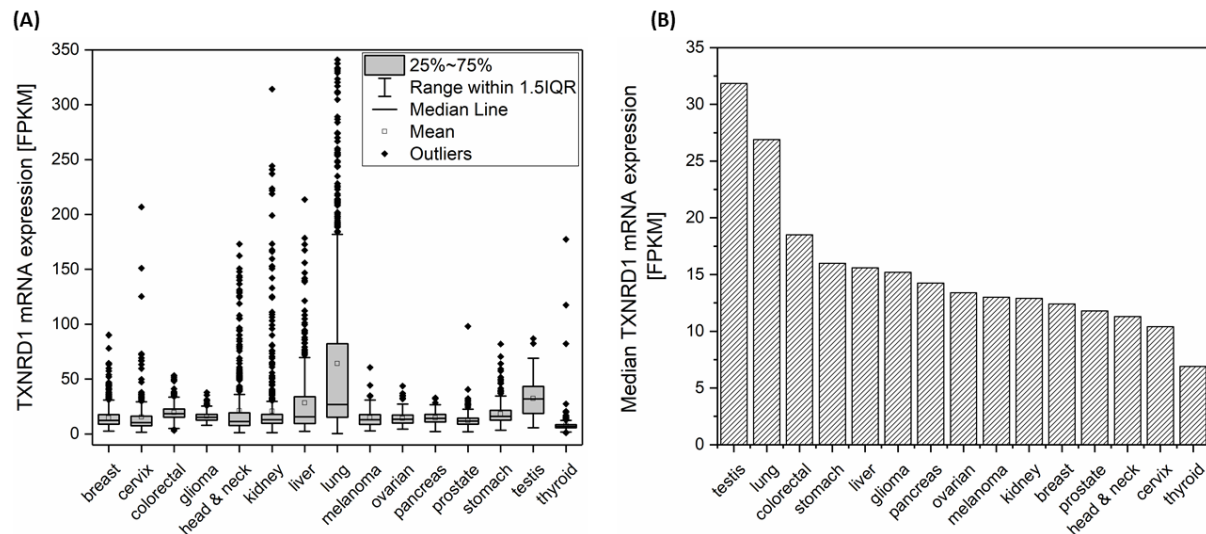


Figure 34. mRNA expression of TXNRD1 gene in 15 different cancer types. Data were collected from the following TCGA datasets: breast (TCGA-BRCA, 1075 patient samples); cervix (TCGA-CESC, 291 patient samples); colorectal (TCGA-COAD & TCGA-READ, 597 patient samples); glioma (TCGA-GBM, 153 patient samples); head & neck (TCGA-HNSC, 499 patient samples); kidney (TCGA-KIRC, 877 patient samples); liver (TCGA-LIHC, 365 patient samples); lung (TCGA-LUAD & TCGA-LUSC, 994 patient samples); melanoma (TCGA-SKCM, 102 patient samples); ovarian (TCGA-OV, 373 patient samples); pancreas (TCGA-PAAD, 176 patient samples); prostate (TCGA-PRAD, 494 patient samples); stomach (TCGA-STAD, 354 patient samples); testis (TCGA-TGCT, 134 patient samples); thyroid (TCGA-THCA, 501 patient samples). (A) RNA-seq data are reported as FPKM (number fragments per kilobase of exon per million reads) according to the cancer tissue. (B) The median TXNRD1 mRNA expression was plotted according to the cancer tissue.

12. Towards personalized medicine in radiotherapy

The choice of radiation therapy in the treatment plan of a given patient is currently driven by clinical and pathological features including the primary site localization, the tumor stage and its histology. However, the increasing understanding of the tumor heterogeneity complexity enables to expose the limitations of this medical framework: each person is fundamentally different from the average of the population. For example, a higher risk of locoregional recurrence was highlighted in HER2 (human epidermal growth factor receptor 2) overexpressing breast cancer patients compared to other ones [251]. Thereby, cancer therapy should be tailored to patients according to their individualized tumor molecular fingerprints. This new medical framework is called “personalized medicine”. Since several years, this approach is frequently used in chemotherapy treatment. In fact, KRAS mutation has been shown to be predictive factor of cetuximab treatment failure in colorectal cancer [252]. Moreover, EGFR mutations have been shown to predict benefit from tyrosine kinase inhibitors [253]. Contrastingly, the use of this approach for clinical decision-making in radiation oncology had not been very widespread. In addition to this decision-making tool, clinicians could take advantage of personalized radiotherapy by providing alternative dosing schedules for patients that may require more or less total dose of radiation.

The further development of personalized medicine in radiotherapy will be associated to the discovery of interesting radiation response biomarkers as well as to the development of companion diagnostics:

- Radiotherapy response biomarker: the most interesting biomarker is a marker of patient sensitivity to radiation therapy which will enable to adjust the treatment to each patient. In fact, highly radiosensitive patients may develop huge side-effects associated to radiation while radioresistant patients may receive an insufficient radiation dose to achieve a satisfactory tumor control.
- Companion diagnostics: according to FDA, companion diagnostics (CD) are “*in vitro* diagnostic devices that provides information that is essential for the safe and effective use of a corresponding therapeutic product” [254]. On a daily basis, these tests will enable to select patients that might benefit from the treatment and exclude the non-responding ones who would only suffer from adverse effects.

Some attempts in developing predictive tools for tumor radiosensitivity have been made including assays based on *ex-vivo* determination of tumor survival fraction at 2 Gy [255]. However, they were impractical for routine clinical applications. Tumor survival determination required primary cancer cells culture *in vitro*, a process that would take several weeks to complete. Thereby, a fast and reliable clinical method enabling a patient radiosensitivity measure still remains to be established. In this thesis, we used genomics to identify radiation sensitive genetic markers. A list of 19 genes, mainly involved in DNA damage repair were significantly associated to a more radiosensitive phenotype in mice. Although these SNPs have to be investigated for radiation response phenotype in humans, our work constitutes a proof-of-concept that GWAS analysis and genomics in general can be helpful for the improvement of radiotherapy treatment.

In addition to this intrinsic radiosensitivity of a person, cancer cells results from mutation accumulations leading to biologically different tumors of a same histology. Moreover, it was reported that even within a single tumor, different regions can have different radiosensitivity due to specific genetic or molecular alterations [256]. Thereby, further treatment designs have to be take into account individual radiosensitivity as well as tumor genetic alteration to optimize the chance of treatment success. For example, the potential use of GNPs as radiosensitizer in clinic will only be able to develop in a context of personalized medicine. We demonstrated that the inhibition of TrxR by gold ions participates to GNP radiosensitization effect. Thereby, the use of genomic assays assessing the mRNA TXNRD1 expression in tumor after biopsy can drive the application of GNP radiosensitizer in clinic.

Altogether, it seems obvious that the analysis of a single biomarker will only give limited information and development of multiplex assays will be needed in the future. In addition to the improvement the daily treatment decision-making, biomarker analysis will help to optimize the design and quality of preclinical and clinical studies. Since few decades, the randomized phase III trials have enrolled large numbers of patients which have the same kind of cancer leading to a high number of subsequent negative clinical trials [256]. In future, personalized medicine will be extended to clinical trials leading to patient enrolment based on biologically tumor features.

PART V: References

13. References

1. Hanahan D, Weinberg RA. The hallmarks of cancer. *Cell* 100(1), 57-70 (2000).
2. Goustin AS, Leof EB, Shipley GD, Moses HL. Growth factors and cancer. *Cancer research* 46(3), 1015-1029 (1986).
3. Hayflick L. Mortality and immortality at the cellular level. A review. *Biochemistry. Biokhimiia* 62(11), 1180-1190 (1997).
4. Bouck N, Stellmach V, Hsu SC. How tumors become angiogenic. *Advances in cancer research* 69 135-174 (1996).
5. Hanahan D, Folkman J. Patterns and emerging mechanisms of the angiogenic switch during tumorigenesis. *Cell* 86(3), 353-364 (1996).
6. Symonds H, Krall L, Remington L *et al.* p53-dependent apoptosis suppresses tumor growth and progression in vivo. *Cell* 78(4), 703-711 (1994).
7. Hanahan D, Weinberg RA. Hallmarks of cancer: the next generation. *Cell* 144(5), 646-674 (2011).
8. Siegel RL, Miller KD, Jemal A. Cancer statistics, 2017. *CA: A Cancer Journal for Clinicians* 67(1), 7-30 (2017).
9. Barton M, Jacob S, Shafiq J, Wong K, Thompson S, Delaney G. Review of optimal radiotherapy utilisation rates. *Prepared for Department of Health and Ageing, Australian Government* (2013).
10. Dasari S, Tchounwou PB. Cisplatin in cancer therapy: molecular mechanisms of action. *European journal of pharmacology* 0 364-378 (2014).
11. Kampan NC, Madondo MT, McNally OM, Quinn M, Plebanski M. Paclitaxel and Its Evolving Role in the Management of Ovarian Cancer. *Biomed Res Int* 2015 413076 (2015).
12. Gong J, Chehraz-Raffle A, Reddi S, Salgia R. Development of PD-1 and PD-L1 inhibitors as a form of cancer immunotherapy: a comprehensive review of registration trials and future considerations. *Journal for Immunotherapy of Cancer* 6 8 (2018).
13. Alsaab HO, Sau S, Alzhrani R *et al.* PD-1 and PD-L1 Checkpoint Signaling Inhibition for Cancer Immunotherapy: Mechanism, Combinations, and Clinical Outcome. *Frontiers in Pharmacology* 8(561), (2017).
14. Bernier J, Hall EJ, Giaccia A. Radiation oncology: a century of achievements. *Nature Reviews Cancer* 4 737 (2004).
15. Webb S. The physical basis of IMRT and inverse planning. *Br J Radiol* 76(910), 678-689 (2003).
16. Sech CL, Ngô C. *Physique nucléaire - 2e éd.: Des quarks aux applications - Cours et exercices corrigés*. Dunod, (2014).

17. Currell FV-B, Balder. Physical and Chemical Processes for Gold Nanoparticles and Ionising Radiation in Medical Contexts. In: *Gold nanoparticles for physics, chemistry and biology*. Scientific W (Ed.^(Eds).World Scientific 509-536 (2017).
18. PodgoršAk EB. *Radiation physics for medical physicists*. (2nd, enl.). Springer, Heidelberg. (2010).
19. Le Caër S. Water Radiolysis: Influence of Oxide Surfaces on H₂ Production under Ionizing Radiation. *Water* 3(1), 235 (2011).
20. Choudhary D, Srivastava M, Sarma A, Kale RK. Effect of high linear energy transfer radiation on biological membranes. *Radiat Environ Biophys* 37(3), 177-185 (1998).
21. Shuryak I, Brenner DJ. Effects of radiation quality on interactions between oxidative stress, protein and DNA damage in *Deinococcus radiodurans*. *Radiat Environ Biophys* 49(4), 693-703 (2010).
22. Anderson A, Hart EJ. Molecular product and free radical yields in the decomposition of water by protons, deuterons, and helium ions. *Radiation research* 14(6), 689-704 (1961).
23. Burns WG, Sims HE. Effect of radiation type in water radiolysis. *Journal of the Chemical Society, Faraday Transactions 1: Physical Chemistry in Condensed Phases* 77(11), 2803-2813 (1981).
24. Barr NF, Schuler RH. The dependence of radical and molecular yields on linear energy transfer in the radiation decomposition of 0.8 N sulfuric acid solutions. *The Journal of Physical Chemistry* 63(6), 808-813 (1959).
25. Crumière F, Vandenborre J, Essehli R, Blain G, Barbet J, Fattahi M. LET effects on the hydrogen production induced by the radiolysis of pure water. *Radiation Physics and Chemistry* 82 74-79 (2013).
26. Ryter SW, Kim HP, Hoetzel A *et al.* Mechanisms of cell death in oxidative stress. *Antioxidants & redox signaling* 9(1), 49-89 (2007).
27. Saccoccia F, Angelucci F, Boumis G *et al.* Thioredoxin reductase and its inhibitors. *Current protein & peptide science* 15(6), 621-646 (2014).
28. Arner ES, Holmgren A. The thioredoxin system in cancer. *Seminars in cancer biology* 16(6), 420-426 (2006).
29. Lu J, Holmgren A. The thioredoxin antioxidant system. *Free radical biology & medicine* 66 75-87 (2014).
30. Sun Q-A, Kirnarsky L, Sherman S, Gladyshev VN. Selenoprotein oxidoreductase with specificity for thioredoxin and glutathione systems. *Proceedings of the National Academy of Sciences* 98(7), 3673-3678 (2001).
31. Couto N, Wood J, Barber J. The role of glutathione reductase and related enzymes on cellular redox homeostasis network. *Free radical biology & medicine* 95 27-42 (2016).
32. Arnér ES, Holmgren A. Physiological functions of thioredoxin and thioredoxin reductase. *European Journal of Biochemistry* 267(20), 6102-6109 (2000).

33. Cerutti PA. Prooxidant states and tumor promotion. *Science* 227(4685), 375-381 (1985).
34. Cadenas E, Davies KJ. Mitochondrial free radical generation, oxidative stress, and aging. *Free radical biology & medicine* 29(3-4), 222-230 (2000).
35. Droge W. Free radicals in the physiological control of cell function. *Physiol Rev* 82(1), 47-95 (2002).
36. Lehnert S. *Biomolecular Action of Ionizing Radiation*. CRC Press, (2007).
37. Roots R, Okada S. Protection of DNA Molecules of Cultured Mammalian Cells from Radiation-induced Single-strand Scissions by Various Alcohols and SH Compounds. *International Journal of Radiation Biology and Related Studies in Physics, Chemistry and Medicine* 21(4), 329-342 (1972).
38. Banath JP, Macphail SH, Olive PL. Radiation sensitivity, H2AX phosphorylation, and kinetics of repair of DNA strand breaks in irradiated cervical cancer cell lines. *Cancer research* 64(19), 7144-7149 (2004).
39. Raisali G, Mirzakhania L, Masoudi SF, Semsarha F. Calculation of DNA strand breaks due to direct and indirect effects of Auger electrons from incorporated ¹²³I and ¹²⁵I radionuclides using the Geant4 computer code. *International journal of radiation biology* 89(1), 57-64 (2013).
40. Ross GM. Induction of cell death by radiotherapy. *Endocr Relat Cancer* 6(1), 41-44 (1999).
41. Giglia-Mari G, Zotter A, Vermeulen W. DNA Damage Response. *Cold Spring Harbor Perspectives in Biology* 3(1), a000745 (2011).
42. Semenenko VA, Stewart RD. A fast Monte Carlo algorithm to simulate the spectrum of DNA damages formed by ionizing radiation. *Radiation research* 161(4), 451-457 (2004).
43. Lieber MR. The mechanism of double-strand DNA break repair by the nonhomologous DNA end-joining pathway. *Annual review of biochemistry* 79 181-211 (2010).
44. Bothmer A, Robbiani DF, Di Virgilio M *et al.* Regulation of DNA end joining, resection, and immunoglobulin class switch recombination by 53BP1. *Molecular cell* 42(3), 319-329 (2011).
45. Brandsma I, Van Gent DC. Pathway choice in DNA double strand break repair: observations of a balancing act. *Genome Integrity* 3(1), 9 (2012).
46. Joiner MC, Van Der Kogel AJ. *Basic Clinical Radiobiology*. CRC Press, (2018).
47. Wang Y, Nartiss Y, Steipe B, Mcquibban GA, Kim PK. ROS-induced mitochondrial depolarization initiates PARK2/PARKIN-dependent mitochondrial degradation by autophagy. *Autophagy* 8(10), 1462-1476 (2012).
48. Surova O, Zhivotovsky B. Various modes of cell death induced by DNA damage. *Oncogene* 32(33), 3789-3797 (2013).
49. Withers HR. Four R's of radiotherapy. *Advances in Radiation Biology* 241-247 (1975).
50. Corner J, Bailey CD. *Cancer nursing: care in context*. John Wiley & Sons, (2009).

51. Cox JD, Ang KK. *Radiation Oncology E-Book: Rationale, Technique, Results*. Elsevier Health Sciences, (2009).
52. Nagane M, Yasui H, Yamamori T *et al*. Radiation-induced nitric oxide mitigates tumor hypoxia and radioresistance in a murine SCCVII tumor model. *Biochemical and Biophysical Research Communications* 437(3), 420-425 (2013).
53. Sinclair WK, Morton RA. X-RAY AND ULTRAVIOLET SENSITIVITY OF SYNCHRONIZED CHINESE HAMSTER CELLS AT VARIOUS STAGES OF THE CELL CYCLE. *Biophysical journal* 5 1-25 (1965).
54. Bese NS, Sut PA, Ober A. The effect of treatment interruptions in the postoperative irradiation of breast cancer. *Oncology* 69(3), 214-223 (2005).
55. Steel GG, Mcmillan TJ, Peacock JH. The 5Rs of radiobiology. *International journal of radiation biology* 56(6), 1045-1048 (1989).
56. Safwat A, Bentzen SM, Turesson I, Hendry JH. Deterministic rather than stochastic factors explain most of the variation in the expression of skin telangiectasia after radiotherapy. *Int J Radiat Oncol Biol Phys* 52(1), 198-204 (2002).
57. Paganetti H, Niemierko A, Ancukiewicz M *et al*. Relative biological effectiveness (RBE) values for proton beam therapy. *Int J Radiat Oncol Biol Phys* 53(2), 407-421 (2002).
58. Mohan R, Mahajan A, Minsky BD. New Strategies in Radiation Therapy: Exploiting the Full Potential of Protons. *Clinical Cancer Research* 19(23), 6338-6343 (2013).
59. Sejpal S, Komaki R, Tsao A *et al*. Early findings on toxicity of proton beam therapy with concurrent chemotherapy for nonsmall cell lung cancer. *Cancer* 117(13), 3004-3013 (2011).
60. Jermann M. Particle therapy patient statistics (per end of 2015) https://ptcog.ch/archive/patient_statistics. *Patientstatistics-updateDec2015.pdf* (2016).
61. Balosso J, Baroni G, Bleicher M *et al*. *Nuclear Physics for Medicine*. (2014).
62. Yock T, Schneider R, Friedmann A, Adams J, Fullerton B, Tarbell N. Proton radiotherapy for orbital rhabdomyosarcoma: clinical outcome and a dosimetric comparison with photons. *Int J Radiat Oncol Biol Phys* 63(4), 1161-1168 (2005).
63. Chung CS, Keating N, Yock T, Tarbell N. Comparative Analysis of Second Malignancy Risk in Patients Treated with Proton Therapy versus Conventional Photon Therapy. *International Journal of Radiation Oncology • Biology • Physics* 72(1), S8 (2008).
64. Hoppe BS, Nichols RC, Henderson RH *et al*. Erectile function, incontinence, and other quality of life outcomes following proton therapy for prostate cancer in men 60 years old and younger. *Cancer* 118(18), 4619-4626 (2012).
65. Schiller KC, Habl G, Combs SE. Protons, Photons, and the Prostate - Is There Emerging Evidence in the Ongoing Discussion on Particle Therapy for the Treatment of Prostate Cancer? *Frontiers in oncology* 6 8 (2016).
66. Bekelman JE, Denicoff A, Buchsbaum J. Randomized Trials of Proton Therapy: Why They Are at Risk, Proposed Solutions, and Implications for Evaluating Advanced Technologies to Diagnose and Treat Cancer. *Journal of Clinical Oncology* 36(24), 2461-2464 (2018).

67. Adams GE. CHEMICAL RADIOSENSITIZATION OF HYPOXIC CELLS. *British Medical Bulletin* 29(1), 48-53 (1973).
68. Lehnert S. *Radiosensitizers and Radiochemotherapy in the Treatment of Cancer*. Taylor & Francis, (2014).
69. Hoppe R, Phillips TL, Roach M. *Leibel and Phillips Textbook of Radiation Oncology - E-Book: Expert Consult*. Elsevier Health Sciences, (2010).
70. Khan Z, Khan AA, Prasad GBKS, Khan N, Tiwari RP, Bisen PS. Growth inhibition and chemo-radiosensitization of head and neck squamous cell carcinoma (HNSCC) by survivin-siRNA lentivirus. *Radiotherapy and Oncology* 118(2), 359-368 (2016).
71. Borm PJ, Kreyling W. Toxicological hazards of inhaled nanoparticles--potential implications for drug delivery. *Journal of nanoscience and nanotechnology* 4(5), 521-531 (2004).
72. Stark WJ, Stoessel PR, Wohlleben W, Hafner A. Industrial applications of nanoparticles. *Chemical Society Reviews* 44(16), 5793-5805 (2015).
73. Mie G. Beiträge zur Optik trüber Medien, speziell kolloidaler Metallösungen. *Annalen der Physik* 330(3), 377-445 (1908).
74. Fang J, Nakamura H, Maeda H. The EPR effect: Unique features of tumor blood vessels for drug delivery, factors involved, and limitations and augmentation of the effect. *Advanced Drug Delivery Reviews* 63(3), 136-151 (2011).
75. Wicki A, Witzigmann D, Balasubramanian V, Huwyler J. Nanomedicine in cancer therapy: Challenges, opportunities, and clinical applications. *Journal of Controlled Release* 200 138-157 (2015).
76. Tong R, Kohane DS. New Strategies in Cancer Nanomedicine. *Annual review of pharmacology and toxicology* 56 41-57 (2016).
77. Shi J, Kantoff PW, Wooster R, Farokhzad OC. Cancer nanomedicine: progress, challenges and opportunities. *Nature reviews. Cancer* 17(1), 20-37 (2017).
78. Karve S, Werner ME, Sukumar R *et al.* Revival of the abandoned therapeutic wortmannin by nanoparticle drug delivery. *Proceedings of the National Academy of Sciences* 109(21), 8230-8235 (2012).
79. Obata Y, Tajima S, Takeoka S. Evaluation of pH-responsive liposomes containing amino acid-based zwitterionic lipids for improving intracellular drug delivery in vitro and in vivo. *Journal of Controlled Release* 142(2), 267-276 (2010).
80. Wang Y-C, Wang F, Sun T-M, Wang J. Redox-Responsive Nanoparticles from the Single Disulfide Bond-Bridged Block Copolymer as Drug Carriers for Overcoming Multidrug Resistance in Cancer Cells. *Bioconjugate Chemistry* 22(10), 1939-1945 (2011).
81. Dicheva BM, Koning GA. Targeted thermosensitive liposomes: an attractive novel approach for increased drug delivery to solid tumors. *Expert Opinion on Drug Delivery* 11(1), 83-100 (2014).

82. Schroeder A, Honen R, Turjeman K, Gabizon A, Kost J, Barenholz Y. Ultrasound triggered release of cisplatin from liposomes in murine tumors. *Journal of Controlled Release* 137(1), 63-68 (2009).
83. Fomina N, Mcfearin C, Sermsakdi M, Edigin O, Almutairi A. UV and Near-IR Triggered Release from Polymeric Nanoparticles. *Journal of the American Chemical Society* 132(28), 9540-9542 (2010).
84. Petersen GH, Alzghari SK, Chee W, Sankari SS, La-Beck NM. Meta-analysis of clinical and preclinical studies comparing the anticancer efficacy of liposomal versus conventional non-liposomal doxorubicin. *Journal of controlled release : official journal of the Controlled Release Society* 232 255-264 (2016).
85. Ma P, Mumper RJ. Paclitaxel Nano-Delivery Systems: A Comprehensive Review. *Journal of nanomedicine & nanotechnology* 4(2), 1000164-1000164 (2013).
86. Murry DJ, Blaney SM. Clinical pharmacology of encapsulated sustained-release cytarabine. *The Annals of pharmacotherapy* 34(10), 1173-1178 (2000).
87. Barenholz Y. Doxil(R)--the first FDA-approved nano-drug: lessons learned. *Journal of controlled release : official journal of the Controlled Release Society* 160(2), 117-134 (2012).
88. Frampton JE. Mifamurtide: a review of its use in the treatment of osteosarcoma. *Paediatric drugs* 12(3), 141-153 (2010).
89. Dinndorf PA, Gootenberg J, Cohen MH, Keegan P, Pazdur R. FDA drug approval summary: pegaspargase (oncaspar) for the first-line treatment of children with acute lymphoblastic leukemia (ALL). *Oncologist* 12(8), 991-998 (2007).
90. Lamb YN, Scott LJ. Liposomal Irinotecan: A Review in Metastatic Pancreatic Adenocarcinoma. *Drugs* 77(7), 785-792 (2017).
91. Maeda H. SMANCS and polymer-conjugated macromolecular drugs: advantages in cancer chemotherapy. *Advanced Drug Delivery Reviews* 46(1), 169-185 (2001).
92. Rosenblum D, Joshi N, Tao W, Karp JM, Peer D. Progress and challenges towards targeted delivery of cancer therapeutics. *Nature Communications* 9(1), 1410 (2018).
93. Gradishar WJ, Tjulandin S, Davidson N *et al.* Phase III trial of nanoparticle albumin-bound paclitaxel compared with polyethylated castor oil-based paclitaxel in women with breast cancer. *Journal of clinical oncology : official journal of the American Society of Clinical Oncology* 23(31), 7794-7803 (2005).
94. Benyettou F, Rezgui R, Ravaux F *et al.* Synthesis of silver nanoparticles for the dual delivery of doxorubicin and alendronate to cancer cells. *Journal of Materials Chemistry B* 3(36), 7237-7245 (2015).
95. Liu J, Luo Z, Zhang J *et al.* Hollow mesoporous silica nanoparticles facilitated drug delivery via cascade pH stimuli in tumor microenvironment for tumor therapy. *Biomaterials* 83 51-65 (2016).
96. Nichols JW, Bae YH. EPR: Evidence and fallacy. *Journal of controlled release : official journal of the Controlled Release Society* 190 451-464 (2014).

97. Lammers T, Kiessling F, Hennink WE, Storm G. Drug targeting to tumors: Principles, pitfalls and (pre-) clinical progress. *Journal of Controlled Release* 161(2), 175-187 (2012).
98. Danhier F. To exploit the tumor microenvironment: Since the EPR effect fails in the clinic, what is the future of nanomedicine? *Journal of controlled release : official journal of the Controlled Release Society* 244(Pt A), 108-121 (2016).
99. Guo T. *X-ray Nanochemistry: Concepts and Development*. Springer International Publishing, (2018).
100. Cho SH. Estimation of tumour dose enhancement due to gold nanoparticles during typical radiation treatments: a preliminary Monte Carlo study. *Physics in medicine and biology* 50(15), N163-173 (2005).
101. Mesbahi A, Jamali F, Garehaghaji N. Effect of photon beam energy, gold nanoparticle size and concentration on the dose enhancement in radiation therapy. *BioImpacts : BI* 3(1), 29-35 (2013).
102. Lechtman E, Chattopadhyay N, Cai Z, Mashouf S, Reilly R, Pignol JP. Implications on clinical scenario of gold nanoparticle radiosensitization in regards to photon energy, nanoparticle size, concentration and location. *Physics in medicine and biology* 56(15), 4631-4647 (2011).
103. Jeynes JC, Merchant MJ, Spindler A, Wera AC, Kirkby KJ. Investigation of gold nanoparticle radiosensitization mechanisms using a free radical scavenger and protons of different energies. *Physics in medicine and biology* 59(21), 6431-6443 (2014).
104. Heuskin AC, Gallez B, Feron O, Martinive P, Michiels C, Lucas S. Metallic nanoparticles irradiated by low-energy protons for radiation therapy: Are there significant physical effects to enhance the dose delivery? *Medical physics* doi:10.1002/mp.12362 (2017).
105. Cho J, Gonzalez-Lepera C, Manohar N, Kerr M, Krishnan S, Cho SH. Quantitative investigation of physical factors contributing to gold nanoparticle-mediated proton dose enhancement. *Physics in medicine and biology* 61(6), 2562-2581 (2016).
106. Martínez-Rovira I, Prezado Y. Evaluation of the local dose enhancement in the combination of proton therapy and nanoparticles. *Medical physics* 42(11), 6703-6710 (2015).
107. Zabihzadeh M, Moshirian T, Ghorbani M, Knaup C, Behrooz MA. A Monte Carlo Study on Dose Enhancement by Homogeneous and Inhomogeneous Distributions of Gold Nanoparticles in Radiotherapy with Low Energy X-rays. *Journal of biomedical physics & engineering* 8(1), 13-28 (2018).
108. Byrne HL, Gholami Y, Kuncic Z. Impact of fluorescence emission from gold atoms on surrounding biological tissue-implications for nanoparticle radio-enhancement. *Physics in medicine and biology* 62(8), 3097-3110 (2017).
109. Sharmah A, Yao Z, Lu L, Guo T. X-ray-Induced Energy Transfer between Nanomaterials under X-ray Irradiation. *The Journal of Physical Chemistry C* 120(5), 3054-3060 (2016).
110. Kakade N, Sharma S. Dose enhancement in gold nanoparticle-aided radiotherapy for the therapeutic photon beams using Monte Carlo technique. *Journal of Cancer Research and Therapeutics* 11(1), 94-97 (2015).

111. Zhang SX, Gao J, Buchholz TA *et al.* Quantifying tumor-selective radiation dose enhancements using gold nanoparticles: a monte carlo simulation study. *Biomedical microdevices* 11(4), 925-933 (2009).
112. Miladi I, Alric C, Dufort S *et al.* The in vivo radiosensitizing effect of gold nanoparticles based MRI contrast agents. *Small* 10(6), 1116-1124 (2014).
113. Chithrani DB, Jelveh S, Jalali F *et al.* Gold nanoparticles as radiation sensitizers in cancer therapy. *Radiation research* 173(6), 719-728 (2010).
114. Kong T, Zeng J, Wang X *et al.* Enhancement of radiation cytotoxicity in breast-cancer cells by localized attachment of gold nanoparticles. *Small* 4(9), 1537-1543 (2008).
115. Taggart LE, McMahon SJ, Currell FJ, Prise KM, Butterworth KT. The role of mitochondrial function in gold nanoparticle mediated radiosensitisation. *Cancer Nanotechnol* 5(1), 5 (2014).
116. Butterworth KT, Coulter JA, Jain S *et al.* Evaluation of cytotoxicity and radiation enhancement using 1.9 nm gold particles: potential application for cancer therapy. *Nanotechnology* 21(29), 295101 (2010).
117. Bobyk L, Edouard M, Deman P *et al.* Photoactivation of gold nanoparticles for glioma treatment. *Nanomedicine : nanotechnology, biology, and medicine* 9(7), 1089-1097 (2013).
118. Chen N, Yang W, Bao Y, Xu H, Qin S, Tu Y. BSA capped Au nanoparticle as an efficient sensitizer for glioblastoma tumor radiation therapy. *RSC Advances* 5(51), 40514-40520 (2015).
119. Joh DY, Sun L, Stangl M *et al.* Selective targeting of brain tumors with gold nanoparticle-induced radiosensitization. *PloS one* 8(4), e62425 (2013).
120. Jain S, Coulter JA, Hounsell AR *et al.* Cell-specific radiosensitization by gold nanoparticles at megavoltage radiation energies. *Int J Radiat Oncol Biol Phys* 79(2), 531-539 (2011).
121. Cui L, Tse K, Zahedi P *et al.* Hypoxia and cellular localization influence the radiosensitizing effect of gold nanoparticles (AuNPs) in breast cancer cells. *Radiation research* 182(5), 475-488 (2014).
122. Wang C, Jiang Y, Li X, Hu L. Thioglucose-bound gold nanoparticles increase the radiosensitivity of a triple-negative breast cancer cell line (MDA-MB-231). *Breast cancer (Tokyo, Japan)* 22(4), 413-420 (2015).
123. Zhang XD, Wu D, Shen X *et al.* Size-dependent radiosensitization of PEG-coated gold nanoparticles for cancer radiation therapy. *Biomaterials* 33(27), 6408-6419 (2012).
124. Kaur H, Pujari G, Semwal MK, Sarma A, Avasthi DK. In vitro studies on radiosensitization effect of glucose capped gold nanoparticles in photon and ion irradiation of HeLa cells. *Nuclear Instruments and Methods in Physics Research Section B: Beam Interactions with Materials and Atoms* 301 7-11 (2013).
125. Khoshgard K, Hashemi B, Arbabi A, Rasaee MJ, Soleimani M. Radiosensitization effect of folate-conjugated gold nanoparticles on HeLa cancer cells under orthovoltage superficial radiotherapy techniques. *Physics in medicine and biology* 59(9), 2249-2263 (2014).

126. Saberi A, Shahbazi-Gahrouei D, Abbasian M, Fesharaki M, Baharlouei A, Arab-Bafrani Z. Gold nanoparticles in combination with megavoltage radiation energy increased radiosensitization and apoptosis in colon cancer HT-29 cells. *International journal of radiation biology* 93(3), 315-323 (2017).
127. Liu CJ, Wang CH, Chien CC *et al.* Enhanced x-ray irradiation-induced cancer cell damage by gold nanoparticles treated by a new synthesis method of polyethylene glycol modification. *Nanotechnology* 19(29), 295104 (2008).
128. Liu X, Liu Y, Zhang P *et al.* The synergistic radiosensitizing effect of tirapazamine-conjugated gold nanoparticles on human hepatoma HepG2 cells under X-ray irradiation. *International journal of nanomedicine* 11 3517-3531 (2016).
129. Guo M, Sun Y, Zhang X-D. Enhanced radiation therapy of gold nanoparticles in liver cancer. *Applied Sciences* 7(3), 232 (2017).
130. Wang C, Li X, Wang Y, Liu Z, Fu L, Hu L. Enhancement of radiation effect and increase of apoptosis in lung cancer cells by thio-glucose-bound gold nanoparticles at megavoltage radiation energies. *Journal of Nanoparticle Research* 15(5), 1642 (2013).
131. Penninckx S, Heuskin AC, Michiels C, Lucas S. The role of thioredoxin reductase in gold nanoparticle radiosensitization effects. *Nanomedicine (London, England)* doi:10.2217/nnm-2018-0171 (2018).
132. Feng G, Kun S, James ZX *et al.* Thio-glucose bound gold nanoparticles enhance radio-cytotoxic targeting of ovarian cancer. *Nanotechnology* 22(28), 285101 (2011).
133. Wolfe T, Chatterjee D, Lee J *et al.* Targeted gold nanoparticles enhance sensitization of prostate tumors to megavoltage radiation therapy in vivo. *Nanomedicine : nanotechnology, biology, and medicine* 11(5), 1277-1283 (2015).
134. Roa W, Zhang X, Guo L *et al.* Gold nanoparticle sensitize radiotherapy of prostate cancer cells by regulation of the cell cycle. *Nanotechnology* 20(37), 375101 (2009).
135. Polf JC, Bronk LF, Driessen WH, Arap W, Pasqualini R, Gillin M. Enhanced relative biological effectiveness of proton radiotherapy in tumor cells with internalized gold nanoparticles. *Applied physics letters* 98(19), 193702 (2011).
136. Li S, Penninckx S, Karmani L *et al.* LET-dependent radiosensitization effects of gold nanoparticles for proton irradiation. *Nanotechnology* 27(45), 455101 (2016).
137. Le Sech C, Takakura K, Saint-Marc C *et al.* Strand break induction by photoabsorption in DNA-bound molecules. *Radiation research* 153(4), 454-458 (2000).
138. Kobayashi K, Frohlich H, Usami N, Takakura K, Le Sech C. Enhancement of X-ray-induced breaks in DNA bound to molecules containing platinum: a possible application to hadrontherapy. *Radiation research* 157(1), 32-37 (2002).
139. Porcel E, Li S, Usami N *et al.* Nano-Sensitization under gamma rays and fast ion radiation. *Journal of Physics: Conference Series* 373(1), 012006 (2012).
140. Porcel E, Liehn S, Remita H *et al.* Platinum nanoparticles: a promising material for future cancer therapy? *Nanotechnology* 21(8), 085103 (2010).

141. Xu R, Ma J, Sun X *et al.* Ag nanoparticles sensitize IR-induced killing of cancer cells. *Cell research* 19(8), 1031-1034 (2009).
142. Lu R, Yang D, Cui D, Wang Z, Guo L. Egg white-mediated green synthesis of silver nanoparticles with excellent biocompatibility and enhanced radiation effects on cancer cells. *International journal of nanomedicine* 7 2101-2107 (2012).
143. Huang P, Yang DP, Zhang C *et al.* Protein-directed one-pot synthesis of Ag microspheres with good biocompatibility and enhancement of radiation effects on gastric cancer cells. *Nanoscale* 3(9), 3623-3626 (2011).
144. Mowat P, Mignot A, Rima W *et al.* In vitro radiosensitizing effects of ultrasmall gadolinium based particles on tumour cells. *Journal of nanoscience and nanotechnology* 11(9), 7833-7839 (2011).
145. Detappe A, Kunjachan S, Rottmann J *et al.* AGuIX nanoparticles as a promising platform for image-guided radiation therapy. *Cancer Nanotechnology* 6(1), 4 (2015).
146. Kleinauskas A, Kim J-K, Choi G-H, Kim H-T, Røe K, Juzenas P. Superparamagnetic magnetite nanoparticles for cancer theranostics. *Reviews in Nanoscience and Nanotechnology* 1(4), 271-283 (2012).
147. Khoei S, Mahdavi SR, Fakhimikabir H, Shakeri-Zadeh A, Hashemian A. The role of iron oxide nanoparticles in the radiosensitization of human prostate carcinoma cell line DU145 at megavoltage radiation energies. *International journal of radiation biology* 90(5), 351-356 (2014).
148. Jong-Ki K, Seung-Jun S, Ki-Hong K *et al.* Therapeutic application of metallic nanoparticles combined with particle-induced x-ray emission effect. *Nanotechnology* 21(42), 425102 (2010).
149. Hainfeld JF, Slatkin DN, Smilowitz HM. The use of gold nanoparticles to enhance radiotherapy in mice. *Physics in medicine and biology* 49(18), N309-315 (2004).
150. Hainfeld JF, Dilmanian FA, Zhong Z, Slatkin DN, Kalef-Ezra JA, Smilowitz HM. Gold nanoparticles enhance the radiation therapy of a murine squamous cell carcinoma. *Physics in Medicine & Biology* 55(11), 3045 (2010).
151. Zhang X-D, Luo Z, Chen J *et al.* Ultrasmall glutathione-protected gold nanoclusters as next generation radiotherapy sensitizers with high tumor uptake and high renal clearance. *Scientific reports* 5 8669 (2015).
152. Jong-Ki K, Seung-Jun S, Hong-Tae K *et al.* Enhanced proton treatment in mouse tumors through proton irradiated nanoradiator effects on metallic nanoparticles. *Physics in Medicine & Biology* 57(24), 8309 (2012).
153. Hainfeld JF, Smilowitz HM, O'connor MJ, Dilmanian FA, Slatkin DN. Gold nanoparticle imaging and radiotherapy of brain tumors in mice. *Nanomedicine (London, England)* 8(10), 1601-1609 (2013).
154. Zhang XD, Chen J, Luo Z *et al.* Enhanced Tumor Accumulation of Sub - 2 nm Gold Nanoclusters for Cancer Radiation Therapy. *Advanced healthcare materials* 3(1), 133-141 (2014).

155. Maggiorella L, Barouch G, Devaux C *et al.* Nanoscale radiotherapy with hafnium oxide nanoparticles. *Future Oncology* 8(9), 1167-1181 (2012).
156. Liu Y, Zhang P, Li F *et al.* Metal-based NanoEnhancers for Future Radiotherapy: Radiosensitizing and Synergistic Effects on Tumor Cells. *Theranostics* 8(7), 1824-1849 (2018).
157. Lux F, Tran VL, Thomas E *et al.* AGuIX((R)) from bench to bedside-Transfer of an ultrasmall theranostic gadolinium-based nanoparticle to clinical medicine. *Br J Radiol* doi:10.1259/bjr.20180365 20180365 (2018).
158. Butterworth KT, McMahon SJ, Currell FJ, Prise KM. Physical basis and biological mechanisms of gold nanoparticle radiosensitization. *Nanoscale* 4(16), 4830-4838 (2012).
159. Turkevich J, Stevenson PC, Hillier J. A study of the nucleation and growth processes in the synthesis of colloidal gold. *Discussions of the Faraday Society* 11(0), 55-75 (1951).
160. Frens G. Controlled Nucleation for the Regulation of the Particle Size in Monodisperse Gold Suspensions. *Nature Physical Science* 241 20 (1973).
161. Oh E, Susumu K, Goswami R, Mattoussi H. One-Phase Synthesis of Water-Soluble Gold Nanoparticles with Control over Size and Surface Functionalities. *Langmuir* 26(10), 7604-7613 (2010).
162. Wang Z, Tan B, Hussain I *et al.* Design of polymeric stabilizers for size-controlled synthesis of monodisperse gold nanoparticles in water. *Langmuir* 23(2), 885-895 (2007).
163. Dougan JA, Karlsson C, Smith WE, Graham D. Enhanced oligonucleotide-nanoparticle conjugate stability using thioctic acid modified oligonucleotides. *Nucleic Acids Research* 35(11), 3668-3675 (2007).
164. Gomes A, Fernandes E, Lima JL. Fluorescence probes used for detection of reactive oxygen species. *J Biochem Biophys Methods* 65(2-3), 45-80 (2005).
165. Burns JM, Cooper WJ, Ferry JL *et al.* Methods for reactive oxygen species (ROS) detection in aqueous environments. *Aquatic Sciences* 74(4), 683-734 (2012).
166. Louit G, Foley S, Cabillic J *et al.* The reaction of coumarin with the OH radical revisited: hydroxylation product analysis determined by fluorescence and chromatography. *Radiation Physics and Chemistry* 72(2-3), 119-124 (2005).
167. Sherman WR, Robins E. Fluorescence of substituted 7-hydroxycoumarins. *Analytical chemistry* 40(4), 803-805 (1968).
168. Manevich Y, Held KD, Biaglow JE. Coumarin-3-carboxylic acid as a detector for hydroxyl radicals generated chemically and by gamma radiation. *Radiation research* 148(6), 580-591 (1997).
169. Sicard - Roselli C, Brun E, Gilles M *et al.* A new mechanism for hydroxyl radical production in irradiated nanoparticle solutions. *small* 10(16), 3338-3346 (2014).
170. Misawa M, Takahashi J. Generation of reactive oxygen species induced by gold nanoparticles under x-ray and UV Irradiations. *Nanomedicine : nanotechnology, biology, and medicine* 7(5), 604-614 (2011).

171. Hespeels F, Heuskin AC, Scifoni E, Kraemer M, Lucas S. Backscattered electron emission after proton impact on carbon and gold films: Experiments and simulations. *Nuclear Instruments and Methods in Physics Research Section B: Beam Interactions with Materials and Atoms* 401(Supplement C), 8-17 (2017).
172. McMahon SJ, Hyland WB, Muir MF *et al.* Biological consequences of nanoscale energy deposition near irradiated heavy atom nanoparticles. *Scientific reports* 1 18 (2011).
173. Wilson R, Xiaojing Z, Linghong G *et al.* Gold nanoparticle sensitize radiotherapy of prostate cancer cells by regulation of the cell cycle. *Nanotechnology* 20(37), 375101 (2009).
174. Otsuka H, Nagasaki Y, Kataoka K. PEGylated nanoparticles for biological and pharmaceutical applications. *Adv Drug Deliv Rev* 55(3), 403-419 (2003).
175. Lopez-Chaves C, Soto-Alvaredo J, Montes-Bayon M, Bettmer J, Llopis J, Sanchez-Gonzalez C. Gold nanoparticles: Distribution, bioaccumulation and toxicity. In vitro and in vivo studies. *Nanomedicine : nanotechnology, biology, and medicine* 14(1), 1-12 (2018).
176. De Jong WH, Hagens WI, Krystek P, Burger MC, Sips AJ, Geertsma RE. Particle size-dependent organ distribution of gold nanoparticles after intravenous administration. *Biomaterials* 29(12), 1912-1919 (2008).
177. Unezaki S, Maruyama K, Hosoda J-I *et al.* Direct measurement of the extravasation of polyethyleneglycol-coated liposomes into solid tumor tissue by in vivo fluorescence microscopy. *International Journal of Pharmaceutics* 144(1), 11-17 (1996).
178. Stella B, Arpicco S, Peracchia MT *et al.* Design of Folic Acid - Conjugated Nanoparticles for Drug Targeting. *Journal of Pharmaceutical Sciences* 89(11), 1452-1464 (2000).
179. Wu PH, Onodera Y, Ichikawa Y *et al.* Targeting integrins with RGD-conjugated gold nanoparticles in radiotherapy decreases the invasive activity of breast cancer cells. *International journal of nanomedicine* 12 5069-5085 (2017).
180. Fathy MM, Mohamed FS, Elbially N, Elshemey WM. Multifunctional Chitosan-Capped Gold Nanoparticles for enhanced cancer chemo-radiotherapy: An invitro study. *Phys Med* 48 76-83 (2018).
181. Foray N, Colin C, Bourguignon M. 100 years of individual radiosensitivity: how we have forgotten the evidence. *Radiology* 264(3), 627-631 (2012).
182. Bennett BJ, Farber CR, Orozco L *et al.* A high-resolution association mapping panel for the dissection of complex traits in mice. *Genome research* 20(2), 281-290 (2010).
183. Bartek J, Hodny Z. SUMO boosts the DNA damage response barrier against cancer. *Cancer cell* 17(1), 9-11 (2010).
184. Sarangi P, Zhao X. SUMO-mediated regulation of DNA damage repair and responses. *Trends in biochemical sciences* 40(4), 233-242 (2015).
185. Galanty Y, Belotserkovskaya R, Coates J, Polo S, Miller KM, Jackson SP. Mammalian SUMO E3-ligases PIAS1 and PIAS4 promote responses to DNA double-strand breaks. *Nature* 462(7275), 935-939 (2009).

186. Wu J, Lu LY, Yu X. The role of BRCA1 in DNA damage response. *Protein & cell* 1(2), 117-123 (2010).
187. Roos WP, Krumm A. The multifaceted influence of histone deacetylases on DNA damage signalling and DNA repair. *Nucleic Acids Res* 44(21), 10017-10030 (2016).
188. Cortellino S, Xu J, Sannai M *et al.* Thymine DNA glycosylase is essential for active DNA demethylation by linked deamination-base excision repair. *Cell* 146(1), 67-79 (2011).
189. Deplus R, Brenner C, Burgers WA *et al.* Dnmt3L is a transcriptional repressor that recruits histone deacetylase. *Nucleic Acids Res* 30(17), 3831-3838 (2002).
190. Mao Z, Hine C, Tian X *et al.* SIRT6 promotes DNA repair under stress by activating PARP1. *Science* 332(6036), 1443-1446 (2011).
191. Huen MS, Huang J, Leung JW *et al.* Regulation of chromatin architecture by the PWWP domain-containing DNA damage-responsive factor EXPAND1/MUM1. *Molecular cell* 37(6), 854-864 (2010).
192. Castillo MH, Button TM, Doerr R, Homs MI, Pruett CW, Pearce JI. Effects of radiotherapy on mandibular reconstruction plates. *American journal of surgery* 156(4), 261-263 (1988).
193. Alkhatib A, Watanabe Y, Broadhurst JH. The local enhancement of radiation dose from photons of MeV energies obtained by introducing materials of high atomic number into the treatment region. *Medical physics* 36(8), 3543-3548 (2009).
194. Casta R, Champeaux JP, Sence M, Moretto-Capelle P, Cafarelli P. Comparison between gold nanoparticle and gold plane electron emissions: a way to identify secondary electron emission. *Physics in medicine and biology* 60(23), 9095-9105 (2015).
195. Brun E, Cloutier P, Sicard-Roselli C, Fromm M, Sanche L. Damage induced to DNA by low-energy (0-30 eV) electrons under vacuum and atmospheric conditions. *The journal of physical chemistry. B* 113(29), 10008-10013 (2009).
196. Brun E, Sanche L, Sicard-Roselli C. Parameters governing gold nanoparticle X-ray radiosensitization of DNA in solution. *Colloids and Surfaces B: Biointerfaces* 72(1), 128-134 (2009).
197. Liu J, Liang Y, Liu T, Li D, Yang X. Anti-EGFR-Conjugated Hollow Gold Nanospheres Enhance Radiocytotoxic Targeting of Cervical Cancer at Megavoltage Radiation Energies. *Nanoscale research letters* 10 218 (2015).
198. Stefancikova L, Porcel E, Eustache P *et al.* Cell localisation of gadolinium-based nanoparticles and related radiosensitising efficacy in glioblastoma cells. *Cancer Nanotechnol* 5(1), 6 (2014).
199. McMahon SJ, Hyland WB, Muir MF *et al.* Biological consequences of nanoscale energy deposition near irradiated heavy atom nanoparticles. *Scientific reports* 1 18-18 (2011).
200. Sotiropoulos M, Henthorn NT, Warmenhoven JW, Mackay RI, Kirkby KJ, Merchant MJ. Modelling direct DNA damage for gold nanoparticle enhanced proton therapy. *Nanoscale* 9(46), 18413-18422 (2017).

201. Carter JD, Cheng NN, Qu Y, Suarez GD, Guo T. Nanoscale energy deposition by X-ray absorbing nanostructures. *The journal of physical chemistry. B* 111(40), 11622-11625 (2007).
202. Nel A, Xia T, Madler L, Li N. Toxic potential of materials at the nanolevel. *Science* 311(5761), 622-627 (2006).
203. Chompoosor A, Saha K, Ghosh PS *et al.* The role of surface functionality on acute cytotoxicity, ROS generation and DNA damage by cationic gold nanoparticles. *Small* 6(20), 2246-2249 (2010).
204. Cheng NN, Starkewolf Z, Davidson RA *et al.* Chemical Enhancement by Nanomaterials under X-ray Irradiation. *Journal of the American Chemical Society* 134(4), 1950-1953 (2012).
205. Gilles M, Brun E, Sicard-Roselli C. Gold nanoparticles functionalization notably decreases radiosensitization through hydroxyl radical production under ionizing radiation. *Colloids and surfaces. B, Biointerfaces* 123 770-777 (2014).
206. Perquin M, Oster T, Maul A, Froment N, Untereiner M, Bagrel D. The glutathione-related detoxification pathway in the human breast: a highly coordinated system disrupted in the tumour tissues. *Cancer Letters* 158(1), 7-16 (2000).
207. Zheng Q, Yang H, Wei J, Tong JL, Shu YQ. The role and mechanisms of nanoparticles to enhance radiosensitivity in hepatocellular cell. *Biomedicine & pharmacotherapy = Biomedecine & pharmacotherapie* 67(7), 569-575 (2013).
208. Schaeublin NM, Braydich-Stolle LK, Schrand AM *et al.* Surface charge of gold nanoparticles mediates mechanism of toxicity. *Nanoscale* 3(2), 410-420 (2011).
209. Jain S, Coulter JA, Butterworth KT *et al.* Gold nanoparticle cellular uptake, toxicity and radiosensitisation in hypoxic conditions. *Radiotherapy and Oncology* 110(2), 342-347 (2014).
210. Xu W, Luo T, Li P *et al.* RGD-conjugated gold nanorods induce radiosensitization in melanoma cancer cells by downregulating $\alpha\beta 3$ expression. *International journal of nanomedicine* 7 915 (2012).
211. Mackey MA, El-Sayed MA. Chemosensitization of cancer cells via gold nanoparticle-induced cell cycle regulation. *Photochemistry and photobiology* 90(2), 306-312 (2014).
212. Connor EE, Mwamuka J, Gole A, Murphy CJ, Wyatt MD. Gold nanoparticles are taken up by human cells but do not cause acute cytotoxicity. *Small* 1(3), 325-327 (2005).
213. Taggart LE, McMahon SJ, Butterworth KT, Currell FJ, Schettino G, Prise KM. Protein disulphide isomerase as a target for nanoparticle-mediated sensitisation of cancer cells to radiation. *Nanotechnology* 27(21), 215101 (2016).
214. Cui L, Her S, Borst GR, Bristow RG, Jaffray DA, Allen C. Radiosensitization by gold nanoparticles: Will they ever make it to the clinic? *Radiotherapy and Oncology* 124(3), 344-356 (2017).
215. Marill J, Anesary NM, Zhang P *et al.* Hafnium oxide nanoparticles: toward an in vitro predictive biological effect? *Radiation Oncology* 9(1), 150 (2014).

216. Bourseau-Guilmain E, Menard JA, Lindqvist E *et al.* Hypoxia regulates global membrane protein endocytosis through caveolin-1 in cancer cells. *Nature communications* 7 11371-11371 (2016).
217. Subiel A, Ashmore R, Schettino G. Standards and Methodologies for Characterizing Radiobiological Impact of High-Z Nanoparticles. *Theranostics* 6(10), 1651-1671 (2016).
218. Laprise-Pelletier M, Simao T, Fortin MA. Gold Nanoparticles in Radiotherapy and Recent Progress in Nanobrachytherapy. *Adv Healthc Mater* 7(16), e1701460 (2018).
219. Dimitriou NM, Tsekenis G, Balanikas EC *et al.* Gold nanoparticles, radiations and the immune system: Current insights into the physical mechanisms and the biological interactions of this new alliance towards cancer therapy. *Pharmacology & Therapeutics* 178 1-17 (2017).
220. He C, Hu Y, Yin L, Tang C, Yin C. Effects of particle size and surface charge on cellular uptake and biodistribution of polymeric nanoparticles. *Biomaterials* 31(13), 3657-3666 (2010).
221. Chithrani BD, Ghazani AA, Chan WC. Determining the size and shape dependence of gold nanoparticle uptake into mammalian cells. *Nano letters* 6(4), 662-668 (2006).
222. Schuemann J, Berbeco R, Chithrani DB *et al.* Roadmap to Clinical Use of Gold Nanoparticles for Radiation Sensitization. *Int J Radiat Oncol Biol Phys* 94(1), 189-205 (2016).
223. Kumar R, Roy I, Ohulchanskyy TY *et al.* In vivo biodistribution and clearance studies using multimodal organically modified silica nanoparticles. *ACS nano* 4(2), 699-708 (2010).
224. Choi HS, Liu W, Misra P *et al.* Renal clearance of quantum dots. *Nature biotechnology* 25(10), 1165-1170 (2007).
225. Albanese A, Tang PS, Chan WCW. The Effect of Nanoparticle Size, Shape, and Surface Chemistry on Biological Systems. *Annual Review of Biomedical Engineering* 14(1), 1-16 (2012).
226. Huang K, Ma H, Liu J *et al.* Size-dependent localization and penetration of ultrasmall gold nanoparticles in cancer cells, multicellular spheroids, and tumors in vivo. *ACS nano* 6(5), 4483-4493 (2012).
227. Huo S, Ma H, Huang K *et al.* Superior penetration and retention behavior of 50 nm gold nanoparticles in tumors. *Cancer research* 73(1), 319-330 (2013).
228. Chou LY, Chan WC. Fluorescence-tagged gold nanoparticles for rapidly characterizing the size-dependent biodistribution in tumor models. *Adv Healthc Mater* 1(6), 714-721 (2012).
229. Sadauskas E, Danscher G, Stoltenberg M, Vogel U, Larsen A, Wallin H. Protracted elimination of gold nanoparticles from mouse liver. *Nanomedicine: Nanotechnology, Biology and Medicine* 5(2), 162-169 (2009).
230. Abdelhalim MA, Jarrar BM. Histological alterations in the liver of rats induced by different gold nanoparticle sizes, doses and exposure duration. *Journal of nanobiotechnology* 10 5 (2012).
231. Zhang X-D, Wu D, Shen X, Liu P-X, Fan F-Y, Fan S-J. In vivo renal clearance, biodistribution, toxicity of gold nanoclusters. *Biomaterials* 33(18), 4628-4638 (2012).

232. Oberdorster G, Oberdorster E, Oberdorster J. Nanotoxicology: an emerging discipline evolving from studies of ultrafine particles. *Environ Health Perspect* 113(7), 823-839 (2005).
233. Cho EC, Xie J, Wurm PA, Xia Y. Understanding the role of surface charges in cellular adsorption versus internalization by selectively removing gold nanoparticles on the cell surface with a I2/KI etchant. *Nano letters* 9(3), 1080-1084 (2009).
234. Paszek MJ, Dufort CC, Rossier O *et al.* The cancer glycocalyx mechanically primes integrin-mediated growth and survival. *Nature* 511(7509), 319-325 (2014).
235. Hirn S, Semmler-Behnke M, Schleh C *et al.* Particle size-dependent and surface charge-dependent biodistribution of gold nanoparticles after intravenous administration. *European journal of pharmaceuticals and biopharmaceutics : official journal of Arbeitsgemeinschaft fur Pharmazeutische Verfahrenstechnik e.V* 77(3), 407-416 (2011).
236. Perrault SD, Walkey C, Jennings T, Fischer HC, Chan WCW. Mediating Tumor Targeting Efficiency of Nanoparticles Through Design. *Nano letters* 9(5), 1909-1915 (2009).
237. Kudgus RA, Walden CA, McGovern RM, Reid JM, Robertson JD, Mukherjee P. Tuning pharmacokinetics and biodistribution of a targeted drug delivery system through incorporation of a passive targeting component. *Scientific reports* 4 5669-5669 (2014).
238. Perrault SD, Chan WCW. In vivo assembly of nanoparticle components to improve targeted cancer imaging. *Proceedings of the National Academy of Sciences* 107(25), 11194-11199 (2010).
239. Arvizo RR, Miranda OR, Moyano DF *et al.* Modulating pharmacokinetics, tumor uptake and biodistribution by engineered nanoparticles. *PLoS One* 6(9), e24374 (2011).
240. Lin F-S, Chen C-H, Tseng F-G *et al.* Radiotherapy of the excretable radioactive gold nanocomposite with intratumoral injection. *Int J Mater Mech Manuf* 1 265-268 (2013).
241. Parr RG, Pearson RG. Absolute hardness: companion parameter to absolute electronegativity. *Journal of the American Chemical Society* 105(26), 7512-7516 (1983).
242. Pearson RG. Hard and soft acids and bases, HSAB, part 1: Fundamental principles. *Journal of Chemical Education* 45(9), 581 (1968).
243. Sabella S, Carney RP, Brunetti V *et al.* A general mechanism for intracellular toxicity of metal-containing nanoparticles. *Nanoscale* 6(12), 7052-7061 (2014).
244. Sobot D, Mura S, Yesylevskyy SO *et al.* Conjugation of squalene to gemcitabine as unique approach exploiting endogenous lipoproteins for drug delivery. *Nature communications* 8 15678-15678 (2017).
245. Liu Q, Luo Q, Halim A, Song G. Targeting lipid metabolism of cancer cells: A promising therapeutic strategy for cancer. *Cancer Letters* 401 39-45 (2017).
246. Ebert MA, Carruthers B. Dosimetric characteristics of a low-kV intra-operative x-ray source: Implications for use in a clinical trial for treatment of low-risk breast cancer. *Medical physics* 30(9), 2424-2431 (2003).

247. Paunesku T, Woloschak GE. Future Directions of Intraoperative Radiation Therapy: A Brief Review. *Frontiers in oncology* 7 300 (2017).
248. Bakhshabadi M, Ghorbani M, Khosroabadi M, Knaup C, Meigooni AS. A comparison study on various low energy sources in interstitial prostate brachytherapy. *Journal of contemporary brachytherapy* 8(1), 74-81 (2016).
249. Yoo MH, Xu XM, Carlson BA, Gladyshev VN, Hatfield DL. Thioredoxin reductase 1 deficiency reverses tumor phenotype and tumorigenicity of lung carcinoma cells. *The Journal of biological chemistry* 281(19), 13005-13008 (2006).
250. Kim SJ, Miyoshi Y, Taguchi T *et al.* High thioredoxin expression is associated with resistance to docetaxel in primary breast cancer. *Clin Cancer Res* 11(23), 8425-8430 (2005).
251. Voduc KD, Cheang MC, Tyldesley S, Gelmon K, Nielsen TO, Kennecke H. Breast cancer subtypes and the risk of local and regional relapse. *Journal of clinical oncology : official journal of the American Society of Clinical Oncology* 28(10), 1684-1691 (2010).
252. Karapetis CS, Khambata-Ford S, Jonker DJ *et al.* K-ras mutations and benefit from cetuximab in advanced colorectal cancer. *The New England journal of medicine* 359(17), 1757-1765 (2008).
253. Mitsudomi T, Morita S, Yatabe Y *et al.* Gefitinib versus cisplatin plus docetaxel in patients with non-small-cell lung cancer harbouring mutations of the epidermal growth factor receptor (WJTOG3405): an open label, randomised phase 3 trial. *The Lancet. Oncology* 11(2), 121-128 (2010).
254. Jorgensen JT. Companion diagnostics: the key to personalized medicine. Foreword. *Expert review of molecular diagnostics* 15(2), 153-156 (2015).
255. Torres-Roca JF. A molecular assay of tumor radiosensitivity: a roadmap towards biology-based personalized radiation therapy. *Personalized medicine* 9(5), 547-557 (2012).
256. Baumann M, Krause M, Overgaard J *et al.* Radiation oncology in the era of precision medicine. *Nature reviews. Cancer* 16(4), 234-249 (2016).